

# **Study of thermal, electrical and fluid dynamic characteristics of arc plasma devices**

*By*  
**Kailash Chandra Meher**  
**PHYS01200904020**

**Bhabha Atomic Research Centre, Mumbai**

*A thesis submitted to the  
Board of Studies in Physical Sciences*

*In partial fulfillment of requirements  
for the Degree of*

**DOCTOR OF PHILOSOPHY**

*of*

**HOMI BHABHA NATIONAL INSTITUTE**



**April, 2015**

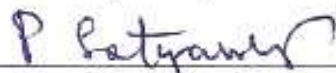
# Homi Bhabha National Institute

## Recommendations of the Viva Voce Committee

As members of the Viva Voce Committee, we certify that we have read the dissertation prepared by **Kailash Chandra Meher** entitled "Study of thermal, electrical and fluid dynamic characteristics of arc plasma devices" and recommend that it may be accepted as fulfilling the thesis requirement for the award of Degree of Doctor of Philosophy.

Chairman – Dr. P Satyamurty

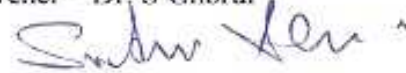
Date:



14/8/15

Guide / Convener – Dr. S Ghorui

Date:

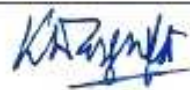


14/8/15

Co-guide - ---

Date:

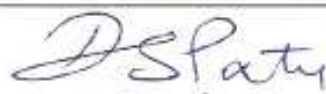
Member 1 – Dr. K Dasgupta



Date:

14/8/15

Member 2- Dr. D S Patil



Date:

14.08.15

Member N – Dr. U Vhandarkar



Date:

14<sup>th</sup> August 2015

Final approval and acceptance of this thesis is contingent upon the candidate's submission of the final copies of the thesis to HBNI.

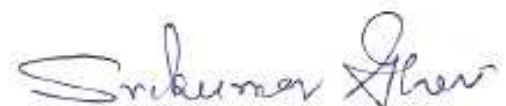
I hereby certify that I have read this thesis prepared under my direction and recommend that it may be accepted as fulfilling the thesis requirement.

Date:

14/08/15

Place:

Mumbai



Guide

## **STATEMENT BY AUTHOR**

This dissertation has been submitted in partial fulfillment of requirements for an advanced degree at Homi Bhabha National Institute (HBNI) and is deposited in the Library to be made available to borrowers under rules of the HBNI.

Brief quotations from this dissertation are allowable without special permission, provided that accurate acknowledgement of source is made. Requests for permission for extended quotation from or reproduction of this manuscript in whole or in part may be granted by the Competent Authority of HBNI when in his or her judgment the proposed use of the material is in the interests of scholarship. In all other instances, however, permission must be obtained from the author.

Kailash Chandra Meher

## **DECLARATION**

I, hereby declare that the investigation presented in the thesis has been carried out by me. The work is original and has not been submitted earlier as a whole or in part for a degree / diploma at this or any other Institution / University.

Kailash Chandra Meher

DEDICATIONS

*Dedicated*

*to.....*

*..... my  
family*

## ACKNOWLEDGEMENTS

At the outset, I thank my Ph D guide, Dr. S Ghorui, for his luminous guidance and encouragement in executing this project from conception to completion. I feel fortunate for being his first student and getting his undivided attention. This is the result of his innovative ideas, restless effort and extraordinary guidance which leads this work to completion.

I would like to thank my Doctoral committee chairman, Dr. P. Satyamurthy Head, ATDS, BARC and other members Dr. K Dasgupta, Associate Director, BTDG, BARC, Dr. D S Patil (Scientist, BARC), Dr. U V Bhandarkar (Associate Professor, IITB) for providing their valuable time and suggestion.

My sincere thanks to Dr. P V A Padmanabhan, Head, TPTS, L&PTD, BARC and Dr. L. M. Gantayet, former Dir. BTDG, BARC for providing facility and support for this work.

I am highly obliged to Shri. S. N. Sahasrabudhe, Retd. scientist, L&PTD, BARC for his constant encouragement and training on the experimental system. His friendly, open-minded and cooperative attitude proved to be an excellent booster in accomplishing this work. My heartfelt thanks to Dr. K Patel , Shri A. K. Tak, Mrs. N Tiwari, (scientist from L&PTD, BARC), Mrs. S B Punjabi, and Miss G Dhamale for their unconditional and kind support during the course of the work.

I would like to express my gratitude, deep regards and sincere thanks to my former Doctoral Committee Chairman, Dr. A. K. Das, former Head, L&PTD, BARC, for providing me the chance to work on the project and support in my work.

Shri. Y Chakravarthy, Shri. S bhandari, Miss V Chaturvedi, Shri. A Pragatheeswaran, Shri. Pravat Swain, Shri. Sushil Kumar, Shri. Kiran Kulkarni, Shri.

Pravin Rai, Shri. Deepak Kumar and Shri. Vikas Tiwari, Shri R Kar, Miss A Bute, Mrs. A Shukla, Mrs. J Bishwal, Mr. P K Soni, Mr. N C Gaur, Mr. D. P. Chopade, Mr. A.N. Sen, Mr. K P Kedare, Mr. D K Baskey, Mr. S. T. Thakur, Mr. V. S. Gosavi, T S Hire, Mr. O Yadav and Mr. K S Ahire extended their friendly support and suggestions whenever I approached them.

My special thanks to my friends Shri. A Majhi, Dr. S K Mohanta, Dr. P K Rath, Shri M Gaddad, Shri D K Gupta, R S Khadane and A D Parmar for their continuous inspiration and encouragement to complete the work.

It is not possible to mention all the names of the persons who offered their unconditional support to me. Here I thank all those who have helped me with my work in the Laser and Plasma technology Division.

The financial support given by the DAE, Government of India, in terms of a fellowship during the course of this work is gratefully acknowledged.

I also appreciate the kind support and affection that I got from all my friends and kept me focused on my work.

My family members have always inspired me to stay on track and it gives me immense pleasure to dedicate this work to my family.

Kailash Chandra Meher

# CONTENTS

	Page No.
Synopsis	xii
List of Publications	xx
List of Figures	xxii
List of Tables	xxxv
CHAPTER 1: Introduction	1-30
1.1 Definition and Types of Plasma	2
1.2 DC Plasma Devices	6
1.3 Definition of the problem	10
1.4 Relevance of the problem	11
1.5 Status of the problem	12
1.6 Scope of the work	29
1.7 Organization of the thesis	29
CHAPTER 2: Experimental Setup	31-51
2.1 Introduction	32
2.2 Experimental setup	33
2.3 Plasma Torch	36
2.4 Power supply	38
2.5 Double Calorimeter	41
2.6 Resistance Temperature Detector	43
2.7 Spectrograph	44

2.8 Optical Fibre	46
2.9 Oscilloscope	47
2.10 Voltage Divider Circuit	48
2.11 10X Probe	49
2.12 Chilled Water Supply Unit	50
CHAPTER 3: Axial Evolution of Radial Heat Flux Profiles	52-74
Transmitted by Atmospheric Pressure Nitrogen and Argon Arcs	
3.1 Introduction:	53
3.2 Determination of the profile parameters	59
3.3 Experimental Set-up	60
3.4 Results and discussion	61
3.5 Conclusions	73
CHAPTER 4: Temperature Measurement of Nitrogen and Argon Plasma Jet	75-99
4.1 Introduction	76
4.2 Boltzmann Plot Method	80
4.3 Experimental Setup	83
4.4 Spectroscopy of Argon Plasma	86
4.5 Spectroscopy of Nitrogen Plasma	87
4.6 Calibration of Spectrograph	88
4.7 Results and Discussion	90

	4.8 Conclusions	98
CHAPTER 5:	Study of Instability in Nitrogen and Argon Plasma Jets	100-112
	5.1 Introduction	101
	5.2 Experimental Setup	104
	5.3 Diagnostic Tools	105
	5.4 Results and Discussion	107
	5.5 Conclusions	112
CHAPTER 6:	Thermodynamic and Transport Properties of Nitrogen Plasma under Thermal Equilibrium and Non-equilibrium Conditions	113-179
	6.1 Introduction	114
	6.2 Determination of Thermodynamic Properties	116
	6.3 Determination of Transport Properties	125
	6.4 Results and Discussion	138
	6.5 Conclusions	178
CHAPTER 7:	Numerical modelling of atmospheric nitrogen plasma torch under thermal equilibrium and non- equilibrium condition	180-205
	7.1 Introduction	181
	7.2 Governing Equation	183

	7.3 Method of Solution	197
	7.4 The Boundary Conditions	198
	7.5 Results and Discussion	200
	7.6 Conclusions	205
CHAPTER 8:	Conclusions	206-211
	8.1 Summary and Conclusions	207
	8.2 Scope for Future Work	211
Bibliography		212-224

## SYNOPSIS

Plasmas having nearly identical electron and heavy species temperatures but significantly different radiation temperatures are termed as thermal plasmas [1]. Such plasmas are usually formed in atmospheric pressure gaseous electric discharges and characterised by their high energy density, high temperature, easier process control and flexibility in producing chemically inert as well as reactive environment for high temperature plasma chemistry and plasma processing. Atmospheric pressure arc plasma devices, subject of this study, belong to this thermal plasma category. The devices find wide applications in industries like cutting, welding, melting, surface treatment, waste treatment, gasification, metallurgy, thin film technology, nano-material synthesis, novel material production, etc. [1-6]. Steep gradients in plasma quantities, extremely high temperature at the core, high fluid dynamic flow fields, highly nonlinear variation in plasma properties and mutual interactions among thermal, chemical, electric, magnetic and fluid dynamic fields are some of the characteristic features of such systems. The nature of the plasma jet delivered by an arc determines the process design, the quality of the processing work done and its suitability for a particular application. Numbers of attempts have been made in the past to study thermal, electrical and fluid dynamic characteristics of different arc plasma devices. However, most of the attempts primarily considers argon as plasma gas and operation at a power level below 20 kW [7-11]. Rarely any studies are made at higher power levels, where processing of high temperature ceramic oxides are possible. Data on thermal, electrical and fluid dynamic characteristics of plasma systems other than Argon are severely limited and serve as the primary driving force for the present study.

The study primarily focuses on nitrogen arcs together with argon over a range of power levels and operating parameters. Industrial nitrogen plasma torches have the advantages of operating with usual tungsten based refractory electrodes and radical rich non-oxidizing high temperature environment for enhanced plasma chemistry and efficient processing. Being a molecular gas, Nitrogen naturally offer higher voltage drop compared to argon for the same electrode configuration and easily associates higher power.

Major contributions from the study include (a) Design and development of a segmented electrode plasma torch suitable for operation with nitrogen as well as argon and capable of operating with electrical power beyond 50 kW. (b) Design and development of a double calorimetric setup for experimental measurement of delivered heat flux profiles under different operating conditions. (c) Development of a CFD model of the developed torch for understanding the physics behind characteristic features observed. (d) Computation of thermodynamic and transport properties of nitrogen plasma under thermal equilibrium and non-equilibrium conditions using Chapman-Enskog Approach. [12,14] (e) CFD simulation of the nitrogen plasma torch using the computed thermodynamic and transport properties and analysis of the observed distribution of temperature, velocity, pressure and potential inside the torch under different operating conditions. (f) Experimental estimation of the heat flux profile delivered by the torch under different operating conditions using double calorimetric setup with argon and nitrogen as plasma gas. (g) Experimental determination of temperature of the emanating plasma jet using emission spectroscopy technique. (h) Study of the features of instabilities exhibited by the torch under different operating conditions and working gases.

While the spectrum of information extracted on thermal, electrical and fluid dynamic characteristics of nitrogen arc devices may be used for newer applications in the frontier areas of plasma processing, the same obtained for argon arc devices are used in the study to enhance credibility of the obtained results through comparison with existing data and generating data in the extended regime of operation where availability of data is scarce. The study offers a detail understanding of the nitrogen plasma devices from both physics point of view as well as technological applications. The global scenario, major objectives, method of approach, design and development of the experimental systems and a systematic account of the results obtained from experimental as well as theoretical studies are presented in the thesis.

With a brief introduction, chapter-1 presents the importance, relevance, objective, scope and current status of the problem considered. Different types of plasma devices, their classifications, underlying principles and important application areas are briefly outlined. Various advantages as well as disadvantages of arc plasma devices in comparison to its competing technologies are presented. Plasma being a current carrying fluid, complexity in behaviour arising out of interaction among thermal, fluid dynamic and electromagnetic field components are also discussed. Necessity of computational fluid dynamic (CFD) simulation for better understanding of such systems and important aspects of experimental studies and associated complexities are outlined. Existing lacunas in understanding, unexplained facts and important but unexplored areas that served as the major driving force behind the research carried out are highlighted. In summary, the chapter sets the background and the motivation for the work presented in the subsequent chapters.

Chapter-2 presents different experimental setups used in this study. The components primarily include a DC plasma torch, an IGBT based power supply, water cooling and water supply system, temperature monitoring system, torch positioning system, concentric double calorimeter, spectrograph with optical fibre, oscilloscope, voltage divider circuit and a computer for data acquisition and control. Description of important features like working principle, experimental procedure, advantages and limitations of the used devices are provided in brief. The segmented electrode plasma torch served as the key device for plasma generation and the double calorimeter played the lead role in the measurement of the plasma heat flux profiles. Special attentions are paid to these two devices which are designed and developed in-house. The spectrograph in association with the computer recorded the spectral data for emission spectroscopic measurement of plasma temperature. The voltage divider circuit together with a multichannel oscilloscope recorded the inherent instability behaviour of the plasma under various operating conditions. This chapter may be considered as a complete reference for all the equipments used in different experiments in this study.

Chapter-3 describes the double calorimetric technique used in determination of heat flux profiles transmitted by a plasma jet under different operating conditions. Axial evolutions of radial heat flux profiles in atmospheric pressure DC non-transferred Argon and Nitrogen plasma jet are determined using the double calorimetric technique. Results are presented for power levels suitable for processing of high temperature ceramic oxides, where the heat flux data reported in literature is rare. Variations of the profile widths and the profile maxima are presented as a function of axial distance as well as power. Relatively uniform profile width over

prolonged axial distance for Nitrogen plasma compared to Argon is an important observation which has the potential to offer much longer dwell time of the injected particles inside the plasma, avoiding the problem of un-melts, especially for ceramics. A comparative study of the heat flux profiles for Argon and Nitrogen plasma is presented. Obtained results are compared with the data reported in literature.

Chapter-4 outlines the details of the optical emission spectroscopic technique used in determination of plasma temperature following Atomic Boltzmann plot method and presents the obtained results. Variation of plasma temperature over a range of axial distances, gas flow rates and power levels are studied for both argon and nitrogen. Typically the axial plasma temperature profile is found to peak near the nozzle exit and decrease as one goes downstream. However, under certain operating conditions a dip in the temperature in the immediate vicinity of the nozzle exit is confirmed. Such dips are usually observed at higher currents where a sharp expansion of the jet is associated immediately after the nozzle exit. Appropriate discussions are provided to explain all the observed facts.

Chapter-5 presents the features of the inherent instabilities observed under different operating conditions in nitrogen and argon plasma torches. The physical and operational state of an arc plasma system is best described in terms of its static and the dynamic characteristics. The static characteristics normally indicate the steady state behaviour whereas the dynamic characteristics describe the evolution of the system behaviour with time. A systematic study of the observed instabilities arising out of interactions among the electromagnetic, fluid dynamic and the thermal fields leading to apparent erratic fluctuation of the plasma quantities inside the arc plasma devices is presented in this chapter. Such instabilities profoundly affect the system performance

and process quality in most of the plasma processing applications. The challenge in development of the next generation high performance arc plasma devices rests on understanding the origin of such instabilities, predicting the regime of stable/unstable operation and determining the control parameters for the excitation or elimination of these instabilities. The chapter summarizes the relevant features observed experimentally in nitrogen and argon plasma systems under different operating regimes with the help of standard non-linear dynamic tools like time series, phase space dynamics and frequency spectra.

Chapter-6 provides the details of the computational procedures used in finding the thermodynamic and transport properties of the nitrogen plasma, for incorporating them in the CFD simulation. The thermodynamic and transport properties of the plasma are indispensable prerequisite for any investigation in plasma chemistry and plasma processing. For CFD simulation in a reactive environment like plasma with mutually interacting electric and magnetic field incorporated with varying degree of temperature, pressure, species, convective and diffusive fluxes, the thermodynamic and transport properties of the plasma need to be computed and updated at every grid point in every iteration as the simulation continues. In the computation, the plasma is assumed to be composed of seven species, namely,  $N_2$ ,  $N_2^+$ ,  $N$ ,  $N^+$ ,  $N^{++}$ ,  $N^{+++}$  and electron. Variation of species densities, mass densities, specific heat, enthalpy, viscosity, thermal conductivity, collision frequency and electrical conductivity as a function of temperature, pressure and different degree of temperature non-equilibrium are computed following the first order perturbation theory of Chapman and Enskog. In the computation, the electron temperature ranges from 300 K to 45,000 K, the ratio of electron temperature ( $T_e$ ) to the heavy particle temperature ( $T_h$ ) ranges from 1 to 30

and the pressure ranges from 0.1 to 7 atmospheres. Obtained results at atmospheric pressure under thermodynamic equilibrium ( $T_e = T_h$ ) are compared with available data in literature and an excellent agreement is observed.

Chapter-7 describes the CFD modelling of a segmented electrode DC plasma torch having seven segments, operating with nitrogen as the plasma gas in the current range of 150A to 800A. Under two-temperature consideration, the system is described by usual Navier-Stokes equations with source terms appropriately modified by electrically conducting nature of the plasma and the associated electromagnetic body forces. The energy equation is split into two parts: one for electrons and the other for the rest of the particles in the system. A finite volume code in combination with a two-temperature property routine (described in chapter-3) solves the region inside the torch with appropriate boundary conditions. A SIMPLE like algorithm solves the associated Navier-Stokes equations in association with the property routine. Governing equations, boundary conditions and the methodology used in the modelling are presented in this chapter. Distribution of temperature, velocity, enthalpy, pressure, potential and current density as obtained from the study under thermal equilibrium and non-equilibrium conditions are discussed and compared with the experimental results.

Chapter-8 summarizes the important conclusions and the scope for future works.

## **References**

1. Boulos M.I., Fauchais P., Pfender E, "Thermal Plasmas, Fundamentals and applications", Vol1, Plenum Press, New-York(1994).

2. Pfender E, "Thermal Plasma Technology: Where Do We Stand and Where Are We Going?", *Plasma Chemistry and Plasma Processing*, **19** 1-31(1999)
3. Fauchais P and Vardelle A, "Pending problems in thermal plasmas and actual development", *Plasma Phys. Control Fusion* **42**, B365-B383(2000)
4. Fauchais P, Montavon G, Vardelle M, Cedelle J, "Developments in direct current plasma spraying", *Surface & Coatings Technology* **201**, 1908–1921(2006)
5. Fauchais P, "Understanding plasma spraying", *J. Phys. D: Appl. Phys.* **37**,R86–R108((2004)
6. Monerie-Moulin F Gitzhofer F Fauchais P and Boulos M, *Thermal Plasma Applications in Minerals Metallurgical Processing (Warrendale, PA: Minerals, Metals and Material Society)* ed N El-Kaddah pp 125(1992)
7. Kishigami T Heberlein J V and Pfender E *Int. Symp. On plasma chemistry - 10 (Bochum)* 1.3-11 pp 1(1991)
8. Ghorui S, Das A K and Venkatramani N, "Study of stagnation enthalpy profiles in a plasma plume: comparison between computation and experiments", *Plasma Sources Sci. Technol.* **9** 108–115, (2000)
9. Asmann M, Wank A, Kim H, Heberlein J and Pfender E 2001 *Plasma Chem. Plasma Process.* **21** 37 (2001)
10. Meng X Pan W Zhang W and Wu C 2001 *Plasma Sci. and Technol.* **3** 953 (2001)
11. Tu X Yu L Yan J Cen K and Cheron B 2008 *Appl. Phys. Letters* **93** 151501(2008)
12. Hirschfelder J. O, Curtis C. F, and Bird R. B, " *Molecular Theory of Gases and Liquids*", (Wiley, New York, 1954).
- 13S. Chapman and T. G. Cowling," *The Mathematical Theory of Non- Uniform Gases*", (Cambridge University Press, Cambridge, 1952).

14. Meher K.C, Tiwari N, Ghorui S and Das A K, "Multi-Component Diffusion Coefficients in Nitrogen Plasma Under Thermal Equilibrium and Nonequilibrium Conditions", *Plasma Chem Plasma Process* 34, 949–974(2014)

**Publications in Refereed Journal:**

**a. Published**

1. Meher K C, Tiwari N, Ghorui S and Das A K, Multi-Component Diffusion Coefficient in Nitrogen Plasma Under Thermal Equilibrium and Non-Equilibrium Condition, *Plasma Chemistry and Plasma Processing*, Vol.-34, pp.-949–974, 2014
2. Meher K C, Tiwari N, Ghorui S and Das A K Axial Evolution of Radial Heat Flux Profile in Atmospheric Pressure Argon and Nitrogen Arcs, *Plasma Sources Sci. Technol. Vol.- 23*, pp. 065017, 2014
3. Meher K C, Tiwari N and Ghorui S, Thermodynamic and transport properties of nitrogen plasma under thermal and chemical non-equilibrium, *Plasma Chemistry and Plasma Processing*, 1090-015-9615,2015 ( in. web)

**c. Under preparation:**

1. Meher K C, Tiwari N and Ghorui S, Numerical modeling of segmented electrode nitrogen plasma torch under thermal equilibrium and non-equilibrium conditions,

**d. Symposium Publications:**

1. Meher K C, Ghorui S and Das A K, Effect of Chemical Non-Equilibrium on Thermodynamic and Transport Properties of Nitrogen Plasma, Proceedings of 26<sup>th</sup> National Conference on Plasma Science and Technology, Birla Institute of Technology, Patna, December, 2011
2. Meher K C, Ghorui S and Das A K, Study of Thermal, Fluid Dynamic and Active Species Characteristics of DC Segmented Electrode Arc Plasma Torches, Proceedings of 27<sup>th</sup> National Conference on Plasma Science and Technology, Pondicherry University, Pondicherry , December, 2012.
3. Meher K C, Ghorui S and Das A K, Study of Binary, Thermal and Ambipolar Diffusion Coefficient in Non-equilibrium Nitrogen Plasma, Proceedings of 28<sup>th</sup> National Conference on Plasma Science and Technology, Kalinga Institute of Information Technology, Odisha, December, 2013
4. Meher K C, Ghorui S and Das A K, Stagnation Enthalpy Profiles of A Plasma Jet Under Normal and Oblique Incidence, 1<sup>st</sup> Plasma Scholars Colloquium, Institute of Plasma Research, Gandhinagar, Gujrat, July 2012
5. Meher K C, Ghorui S, Sahasrabudhe S N and Das A K, Study of Inherent Instabilities in Argon and Nitrogen Plasma Torches, 2<sup>nd</sup> Plasma Scholars Colloquium, CEERI Pilani, Rajasthan, July 2013
6. Meher K C, Ghorui S, Sahasrabudhe S N and Das A K, Heat flux characterization of argon and nitrogen plasma, NSEP MI, Pune, February, 2014

Signature of Student:

Date:

Doctoral Committee:

S. No.	Name	Designation	Signature	Date
1	Dr. P. Satyamurthy, OS & Head, ATDS, BARC	Chairman	P Satyamurthy	15/7/14
2	Dr. S. Ghorui, SO(G), L&PTD, BARC	Guide & Convener	S Ghorui	15/7/14
3	Dr. K. Dasgupta, OS & Head L&PTD, BARC	Member	Not present	
4	Dr. D. S. Patil, OS and Head PPS, L&PTD, BARC	Member	D S Patil	15-7-14
5	Dr. U.V. Bhandarkar, Dept. of Mech. Engg, IITB	Member	U V Bhandarkar	15/7/14.

AK Mahanta  
24-12-2014

## List of figures

Figure Number	Figure Caption	Page Number
Fig. 1.1	Classification of plasma depending on electron number density and electron temperature	2
Fig.1.2	Variation of electron and heavy particle temperature in arc plasma devices	4
Fig.1.3	Classification of arc plasma devices	5
Fig.1.4	Transferred and non-transferred arc mode of operation for DC	5
Fig.1.5	Application areas of DC plasma torches	6
Fig. 1.6	Design and working of simplest DC plasma torche	7
Fig. 2.1	Schematic diagram of the complete experimental setup	33
Fig. 2.2	Photograph of the experimental setup in operating condition	34
Fig. 2.3 (a)	Image of impinging argon plasma jet	35
Fig. 2.3 (b)	Impinging nitrogen plasma jet and OES setup	35
Fig. 2.4 (a)	Schematic figure of the plasma torch	36
Fig. 2.4 (b)	Photograph of the plasma torch	36
Fig. 2.5	Power supply and control unit	39
Fig. 2.6 (a)	The double calorimeter assembly	42
Fig. 2.6 (b)	Top view of calorimeters	42
Fig. 2.7	Calorimeter assembly	42

Fig. 2.8	RTD PT100	43
Fig.2.9 (a)	The spectrograph	45
Fig.2.9 (b)	Internal ray diagram of spectrograph	45
Fig. 2.10	The optical fibre	46
Fig 2.11	The oscilloscope	47
Fig. 2.12	Circuit diagram of voltage divider circuit	48
Fig.2.13 (a)	The 10X probe	49
Fig.2.13 (b)	Circuit diagram of the probe	49
Fig. 2.14	Chilled water supply unit	50
Fig. 2.15	Chilled water supply unit water flow diagram	51
Fig. 3.1 (a)	Image of the nitrogen plasma jet	55
Fig. 3.1 (b)	Image of the argon plasma jet	55
Fig. 3.2 (a)	The experimental setup	60
Fig. 3.2 (b)	Image of the nitrogen plasma jet impinging on a double calorimeter	60
Fig. 3.2 (c)	Detail schematic of the plasma torch transmitting the plasma jet.	60
Fig.3.3	V-I characteristics of the torch in Argon and Nitrogen plasma.	62
Fig.3.4	Variation of heat flux distribution of Argon plasma with axial distance at power level of (a) 6.6 kW, (b) 10.8 kW, (c) 15.8 kW, (d) 20.0 kW, (e) 24.9 kW, (f) 30.4 kW, (g) 40.0 kW, (h) 45.4 kW and (i) 52.0 kW. The gas flow rate is 30	64

	slm	
Fig. 3.5	Variation of the radial heat flux profile as a function of power at the three axial locations (a) 2.5 cm (b) 3.5 cm and (c) 4.5 cm.	65
Fig.3.6	Variation of heat flux distribution of Nitrogen plasma with axial distance at power levels of (a) 31.9 kW, (b) 41.6 kW, (c) 47.2 kW and (d) 51.0 kW. The gas flow rate is 17.5 slm.	66
Fig.3.7	Variation of heat flux distribution of Nitrogen plasma with power level at axial distance of (a) 0.15 m, (b) 0.10 m and (c) 0.05 m from nozzle exit respectively. The gas flow rate is 17.5 slm.	66
Fig.3.8	Variation of $\Phi_0$ for Argon plasma with respect to (a) power and (b) axial distance. The voltage - current values are 66 V - 100 A, 72 V - 150 A, 75 V - 200 A, 80 V - 250 A, 83 V - 300 A, 87 V - 350 A, 100 V - 400 A, 101 V - 450 A and 104 V - 500 A. The gas flow rate and nozzle diameter are 30 slm and 0.010 m respectively.	67
Fig.3.9	Variation of maximum value of heat flux for Nitrogen plasma with respect to (a) power and (b) axial distance. The voltage - current values are 156 V - 205 A, 160 V - 262 A, 159 V - 296 A and 161 V - 317 A. The gas flow rate and nozzle diameter are 17.5 slm and 0.010m respectively.	68
Fig.3.10	Variation of $R_g$ in Argon with (a) power and (b) axial distance. The voltage - current values with increasing power	70

are 66 V - 100 A, 72 V - 150 A, 75 V - 200 A, 80 V - 250 A, 83 V - 300 A, 87 V - 350 A, 100 V - 400 A, 101 V - 450 A and 104 V - 500 A. The gas flow rate and nozzle diameter are 30 slm and 0.010 m respectively.

Fig.3.11	Variation of $R_g$ in Nitrogen with (a) power and (b) axial distance. The voltage - current values are 156 V - 205 A, 160 V - 262 A, 159 V - 296 A and 161 V - 317 A. The gas flow rate and nozzle diameter are 17.5 slm and 0.010m respectively.	70
Fig.3.12	Comparison of profile parameters of Argon plasma with data reported in literature. (a) Variation of with axial distance: the curves indexed (a) to (i) correspond to present study, the rests are from literature (b) Variation of $R_g$ with axial distance. Figures in the brackets indicate electrical power input corresponding to different curves as intercepted by the arrow	72
Fig. 4.1(a)	A typical Boltzmann plot for Argon plasma	81
Fig. 4.1(b)	A typical Boltzmann plot for Nitrogen plasma	81
Fig. 4.2	Schematic of the experimental setup	82
Fig. 4.3	Actual experimental setup	83
Fig. 4.4	Schematic of the imaging spectrograph	84
Fig. 4.5(a)	Typical argon spectrum	84
Fig. 4.5(b)	Typical nitrogen spectrum	85

Fig. 4.6	Schematic of the atomic transitions in Argon producing the considered atomic line radiation	87
Fig. 4.7	Schematic of the atomic transitions in Nitrogen producing the considered atomic line radiation	89
Fig. 4.8	Wavelength of radiation emitted by calibration lamp	89
Fig. 4.9	Schematic for the spectrograph calibration.	90
Fig. 4.10	Variation of nozzle exit temperature of Argon plasma.	91
Fig. 4.11	Axial temperature profile of argon plasma at 15 slpm gas flow rate.	93
Fig. 4.12	Axial temperature profile of argon plasma at 20 slpm gas flow rate	94
Fig. 4.13	Axial temperature profile of argon plasma at 25 slpm gas flow rate	95
Fig. 4.14	Variation of axial temperature in nitrogen plasma jet at 15 slpm of gas flow rate	96
Fig. 4.15	Variation of axial temperature in nitrogen plasma jet at 15 slpm of gas flow rate	97
Fig. 4.16	Variation of central axis temperature of nitrogen plasma at the nozzle exit as a function of arc current and comparison with simulation results [chaper-7].	98
Fig. 5.1	plasma generation in DC plasma torch	102
Fig. 5.2	Experimental arrangement for acquiring voltage fluctuation data	104
Fig.5.3	Circuit diagram of the voltage divider circuit	105

Fig. 5.4	Features of voltage instability in Argon as a function of gas flow rate at a fixed arc current.	109
Fig. 5.5	Features of voltage instability in Argon as a function of current at a fixed gas flow rate of 30slpm	110
Fig. 5.6	Features of voltage instability in Nitrogen plasma at the gas flow rate of 15 slpm and different arc currents.	111
Fig. 6.1	Algorithm for computing partition function	117
Fig. 6.2	Algorithm for computing the thermodynamic and transport properties	119
Fig. 6.3	Summary of the schemes used for computation of different diffusion coefficients under the framework of two-temperature non-equilibrium plasma.	132
Fig. 6.4	Mole fraction of different species in nitrogen plasmas under different degrees of non-equilibrium at atmospheric pressure: (a) $T_e/T_h=1$ , (b) $T_e/T_h=2$ , (c) $T_e/T_h=5$ , (d) $T_e/T_h=10$ .	140
Fig. 6.5	Variation of total number density as a function of electron temperature with pressure as parameter.	140
Fig. 6.6	Electron number density variation: (a) 0.1 atmosphere, (b) 1 atmosphere, (c) 4 atmospheres, (d) 7 atmospheres. Number associated with each curve indicates $T_e/T_h$ ratio.	142
Fig. 6.7	Total enthalpy variation: (a) 0.1 atmosphere, (b) 1 atmosphere, (c) 4 atmospheres, (d) 7 atmospheres. Number associated with each curve indicates $T_e/T_h$ ratio.	142

Fig. 6.8	Variation of specific heat ( $c_p$ ) of electrons as a function of temperature: (a) 0.1 atmosphere, (b) 1 atmospheres, (c) 4 atmospheres, (d) 7 atmospheres. Number associated with each curve indicates $T_e/T_h$ ratio.	143
Fig. 6.9	Variation of specific heat of heavy particles as a function of temperature: (a) 0.1 atmosphere (b) 1 atmosphere, (c) 4 atmospheres, (d) 7 atmospheres. Number associated with each curve indicates $T_e/T_h$ ratio.	143
Fig. 6.10	Variation of binary diffusion coefficients (BDC) of the considered species in nitrogen plasma as a function of electron temperature at $P=1$ atm.	147
Fig. 6.11	Behaviour of selected general diffusion coefficients (GDC) as a function of electron temperature and thermal non-equilibrium at $P=1$ atm.	152
Fig. 6.12	Behaviour of general ambipolar diffusion coefficients (GADC) as a function of electron temperature and thermal non-equilibrium at $P=1$ atm.	157
Fig. 6.13	Behaviour of general ambipolar diffusion coefficients (GADC) as a function of electron temperature and thermal non-equilibrium at $P=1$ atm.(continued)	158
Fig. 6.14	Behaviour of general ambipolar diffusion coefficients (GADC) as a function of electron temperature and thermal non-equilibrium at $P=1$ atm.	159
Fig. 6.15	Variation of thermal diffusion coefficients (TDC) of	160

different species in nitrogen plasma as a function of electron temperature at three different pressures: 0.1 Atm, 1 atm and 2 atm.

Fig. 6.16	Variation of thermal ambipolar diffusion coefficients (TADC) of the species in nitrogen plasma as a function of electron temperature at three different pressures: 0.1 Atm, 1 atm and 2 atm.	161
Fig. 6.17	Comparison of diffusion coefficient data (a) Thermal diffusion coefficient of electron (b) Binary diffusion coefficient involving electron and first ion of nitrogen (c) Binary diffusion coefficient involving nitrogen atoms and (d) Binary diffusion coefficient involving nitrogen atom and first ion of nitrogen. In each graph, solid lines present results of this work and symbols present data reported in literature. Obtained results are in excellent agreement with most of the recently calculated results.	164
Fig. 6.18	Components of the thermal conductivity of nitrogen under thermal and chemical equilibrium at atmospheric pressure	165
Fig. 6.19	Translational thermal conductivity of electrons: (a) 0.1 atmosphere, (b) 1 atmosphere, (c) 4 atmospheres, (d) 7 atmospheres. Number associated with each curve indicates $T_e/T_h$ ratio.	166
Figure 6.20	Translational thermal conductivity of heavy particles (a) 0.1 atmosphere, (b) 1 atmosphere, (c) 4 atmospheres, (d) 7	166

atmospheres. Number associated with each curve indicates  $T_e/T_h$  ratio.

- Figure 6.21 Reactive thermal conductivity of electrons: (a) 0.1 atmosphere, (b) 1 atmosphere, (c) 4 atmospheres, (d) 7 atmospheres. Number associated with each curve indicates  $T_e/T_h$  ratio. 167
- Figure 6.22 Reactive thermal conductivity of heavy particles: (a) 0.1 atmosphere, (b) 1 atmosphere, (c) 4 atmospheres, (d) 7 atmospheres. Number associated with each curve indicates  $T_e/T_h$  ratio. 167
- Figure 6.23 Variation of total thermal conductivity as a function of  $T_e$ ,  $\theta$  and pressure: (a) 0.1 atmosphere, (b) 1 atmosphere, (c) 4 atmospheres, (d) 7 atmospheres. Number associated with each curve indicates  $T_e/T_h$  ratio. 168
- Figure 6.24 Variation of electrical conductivity as a function of  $T_e$ ,  $\theta$  and pressure: (a) 0.1 atmosphere, (b) 1 atmosphere, (c) 4 atmospheres, (d) 7 atmospheres. Number associated with each curve indicates  $T_e/T_h$  ratio. 169
- Figure 6.25 Variation of viscosity as a function of  $T_e$ ,  $\theta$  and pressure (a) 0.1 atmosphere, (b) 1 atmosphere, (c) 4 atmospheres, (d) 7 atmospheres. Number associated with each curve indicates  $T_e/T_h$  ratio. 169
- Figure 6.26 Volumetric collision frequency as a function of  $T_e$ ,  $\theta$  and pressure: (a) 0.1 atmosphere, (b) 1 atmosphere, (c) 4 170

atmospheres, (d) 7 atmospheres. Number associated with each curve indicates  $T_e/T_h$  ratio.

Figure 6.27(a)	Figure 6.27(a) Comparison of calculated mass density with previously reported results	171
Figure 6.27(b)	Figure 6.27 (b) Comparison of calculated enthalpy with previously reported results	172
Figure 6.27(c)	Figure 6.27 (c) Comparison of calculated specific heat with previously reported results	172
Figure 6.27(d)	Figure 6.27 (d) Comparison of calculated electrical conductivity with previously reported results	173
Figure 6.27(e)	Figure 6.27 (e) Comparison of calculated thermal conductivity with previously reported results	173
Figure 6.27(f)	Figure 6.27 (f) Comparison of calculated viscosity with previously reported results	174
Figure 6.28	Effect of chemical non-equilibrium on transport and thermodynamic properties at $p=1\text{Atm}$ and $T_e/T_h = 1$ : (a) Total thermal conductivity, (b) Viscosity, (c) Electrical conductivity, (d) Enthalpy.	176
Figure 6.29	Effect of chemical non-equilibrium on transport and thermodynamic properties at $p=7\text{Atm}$ and $T_e/T_h = 1$ : (a) Total thermal conductivity, (b) Viscosity, (c) Electrical conductivity, (d) Enthalpy	177
Figure 6.30	Effect of chemical non-equilibrium on transport and thermodynamic properties at $p=1\text{Atm}$ and $T_e/T_h = 3$ : (a)	177

	Total thermal conductivity, (b) Viscosity, (c) Electrical conductivity, (d) Enthalpy.	
Figure 6.31	Effect of chemical non-equilibrium on transport and thermodynamic properties at $p=7$ Atm and $T_e/T_h=3$ : (a) Total thermal conductivity, (b) Viscosity, (c) Electrical conductivity, (d) Enthalpy.	178
Fig. 7. 1	Stress components in a fluid element in Cartesian coordinate and cylindrical coordinate system.	186
Fig. 7. 2	Variation of radiation loss with temperature in nitrogen plasma	192
Fig. 7. 3	Computational domain used in the study.	198
Fig. 7.4	Nitrogen plasma temperature distribution inside the plasma torch for different currents, (a) 170A, (b) 180A, (c) 200A and (d) 210A.	200
Fig. 7.5	Axial and radial plasma temperature profile of nitrogen plasma. (a) axial temperature profile, (b) radial temperature profile.	201
Fig. 7.6	Potential distribution inside the torch at different currents, (a) 170A, (b) 180A, (c) 200A and (d) 210A.	201
Fig. 7.7	Variation of axial potential for different current values in the plasma column	202
Fig. 7. 8	Velocity distribution inside the plasma torch	203
Fig. 7. 9	Comparison of experimental and simulated arc voltages	204

Fig.7.10 Comparison of experimental and simulated plasma  
temperature

204

## List of Tables

Number of table	Table caption	Page number
Table 1.1	Power range of plasma torch used for various applications.	7
Table 1.2	Properties of plasma forming gases	8
Table 1.3	Properties of elements used in plasma torch components	9
Table 2.1	Power supply specification	40
Table. 2.2	Technical specification of HF unit	41
Table 2.3	Technical specification of RTD	44
Table 2.4	Technical specification of spectrograph	45
Table 2.5	Optical fibre specification	46
Table 2.6	Technical specification of oscilloscope	48
Table 2.7	Technical specification of the probe	49
Table 2.8	Chilled water supply unit specification	51
Table 4.1.	Definition of different types of plasma temperature	77
Table 4.2	Spectroscopic data for Argon atomic lines	86
Table 4.3	Spectroscopic data for Nitrogen atomic lines	88
Table 5.1	Different types of dynamics and their representation	105

Table 6.1	Explicit form of internal partition function	117
Table 6. 2	Explicit form of the translational partition function	118
Table 6.3	Reactions, rate constants, associated Saha equations and reaction energies for nitrogen plasma system	120
Table. 6.4	Entities used in the computation of thermodynamic and transport properties	120
Table 6.5	Rotational vibrational constants of N <sub>2</sub> plasma system, D <sub>0</sub> is the dissociation energy of the molecules.	121
Table 6.6	Formulae for specific energy of various species of particles	122
Table 6.7	Specific enthalpy of various species of particles	124
Table 6.8	The interaction chart for Nitrogen plasma.	126
Table-6.9	The net change in enthalpy in different reactions	136
Table 7.1	Terms of the general governing equation (7.28)	196
Table-7.2	Boundary conditions used in the simulation	199

# **CHAPTER-1: Introduction**

## **Outline of the Chapter**

**1.1 Definition and Types of Plasma**

**1.2 DC Plasma Devices**

**1.3 Definition of the Problem**

**1.4 Relevance of the Problem**

**1.5 Status of the Problem**

**1.6 Scope of the Work**

**1.7 Organisation of the Thesis**

# Chapter 1

## Introduction

### 1.1 Definition and Types of Plasma

The term ‘plasma’ was first applied by Langmuir in 1928 to ionized gas in electric discharge. It is the fourth state of matter composed of charge (electrons, ions and radicals) and neutral particles. Almost 99% of all the matter existing in the universe is found to be in this state and it is produced by ionizing gases to a certain degree of ionization. Because of the presence of charged particles it possesses electrical conductivity like that of metals. In our day to day life we come across different naturally occurring as well as manmade plasma. Ionosphere, solar corona, aurora borealis are examples of naturally occurring plasma where as among laboratory plasma, flames, glow discharge, fluorescent plasma, high pressure arcs, RF discharges and MHD generators are common. Basically, plasma is characterized by its electron number density ( $n_e$ ) and electron temperature ( $T_e$ ). Depending on these two parameters, naturally occurring and laboratory plasma are classified as given in fig 1.1.

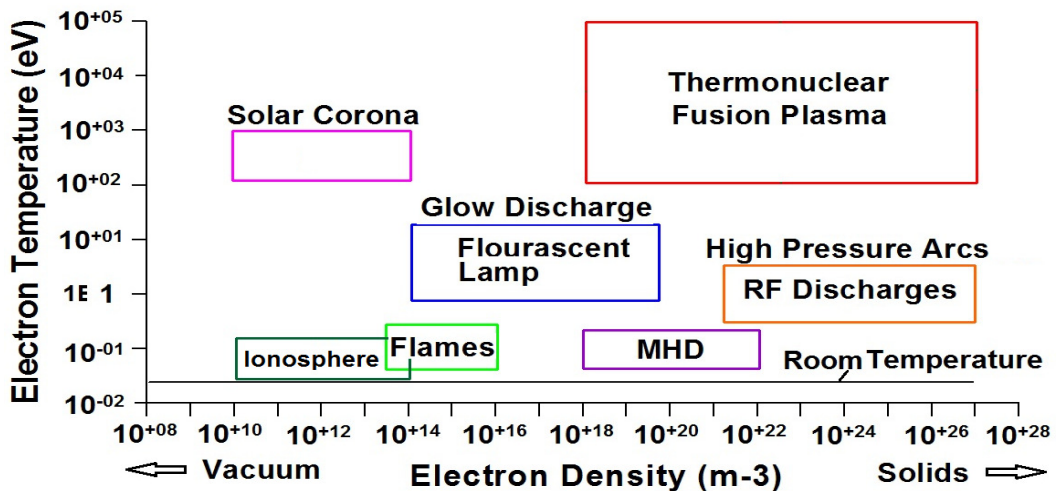


**Fig. 1.1 Classification of plasma depending on electron number density and electron temperature**

Plasma produced in laboratory is again classified as thermal plasma and non-thermal plasma depending on their state of thermal equilibrium. In plasma physics, the state of thermal equilibrium is defined in terms of the electron temperature ( $T_e$ ) and heavy particle (atoms, ions and molecules etc) temperature ( $T_h$ ) which is related to the kinetic energy of the electrons and heavy particles respectively. In case of thermal plasma the electron temperature ( $T_e$ ) is equal to the heavy particle temperature ( $T_h$ ) and in case of non-thermal plasma the electron temperature ( $T_e$ ) differs from the heavy particle temperature ( $T_h$ ). Plasma generated at lower gas pressure such as RF plasma, glow discharge etc. are non-thermal plasma where as the plasma generated at atmospheric or near atmospheric pressure such as MHD generator, dc plasma, inductively coupled plasma etc. are known as thermal plasma. Hence thermal plasma are characterized by high electron number density and high gas temperature where as non-thermal plasma are characterized by low electron density and low gas temperature.

This study is concerned with DC arc plasma devices and plasma produced in atmospheric pressure i.e. thermal plasma. However in arc plasma systems, in some location such as the vicinity of the anode, the electron temperature may differ from heavy particle temperature leading to thermal non-equilibrium. Variation of the electron temperature ( $T_e$ ) and heavy particle temperature ( $T_h$ ) with pressure in arc plasma devices is shown in figure 1.2.

Thermal plasma devices are again classified into AC plasma devices and DC plasma devices according to the type of electric field applied to produce the plasma. Depending upon the mode of energy coupling the AC arc plasma devices are again divided into two groups: one utilizes electrodes which operate with AC electric

current oscillating at a frequency of 50 Hz and the gas is heated by ohmic heating and the other one is electrodeless RF inductively coupled plasma devices, where the electrical energy is transferred to the gas by electromagnetic induction as well as through Ohmic heating of the arc formed by the eddy current generated in the plasma. DC plasma devices include the DC plasma generators or gas heaters.

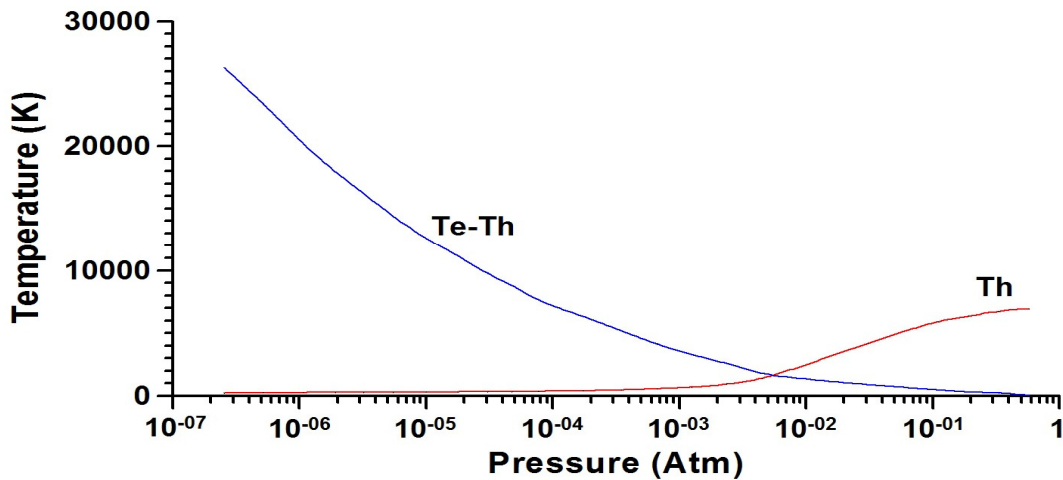


**Fig.1.2 Variation of electron and heavy particle temperature in arc plasma devices**

According to the mode of operation they are again classified transferred arc plasma devices and non-transferred arc plasma devices. In transferred arc plasma devices, the arc is established between the cathode and the job which acts as the anode. However, in non-transferred arc plasma torches, the arc is established between the cathode and a nozzle which behaves as the anode. The classification of the plasma devices working at atmospheric pressure is shown in figure 1.3.

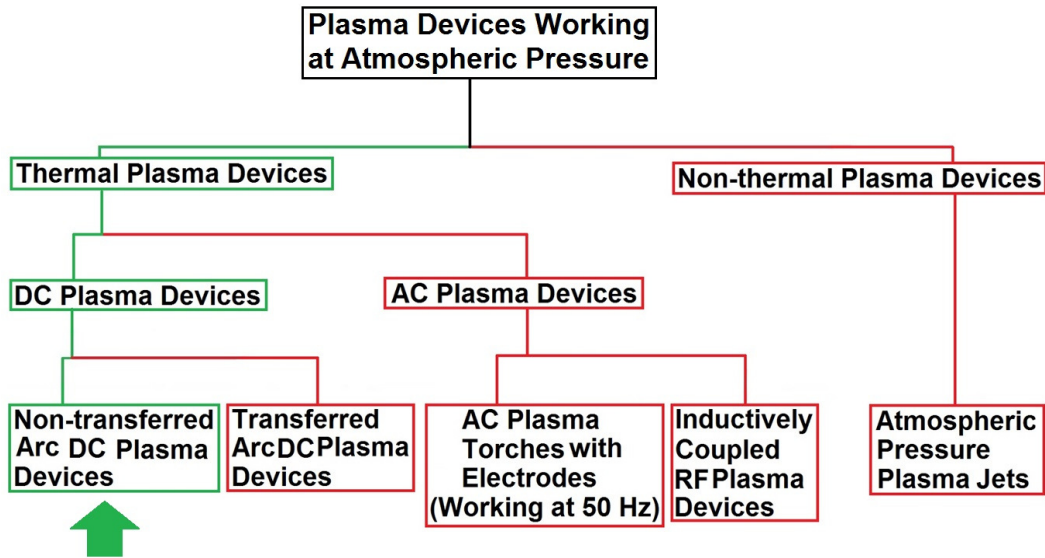


**Fig.1.3 Classification of arc plasma devices**

Figure 1.4 shows the DC plasma torch operating in transferred and non-transferred arc mode respectively.

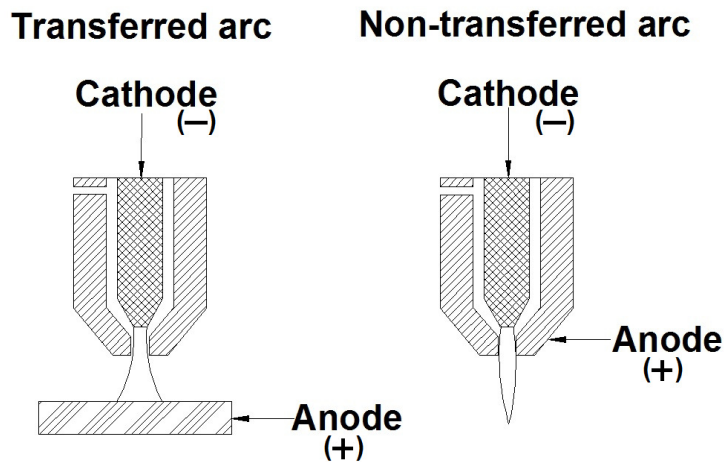


**Fig.1.4 Transferred and non-transferred arc mode of operation for DC**

This study is concerned with non-transferred arc segmented DC plasma torches. There is a wide range of DC plasma torches which are used in different types of processing works and they differ from each other according to the range of applied electrical power. A wide range of DC plasma torches used for different applications and their voltage and current range within which they are operated is shown in figure 1.5.

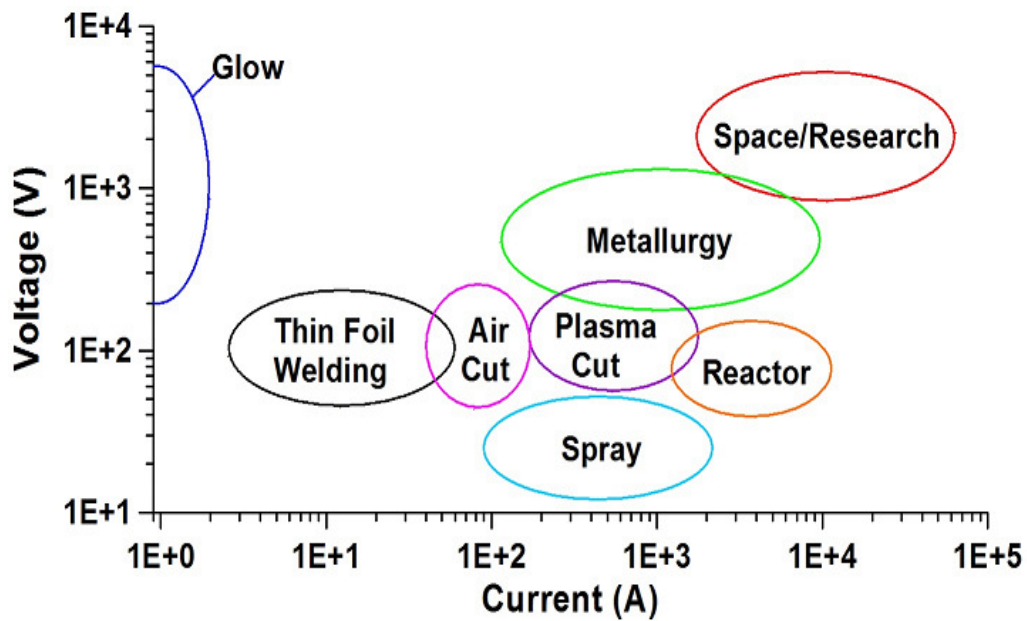
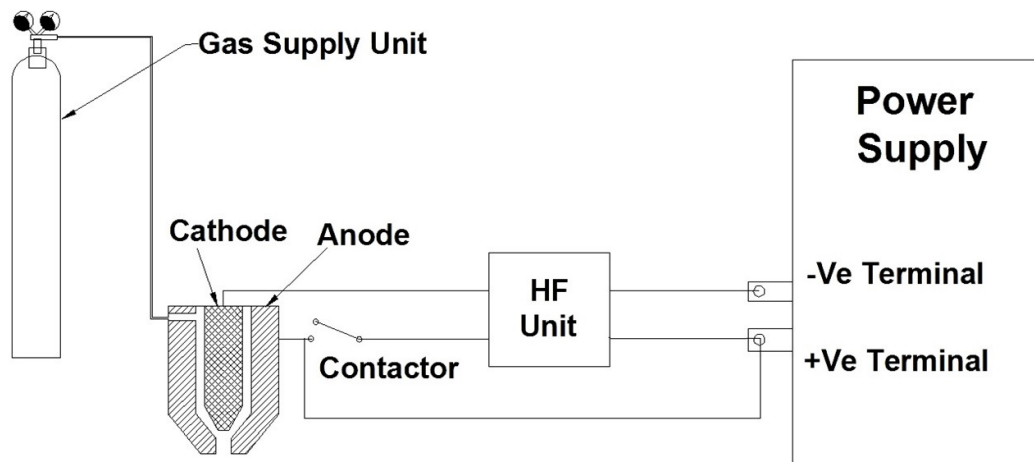


Fig.1.5 Application areas of DC plasma torches

## 1.2 DC Plasma Devices

DC plasma torch is a simple device to produce high temperature, high energy density and high enthalpy plasma jet. As shown in figure 1.6, the simplest DC plasma torch contains two electrodes: one is cathode and the other is anode. As the name indicates, the cathode is connected to the negative terminal and the anode is connected to the positive terminal of DC power supply respectively. An arc is established between the cathode and anode which heats up the gas passing through the gap between them by Ohmic heating and generates the high temperature plasma jet emanating from the nozzle exit. The initial breakdown of the gas between the electrodes is achieved by spark (known as the pilot arc) generated between the two electrodes using a high frequency electric field between them or by a momentary short circuit of the two electrodes. The arc thus formed is known as the pilot arc.



**Fig. 1.6 Design and working of simplest DC plasma torch**

The initial ionization develops an electrically conducting medium between the electrodes and the charge particles are driven by the potential difference applied between them. The power of the plasma torch can be increased by increasing the voltage drop across the electrodes. This is achieved by increasing the distance between the cathode and anode which needs adding anode like segments between them. A large variety of DC plasma torches operating at different level of electrical power with transferred arc and non-transferred arc mode is available [1]. Table 1.1 presents the power level of plasma torch used for various application.

**Table 1.1 Power range of plasma torch used for various applications.**

Sr. No.	Power Range (kW)	Purpose of Use
1	0.1 – 1	Welding of foils.
2	1 - 10	Cutting, welding thin plates.
3	10 – 100	Plasma cutting, welding, melting, spraying, machining and material processing.
4	100 - 1000	Under water cutting, plasma spraying and plasma metallurgy.
5	>1000	High enthalpy sources, wind tunnels and plasma heaters.

There is a wide range of gases used for plasma generation and the choice of plasma generating gas depends on the purpose of application. For example, for generating a chemically inert environment, inert gases like argon, helium are used, whereas for plasma assisted chemical processes, gases like oxygen, nitrogen are used. A list of the commonly used gases and their properties is given in Table 1.2.

**Table 1.2 Properties of plasma forming gases**

<b>Gas</b>	<b>Dissociation energy (eV)</b>	<b>First Ionization energy (eV)</b>	<b>Second ionization energy (eV)</b>	<b>Third ionization energy (eV)</b>
Argon	-----	15.7596112	27.62967	40.735
Helium	-----	24.587387936	54.41776311	-----
Neon	-----	21.564540	40.96296	63.4233
Hydrogen	4.52	13.598434005136	-----	-----
Oxygen	5.15	13.618054	35.12111	54.93554
Nitrogen	9.79	14.53413	29.60125	47.4453

The choice of electrode material plays the most important role in making a plasma torch for various applications. Material used for making the cathode includes the refractory materials such as tungsten, copper, hafnium, zirconium etc. Tungsten electrodes works well with non-oxydizing gases but to produce oxydizing plasma, tungsten cathode cannot be used as it is immediately oxydized. To work with oxygen or oxydizing gases (such as air) we need hafnium, zirconium or copper. Hafnium also gets oxidized but there is a major difference when compared with tungsten. Tungsten oxide has melting point nearly 2000K lower than that of tungsten metal. On the other

hand, hafnium oxide has melting point nearly 500K higher than pure hafnium. Due to lower melting point, oxidized tungsten cathode gets completely eroded away in less than a minute at the arc initiates. Anode material is usually made up of copper because of its good thermal and electrical conductivity. A list of the material used for making the electrodes with their useful properties is given in Table 1.3.

This study deals with a segmented DC non-transferred arc plasma torch with a tungsten rod type cathode which can run with argon as well as with nitrogen as plasma forming gas.

**Table 1.3 Properties of elements used in plasma torch components**

Sl. No.	Element	Thermal conductivity	Electrical conductivity	Thermal expansion coefficient	Melting point
1	Copper (Cu)	400	16.78	16.5	1084 (Cu)
					1235 (Cu <sub>2</sub> O Red)
					1201 (CuO, Black)
2	Zirconium (Zr)	22.6	421.0	5.7	1855 (Zr)
					2715 (ZrO <sub>2</sub> , White)
3	Hafnium (Hf)	23.0	331.0	5.9	2230 (Hf)
					2758 (HfO <sub>2</sub> , off white)
4	Tungsten (w)	173.0	52.8	4.5	3422 (W)
					1473 (WO <sub>3</sub> , Yellow-Bright green)

### 1.3 Definition of the Problem

Thermal plasma jets are unique for a number of industrial processes because of its ability to produce high enthalpy, high temperature chemically inert as well as active environment with easier process control. Argon and nitrogen are among the most commonly used plasma generating gases having wide spectrum of applications like cutting, welding, melting, spraying, chemical synthesis, nano-structure production, waste treatment, gasification, densification, metallurgical applications etc. [2]. Mostly Argon is used for producing chemically inert environment whereas nitrogen is used for a number of plasma assisted chemical processes like preparation of syngas [3], plasma nitriding [4,5,6] and nanostructure generation [7] etc. Use of nitrogen as plasma forming gas has the additional benefits that it can operate with usual tungsten based refractory electrode plasma torches. Being molecular gas, it can provide higher voltage drop with the same electrode configuration. While typical plasma jet in Argon is short (~ 5 cm), the same in nitrogen plasma may be greater than 30 cm. The type of plasma jet may be very useful for large number of processing applications. However, availability of data on thermal, fluid dynamic and electrodynamic behaviour of nitrogen plasma is rare and that for argon plasma is mostly limited to lower power (<15 kW). The problem under the present study is defined as the investigation of thermal, fluid dynamic and electrodynamic behaviour of nitrogen arcs through experiments, modelling and simulation and similar study in argon plasma for extraction of data in regimes not already covered in literature and for sake of comparison.

#### **1.4 Relevance of the Problem**

A thermal plasma jet derives its potential from its unique properties like availability of huge concentrated heat flux, extremely high gas temperature and enthalpy and copious presence of highly reactive nascent atomic and ionic species. Because of such unique properties, the thermal plasma jets find wide usage in variety of application areas. However, one important thing the area is lacking is rigorous thermal and fluid dynamic characterization of different plasma sources. Without this it may not be possible to explore the full potential of these devices. While some studies have been made for argon plasma torches at lower powers (<15 kW), similar studies for nitrogen plasma torches are rare. Needless to mention that thermal plasma jets of molecular gasses like nitrogen are important as they possess higher enthalpy, higher power content and much longer jet length compared to plasma jets of monatomic gasses like argon, helium etc. Many of the processing applications require operation at higher power for higher throughput as well as for process need. Studies of thermal and fluid dynamic behaviour of plasma devices operating at high power, addressed in this study are therefore very much important. In processes like spraying of high melting point materials (ceramics like  $Y_2O_3$ ,  $Al_2O_3$ ,  $Zr_2O_3$  and refractory metals like W etc.), the degree of melting of the particle should be such that the particles melt properly but not boil or vaporise. In processes like spherodization, densification and nanoparticle generation of such high melting point material, the powder particle should properly melt or completely vaporize. Hence they need high power plasma jet with long enough dwell time of the injected particles inside the plasma under high heat flux. Obtained long nitrogen plasma jet with uniform heat flux profile, offers much easier

control over the melting or evaporation of particles through proper management of the particle residence time inside the plasma under high heat flux.

Inherent instabilities in arc are important factors as it can severely affect the performance of a plasma device for any processing application. This important aspect is addressed in this study by analyzing the voltage fluctuation behaviour in argon and nitrogen plasma under different operating conditions.

From device engineering point of view, CFD simulation studies are extremely important for optimization of device design. For any CFD related study involving special fluid like plasma, the primary prerequisites are the relevant thermodynamic and transport properties under different operating conditions. The thermodynamic and transport properties of nitrogen plasma derived in this study under thermal equilibrium and non-equilibrium conditions enable CFD simulation of nitrogen plasma devices under equilibrium as well as non-equilibrium. Assuming plasma in thermal equilibrium, the nitrogen plasma devices are modelled through relevant Navier-Stokes equation appropriately modified by additional source terms originating from electromagnetic interactions. The equations are solved using standard CFD simulation technique to determine the distribution of quantities inside the device like temperature, current density, pressure, velocity, enthalpy, species density etc. Such simulation studies are very much important as device designs can be optimized without actually making the device.

### **1.5 Status of the Problem**

Argon is the most common and frequently used plasma generating gas for creating chemically inert high temperature environment. Argon plasma has been studied

intensively and many aspects of argon plasma have already been investigated by different groups of researchers in many different ways. However, not enough studies have been made on Nitrogen plasma. Although, number of reports dealing with binary mixture of gases, where nitrogen is used to increase arc voltage, can be found in the literature. The reported studies mostly focus on Argon plasma generated at lower power level lying within 15 kW of electrical power. Use of plasma in the field of metallurgy or waste treatment needs higher plasma power. Molecular gases like nitrogen associates higher electrical power and can operate with usual tungsten cathode plasma torches. The following gives a review of the earlier works in different relevant areas.

### **Determination of Heat Flux Profile of Nitrogen and Argon Plasma Jet**

Heat flux of the plasma jet highly influences the heat transfer to matter in plasma-matter interaction. The nature of the heat flux profile of a plasma jet determines the quality of the process and its suitability for a particular application. Number of attempts has been made in the past to determine the shape of the heat flux profiles offered by such devices as a function of axial distance, power level, flow rate of plasma gas, nozzle diameter and nature of plasma gas. However, as mentioned earlier, most of the studies focussed on Argon as plasma gas and operation at a power level below 12 kW [8-13]. Kishigami et.al. [8] employed an array of thermocouples at different depths of the substrate to determine the radial heat flux profile delivered by an Argon jet at a power level less than 9 kW. Moulin et.al.[9] determined the heat flux profile delivered by a DC Argon-Hydrogen jet using double calorimetric technique. The maximum power level considered was 40 kW. The profile was assumed to be Gaussian and the profile parameters were determined from the measured heat fluxes

using iterative technique. Ghorui et.al. [10] used similar technique to determine the profile parameters of Argon plasma jet at power level less than 16 kW. Through a systematic study of least mean square deviation in the off axis measurements, it was observed that an exponential profile gives a slightly better match with the experimental results compared to a Gaussian profile. Employing enthalpy probe, Asman et.al. [11] determined the radial heat flux profile in triple torch plasma system, each torch operating at power level less than 10 kW. Meng et.al. [12] used thermocouples embedded in an insulating  $ZrO_2$  matrix to determine the radial heat flux profile of an Argon plasma jet operating at 8 kW using transient method. Stationary and non-stationary behaviour of heat flux delivered by an atmospheric pressure double arc Argon plasma jet at power level less than 12 kW was studied by Tu et.al [13] using commercial water cooled heat flux meter.

Plasma torches operating with Nitrogen as plasma gas offer radical rich non-oxidizing high temperature environment for plasma chemistry and processing. However, work on finding the nature of the heat flux profiles offered by such plasma torches is rare. Cheron et.al. [14] reported measurement of parietal heat flux in a low pressure (1.5 mbar) Nitrogen plasma wind tunnel operating at an electrical power of 14 kW with the help of copper constantan thermocouple and copper slug. To the best of the authors' knowledge, no systematic study of heat flux is reported in literature for power level more than 15 kW in Nitrogen plasma.

The present study on axial evolution of radial heat flux profile transmitted by atmospheric pressure Nitrogen and Argon arcs focus on plasma torches operating at power level ranging from 6.6 kW to 52 kW in Argon and 32 kW to 51 kW in Nitrogen.

## **Determination of Plasma Jet Temperature using Optical Emission Spectroscopy**

Temperature of the plasma jet is another important parameter which decides the applicability of the plasma jet for particular application. In all types of application, distribution of plasma temperature decides the efficiency of the process and quality of the product. For example, in plasma assisted chemical processes, temperature governs the rate of chemical reactions by providing the required reaction energy and degree of ionisation. Similarly in processes like plasma spray, spherodization, densification, it decides degree of melting of the injected power particles. Hence for process optimization and control, it becomes necessary to have adequate idea of the plasma temperature distribution and its correlation with different operating parameters.

A large volume of articles on plasma temperature measurement which are based on different techniques exists today. The plasma temperature measuring techniques are divided into two broad categories: invasive and non-invasive techniques. In invasive techniques (also known as intrusive technique) the plasma is disturbed by the measurement as they basically rely on the probes (Langmuir probe, enthalpy probe and melting point of different materials etc.) and in case of non-invasive techniques (or non-intrusive techniques) the plasma is not disturbed by the measurement as they are usually based on the spectroscopic techniques (Absolute line intensity method, relative line intensity method, Boltzmann plot method and laser light scattering method etc.). While intrusive methods cannot be used in very high temperature region such as vicinity of the nozzle exit, non-intrusive methods can be used at any point along the jet. Most of the reports are based on either argon plasma or plasma produced using binary mixtures of gases [15-28]. Adcock et. al. [15] has determined excitation temperature argon plasma in a DC plasma torch which utilizes a

convergent-divergent nozzle. The excitation temperature has been determined from neutral argon atomic lines using Boltzmann plot method. The torch power was varied from 18.6 to 61.1 kW. Synders et. al.[16] determined gas temperature and velocity profile at the exit plane of a plasma torch for an argon plasma using high resolution Doppler shifted line-shape analysis of scattered laser light. The data obtained from laser light scattering has been compared with values obtained with results obtained from emission spectroscopy. The electrical power was varied from 7.2 kW to 22.9 kW. It was shown that the gas temperature increases with increase in power and then saturates but that of the electron keeps on increasing. This leads to departure from LTE at higher power level. Fincke et. al.[17] determined temperature and velocity profile in argon plasma jet using enthalpy probe and laser light scattering and the obtained results have been compared. The current varies for 400A to 900A. Joshi et. al.[18] determined the excitation temperature of argon plasma produced in a spray torch using atomic Boltzmann plot method. The axial temperature of an inhomogeneous, axisymmetric, plasma column was determined using modified atomic Boltzmann plot technique without using Abel inversion technique. Electrical power applied to the plasma torch varies from 5 to 10 kW. Gregori et. al.[19] determined electron temperature and density in a DC argon plasma jet, generated at atmospheric pressure, using Thomson scattering. Assymetry of the plasma jet and dependence of the electron temperature on scattering angle has also been shown. The input electrical power lies between 21 to 24.5 kW. Feng et. al.[20] determined the temperature of Ar/H<sub>2</sub> and Ar/N<sub>2</sub> plasma jets using enthalpy probe. The plasma is generated at atmospheric pressure. Calibration of enthalpy probe and error induced by enthalpy probe is also discussed. The electrical power applied to the torch was 9 kW. Tu et.

al.[21] analysed the electrical and spectroscopic characteristics of an atmospheric double arc argon plasma jet. In addition to the study of instabilities associated with double arc plasma torch, excitation temperature of the argon plasma jet was determined from neutral argon lines using Boltzmann plot method. Results for electron number density measurement have also been presented. Existence of LTE in the core region was shown. Wang et. al.[22] directly measured the thermal temperature of a 100 kW DC argon plasma jet using an Alexandrite effect spectropyrometer which measures the temperature from the continuum. The obtained results are compared with that obtained from OES of the jet. Hlina et. al.[23] performed a time resolved tomographic measurement of plasma temperature in an argon plasma jet. Two dimensional temperature profile of the plasma jet perpendicular to the torch axis has been obtained. The torch current was fixed at 200A. Emile et. al.[24] determined the temperature and number density of electron in an atmospheric pressure DC laminar argon plasma jet. The electrical power applied is 1.3 kW. A study of the amount of entrained air has also been presented.

A large number of reports are also available on temperature measurement of argon-nitrogen plasma jet. Nitrogen was basically used to increase arc voltage. Jian-Hua et. al.[25] performed spectroscopic analysis of argon-nitrogen plasma generated by a double anode DC plasma torch. Rotational and vibrational temperature at the torch nozzle exit was determined from first negative system of  $N_2^+$ . Excitation temperature is determined by Boltzmann plot method. Results for rotational temperature, vibrational temperature, and excitation temperature are presented. Equality of the excitation, rotational and vibrational temperature indicates the validity of LTE. The total applied electrical power applied is 8kW. Belevstev et.

al.[26]presented optical emission spectroscopic study of argon and nitrogen plasma jets inside and outside the plasma torch. The excitation temperature is determined using relative intensity of spectral lines for argon and nitrogen as well as from spectral emission of evaporated copper from the anode. The rotational temperature of nitrogen was determined using two methods, the first one is line by line numerical simulation of rotational structure of the (0-0) and (0-1) bands of  $N_2^+$  and in the far relaxation zone of CN 'violet' bands of principal sequence ( $\Delta v=0$ ) and the second method is based in comparing the intensities of single lines with those of band heads. The current varies from 150 A to 500 A. Tu et. al. [27] has analysed electrical and optical characteristics inside and outside of a double anode plasma torch operating in argon-nitrogen with electrical power of less than 10 kW. Electronic and excitation temperature was determined from argon atomic lines using Boltzmann plot method. Rotational and vibrational temperature of nitrogen was determined from the rotational and vibrational spectrum. Measurement of electron number density indicates the existence of LTE. Vardelle et. al.[28] performed plasma and particle diagnostics in nitrogen-hydrogen and nitrogen-argon plasma jet. For plasma jet temperature measurement, absolute intensity of atomic lines is used for temperature above 7000 K, molecular spectroscopy is used to measure temperature lying between 4000K and 7000K and melting point of different materials (alumina, tungsten etc.) has been used for temperature below 4000 K.

Very few articles report about temperature measurement of pure nitrogen plasma [29,30] and most of them deal with the rotational and vibrational temperature of the nitrogen plasma. But in the core region of the thermal plasma jets, nitrogen cannot exist in molecular form and hence rotational and vibrational temperature

cannot be taken as good representative for the temperature of the core region. Atomic or ionic lines can infer about the appropriate temperature along the jet axis. To the best of author's knowledge, no study on finding the nitrogen plasma temperature from atomic and ionic lines using Boltzmann plot technique has been reported. Jahn et. al.[29] determined temperature distribution of the jet using emission spectroscopy along with average temperature from the power input in argon and nitrogen plasma. Absolute intensity method was used to measure the plasma temperature. The power of the plasma varied from 5 to 20 kW. It has been shown that, the temperature determined from emission spectroscopy is time averaged and it is biased towards the peak temperature. Prevosto et. al.[30] presented radial distribution of electron and heavy particle temperature of dc nitrogen plasma using a sweeping Langmuir probe. The plasma is generated at 25 kW of electrical power and the measurements are made at an axial distance of 3.5 mm from the nozzle exit. The temperature values are time averaged temperature.

In this study, axial variation of temperature of the argon and nitrogen plasma jet has been determined from the atomic and ionic lines using Boltzmann plot method. Influence of various operating parameter on the plasma temperature has been analysed.

### **Measurement of Voltage Fluctuation in Argon and Nitrogen Plasma Jets**

The simplest DC plasma torch contains two electrodes and the gas passing between the electrodes is heated by the arc established between them through Ohmic heating. The point where the arc connects the cathode is called as 'cathode spot' and the point where it connects the anode is called as 'arc root'. In spite of the large number of

potential applications, its development and efficient utilization is obstructed by number of problems associated with it [31,32]. Frequent failure of electrodes due to electrode erosion and fluctuation in the emanating plasma jet are among them. These problems affect the device life time and leads to bad and improper performance of the device. There is always non-uniform fluctuation in the plasma jet which badly affects almost all the processes which utilize DC plasma torch as processing tool. This fluctuation in plasma jet is caused by fluctuation in the power of the plasma. The power of the plasma fluctuates because of fluctuation in the arc voltage. The arc voltage fluctuates either because of the change in voltage of the input electrical power from the power supply or change in the length of the arc. Basically there are three reasons for the plasma jet fluctuation: fluctuation induced by the power source, fluctuation due to inherent movement of the arc root over the anode surface and fluctuation due to fluid dynamic effects. Usually a constant current DC power supply is used for plasma generation. The input current to the plasma torch contains ripple induced by three phase input power supply. Thus the voltage and hence power of the plasma fluctuates with input frequency of 150 Hz. This fluctuation is independent of any change in the operating condition. This kind of power variation can be reduced by using an appropriate power supply. The voltage and hence power of the plasma also fluctuates because of change in the length of the arc. The arc length changes either because of the movement of the arc root over the anode surface or change in the arc length due to fluid dynamic effect without changing the arc root position. The fluid dynamic force tries to push the arc downstream of the anode nozzle and the electromagnetic force tries to keep the arc length minimum in order to maintain minimum energy. So there is a competition between the two balancing forces acting in

opposite directions. This causes variation in length of the arc. As the plasma jet fluctuates so does the velocity, temperature and pressure of the plasma jet. Since DC arc plasma jets are mostly used for processing applications, the fluctuation of the plasma jet highly affect the process. For example, in ideal plasma spray process, it is needed that the particles should melt properly before they impact on the substrate. However, the fluctuation in plasma jet temperature may lead to non-uniform heating of the injected particles. Further the variation in plasma pressure and velocity results in variation in particle residence time and change in particle trajectory. Hence most of the particle may not go through the plasma or deviate from the path or may not reach the substrate. This results in poor efficiency of the plasma spray process as most of the particles may not be heated properly or may not reach the target. Movement of the arc root also affect the device life time. If the arc sticks to a point on the anode surface, the high energy density of the arc melt and even vaporize the material at the point of contact and the anode gets eroded. This process gradually damages the anode. Hence movement of the arc root on the surface of the anode is needed for longer life time of the anode. Thus periodic motion of the arc root with small change in voltage may be favourable for device safety and other processes. This may also open path for the further development of the thermal plasma technology. Since the arc and the plasma jet instability is one of the important problems in thermal plasma technology, a large volume of articles exists on this. Since thermal plasma spraying is a common application of DC plasma torch and highly affected by the instability in the plasma jet most of the reports deal with spray plasma torch utilizing mixture of binary gases for plasma generation at lower power level. The reports usually consider the arc current and gas flow rate as the influencing parameter. A typical review on the application of

non-linear dynamic techniques for the analysis of the instability in arc plasma devices is presented by Ghorui et. al.[33]. Coudert et. al.[34] analysed the voltage fluctuation for a spray plasma torch operated with a mixture of argon and hydrogen as plasma generating gas. Fluctuation of the plasma jet was analysed in terms of the nozzle diameter and arc current. A relationship has also been established between the nozzle diameter, arc current, gas flow rate and mean spot lifetime. The torch was operated upto 40 kW of electrical power. Result for the mean electric field within the arc column and the mean position of the arc root has also been presented. The lifetime of the upstream arc spot was found to be more than that of the downstream spot by 30-40%. In another work by Coudert et. al.[35], effect of Helmholtz oscillation on arc voltage fluctuation for two different plasma torches has been presented. Both the torches were operated with mixture of argon and hydrogen with same gas flow rate and operating conditions. The two different torches show different voltage fluctuation behaviour because of different electrode configuration. Ghorui et. al. [36] presented an experimental approach to identify the sources of instability in arc plasma devices utilizing the phenomenon of demixing of arcs. The observed behaviour such as steady, takeover and restrike mode of instabilities are said to be originating from thin boundary layer over the anode wall primarily at the location of anodic arc root and the bulk core flow apparently not play much role in the observed instabilities. Arc current was found to be the main controlling parameter of the frequency of fluctuation rather than the flow rates. Krowka et.al.[37] reported that, instability in DC plasma torch is mainly originated due to Helmholtz oscillation and motion of the arc root over the anode surface. Mixture of argon and hydrogen was used as plasma forming gas. It is shown that the Helmholtz frequency mainly depends on the cathode cavity volume

and usually ranges between 4 to 5 kHz. Restrike mode has been identified as the main mode of arc instability. The characteristic time for the restrike mode is much lower than that of the Helmholtz oscillation. It is shown that when the restrike frequency reaches the Helmholtz one both modes are locked together and a pulsed arc is generated. Ghorui et. al.[38] analysed the fluctuating voltage signals generated from an atmospheric arc discharge produced in hollow electrode plasma torch operating with and without magnetic field. It was shown for the first time that the instability found in arc discharge is chaotic in nature. Effect of various operating parameters such as gas flow rate, gas composition, arc current and strength of magnetic field on the arc root dynamics were analysed. In another work by Ghorui et.al.[39] it was shown that the voltage, acoustic and optical signal generated by a hollow cathode plasma torch exhibit chaotic behaviour. The origin of each of the fluctuation and mutual correspondence among them were described in detail. Duan et. al. [40] reported on the different form of arc instability such as steady, takeover and restrike with the help of high-speed end-on observation of argon-helium arc. Effect of arc current, gas flow rate, gas injection type and different amount of wear in anode were analysed. Tu et. al.[27] reported on the arc instability and dynamic characteristics of the double arc argon – nitrogen plasma torch. In this experiment, restrike mode has been identified as the typical mode of voltage fluctuation. Zhao et. al.[41] reported on the fluctuation characteristics of two types of plasma torches. The arc voltage and the spectral intensity signal shows that the fluctuation of the plasma jet is caused due to power supply output, arc root movement and fluid dynamic effect. Cheron et. al. [42] analysed the dynamic behaviour of a double arc plasma torch using nitrogen as plasma generating gas. The voltage signal exhibit two characteristic frequencies one at 150

Hz because of the three phase power supply and 6.7 kHz frequency which is ascribed to the generation of the acoustic wave in the region of first anode attachment. The results were obtained under lower chamber pressure.

The present study focuses on analysis of the instability in a segmented non-transferred arc DC plasma torch operating in Argon and Nitrogen. The effect of arc current and gas flow rate on the voltage fluctuation is analysed.

### **Thermodynamic and Transport Properties of Nitrogen Plasma under Thermal Equilibrium and Non-equilibrium Conditions:**

Inside thermal plasma devices, depending on geometry of the electrodes and operating conditions, temperature may vary over tens of thousands of degree Kelvin, pressure may vary from several atmospheres to sub-atmosphere and electron temperature may differ widely from corresponding heavy species temperature, depending on locations [43]. Existence of sharp gradients in temperature, pressure and species densities, often encountered in such plasma devices, necessitates a thorough understanding of the highly nonlinear behaviour of associated thermodynamic and transport properties. In recent days, numerical simulation of such devices is gaining rapid momentum. Appreciable savings of time and cost is realized through this in understanding of device behaviour under different device designs. Thermodynamic and transport property data stand as the primary prerequisite for any such simulation to pursue.

Numbers of attempts have been made in the past to understand the thermodynamic and transport properties of nitrogen plasma [44-53]. Apart from slight deviations originating from different sets of collision integrals used in different

studies, most of these computed properties exhibit an overall good agreement. Under LTE (local thermodynamic equilibrium), the work done by Murphy and Arundell [50] needs special mention. An extensive investigation on the thermodynamic and transport property data of atmospheric-pressure nitrogen is performed in the temperature range from 300 to 30,000 K. Pressure dependence of the properties is also addressed by Murphy in another study [53]. Under thermal non-equilibrium, the thermodynamic and transport property of nitrogen plasma was first calculated by Colombo et.al. [51]. Later, the same was computed by Wang et.al. and it was shown that the computed properties under thermal non-equilibrium, heavily depend upon the definition of screening length, especially at higher temperature. It was a question, whether both electrons and ions or only electrons should be considered in the definition of shielding length under screened Coulomb potential. Although, there was no reason why effect of ions should not be considered in the shielding when they can influence the shielding mechanism in an obvious manner, works other than Wang et.al assumed shielding by electrons only for computation of the thermodynamic and transport properties.

In a recent work by Ghorui et.al.[54] choice of appropriate form of shielding distance in the estimation of collision integrals under screened coulomb potential for two-temperature non-equilibrium plasma is addressed. A revised definition of the shielding distance is proposed which incorporates electrons and ions both and gives property values in close agreement with experimentally observed results [54]. The present work employs this approach and determines the complete set of thermodynamic, and transport property values for nitrogen plasma under thermal equilibrium and non-equilibrium conditions. In the calculation, electron temperature

ranges from 300 to 50,000 K, the ratio of electron temperature ( $T_e$ ) to the heavy particle temperature ( $T_h$ ) ranges from 1 to 20 and the pressure ranges from 0.1 to 7 atmospheres. Under atmospheric pressure, results obtained for thermodynamic equilibrium ( $T_e=T_h$ ) are compared with number of published results under similar conditions.

Under chemical non-equilibrium, number densities inside the plasma are influenced by diffusive particle fluxes originating from species and temperature gradients. The ultimate effect can be accounted for by including a modified rate constant in the associated rate equations in place of chemical-equilibrium rate constants and defining a chemical non-equilibrium parameter 'r' as the ratio of the modified rate constant to the equilibrium rate constant [55]. Effects of chemical non-equilibrium on the computed properties are presented with 'c' ranging from 0.5 to 2.

In summary, primary appeal of the present work on thermodynamic and transport properties rests on the fact that it presents properties under thermal non-equilibrium, not included in the scope of earlier works on equilibrium plasmas [50,53]. It includes the effects of both ions and electrons in the screening, not considered in the work on non-equilibrium properties by Colombo et.al.[51]. It offers results that appreciably differ from the non-equilibrium results by Wang et. al. [52] which presented results including the effect of electrons alone as well as results including the effects of both ions and electrons in the screening. The mismatch between experimental and theoretical results, observed in the earlier studies at higher temperatures [54], has been removed to a great extent in this study. A revised definition of screening length, recently proposed by Ghorui et. al. [54] is followed. It is based on the assumption that higher mobility of the electrons redistributes any

change in the potential at the rate of  $T_e$  and single temperature  $T_e$  may be used while both electrons and ions are being considered in the estimation of the screening of potential. Finally, the work presents properties of the nitrogen plasma under chemical non-equilibrium as well, not addressed in the earlier studies.

### **Numerical Modelling of Atmospheric Nitrogen Plasma Torch under Thermal Equilibrium and Non-Equilibrium Condition:**

As described earlier, numerical simulation plays a very important role in design and development of arc plasma devices. This is firstly because no invasive diagnostic probe can withstand the extremely high temperature at the core inside the plasma torches. Secondly, mechanical obstruction due to the torch wall itself, does not allow any direct probing of the plasma inside the device. A large number of simulation studies exist on simulation of arc plasma jets [56-69]. However, most of them deal with argon plasma [56-63]. Most of the simulation studies in nitrogen plasma reports in transferred arc plasma devices [64-67] and few works are concerned with non-transferred arc plasma torches operating with mixture of nitrogen with other gases or pure nitrogen[68,69]. Chen et. al.[64] analysed the anode contraction region of wall stabilized, axis-symmetric nitrogen arc operating in transferred arc mode at a current level of 250 A. Results for temperature distribution, velocity field, current density distribution, pressure distribution, self induced magnetic field distribution, Lorentz force distribution has been presented. Wilhelmi et. al. [65] analysed different types of arc attachments formed on the anode surface for a wall stabilized axis-symmetric high current transferred arcs established in argon and nitrogen. The arc current for nitrogen was 250A and 400A and that for argon was 250A. It is seen that, nitrogen arcs form constricted arc root for all the current values and the argon forms

diffuse arc root in absence of any cathode jet. However, under the influence of superimposed cathode jet, nitrogen forms diffuse arc root attachment. Velocity field for induced anode jet has also been presented. Chau et. al. [66] presented the numerical simulation of a 1.2 MW DC transferred arc plasma torch with well type cathode. The gas flow rate for the study was taken to be 1000 slpm (standard litre per minute) of pure nitrogen. Results for velocity and temperature distribution of cold gas and hot gas are presented. Peng et. al. [67] presented a numerical model for nitrogen arc in a pilot scale furnace based on a graphite cathode and fly ash anode or melting anode. The effects of melting anode and various parameters such as the current, terminal voltage and plasma length on the characteristics are investigated experimentally and numerically. In this study, the arc current varies from 100A to 700A and the axial distance varies from 80 mm to 240 mm. So the maximum calculated voltage is 200 V. Among the reported studies on non-transferred arc DC plasma torch, Selvan et. al. [68] presented a three dimensional model for plasma spray torch operated in mixture of Ar-N<sub>2</sub> for given arc current and gas flow rate. The most appropriate size of the arc which produces the actual physical situation has been predicted using thermodynamic principle of minimum entropy production. The only work on a DC nitrogen plasma torch operating in non-transferred arc mode is presented by Ghorui et.al. [69] Effect of chemical and thermal non-equilibrium on different processes and distribution of different physical quantities in nitrogen arc was shown by comparing the results of equilibrium and non-equilibrium condition.

## **1.6 Scope of the Work:**

The scope of work under the present study includes the following:

1. Design and development of a segmented non-transferred arc DC plasma torch which can operate with argon and nitrogen at the low ( $< 25$  kW) as well as medium power level (15-50 kW).
2. Determination of heat flux profile of the nitrogen and argon plasma jet under different operating conditions.
3. Determination of temperature of the nitrogen and argon plasma jet for different operating condition.
4. Study of instabilities in the arc voltage in nitrogen and argon plasma, under different operating conditions.
5. Determination of thermodynamic properties and transport coefficients of nitrogen plasma as function temperature and pressure under state of thermal equilibrium and non-equilibrium conditions.
6. Modelling and simulation of the nitrogen plasma jet and comparison with experimental data.

## **1.7 Organisation of the Thesis:**

The thesis is organised in the following manner. After a brief introduction on different types of plasmas and plasma generation processes in DC thermal plasma devices, chapter one describes relevance, status and scope of the work under the present study. Chapter 2 gives detail descriptions of different experimental setups

used in the study. Heat flux profile of nitrogen and argon plasma jet under different working condition, as determined from the experimental data, are presented in chapter 3. Chapter 4 details the measurement of the temperature of the argon and nitrogen plasma jets under different operating conditions through emission spectroscopic study. The instabilities in arc voltage observed in argon and nitrogen plasma torches are investigated in chapter 5. Ab-initio computation of thermodynamic and transport properties of nitrogen plasma under thermal equilibrium and non-equilibrium condition is presented in chapter 6. Chapter 7 presents the CFD simulation of the nitrogen plasma device used in this study under different operating conditions employing the thermodynamic and transport properties obtained in chapter-6. Conclusions and scope for future works are presented in chapter 8.

# **CHAPTER-2: Experimental Setup**

## **Outline of the Chapter**

**2.1 Introduction**

**2.2 Experimental Setup**

**2.3 Plasma Torch**

**2.4 Power Supply**

**2.5 Double Calorimeter**

**2.6 Resistance Temperature Detector**

**2.7 Spectrograph**

**2.8 Optical Fibre**

**2.9 Oscilloscope**

**2.10 Voltage Divider Circuit**

**2.11 10X Probe**

**2.12 Chilled Water Supply Unit**

# **Chapter: 2**

## **Experimental Setup**

### **2.1 Introduction:**

DC plasma torches are the devices that convert DC electrical power into high enthalpy high temperature controlled jet of plasma. A simple DC plasma torch may consist of just two electrodes: a cathode and an anode. Depending on the electrical power needed for a particular application and type of plasma gas, plasma torches appear in different designs [1]. Their suitability for a specific application is decided by obtainable parameters of the plasma jet like temperature, heat flux, plasma dimension, plasma volume, plasma constituent and its enthalpy content.

The torch used in this study consists of seven segments including the cathode and the anode. The intermediate floating electrodes are used to increase the length of the arc between the cathode and the anode. The tungsten cathode used in the torch can run with non-oxidising plasma gasses like argon and nitrogen. Different setups used in the study for characterization of thermal and fluid dynamic behaviour of the arc include double calorimetric setup for heat flux profile determination, emission spectroscopy setup for plasma temperature measurement and voltage instability setup for measurement of instabilities in voltage fluctuation. In the subsequent sections, role of different experimental setups are provided. Section 2.2 describes the overall experimental setup and different experimental units attached to it. Section 2.3 and 2.4 illustrates the details of the DC plasma torch and the constant current DC power supply respectively. Descriptions of the double calorimeter and the resistance temperature detector (RTD) are given in section 2.5 and 2.6 respectively. Sections 2.7,

2.8 and 2.9 describe respectively the spectrograph, optical fibre and the oscilloscope. Voltage divider circuit used for study of arc voltage fluctuation is described in section 2.11. The temperature controlled chilled water supply unit, catering to relevant components of the system is described in section 2.12.

## 2.2. Experimental Setup

The complete experimental setup consists of a DC segmented non-transferred arc plasma torch, an IGBT based constant current DC power supply, chilled water supply system, water temperature measurement and display unit, torch movement system, set of two concentric calorimeters, spectrograph with optical fibre, oscilloscope and probe, voltage divider circuit, flow meters for gas and water flow measurement and a digital computer for data acquisition. The scheme and the experimental setup are shown in figure 2.1 and figure 2.2 respectively.

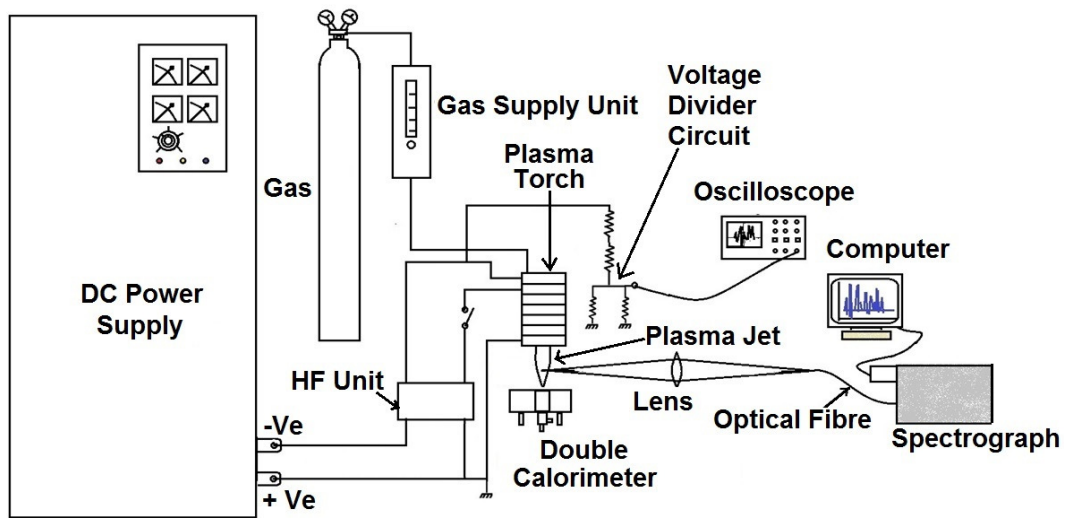


**Fig.2.1 Schematic diagram of the complete experimental setup**

The plasma torch used in this study contains seven segments including a cathode, an anode, an auxiliary anode and four number of constrictor segments between auxiliary anode and main anode.

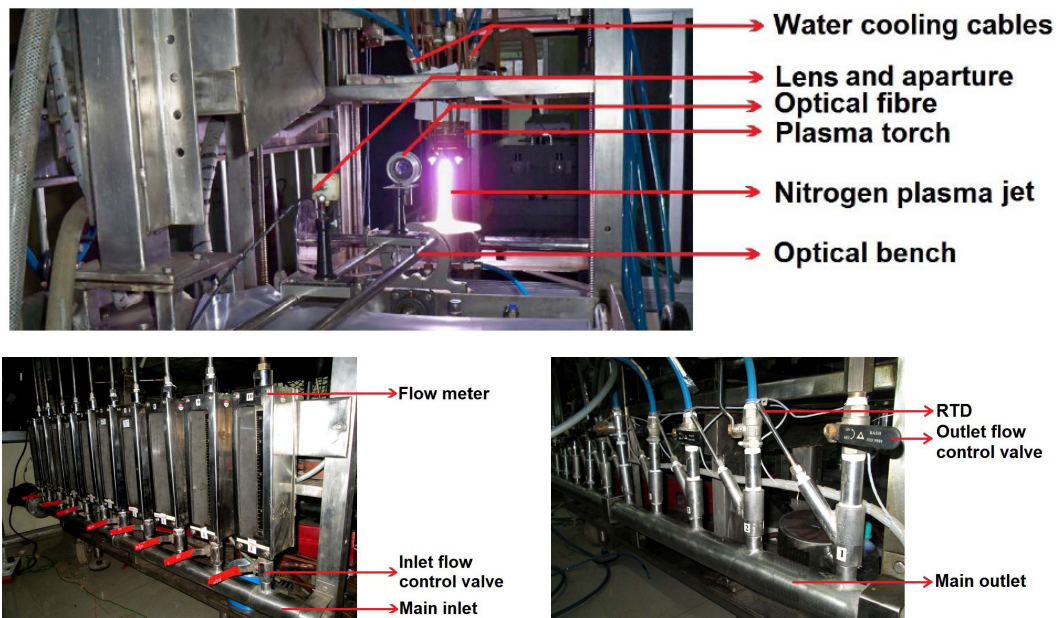


**Fig. 2.2 Photograph of the experimental setup in operating condition**

The torch is powered by an IGBT based constant current DC power supply which can provide 1000 A of DC current with a maximum load voltage of 100 V or equivalently it can provide 100 kW of DC electrical power. The plasma generating gas is controlled and measured by the gas supply unit attached with the power supply. The gas flow meters can measure maximum gas flow rate of 50 slpm with a precision of 1.25 slpm. For measurement of the device efficiency and calorimetric measurements, chilled water is supplied by the water supply unit. The flow meters used for water flow rate measurement can measure minimum flow rate of 2 slpm with a precision of 0.5 slpm. Temperature of the cooling water at inlet and at the outlet of the segments and calorimeter are measured by Pt100 resistance temperature detectors (RTD) and displayed on a temperature measurement and display unit with a precision

of  $0.1^{\circ}\text{C}$ . Proper position of the plasma torch over the calorimeters for heat flux study and plasma jet temperature measurement is achieved by XYZ-motion system which enables torch movement in three directions. Fluctuation of the arc voltage, Heat flux profile and temperature of the plasma jet characterize the plasma jet. Heat flux profile of the plasma jet is determined by the double calorimetric setup and temperature of the plasma jet is determined by optical emission spectroscopy (OES). The required emission spectrum of the plasma is acquired by using the optical arrangement utilizing a convex lens of appropriate focal length, an optical fibre and a spectrograph. Figure 2.3 (a) and figure 2.3 (b) show the experimental setup used for heat flux profile determination and OES.

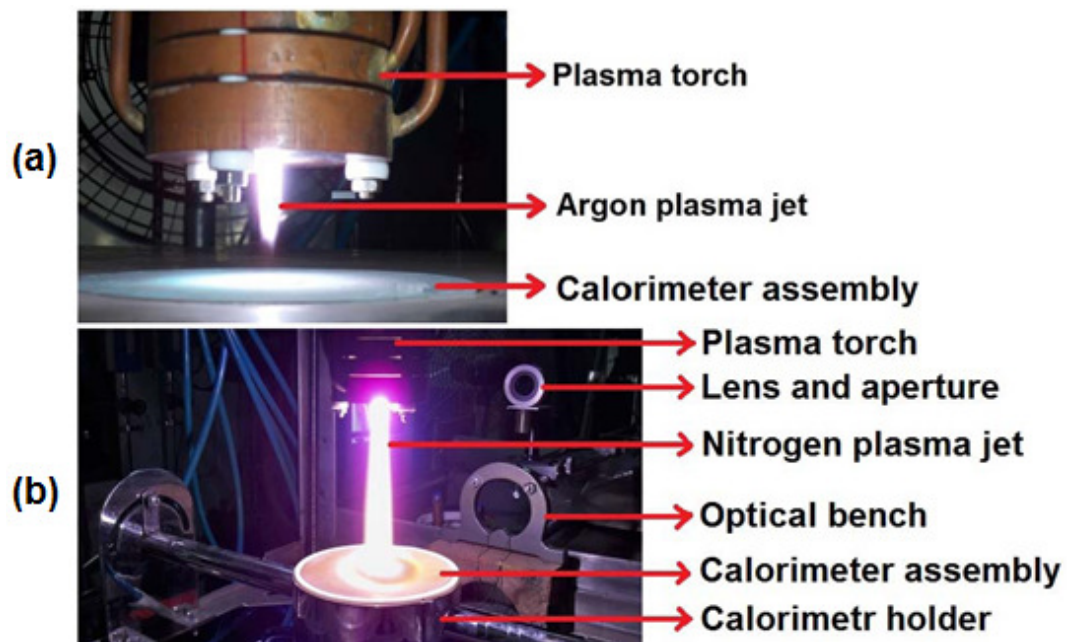


**Fig. 2.3 (a) Image of impinging argon plasma jet and (b) Impinging nitrogen plasma jet and OES setup**

The voltage divider circuit and oscilloscope are used for measuring the fluctuation in the arc voltage. A fraction of the arc voltage is drawn using the voltage divider circuit and used as the signal.

### 2.3. Plasma Torch

The DC plasma torch used in this study is presented in figure 2.4 (a). It has been designed and developed in the laboratory. The image of the plasma torch is given in figure 2.4 (b).

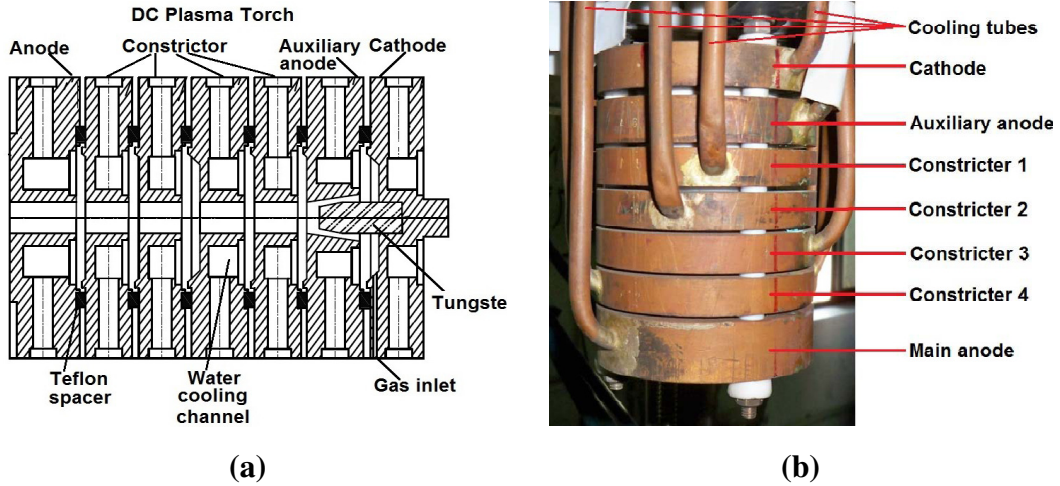


**Fig. 2.4 (a) Schematic figure of the plasma torch and (b) photograph of the plasma torch**

In order to withstand high temperature of the plasma, each component is cooled separately by chilled water. Since, anode receives maximum heat flux from the plasma, the volumetric flow rate of cooling water for anode is kept around 15 slpm (Standard litre per minute). The cooling water flow rate for rest of segments is around 10 slpm. The segments are thermally and electrically insulated from each other using Teflon spacer which can withstand a temperature up to 400 K. The design of the segments is such that, the Teflon spacers are well protected from direct heat of the plasma. Salient features of various segments are described below.

#### **Cathode:**

Cathode is one of the most important components of the torch as the arc is established between the cathode and anode. Ideally, the cathode material should have

very low work function, good electrical conductivity and high melting point. Mostly, electrodes of refractory material are used for this purpose while working with inert or non-oxidizing gases. The cathode used in the torch is a rod type cathode made up of tungsten with 2% thorium by weight (known as Thoriated Tungsten). It acts as a thermionic emission type cathode. The tip of the cathode is truncated cone with cone angle of  $48^{\circ}$  which allows high current application and the lower portion is cylindrical in shape with diameter of 10 mm. The Tungsten cathode is embedded on a OFHC (Oxygen Free High Conductivity) copper matrix which provides the necessary cooling from the bottom. Cooling water flow rate is set at 10 slpm which is sufficient for adequate cooling. Electron emission from cathode also causes significant cooling of the electrode.

**Anode:**

It is another electrode of the plasma torch. The anode is made up of OFHC copper which has excellent thermal and electrical conductivity. The nozzle inner diameter is 10 mm. The width of the anode i.e. the length of the nozzle is 21mm. Since during operation, the arc attaches from cathode to anode and as the heat flux incident by the arc on the anode surface is of the order of  $\text{MW} / \text{m}^2$  which can melt and even vaporize any material, it needs to be cooled sufficiently. The flow rate of cooling water is set properly so that it can save the anode from melting or getting punctured.

**Auxiliary Anode:**

The segment next to cathode is called as auxiliary anode. It is used for initiating the arc by igniting the pilot arc. A high frequency electric field (3 kV 3 MHz) is applied

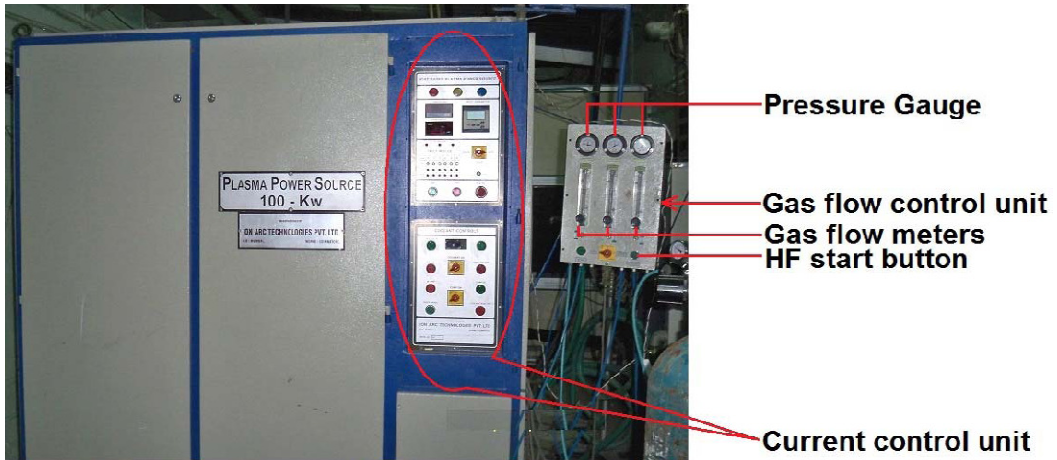
between the cathode and the auxiliary anode for initiating the arc and to breakdown the gas between the two electrodes. The auxiliary anode is also made up of OFHC copper. As shown in figure 2.4 (a), the inner cavity of auxiliary anode is in converging in shape (angle  $40^{\circ}$ ). In this study, cooling water flow rate for this component is usually set at 10 lpm which sufficiently cools the segment.

### **Constrictor Segments:**

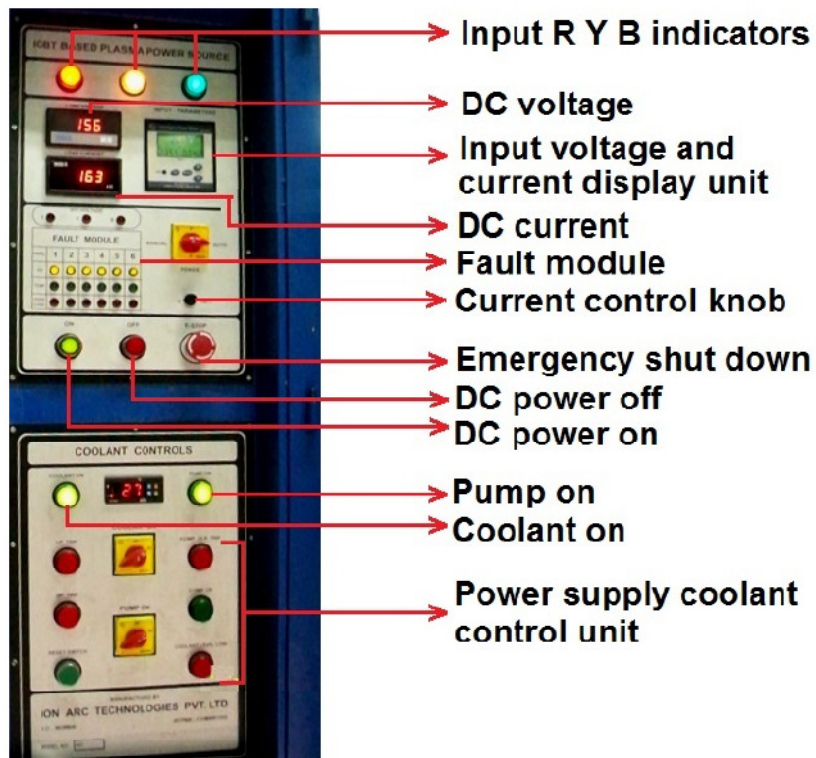
There are four intermediate segments in the torch placed between the auxiliary anode and main anode as shown in figure-2. The segments are having inner diameter same as that of the anode but of lower thickness. They are used to constrict the plasma as well as to increase the plasma power by increasing the arc voltage. The channel diameter is 10 mm for all the segments. The segments are cooled separately and set flow rates are 10 lpm each.

### **2.4. Power Supply**

An IGBT based constant current DC power supply is used to provide the necessary power to generate the plasma (Ion Arc Technology Pvt. Ltd.). As shown in figure 2.1, the cathode of the torch is connected to negative terminal and anode is connected to positive terminal of the DC power supply. Image of the power supply and its control units is shown in figure 2.5. The power source can provide 100 kW of DC electrical power at its full capacity. A gas control unit is also attached with the power supply. The power supply has an inbuilt HF electric field generator. The HF unit can produce peak voltage of 3000 V at a frequency of 3 MHz which initiates the pilot arc. The specification of the power supply and the embedded HF electric field generator are given in Table 2.1 and Table 2.2 respectively [70].



**Constant current DC power supply**



**Current control unit**

**Fig. 2.5 Power supply and control unit**

**Table 2.1 Power supply specification**

Manufacturer	Ion Arc Technology. Pvt. Ltd.
Power supply output specification	
Maximum power output	100 kW
Open circuit voltage	375 V DC
Max Load Voltage	100V DC
Max Load current	1000A DC
Min Load current	150A DC
Power supply input specification	
Input voltage	415V AC
Phase	3 $\phi$
Frequency	50Hz
Coolant Unit Specification	
Pump Specification	
Input voltage	230V
Type	1 $\phi$
Frequency	50Hz
Power	0.5 Hp
Compressor Specification	
Input voltage	415V
Phase	3 $\phi$
Frequency	50Hz
Capacity	5TR
Coolant tank specification	
Storage Capacity	125L

**Table. 2.2 Technical specification of HF unit and gas control unit.**

High frequency (HF) electric field production unit	
Input voltage	230 V
Input current	5A
Type	1 $\phi$
Output voltage	3000 V (3 kV)
Output current	~ 1A
Frequency	3 MHz
Operating mode	Auto and Manual
Time duration for which HF electric field is applied	1 s (In auto mode) and 3 s in manual mode)
Pressure guage (3 numbers)	
Minimum pressure reading	0 psi or 0 kg/cm <sup>2</sup>
Maximum pressure reading	200 psi or 14 kg/cm <sup>2</sup>
Minimum pressure measurement	5.0 psi or 0.25 kg/cm <sup>2</sup>
Precision	5.0 psi or 0.2 kg/cm <sup>2</sup>
Flow meters (3 numbers, two for argon and one for nitrogen)	
Minimum reading	0.0 slpm
Maximum reading	50.0 slpm
Minimum measurable flow rate	5.0 slpm
Precision	1.25 slpm

## 2.5. Double Calorimeter

The double calorimeter setup is used for determining the heat flux profile of the plasma jet. It consists of two concentric calorimeters. The complete assembly of calorimeters and their top view are shown in figure 2.6 (a) and figure 2.6 (b)

respectively. The calorimeters are made up of OFHC copper. The outer diameter of the outer calorimeter is 150 mm and that of the inner probe is 25 mm. The image of the calorimeters with a nitrogen plasma jet impinging over it is shown in figure 2.7.

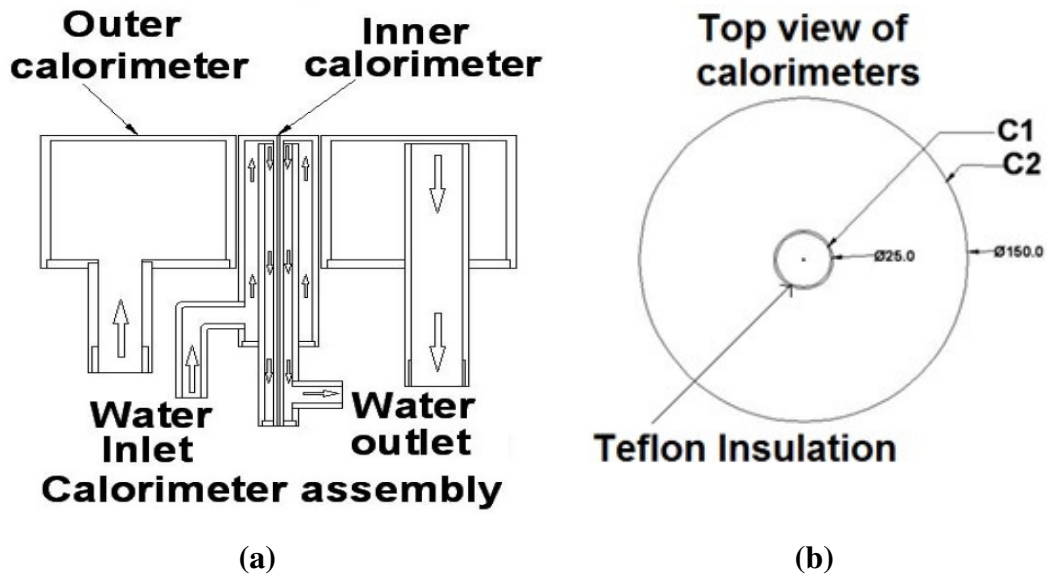


Fig. 2.6 (a) The double calorimeter assembly, (b) top view of calorimeters

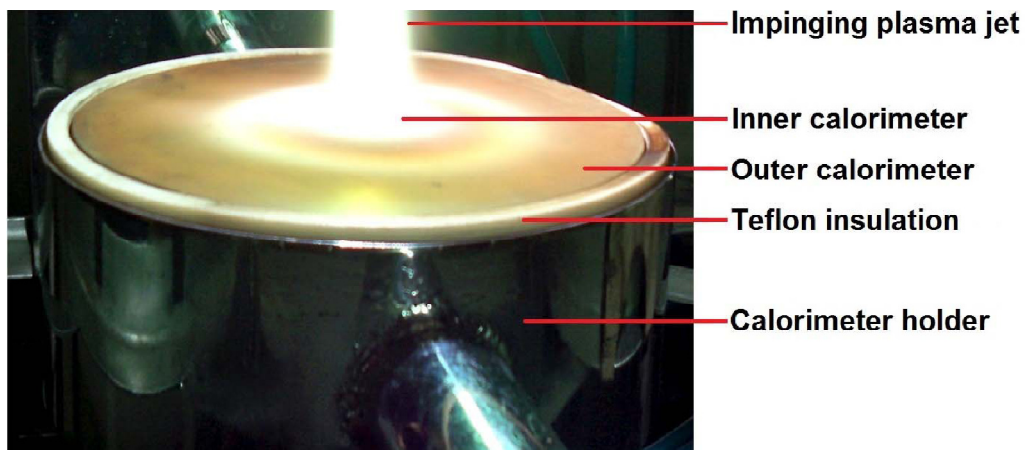


Fig. 2.7 Calorimeter assembly

Width of both the calorimeters is 50 mm. The extent of the calorimeters is so chosen that, they will be able to receive most of the convective heat from the impinging plasma jet. The two calorimeters are thermally insulated from each other by a Teflon

sheet of thickness 1 mm at their bottom and by air at the top. This prevents heat conduction between the calorimeters which will introduce error in calculation otherwise. The two calorimeters are cooled by chilled water and the rise in temperature of the cooling water running through the calorimeters is used for calculating the heat flux profile of the plasma jet. It is designed in such a manner that the cooling water can only exit after it fills the calorimeter completely.

## **2.6. Resistance Temperature Detector (RTD)**

Temperature monitoring plays a basic need for safe operation of the device. To save the device components and other parts from the intense heat of the plasma, they are cooled by water. For safe operation, it is required that, the temperature of water at inlet and outlet should lie within safe range i.e. the water running through the system should not start boiling. Temperature of the cooling water at the inlet and outlet of different torch segments and calorimeters is monitored using resistance temperature detectors (RTD). In this study, RTD PT 100 (Omega Engineering) is used for measuring the temperature. A photograph of the RTDs used in the experiments is shown in figure 2.8. Technical specifications are provided in Table 2.3.



**Fig. 2.8 RTD PT100**

**Table 2.3 Technical specification of RTD**

Manufacturer	Omega Engineering
Type	PT100
Accuracy	+/- 0.1 C at 0 °C
Temperature range	-200 to 600 °C

## **2.7. Spectrograph**

Temperature of the plasma jet is determined using optical emission spectroscopic technique. Boltzmann plot method is used to calculate the temperature using the intensity of emitted line radiation. The required spectrum of argon and nitrogen plasma jet is acquired using a high resolution spectrograph HR4000 (Ocean Optics). It can be used in the wavelength range of 400 nm to 487 nm. As shown in figure 2.1, a particular zone of the plasma jet is focused at the end of the optical fibre. The other end of the optical fibre is connected to the spectrograph. Light coming from the optical fibre is incident on the concave mirror M1 and the parallel beam of light falls on the grating. The image of the spectrograph and internal ray diagram are shown in figure 2.9 (a) and (b) respectively. The diffracted light falls on the concave mirror M2 which reflects the light on the CCD array which is placed at the focal plane of the mirror. The focal length of both the mirrors is 101.6 mm. The grating used in the spectrograph has 2400 lines/mm. Efficient response of the grating lies in the wavelength range of 260nm to 780 nm. It utilizes a linear CCD detector Toshiba TCD1304AP. It has 3648 pixels and size of each pixel is 8  $\mu\text{m}$  x 200  $\mu\text{m}$ .

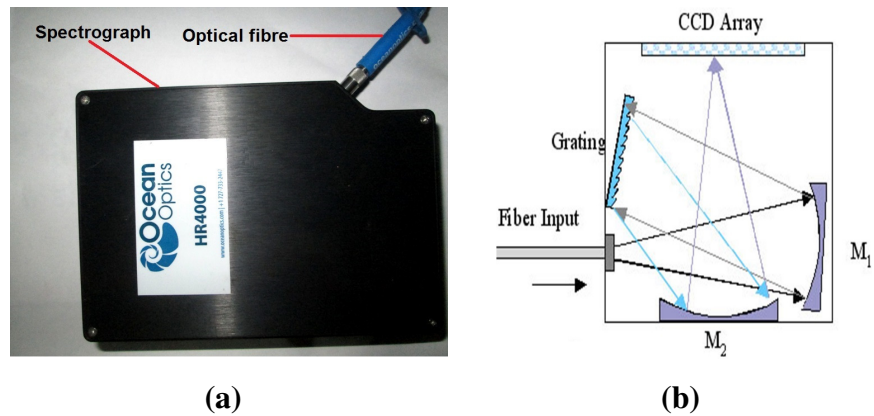


**Fig.2.9 (a) The spectrograph (b) Internal ray diagram of spectrograph**

The slit width is  $5\mu\text{m}$  and it is fixed for the system. The technical specification of the spectrograph is given in Table 2.4. [71]

**Table 2.4 Technical specification of spectrograph**

Manufacturer	Ocean Optics
Detector details	
Detector:	Toshiba TCD1304AP linear CCD array or equivalent
Detector range:	200-1100 nm
Pixels:	3648 pixels
Pixel size:	$8\mu\text{m} \times 200\mu\text{m}$
Optical bench	
Design:	$f/4$ , Symmetrical crossed Czerny-Turner
Focal length:	101.6 mm input and output
Slit:	$5\mu\text{m}$
Grating options:	2400 lines/ mm with 5 micrometer slit
Spectroscopic	
Wavelength range:	400 nm to 487 nm
Optical resolution:	0.15 nm
Signal-to-noise ratio:	300:1 (at full signal)

## 2.8. Optical Fibre

The role of optical fibre is to transmit light from the focal plane of the lens to the spectrograph. The optical fibre used for this purpose is QP200-2-UV-VIS (Ocean Optics) which is transparent for UV and visible range. Image of the optical fibre is shown in figure 2.10. It can transmit light in the wavelength range of 300 nm to 1100 nm and the relative transmission is nearly uniform in the wavelength range of 300 nm to 900 nm. Since the argon and nitrogen spectrum of our interest lies in this wavelength range it can serve our purpose. Its technical specification is given in Table 2.5 [71]



**Fig. 2.10 The optical fibre**

**Table 2.5 Optical fibre specification**

Manufacturer	Ocean Optics
Model	QP200-2-UV-VIS
Transmission range	300 nm to 1100 nm
Preferable range	300 nm to 900 nm
Core diameter	200 $\mu\text{m} \pm 4 \mu\text{m}$

## 2.9. Oscilloscope

The power content of the plasma jet is directly proportional to the arc voltage and the arc voltage is proportional to the arc length. The inherent instabilities in arc causes the arc length and hence the power content of the arc to vary. In this study the time evolution of the change in arc voltage is recorded using a 350 MHz four channel digital storage oscilloscope (DSO) HMO3524 (Hameg Instruments). The image of the oscilloscope is shown in figure 2.11 and its technical specification is given in Table 2.6. [72] For collecting data chosen sampling rates are 10 MSa /s and 25 MSa/s. The corresponding time bases are 5 ms and 10 ms respectively. The total time for which the data has been recorded is 60 ms and 120 ms respectively.

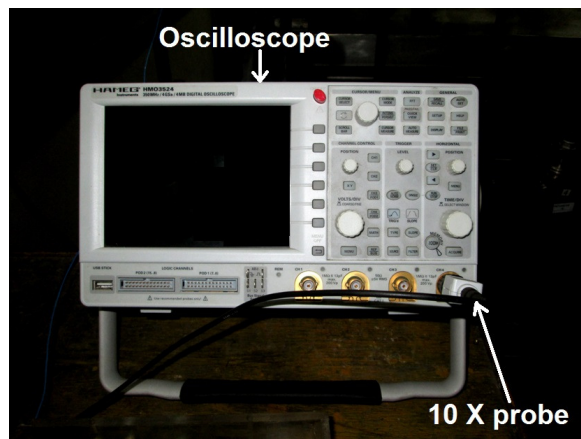


**Fig 2.11 The oscilloscope**

Total 24000 data points are collected during the experiment. Time interval between two consecutive data points is 2.5  $\mu$ s and 5.0  $\mu$ s respectively. Since the frequency of voltage fluctuation is of the order of kHz, the above settings are appropriate to reliably reconstruct the signal as per Nyquist's criteria.

**Table 2.6 Technical specification of oscilloscope**

Manufacturer	Hameg instruments
Model	HM3524
Band width	350 MHz
Channel	4
Sampling rate per channel	2 X 4 Giga Samples/ sec 4 X 2 Giga Samples/ sec
voltage sensitivity	1 mV/Div to 5 V/Div
Maximum Input Voltage	200 V (DC + peak AC)
The time sensitivity	1 ns/Div to 20 ms/Div.
Maximum number of data points that can be stored	24000

### 2.10. Voltage Divider Circuit

Since the maximum input voltage to the oscilloscope is 200 V (DC + peak AC), connecting the oscilloscope directly across the electrodes may damage it. So a fraction of the voltage drop across the electrodes of the plasma torch is used as input signal to the oscilloscope. The circuit diagram of the voltage divider circuit is given in the figure 2.12. Terminal 1 and terminal 3 are connected to the cathode and anode of the plasma torch respectively. Input signal for the voltage fluctuation is drawn across the terminal 2 and terminal 3. The amplitude of the fluctuating component of voltage signal is found to be around 20 Vpp.

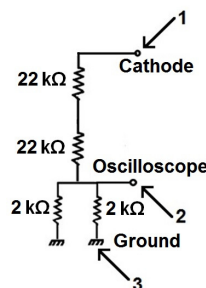


**Fig. 2.12 Circuit diagram of voltage divider circuit**

### 2.11. 10X Probe

The oscilloscope is connected to the probe using a 10X probe HZ350 (Hameg Instruments). The image of the probe is given in the figure 2.13. It allows only 1/10 of the original voltage to the oscilloscope. Table 2.7 contains the technical specification of the probe. [72]

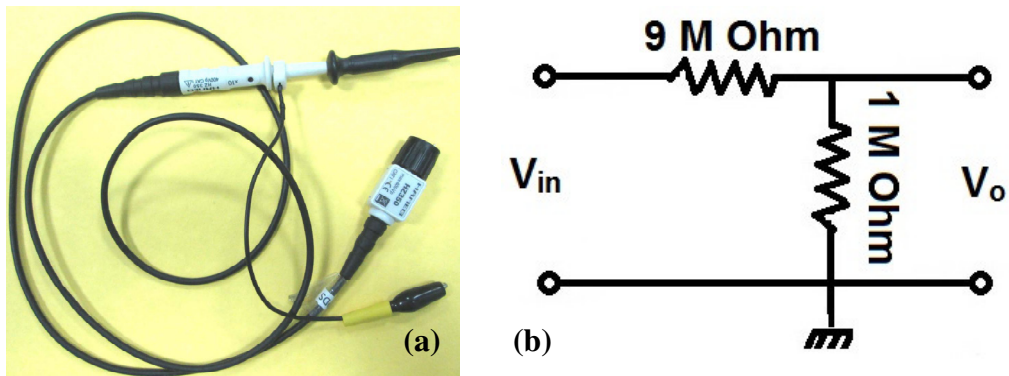


**Fig.2.13 (a) The 10X probe and (b) Circuit diagram of the probe**

**Table 2.7 Technical specification of the probe**

Manufacturer	Hameg instruments
Model	HZ350
Attenuation ratio	10:1
Band width	350 MHz
Rise time	< 1.0 ns
Input impedance	10 Mohms  12pF
Max Voltage	400 V (DC + peak AC)

## 2.12. Chilled Water Supply Unit

The temperature of the plasma in the core region is of the order of 10000 K. It has the ability to melt and evaporate any material including the torch components. To maintain device integrity, required cooling water for the experimental system is provided by a chilled water supply unit. The image of the chilled water supply unit and internal flow structure are shown in figure 2.14 and 2.15 respectively. Demineralised water is used as the coolant. It includes two pumps of capacity 3 Hp and 10 Hp respectively, a water tank of capacity 500 litres and three heat exchangers to cool the water in the tank. While this is a centralized coolant supply unit for a number of experimental systems, one loop of the chilled water supply system circulates chilled water to the torch and other parts of the experimental setup. Although, the possible minimum coolant temperature is 5°C, the inlet water temperature is set at 27°C to avoid condensation inside the torch. Other technical details of the chilled water supply unit are given in Table 2.8.

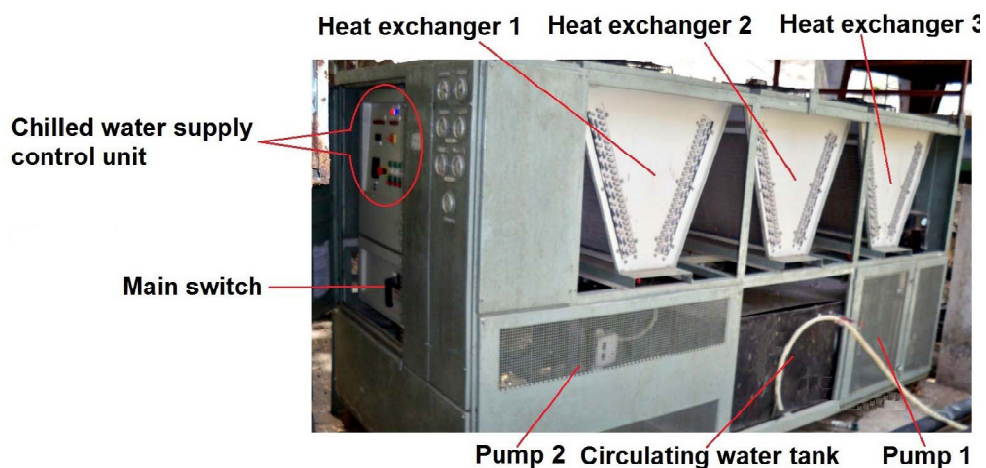


**Fig. 2.14 Chilled water supply unit**

## Chilled water Supply Unit

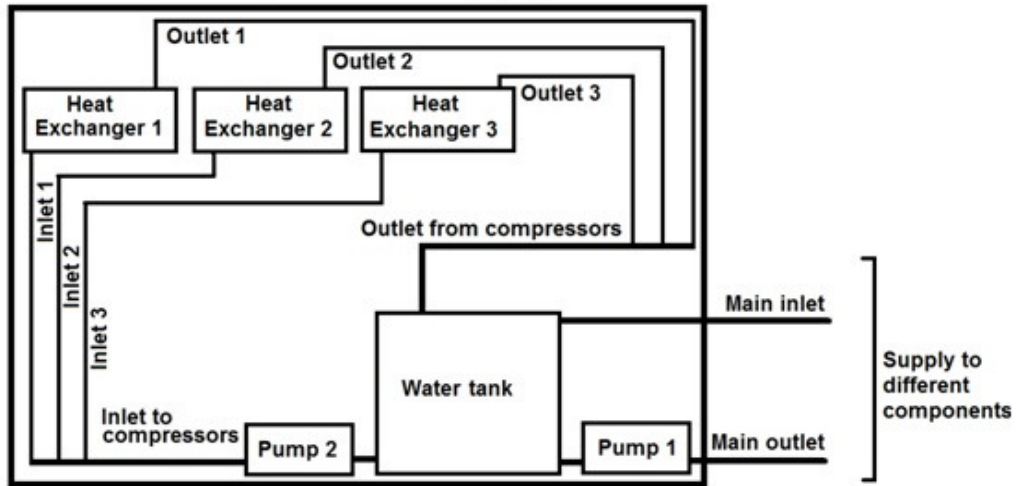


**Fig. 2.15 Chilled water supply unit water flow diagram**

**Table 2.8 Chilled water supply unit specification**

Parameter	Value
Inlet temperature	35 - 40 <sup>0</sup> C
Outlet temperature	5 <sup>0</sup> C to ambient temperature
Temperature stability	± 0.5 <sup>0</sup> C
Refrigeration load	30 TR (105 kW)
Fluid	Demineralised water
Flow rate	50-200 LPM (140 slpm nominal)
Power	25 kW
Electrical specification	
Power supply	415V ± 10%, 3phase, 50Hz

## **CHAPTER-3:**

# **Axial Evolution of Radial Heat Flux Profiles Transmitted by Atmospheric Pressure Nitrogen and Argon Arcs**

### **Outline of the chapter**

**3.1 Introduction**

**3.2 Determination of Profile Parameter**

**3.3 Experimental Setup**

**3.4 Results and Discussion**

**3.5 Conclusions**

## Chapter 3

# Axial Evolution of Radial Heat Flux Profiles Transmitted by Atmospheric Pressure Nitrogen and Argon Arcs

### 3.1 Introduction:

This chapter deals with the determination of the radial heat flux profile of argon and nitrogen plasma jet and its axial variation. The nature of the heat flux profiles delivered by a plasma jet determines the process design, the quality of the processing work done and its suitability for a particular application. Number of attempts has been made in the past to determine the shape of the heat flux profiles offered by such devices as a function of axial distance, power level, flow rate of plasma gas, nozzle diameter and nature of plasma gas. However, most of the studies focussed on Argon as plasma gas and operation at a power level below 40 kW. Plasma torches operating with Nitrogen as plasma gas offer radical rich non-oxidizing high temperature environment for plasma chemistry and processing. They are routinely used in commercial processes like nitriding, wear resistant coatings and have the ability to operate with usual tungsten based refractory electrodes. Being a molecular gas, Nitrogen naturally offer higher voltage drop across the arc for the same electrode configuration and associates higher power. However, work on finding the nature of the heat flux profiles offered by such plasma torches is rare. An extensive review of earlier works on finding the radial heat flux profile of argon and nitrogen plasma jets and its variation with respect to different operating conditions has been presented in chapter 1.

To the best of the authors' knowledge, no systematic study of heat flux is reported in literature for power level more than 15 kW in Nitrogen plasma. The present study on axial evolution of radial heat flux profile transmitted by atmospheric pressure Nitrogen and Argon arcs focuses on plasma torches operating at power level ranging from 6.6 kW to 52 kW in Argon and 32 kW to 51 kW in Nitrogen. Ideal plasma spraying condition requires that all the injected particles get uniformly heated and entrained by the plasma jet, their temperature remains above their melting point but below the boiling point before they reach the substrate. Injected particles usually inherits a distribution in the velocity vectors due to collision with the injector wall and among themselves depending on the particle type, particle size distribution, particle morphology, surface functionality, injector wall morphology and velocity of the carrier gas. For thinner jet diameter, the distribution makes the particles with heavier masses cross the plasma jet while those with smaller masses fail to reach the jet. Melting of the injected particles depend on their trajectories, residence time and masses. Many of the times the particles are only partially melt due to limited time of passage in the high temperature zone [32]. Such problems of partially melts and unmelts are severe for high melting point ceramic particles like  $Y_2O_3$ ,  $Al_2O_3$  etc. Residence time of the injected particles inside the plasma depend on the length of the plasma jet and is usually short due to limited spatial extent of the plume. A relatively broad and long plasma jet having high power and axially uniform radial heat flux profile is best suited for spraying application of ceramics. Better control over the process may be achieved through adjustment of the axial location of the job and thereby controlling the dwell time and physical state of the particles inside the plasma.

For a broader plasma jet at higher power, a nozzle exit diameter of 10 mm is

chosen instead of shorter diameters used in the earlier studies. Segmented electrode torch configuration is chosen to achieve an easy enhancement of input power. Studies are made with electrical power beyond 40 kW to enable efficient melting. Results with lower power are included to obtain a comparison with the studies available in literature at lower power and understand the shift in behaviour as one move from lower to higher power regime.

In case of Argon plasma, it has been observed that even around 50 kW, the jet length is short as shown in figure 3.1(a) and the peak of the heat flux profile drops by more than 60 % as one moves along the axis by a distance of 20 mm. However, for Nitrogen plasma a remarkably different scenario is observed. A huge long jet is observed in figure 3.1 (b). For power level beyond 40 kW, the peak of the heat flux profile drops by less than 50% even after traversing a distance of 100 mm after the nozzle exit. The radial extent of the profile remains constant within 10% up to a distance of 50 mm and the same remains constant within 20% up to a jet length of 150mm. It is obvious that such long uniform jet has huge potential in processing applications.

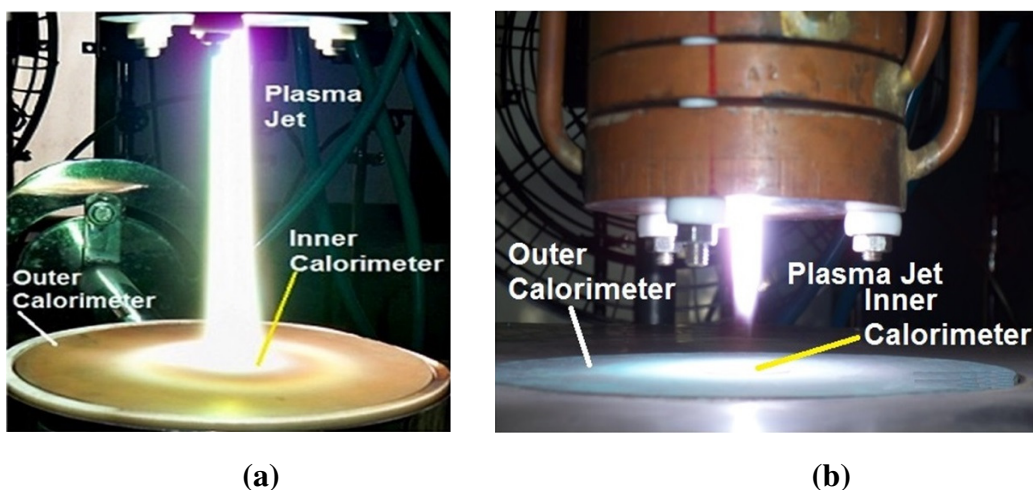


**Fig. 3.1 (a) image of the nitrogen plasma jet and (b) image of the argon plasma jet.**

Electromagnetic body force plays significant role in influencing temperature and velocity distribution inside a plasma torch [73]. A current carrying segment produces its own magnetic field which interacts with the passing current itself and exerts a force on the segment in a direction perpendicular to both the current and the magnetic field. The plasma column inside a plasma torch may be considered as composed of such contiguous current carrying elements. In a perfectly cylindrical plasma column, the thermal expansive force (caused by Ohmic Joule heating) accurately balances the radially inward compressive force via JXB pinch effect. However, in a plasma torch the incoming cold gas gets heated by the arc, forms plasma and comes out as a plasma jet. In the process, it may distort the current carrying segments resulting in an asymmetric distribution of magnetic pressure. Degree of distortion depends on electrode configuration, operating parameters and the flow conditions. A diverging configuration of the current density vector with respect to the central axis (as happens when an arc tries to connect with the anode) exerts a thrust on the body of the plasma producing high velocity long plasma jet. On the other hand, a converging configuration produced in some manner in some part of the plasma (happens when an expanded jet is forced to enter a thin nozzle), may act as a barrier to the flow leading to a reduced length of the emanating plasma jet. Such effects are well studied in literature and detail mechanisms are illustrated in number works [74,75]

To account for limitation of the present study it may be pointed out that the plasma jets are inherently unstable [36,76]. Double calorimetric technique used in this study to determine the heat flux profiles ignores this non-stationary feature of the jets

and the presented results are only average values of the time-integrated measurements. However, enough care has been taken to ensure steady state before taking data for any revised set of parameter values. Although actual profile may be little different depending on operating conditions, approximate nature of the heat flux profile is assumed to be Gaussian in the calculation as they give fairly accurate averaged results [9,10]. It may also be remarked that the heat flux profile is determined using a water-cooled calorimeter, whose temperature remains below 400 K. However, an actual substrate to be processed using this jet is usually not water cooled and may have temperature far above this value. Heat flux received by such a substrate under similar condition may not be the same. Heat flux determined in the study is due to the torch alone. Processing applications like plasma spray, unavoidably use some powder-laden carrier gas which can influence the heat flux as well as the spatial extent of the jet. Such effects are beyond the scope of the present study. The inner and the outer calorimeters are thermally isolated at the top by an air gap and at the bottom by a layer of teflon. Heat transfer from one calorimeter to the other may happen through convective heat transfer in the sandwiched thin layer of air. The effect is not accounted in the calculation and assumed to be negligible. Constricted connection of the arc over the anode at one location forming an arc root [77] inherently introduces a spatial asymmetry in the emanating plasma jet making it non-axisymmetric. However, fast spontaneous movement of the arc root over the anode [77] is expected to result in a good time averaged axi-symmetric behaviour justifying the profile shape used. Variation in the heat transfer due to micro-structural deformation over the calorimeter surface caused by high heat flux is not taken into account. From visual inspection of the calorimeters, such defects were not prominent. In actual spraying applications

micro-structural defects are significant and sometimes deliberately introduced as a part of the surface preparation by sand blasting etc. Presence of high concentration of such defects on those surfaces may alter the actual surface area and influence the heat transfer. Such effects are also beyond the scope of the present study. It may be remarked that the type of fluid flow over the calorimeter surface may also influence the effective heat transfer. Under laminar flow conditions, the thickness of the boundary layer varies as the inverse square root of the plasma velocity at the stagnation point. The calorimeter may experience reduced heat flux due to higher thickness of the boundary layer as distance increases. It is highly possible that the dissociated nitrogen atoms recombine over the calorimeter surface maintained at temperature below the dissociation temperature of the nitrogen molecules. Energy associated with recombination of the Nitrogen atoms gets released and may contribute to the measured heat flux. The stagnation profiles so determined include this component as well. For argon, although it is monatomic, the experiment for determination of heat flux is performed in open atmosphere, primarily composed of molecular gasses. There is a chance that the entrained molecular gases get dissociated in the high temperature core and recombine over the calorimeter surface in similar manner contributing towards additional heat flux.

A brief description of the method of determination of the heat flux profiles is presented in section-3.2. Details of the experimental setup and the operational condition are presented in section-3.3. Experimental results are presented in section-3.4. Heat flux profile parameters obtained from the study under different experimental conditions are compared with those reported in literature. As both nozzle diameter of the torch and the operational power regime in the study are higher compared to most

of the results reported in literature, it is not possible to compare results under identical operating conditions. However, for Argon plasma, some results are available in literature with overlapping power levels. A comparison of the results in those regions gives some idea on reliability of the obtained data and helps us to better understand the behaviour in the extended parametric regime. Conclusions are presented in section-5.

### 3.2. Determination of the profile parameters:

Radial distributions of heat flux of a plasma jet emanating from a DC plasma torch can be approximated as:

$$\phi(r) = \phi_0 \exp\left[-\left(r/R_g\right)^n\right] \quad (3.1)$$

where,  $\phi_0$  is the maximum of the heat flux,  $R_g$  is the width of the profile and  $n$  indicates the shape of the profile.  $n$  is '1' for exponential, '2' for Gaussian and so on. It was our choice to take  $n=2$  in the present study as it has been widely accepted as presenting sufficiently accurate heat flux profile for plasma jets transmitted by DC arcs [9,10]. When such a plasma jet impinges normally along the central axis of a concentric double calorimeter [figure 3.1], the power received by the inner ( $H_1$ ) and the outer ( $H_2$ ) calorimeter may be expressed as:

$$H_1 = 2\pi \int_0^{d_1/2} \phi(r) r dr \quad (3.2)$$

$$H_2 = 2\pi \int_0^{d_2/2} \phi(r) r dr - H_1 \quad (3.3)$$

Where,  $d_1$  and  $d_2$  are the diameters of the inner and the outer calorimeter respectively.

The values of  $H_1$  and  $H_2$  are determined from the inlet and the outlet temperature of the cooling water using basic calorimetric principle:

$$H_1 = m_1 S_w (T_1 - T_{in}) \quad (3.4)$$

$$H_2 = m_2 S_w (T_2 - T_{in}) \quad (3.5)$$

Where,  $m_1$  and  $m_2$  are the water flow rates through the inner and the outer calorimeter respectively.  $S_w$  is the specific heat of water.  $T_1$  and  $T_2$  are the respective outlet temperatures and  $T_{in}$  is the inlet temperature for both the calorimeters.

For the chosen Gaussian profile, equation (3.1) and (3.2) can be integrated to obtain an iterative expression for determination of  $R_g$  as [10]:

$$R_g = \sqrt{\frac{d_1^2}{4 \ln(1 + H [\exp(-d_2^2/4R_g^2) - 1])}} \quad (3.6)$$

where,  $H = H_1/(H_1 + H_2)$ . For a given operating condition,  $H_1$  and  $H_2$  are determined experimentally and the two unknowns ( $\phi_0$  and  $R_g$ ) of the profile (equation-3.1) are obtained by solving equation (3.6). Once the value of  $R_g$  is determined, the other profile parameter  $\phi_0$  is estimated from (3.2).

### 3.3. Experimental Set-up

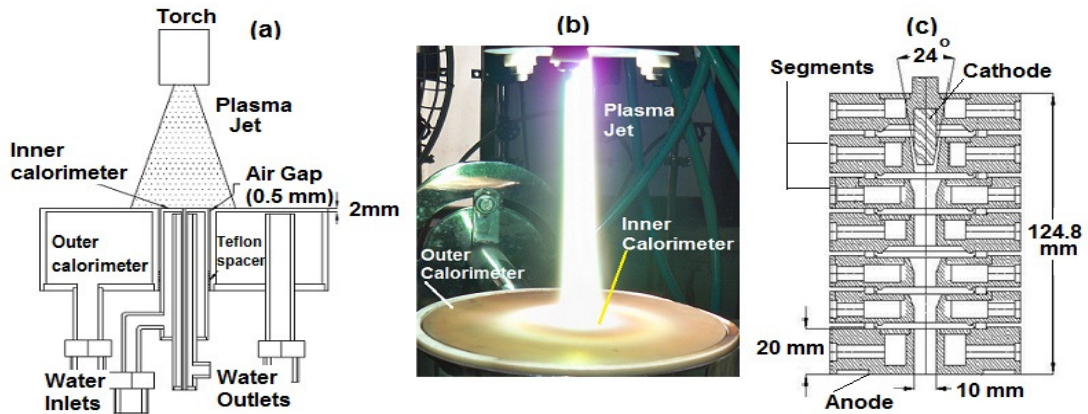


**Fig. 3.2 (a) The experimental setup (b) Image of the nitrogen plasma jet impinging on a double calorimeter (c) Detail schematic of the plasma torch transmitting the plasma jet.**

Schematic of the experimental setup, an image of the actual plasma jet impinging on a double calorimeter and the details of the plasma torch are presented in Figure 3.2(a), (b) and (c) respectively. The specially designed double calorimeter, made of Oxygen free high conductivity (OFHC) copper, houses the cylindrical inner calorimeter (outer diameter 25 mm) exactly at the centre of the outer calorimeter (inner diameter 26mm and outer diameter 150 mm). To prevent cross flow of heat from one calorimeter to the other through conductive transfer, the surrounding outer calorimeter is separated from the inner calorimeter by a uniform air gap of thickness 0.5 mm at the top. A sand-witched layer of Teflon of thickness 0.5 mm between the calorimeters at the bottom holds the calorimeters firmly at their position as well as maintains uniformity of the gap at the top. Inlet supplies and outlet discharges of the calorimeters are designed in a manner that water flows out of the system only after complete filling of the calorimeters under vertical configuration. The calorimeter is firmly fixed on a stationary platform, below a X-Y-Z motion stand (controlled by servo motor), over which the plasma torch is mounted vertically. Details of the other components used in the experimental setup have been discussed in chapter – 2. The gas flow rate of argon was set at 30 slm and that of nitrogen was set at 17.5 slm.

#### **3.4. Results and discussion**

The plasma torch is characterized through V-I characteristics, typical distribution of temperature inside the torch and the resulting arc voltages under different operating currents. The measured heat flux profiles with Argon and Nitrogen as plasma gas under different operating conditions followed by analysis of these heat flux profiles are presented for a clearer picture about the variation of profile parameters with electric power input and axial distance. The differences in the observed behaviour of

the Nitrogen and the Argon plasma jets are brought out. Possible reasons for the observed differences are explained.

### 3.4.1 Torch characteristics

For the same power level, the plasma jets generated by the torch with Argon and Nitrogen as the plasma gas are found to be distinctly different. While the arcs in Argon are easily sustained at current below 100 A, the same in Nitrogen could not be sustained below 100A due to requirement of higher power under the present electrode configuration. It may be observed from the V-I characteristics presented in Figure 3.3 that as current increased, voltage in Argon increased almost linearly with current. However, the same in Nitrogen remains nearly constant around 159 V for the range of currents considered. While the first is well studied in literature [75] the observed interesting behaviour in Nitrogen is rarely probed. To investigate the behaviour, the torch has been modeled for Nitrogen plasma within the framework of LTE (Local thermal equilibrium) laminar simulation model following Ref.[43] and experimentally realized arc voltages are found to be very close to the simulated ones. A detail fluid dynamic simulation study of the system under different operating conditions is presented in chapter-7.

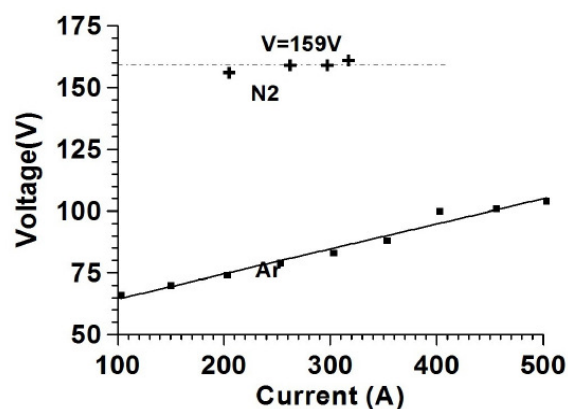
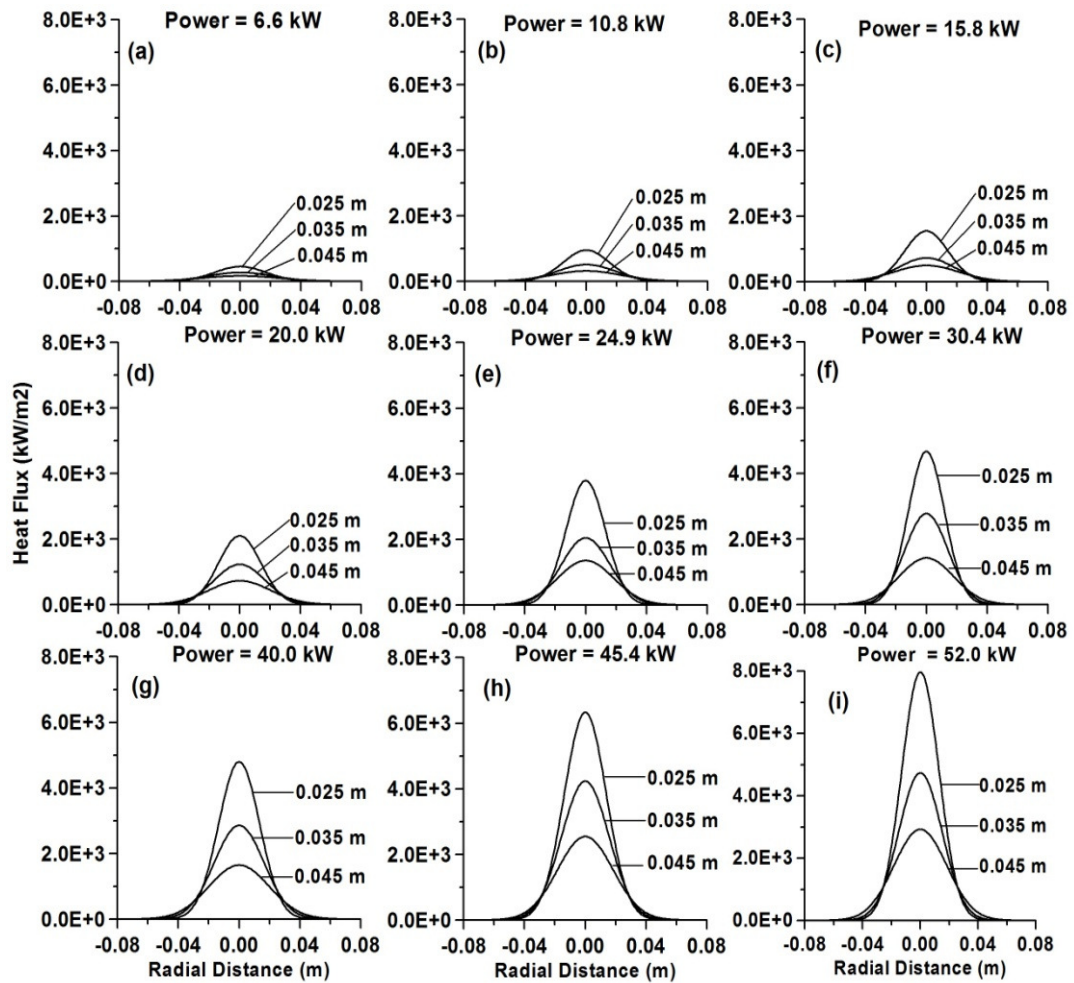


Fig.3.3 V-I characteristics of the torch in Argon and Nitrogen plasma.

Radial distribution of heat flux for Argon plasma jet at different axial locations is shown in Figure 3.4 at different power levels starting from 6.6 kW to 52 kW. Power is increased roughly by 5 kW in each step and corresponding heat flux profiles at three different axial locations are estimated. The peak heat flux reduces almost uniformly with increase in the axial distance. At an axial distance of 2.5 cm, the highest heat flux varies from 0.45 kW/m<sup>2</sup> to 8 kW/m<sup>2</sup> as the power level goes up from 6.6 kW to 52 kW. Nearly 16 times increase in the peak heat flux is observed for an increase in the torch power by eight times. This is an important observation for spraying application where choice of appropriate power of the torch plays a decisive role in the ultimate quality of the processing job done and efficiency of the process.

An explicit dependence of the received heat flux on the electrical power input to the torch is depicted in Figure 3.5. Apart from the measured distribution, it is observed that at a particular location the increase in the received heat flux with increase in the input electrical power is not uniform. Sometimes the power is increased but no appreciable increase is observed in the received heat flux. One very important but rarely discussed aspect of such devices is reflected in these results. The jet exiting from the torch has its origin inside the torch where an arc connects the cathode to the anode and heats the gas flowing in between forming the emanating plasma jet. Depending on operating current, gas flow, electrode material, geometry of the torch and other environmental conditions, the extent of the arc in the configuration space and the magnitude of the associated electromagnetic body forces (through  $\mathbf{J} \times \mathbf{B}$  force where,  $\mathbf{J}$  is the current density and  $\mathbf{B}$  is the magnetic field produced by the current) acting on various parts of the plasma are decided. Under certain operating conditions, an increase in the current to increase power may enhance the diameter of the plasma

core inside the torch, decreasing the thickness of surrounding colder boundary layer. Enhanced conductive and radiative heat transfer from the plasma to the wall may result in a poor rise in the transmitted heat flux in the associated cases. The same may affect the fluid dynamic pattern of the jet outside the torch.



**Fig.3.4** Variation of heat flux distribution of Argon plasma with axial distance at power level of (a) 6.6 kW, (b) 10.8 kW, (c) 15.8 kW, (d) 20.0 kW, (e) 24.9 kW, (f) 30.4 kW, (g) 40.0 kW, (h) 45.4 kW and (i) 52.0 kW. The gas flow rate is 30 slm

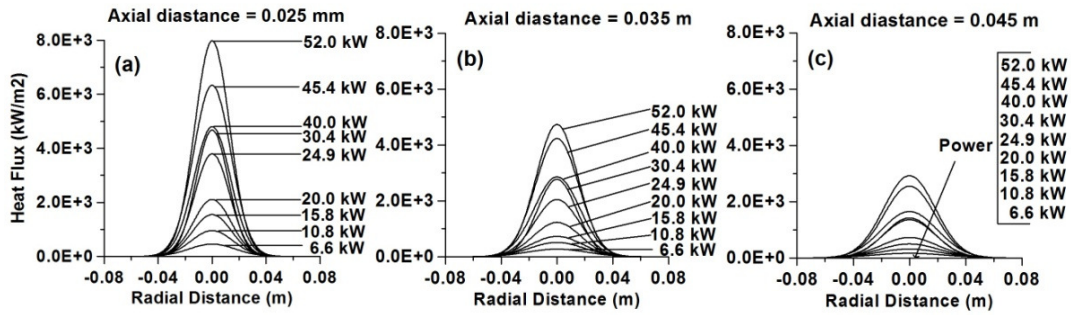


**Fig. 3.5** Variation of the radial heat flux profile as a function of power at the three axial locations (a) 2.5 cm (b) 3.5 cm and (c) 4.5 cm.

### 3.4.3 Behaviour of heat flux profiles in Nitrogen plasma jet

Considering the fact that the Nitrogen plasma jet was appreciably long compared to Argon the study on heat flux measurements were carried out at three different axial distances from the nozzle exit (5 cm, 10 cm and 15 cm) and at four different power levels (31.9 kW, 41.6 kW, 47.2 kW and 51.0 kW). Measured distribution of radial heat flux are presented in Figure 3.6. Unlike Argon plasma, the decrease in the received heat flux with increase in distance from the nozzle exit is not uniform at lower powers. The drop in the peak heat flux value is high over the first few centimetres after the nozzle exit and it reduces fast as the jet propagates [Fig. 3.6(a)-(c)]. However, the drop is found to be nearly uniform at higher power [ Fig. 3.6 (d) ].

The variations in the radial distribution of the heat flux with power at three axial locations are presented in Figure 3.7. Although, an increased heat flux with increasing power is observed in general, associated decrease or increase in the heat flux depends on axial location. Change in the jet flow pattern associated with corresponding change in the electromagnetic body forces inside the torch due to variation in the input power may be responsible for the observed non-uniformity.

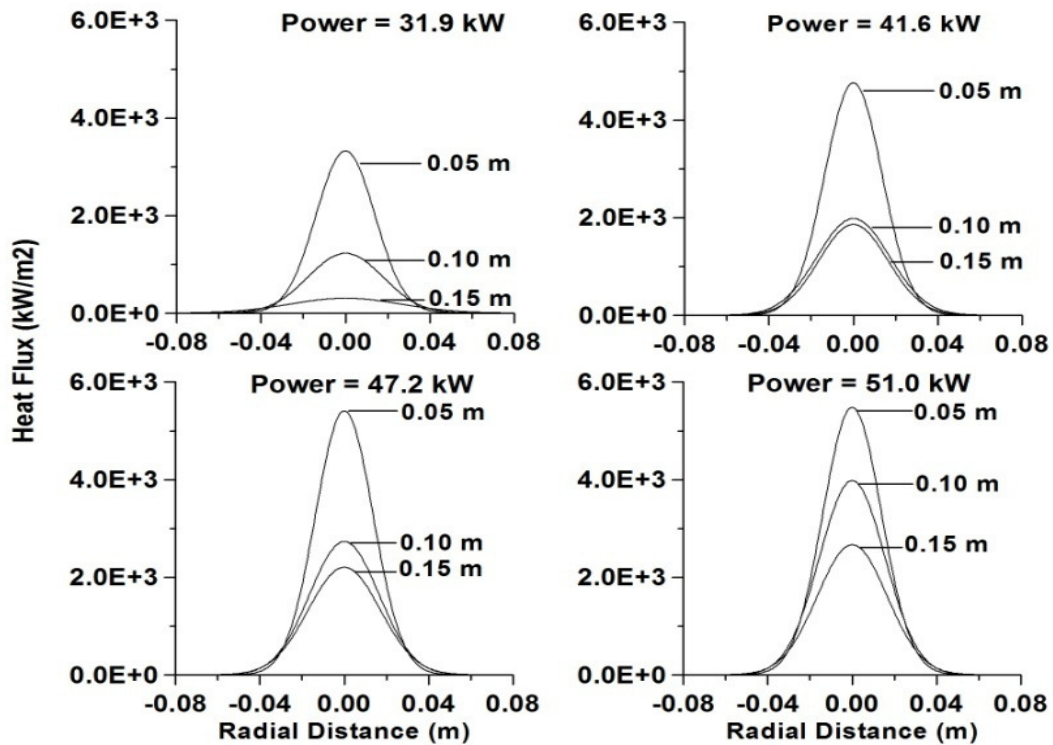


**Fig.3.6** Variation of heat flux distribution of Nitrogen plasma with axial distance at power levels of (a) 31.9 kW, (b) 41.6 kW, (c) 47.2 kW and (d) 51.0 kW. The gas flow rate is 17.5 slm.

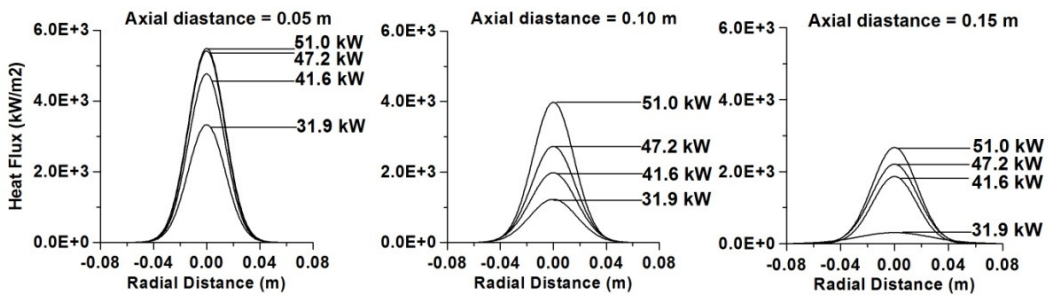


**Fig.3.7** Variation of heat flux distribution of Nitrogen plasma with power level at axial distance of (a) 0.15 m, (b) 0.10 m and (c) 0.05 m from nozzle exit respectively. The gas flow rate is 17.5 slm.

#### 3.4.4 Variation of maximum heat flux ( $\Phi_0$ ) in Argon and Nitrogen plasma

For a detail analysis of the heat flux profiles in Argon plasma, we plot an explicit variation of  $\Phi_0$  as a function of axial distance and power input to the torch as shown in Figure 3.8. The same for Nitrogen plasma is plotted in Figure 3.9. It is observed

[Figure 3.8 (a)] that the rise in  $\Phi_0$  with power is nearly linear as one goes closer to the nozzle exit but shifts towards a quadratic dependence as one moves away.

The plot of  $\Phi_0$  as a function of axial distance is presented in Fig. 3.8 (b). It shows that at lower power the jet actually loses little of its power as it propagates. However, at higher power the same loss becomes reasonably high. It is also observed that for a given power, the drop in  $\Phi_0$  with axial distance is quadratic at higher power and approaches nearly a linear behaviour at lower power. Higher plasma temperature at higher power leads to substantial power loss through radiative and conductive transport and may account for the observed features.

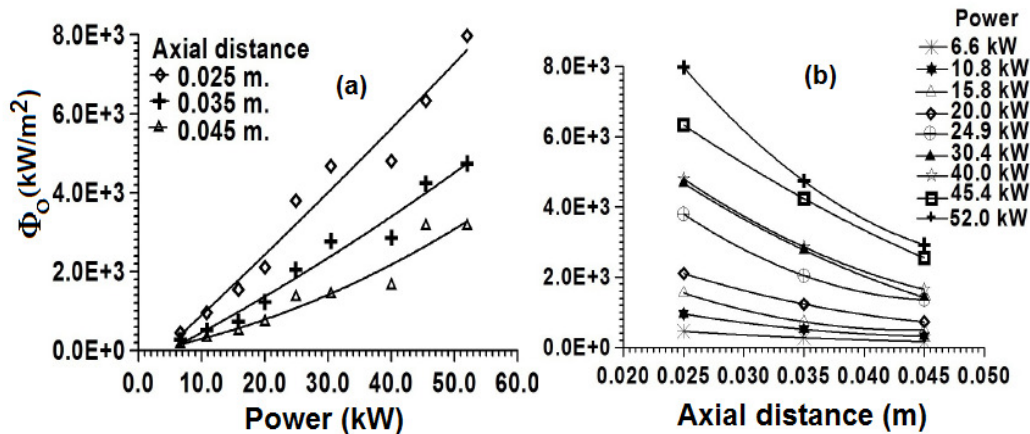


**Fig.3.8** Variation of  $\Phi_0$  for Argon plasma with respect to (a) power and (b) axial distance. The voltage - current values are 66 V - 100 A, 72 V - 150 A, 75 V - 200 A, 80 V - 250 A, 83 V - 300 A, 87 V - 350 A, 100 V - 400 A, 101 V - 450 A and 104 V - 500 A. The gas flow rate and nozzle diameter are 30 slm and 0.010 m respectively.

For Nitrogen, the behaviour of  $\Phi_0$  as a function of power and axial distance is presented in Figure 3.9(a) and (b) respectively. Although the measurements are carried out at different axial distances and at higher powers, the observed behaviour is substantially different from that in Argon. For the same power and axial location, the heat flux value in Nitrogen is in general higher than that in Argon. The notable fact is that the behaviour is position dependent. While at an axial distance of 10cm,  $\Phi_0$

increases quadratically with power with no sign of saturation, the same measured at an axial distance of 5 cm and 15 cm clearly indicate a saturation tendency at higher power. Formation of arc root and associated complicated body forces under constricted connection inside the torch often results in a flow configuration that includes constriction and expansion regions along the length of the transmitted jet. Many times such regions are visually detectable and may account for the observed behaviour.

Similar to Argon,  $\Phi_0$  in Nitrogen exhibits a sharp decrease with distance in the immediate vicinity of the nozzle exit [Figure 3.9 (b)]. At longer axial distances the rate of decrease is lesser. As power increases, the zone of sharp drop in  $\Phi_0$  gets extended. High radiative and conductive losses from the plasma at higher temperature (near nozzle exit) can account for the observed behaviour.

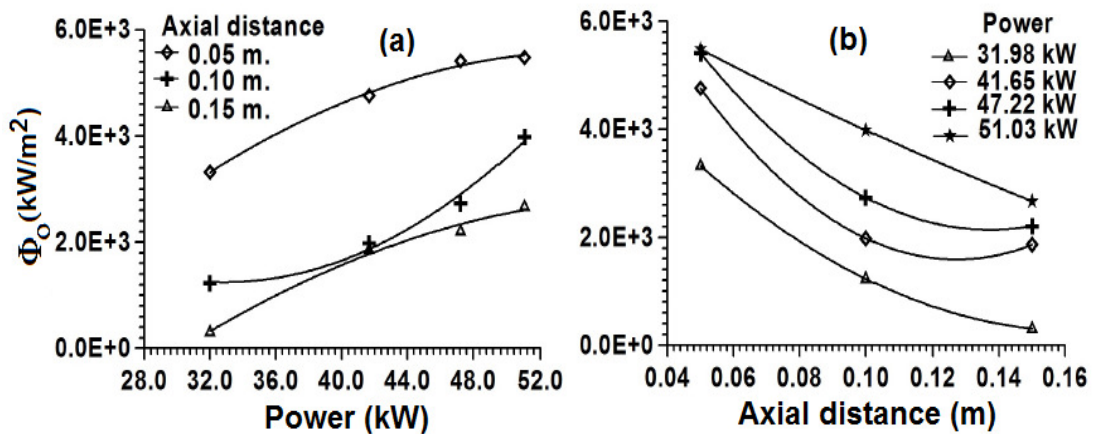


**Fig.3.9** Variation of maximum value of heat flux for Nitrogen plasma with respect to (a) power and (b) axial distance. The voltage - current values are 156 V - 205 A, 160 V - 262 A, 159 V - 296 A and 161 V - 317 A. The gas flow rate and nozzle diameter are 17.5 slm and 0.010m respectively.

### **3.4.5 Variation of width ( $R_g$ ) of heat flux profile width for Argon and Nitrogen plasma**

Extent of the plasma jet in physical space is characterized by the parameter  $R_g$ . It is an important parameter as it actually determines the extent of the effective process zone. Usually, the iso-temperature contours in a plasma jet take the shape of part of an ellipse [78] with tapering at top and bottom and expansion in the middle. Under this ideal configuration, as one move axially away from the nozzle exit, the value of  $R_g$  first increases, then reaches a steady value near the middle of the ellipse and finally decreases again. If the jet length is huge, the nearly steady value of  $R_g$  in the middle section continues for a fairly long distance along the axis [79]. Increase in input electrical power through increase in current induces two simultaneous competing phenomena inside the torch that actually control the ultimate value of  $R_g$ . The first one tries to reduce the value of  $R_g$  through radially inward pinching action by  $JXB$  body force. Higher the current, higher is the  $JXB$  pinching force and lesser is the value of  $R_g$ . The second one acts in opposite to the first one and tries to increase the value of  $R_g$  through  $J^2/\sigma$  ( $\sigma$  is the electrical conductivity of the plasma) heating expansion. Higher the current, higher is the heating effect and higher is the value of  $R_g$ . At relatively lower current, the pinching contraction exceeds the heating expansion and the value of  $R_g$  keeps on decreasing as current (power) increases. This is what is seen at lower powers in Figure 3.10 (a). However, as current keeps on increasing a time comes when finally heating effect supersedes the pinching effect and value of  $R_g$  starts increasing with increase in power as seen in Fig 3.10 (a) at higher power. Exiting from the nozzle, the Argon plasma jet expands as it propagates away from the nozzle exit

and the value of  $R_g$  exhibits almost a linear increase with increase in the axial distance as shown in Figure 3.10 (b).

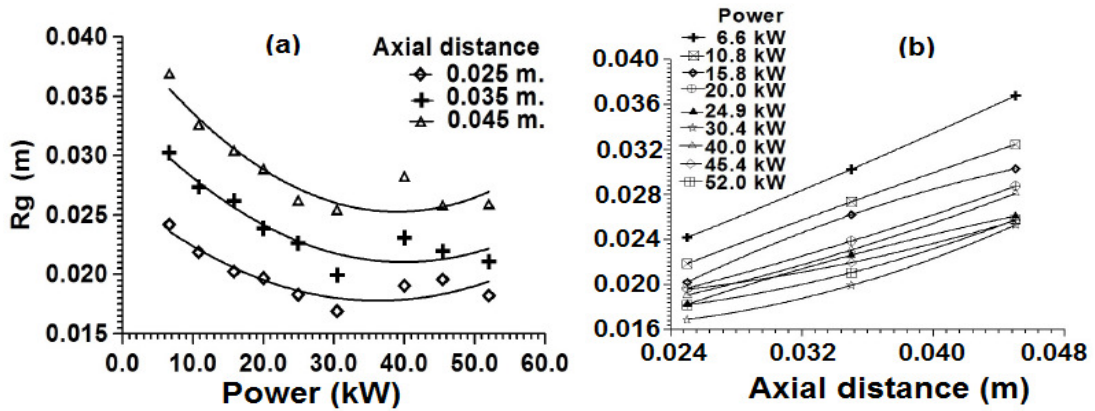


**Fig.3.10** Variation of  $R_g$  in Argon with (a) power and (b) axial distance. The voltage - current values with increasing power are 66 V - 100 A, 72 V - 150 A, 75 V - 200 A, 80 V - 250 A, 83 V - 300 A, 87 V - 350 A, 100 V - 400 A, 101 V - 450 A and 104 V - 500 A. The gas flow rate and nozzle diameter are 30 slm and 0.010 m respectively.

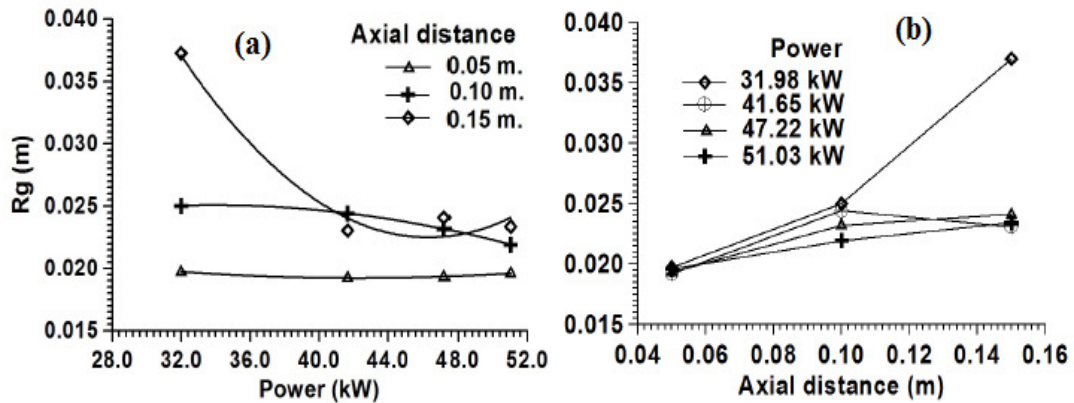


**Fig.3.11** Variation of  $R_g$  in Nitrogen with (a) power and (b) axial distance. The voltage - current values are 156 V - 205 A, 160 V - 262 A, 159 V - 296 A and 161 V - 317 A. The gas flow rate and nozzle diameter are 17.5 slm and 0.010m respectively.

The variation of  $R_g$  in Nitrogen plasma with axial distance and electrical input power exhibits distinctly different features compared to that in Argon [Figure 3.11]. The plot of  $R_g$  as a function of power in Fig.3.11 (a) shows that the effect of increase or decrease in power is most significant in the tail region of the jet. For the regions, closer to the nozzle exit, the value of  $R_g$  maintains nearly a constant value irrespective

of the operating power. However, as the jet propagates it expands and a higher value of  $R_g$  is noted at longer distances [Fig.3.11 (b)]. Because of lower axial velocity at lower power, the jet gets scope for higher radial expansion at shorter axial distances resulting in the observed significantly higher  $R_g$  values at lower power. However, as seen in Figure 3.11 (b), at higher power the balance between the  $J X B$  compressive force and the thermal expansive force maintains a nearly uniform width of the plasma column over a long axial distance and a range of power levels.

#### **3.4.6 A Comparison of the heat flux data with the reported studies:**

A comparison of the results from the present work with those reported in literature is presented in this section. It may be pointed out that the comparison is only for Argon. For Nitrogen, any such comparison is not presented, because of inability to find any data on heat flux of Nitrogen jet in literature that may give any meaningful comparison. For Argon plasma the comparison is made with data that corresponds to a plasma torch of nozzle diameter 7 mm (instead of 10 mm in the present study) and a gas flow of 60 slm (instead of 30 slm in the present study)[9]. As a natural consequence, the study [9] had a longer and thinner plasma jet compared to the present one for the same power. Also, as the same power is being distributed over a smaller cross section, their value of  $R_g$  will be smaller and the same for  $\Phi_0$  will be higher compared to the corresponding cases in the present study. Nevertheless, the comparison will reflect consistency of the results obtained in the present study as well as give an idea about the influence of gas flow and nozzle diameters on the heat flux properties of plasma jets at comparable power levels. As the present study focuses on

the higher power regime, the change in the behaviour as one goes to higher power also will be reflected.

It is observed that nearly similar trend of behaviour is exhibited by  $\Phi_o$  and  $R_g$  as a function of axial distance in both the studies [Figure 3.12]. Both of them show decreasing tendency of  $\Phi_o$  and increasing tendency of  $R_g$  with increase in axial distance. At a given axial distance,  $\Phi_o$  and  $R_g$  respectively increases and decreases with increase in electrical power. However, the rate of increase or decrease is slightly different due to different electrode configuration. For identical electrical power level, the realized value of  $\Phi_o$  in the present study is lower than the same in reference [9] and exactly the reverse is observed for  $R_g$ . The behaviour is completely in agreement with the expectation as discussed above. The important point to be noted is that the present study is able to achieve nearly three times higher jet width (nine times higher jet cross-section) and more than three times higher peak heat flux compared to the earlier study[10] within the range of operating parameters considered.

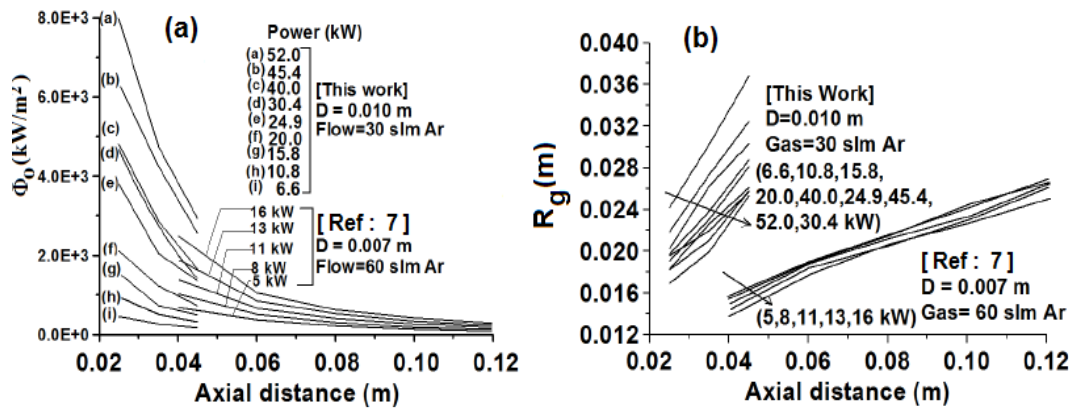


**Fig.3.12 Comparison of profile parameters of Argon plasma with data reported in literature. (a) Variation of  $\Phi_o$  with axial distance: the curves indexed (a) to (i) correspond to present study, the rests are from literature (b) Variation of  $R_g$  with axial distance. Figures in the brackets indicate electrical power input corresponding to different curves as intercepted by the arrow.**

### 3.4.7 An Estimate of experimental error

The heat ( $H$ ) received by the calorimeter is calculated as:

$$H = \rho \cdot F \cdot S_w \cdot (T_2 - T_1) \quad (3.7)$$

Where,  $F$  is the flow rates water measured from the flow meters (in litre per minute, LPM),  $\rho$  and  $S_w$  are respectively density and specific heat of water,  $T_2$  and  $T_1$  are the outlet and inlet water temperatures. The maximum error in the measurement of heat received may therefore be calculated as:

$$\delta H / H = \delta F / F + 2 \cdot (\delta T / T) \quad (3.8)$$

The used setup allows:  $\delta F = 0.25$  LPM and  $\delta T = 0.1$  C. During experiment  $F_{\min} \sim 4.0$  LPM, and  $T_{\min} \sim 31.3$  C. Using these values, the maximum possible error in the measurement of  $H$  comes to be  $\sim 6.9$  %.

### 3.5. Conclusion

Processes like plasma spraying and synthesis of nano-particles of very high melting point materials demand melting or complete evaporation of the injected particles. Such processes require high power of the plasma jets together with long enough dwell time of the injected particles inside the plasma under high heat flux. A longer plasma jet with uniform heat flux profile may offer easier control over the melting or evaporation process through proper management of the particle residence time inside the plasma. While the heat flux data for Argon at relatively lower power is available in literature, the same at higher power is rare. Although, Nitrogen is long known for its higher arc voltage compared to Argon and its ability to work with common thoriated tungsten based cathodes, almost no data is available in literature about associated heat flux and its evolution with axial distance and input power. The present work focused experimentally in this area and carefully determined variation in

heat flux profile for Argon and Nitrogen plasma over a wide range of power level and axial distance using double calorimetric technique. A specially designed thoriated tungsten based segmented electrode plasma torch with nozzle diameter 10 mm is used for generation of the plasma at different power levels. For Argon plasma, the power is varied from 6.6 kW to 52 kW and for Nitrogen plasma the same is varied from 32 kW to 51 kW. Obtained heat flux profiles under various operating conditions at different axial distances are characterized in terms of profile width  $R_g$  and peak heat flux  $\Phi_0$ . Consistency and reliability of the obtained data are established through comparison of the results for Argon with those reported in literature.

For similar power, Nitrogen is found to offer nearly three times longer plasma jet compared to Argon. An increase in  $\Phi_0$  with increase in power and a decrease in the same with increasing distance from the nozzle exit are observed. It has been observed that the increase or the decrease is not linear. Degree of nonlinearity increases with increase in power. Huge radiation loss from the jet at higher power may account for the enhanced nonlinearity with increased power. The balance between radially inward electromagnetic body force and the thermal expansive force is found to play a significant role in determining the width of the plasma jets in the downstream locations. The observed nonlinear behaviour of  $R_g$  in Argon and the nearly linear behaviour of  $R_g$  in Nitrogen as a function of electrical power are explained from this. Formation of arc root under constricted connection at higher power and associated instabilities are also found to affect the delivered heat flux. The long thick nitrogen plasma jet of nearly uniform thickness observed at higher power may find important applications in variety of high temperature processing industries.

# **CHAPTER-4: Temperature Measurement of Nitrogen and Argon Plasma Jet**

## **Outline of the Chapter**

**4.1 Introduction**

**4.2 Boltzmann Plot Method**

**4.3 Experimental Setup**

**4.4 Spectroscopy of Argon Plasma**

**4.5 Spectroscopy of Nitrogen Plasma**

**4.6 Calibration of Spectrograph**

**4.7 Results and Discussion**

**4.8 Conclusion**

# Chapter 4

## Temperature Measurement of Nitrogen and Argon Plasma Jet

### 4.1. Introduction:

From application point of view, temperature of a plasma jet plays a decisive role in plasma chemistry, process design and process control. For example, in plasma assisted chemical processes, temperature field governs the rate of chemical reactions and in processes like plasma spray, spherodization, densification, it decides the degree of melting and trajectories of the injected power particles. Knowledge of plasma temperature distribution and its dependence on various operating parameters helps in optimizing the process. In this chapter, details of the plasma temperature measurement using Boltzmann plot method for nitrogen and argon plasma jets are presented.

### Temperature in plasma:

Plasma is composed of number of species of charged and neutral particles including molecules, molecular ions, atoms, ions of atomic species, radicals and electrons. So definition of temperature in plasma is quite broad and we encounter different types of plasma temperatures like  $T_{kin}$ ,  $T_{exc}$ ,  $T_{ion}$ ,  $T_e$ ,  $T_{rot}$ ,  $T_{vib}$  and  $T_{rad}$  [80] as described in Table-4.1.

**Table 4.1 Definition of different types of plasma temperature**

Sr. No.	Definition of Plasma temperature	Notation	Meaning
1	Kinetic temperature	$T_{kin}$	It represents the average kinetic energy of the particles and the particles are distributed according to the Maxwell Boltzmann statistics corresponding to this temperature.
2	Excitation temperature	$T_{exc}$	This corresponds to the temperature at which the excited particles are distributed in Maxwell – Boltzmann distribution.
3	Ion temperature	$T_{ion}$	This corresponds to the temperature at which the ions are distributed in Maxwell – Boltzmann distribution.
4	Electron temperature	$T_e$	It is related to the average kinetic energy of electrons and the electrons are distributed in Maxwell – Boltzmann distribution according to this temperature.
5	Rotational temperature	$T_{rot}$	It is related to the rotational energy levels of the molecules or radicals and it represents the temperature according to which the molecules or radicals are distributed in Maxwell – Boltzmann statistics in virtue of their rotational energy.
6	Vibrational temperature	$T_{vib}$	It is related to the vibrational energy levels of the molecules or radicals and it represents the temperature according to which the molecules or radicals are distributed in Maxwell – Boltzmann statistics in virtue of their vibrational energy.
7	Radiation temperature	$T_{rad}$	It represents the energy of the photon.

In plasma under complete thermal equilibrium (CTE), all these temperature are equal i.e.  $T_{rot} = T_{vib} = T_{kin} = T_{exc} = T_{ion} = T_{rad} = T_e$ . CTE can be observed only in high density high temperature plasma having large volume so that the radiation from particles is absorbed within the plasma itself. However, none of the laboratory plasma

is found to be in LTE. Plasmas in thermal plasma devices are found to be in local thermal equilibrium (LTE). In this except radiation temperature, all other temperature are equal i.e.  $T_{\text{rot}} = T_{\text{vib}} = T_{\text{kin}} = T_{\text{exc}} = T_{\text{ion}} = T_e \neq T_{\text{rad}}$ . In plasma which contains species of particles having large mass difference such as electrons and heavy particles, electrons can gain energy from the electromagnetic field faster than other. The electron temperature ( $T_e$ ) and ion temperature ( $T_{\text{ion}}$ ) may be different leading to thermal non-equilibrium, especially in low pressure plasmas. When the pressure exceeds 0.1 bar, the number density of particles is quite high and the electrons may efficiently transfer energy to the heavy particles through collisions, equilibrating electron temperature ( $T_e$ ) and heavy particle temperature ( $T_h$ ). Atmospheric pressure thermal plasma are collision dominated and typically exhibits LTE.

#### **Radiations from plasma:**

A typical spectrum from LTE plasma exhibits line radiation super imposed with continuum radiation. Different types of radiations and their origins are described below.

##### 1. Bremsstrahlung radiation (free-free transition)

Transition between two free energy levels which gives rise to energy exchange is called free-free transition. This radiation is originated from the charged particles when accelerated or retarded in the electromagnetic field of other charged particles. Basically, these transitions are classified as bremsstrahlung and cyclotron radiation. In bremsstrahlung, the charged particles are accelerated in the electric field of other charged particles. It is also known as 'braking radiation'. Since the initial states and the final states

are continuous, the bremsstrahlung radiation is also continuous. In cyclotron radiation, the charge particle undergoes gyration under a magnetic field.

2. Recombination radiation: (free-bound transition)

It forms a continuum radiation and emitted when the electrons recombine with ions. This continuum is characterized by edges.[81]

3. Line radiation: (bound-bound transition)

This radiation corresponds to transition of electron between the discrete or bound energy levels of atoms, ions or molecules. In low temperature plasma, molecular spectrum may also be observed if molecular gas is used for plasma generation. [81]

In this work, axial temperature of the argon and nitrogen plasma jet is determined is by optical emission spectroscopy using Boltzmann plot method. The measurement is done at several locations along the axis of the plasma jet. As the plasma jet is prone to fluctuations, the temperature at a given particular location also changes and so does the intensity of the lines. To achieve reasonably good average, presented data are averaged over five measurements for each axial location under a given operating conditions. Hence the obtained plasma jet temperature is a time averaged. Details of the plasma temperature measurement using Boltzmann plot method and obtained results for nitrogen and argon plasma jet are presented in the subsequent sections.

#### 4.2. Boltzmann plot method:

Under this technique plasma is assumed to be in local thermal equilibrium and optically thin so that self absorption of line is negligible. The emission coefficient for a line radiation from an upper level  $u$  to a lower level  $i$  may be written as,

$$\epsilon_{ui} = \frac{1}{4\pi} h \nu_{ui} n_u A_{ui} l \quad (4.1)$$

Where  $A_{ui}$  is the Einstein coefficient of spontaneous emission or transition probability ( $s^{-1}$ ),  $\nu_{ui}$  is the wave number ( $cm^{-1}$ ),  $l$  is the path length,  $h$  is the Plank's constant,  $c$  is the velocity of light.  $n_u$  is the number density of the atoms in the state  $u$  and it is given by Maxwell-Boltzmann relation as

$$\frac{n_u}{n_0} = \frac{g_u}{g_0} e^{\left(-\frac{E_u}{kT}\right)} \quad (4.2)$$

Where,  $n_0$  is number density of the atoms or ions in the ground state,  $g_u$  and  $g_0$  are the statistical weight of the upper and lower energy state respectively,  $k$  is the Boltzmann constant, and  $T$  is the temperature.

Substituting  $n_u$  in equation (4.1), emission coefficient for a line radiation becomes,

$$\epsilon_{ui} = \frac{1}{4\pi} \frac{hcn_0}{\lambda_{ui}} \frac{g_u}{g_0} A_{ui} l e^{\left(-\frac{E_u}{kT}\right)} \quad (4.3)$$

Where,  $\lambda_{ui}$  is the wave length of the transition and it is given as,  $\lambda_{ui} = \frac{c}{\nu_{ui}}$ .

Taking logarithm on both sides, we get

$$\ln\left(\frac{\epsilon_{ui}\lambda_{ui}}{g_u A_{ui}}\right) = \ln\left(\frac{hc n_0}{g_0}\right) - \frac{E_u}{kT} \quad (4.4)$$

This can be written as,

$$\ln\left(\frac{\epsilon_{ui}\lambda_{ui}}{g_u A_{ui}}\right) = C - \frac{E_u}{kT} \quad (4.5)$$

Where, C is some constant.

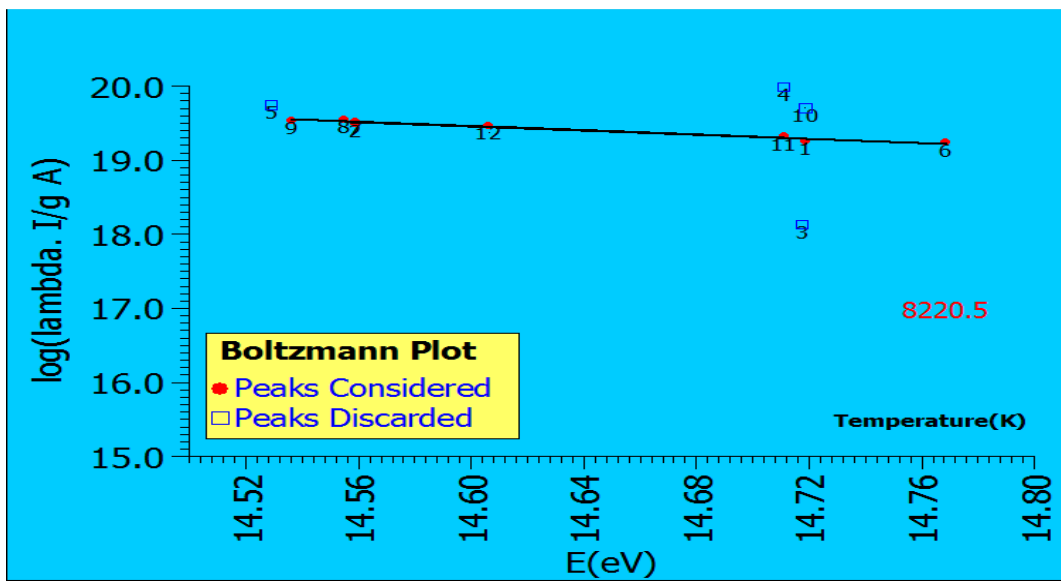


Fig. 4.1(a) A typical Boltzmann plot for Argon. Numbers indicate the peaks of corresponding spectra [e.g. Fig.4.5(a)]

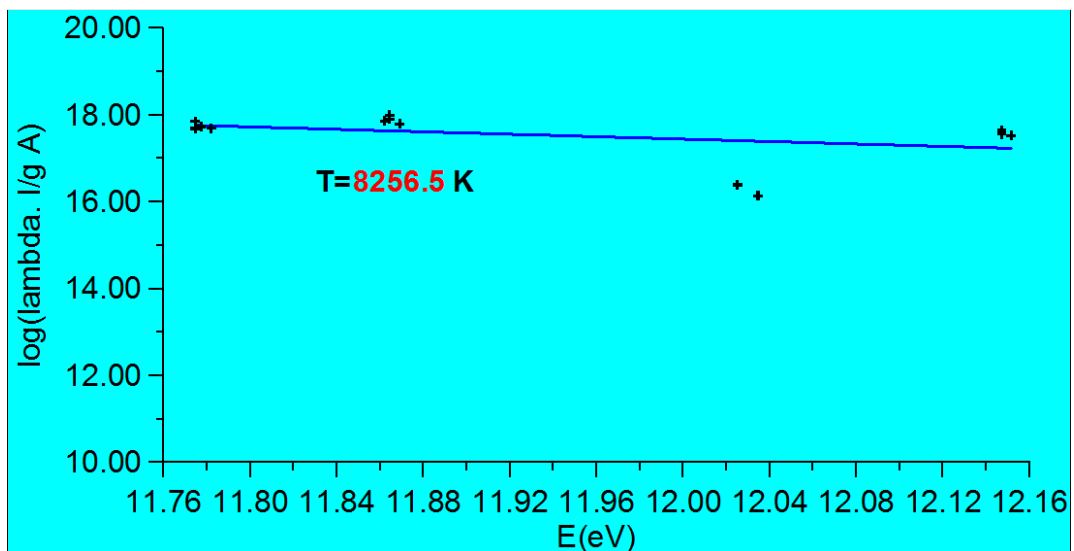
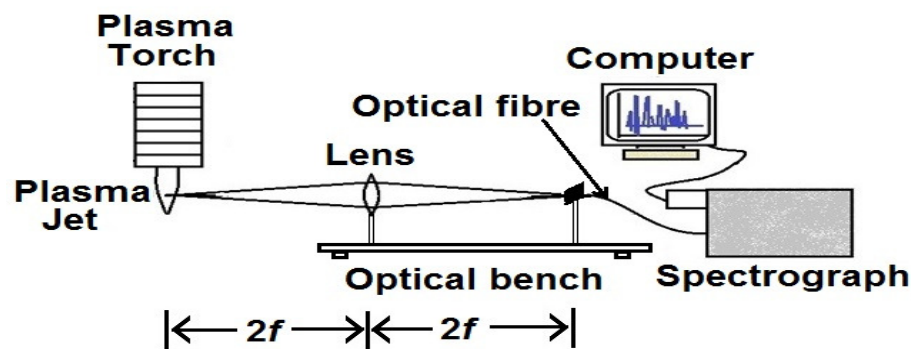


Fig. 4.1(b) A typical Boltzmann plot for Nitrogen.

It is obvious that equation 4.5 is a linear equation. A plot of the term  $\ln\left(\frac{\epsilon_{ui}\lambda_{ui}}{g_u A_{ui}}\right)$  in eq.4.1 as a function of  $E_u$  will result in a straight line. Slope of this line will be equal to  $(1/kT)$ . Once the slope is determined, temperature of the plasma can be calculated.

A typical Boltzmann plot for argon plasma is shown in Fig.4.1(a). It may be mentioned that the plasma under consideration is actually under PLTE (partial local thermal equilibrium) and not LTE. Because of this, depending on operating condition, several levels may remain away from equilibrium with the other associated levels. In Boltzmann plot, the lines originating from these levels deviate significantly from above mentioned linear behaviour. In the example of Fig.4.1(a), the states corresponding to lines 3,4,5 and 10 are not in equilibrium with the other states.

A typical Boltzmann plot for nitrogen plasma is shown in Figure 4.1(b). Although a large number of lines are observed in the nitrogen spectrum, many of the emitted lines associate either the same or very closely spaced upper energy levels. Observed clubbing of many lines in the plot originate from this. Such clubbed data points do not add effectively in determination of temperature by linear fit. The used setup for emission spectroscopy and recorded lines form argon and nitrogen plasma are detailed in the next section.



**Fig. 4.2 Schematic of the experimental setup**

### 4.3. Experimental Setup:

The schematic of the experimental setup for the emission spectroscopy is given in figure 4.2. With the help of a lens mounted on an optical bench, an inverted image of the plasma jet is focussed on a screen with magnification '1'. The intensity of the image on the screen is then scanned by a spectrograph with the help of an optical fibre. The actual picture of the experimental set up under operating condition used for plasma spectroscopy is shown in figure 4.3.

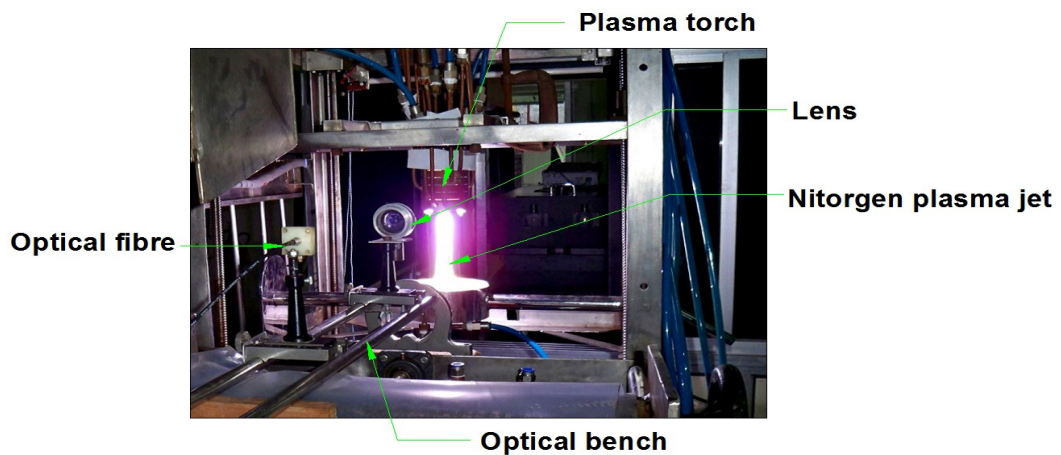


**Fig. 4.3 Actual experimental setup**

Emission spectrum from a particular zone of the jet is recorded using the optical arrangement consisting of a lens, an optical fibre and a spectrograph (Ocean optics, USB 2000). Since the object distance and the image distance are  $2f$ , where  $f$  is the focal length of the lens, a real inverted image of the plasma jet with same dimension is formed on the image plane perpendicular to the lens axis. The optical fibre placed on the image plane focuses on a particular location of the plasma jet and project it on the grating of the spectrograph after passing through the slit. The slit width is  $5\ \mu\text{m}$ . The image formation in the spectrograph is given in figure 4.4. After reflection from the plane mirror, the light is incident on the concave mirror which reflects the light on the grating. The dispersed spectrum is than reflected by the concave mirror onto the CCD

detector which produces the image of the spectrum. Typical spectra recorded for argon and nitrogen plasma are presented in Fig. 4.5 (a) and Fig. 4.5(b) respectively. The green region for argon plasma emission and the red region for nitrogen plasma emission are chosen from the fact that the energy levels of the upper state are well dispersed in energy values for these lines. All the observed lines in argon and nitrogen are originating from atomic transition.

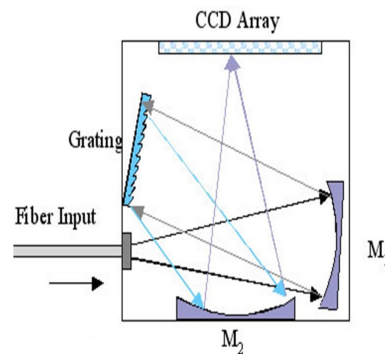


**Fig. 4.4 Schematic of the imaging spectrograph**

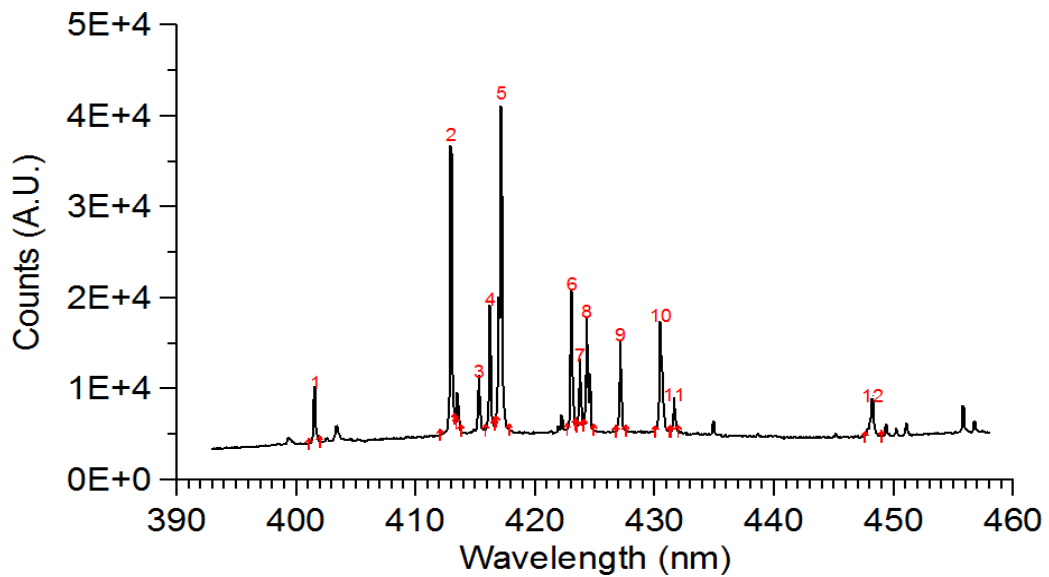
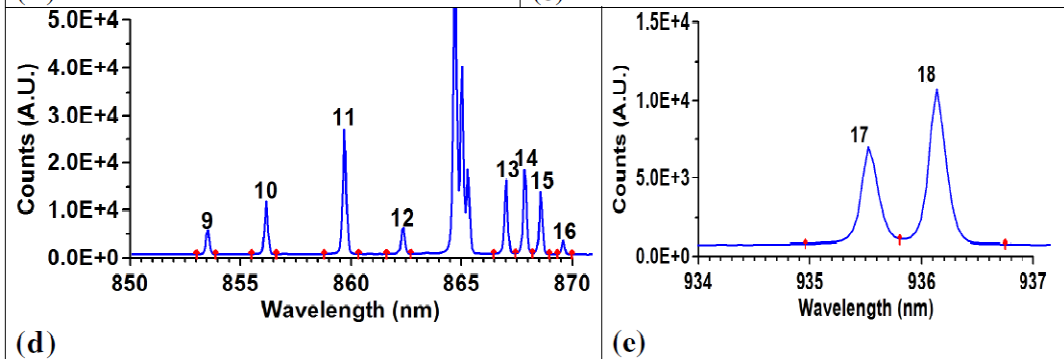
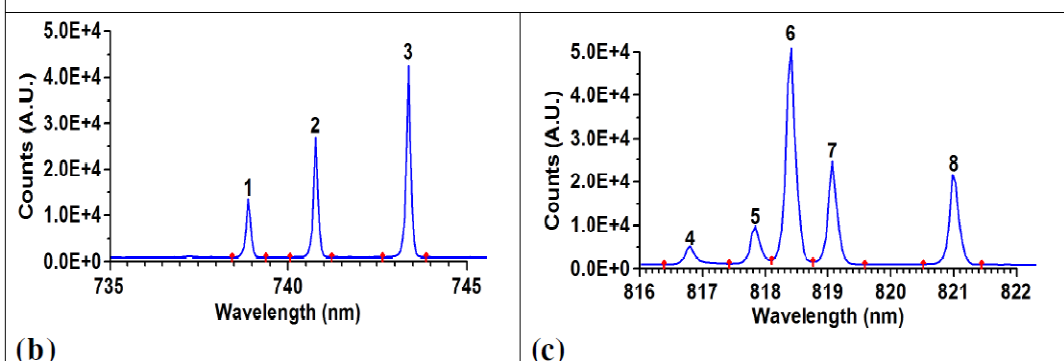
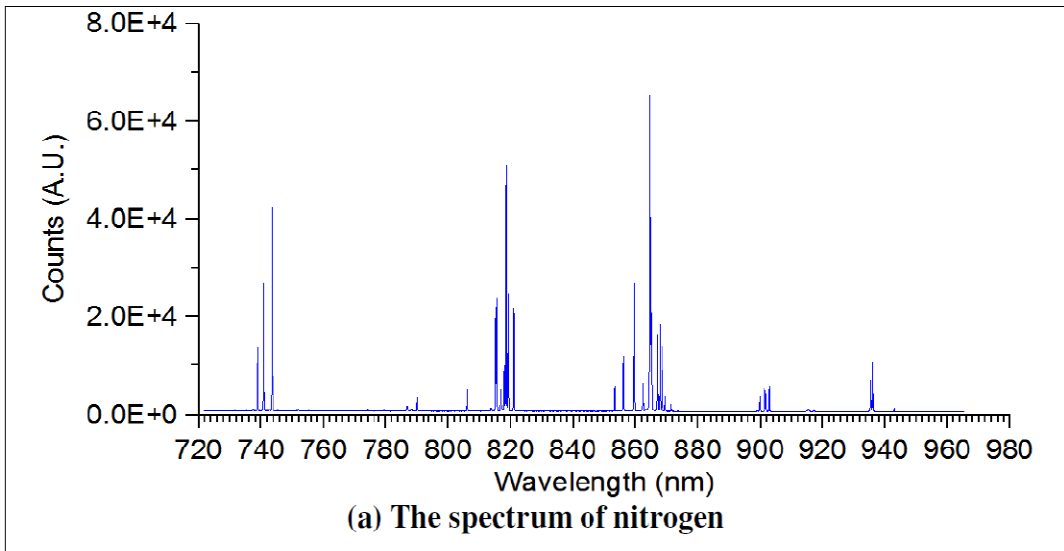


**Fig. 4.5(a) Typical spectrum of Argon Plasma**



(b-e) The peaks, considered in the estimation of plasma temperature through emission spectroscopic study.

Fig. 4.5(b) Typical line spectrum of nitrogen plasma

#### 4.4. Spectroscopy of argon plasma:

Twelve atomic lines have been considered with wavelength range 400 nm to 450 nm for emission spectroscopic study of the argon plasma temperature [Fig.4.5(a)]. Associated electronic transitions giving rise to the lines are presented in figure 4.6. Necessary spectroscopic data for determination of temperature are tabulated in Table 4.2.

Table 4.2 Spectroscopic data for argon atomic lines

Sr. No.	Wavelength (nm.)	Energy of upper level $E_k$ (cm-1)	Transition probability of upper level ( $G_k$ )	Einstein coefficient ( $A_{ki}$ ) ( $S^{-1}$ )	Relative intensity (au)
1	404.4418	118469.0508	5	3.33e+05	50
2	415.8591	117183.5901	5	1.40e+06	400
3	418.1884	118459.5975	3	5.61e+05	50
4	419.0713	116999.3259	5	2.80e+05	100
5	420.0675	116942.7542	7	9.67e+05	400
6	425.9362	118870.9170	1	3.98e+06	200
7	426.6287	117183.5901	5	3.12e+05	100
8	427.2169	117151.3264	3	7.97e+05	150
9	430.0101	116999.3259	5	3.77e+05	100
10	433.3561	118469.0508	5	5.68e+05	100
11	434.5168	118407.4303	3	2.97e+05	25
12	451.0733	117562.9553	1	1.18e+06	100

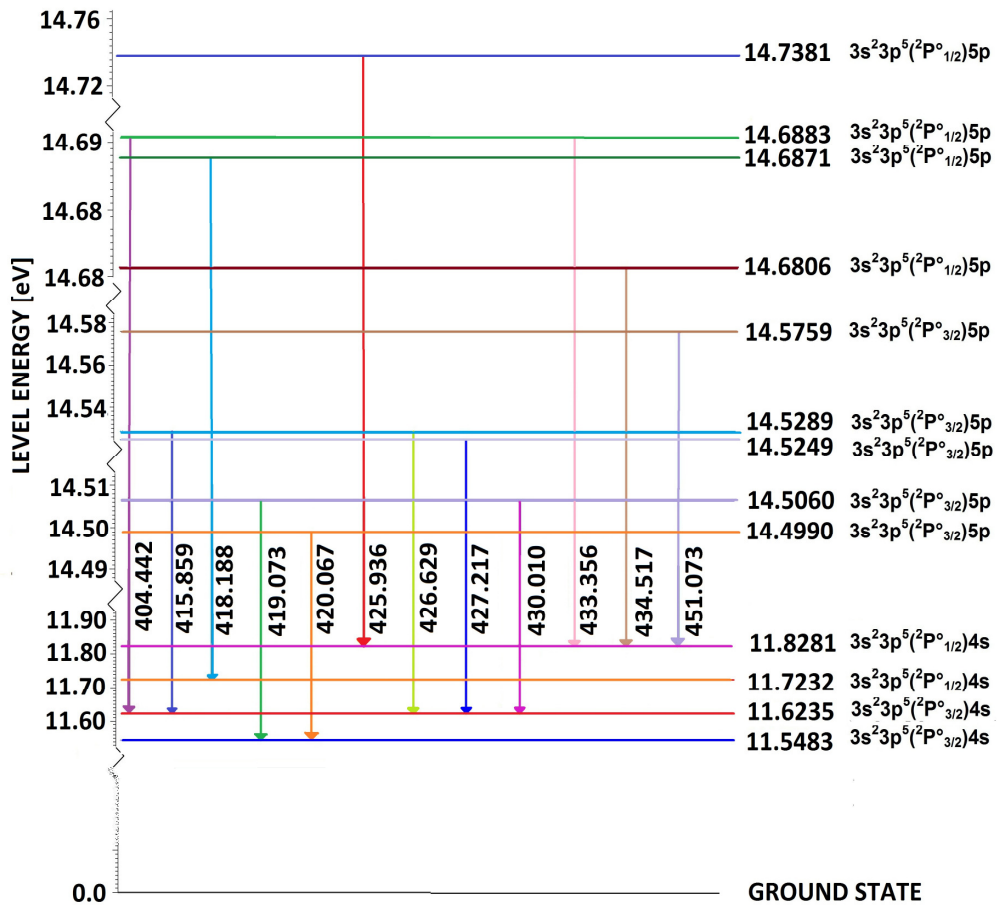


**Fig. 4.6 Schematic of the atomic transitions in Argon producing the considered atomic line radiation**

#### 4.5. Spectroscopy of Nitrogen plasma:

Eighteen atomic lines have been considered with wavelength range 740 nm to 950 nm for emission spectroscopic study of the nitrogen plasma temperature [Fig.4.5(b)]. Associated electronic transitions giving rise to the lines are presented in figure 4.7. Necessary spectroscopic data for determination of temperature are tabulated in Table 4.3.

**Table 4.3 Spectroscopic data for nitrogen atomic lines**

Sr. No.	Wavelength (nm.)	Energy of upper level $E_k$ (cm-1)	Transition probability of upper level ( $G_k$ )	Einstein coefficient ( $A_{ki}$ ) ( $S^{-1}$ )	Relative intensity (au)
1	742.364	96750.840	5.64e+06	4	685
2	744.229	96750.840	1.19e+07	4	785
3	746.831	96750.840	1.96e+07	4	900
4	820.036	95475.310	4.68e+06	2	250
5	821.072	95493.690	5.23e+06	4	300
6	821.634	95532.150	2.26e+07	6	570
7	822.314	95475.310	2.62e+07	2	400
8	824.239	95493.690	1.31e+07	4	400
9	856.774	97805.840	4.86e+06	4	500
10	859.400	97770.180	2.09e+07	2	570
11	862.924	97805.840	2.67e+07	4	650
12	865.589	97770.180	1.07e+07	2	500
13	870.325	94770.880	2.16e+07	2	500
14	871.170	94793.490	1.29e+07	4	570
15	871.883	94830.890	6.54e+06	6	500
16	872.889	94770.880	3.75e+06	2	250
17	874.736	94793.490	9.65e+05	4	200
18	938.680	96787.680	2.13e+07	4	500

The required spectroscopic data are collected from the NIST atomic spectra database.

#### **4.6 Calibration of the spectrograph:**

Before recording the spectrum, the spectrograph is calibrated using a standard Hg-Ar lamp. The list of the standard wavelengths from the calibration lamp is shown in figure 4.8. Shift in the wave length is determined by recording spectra of the calibration lamp [figure 4.9] and measuring associated shift from corresponding standard wavelength positions. Accordingly, a correction factor is then added to the observed wavelength. Observed shifts in the used spectrometer are within 3.2 to 3.5 nm.

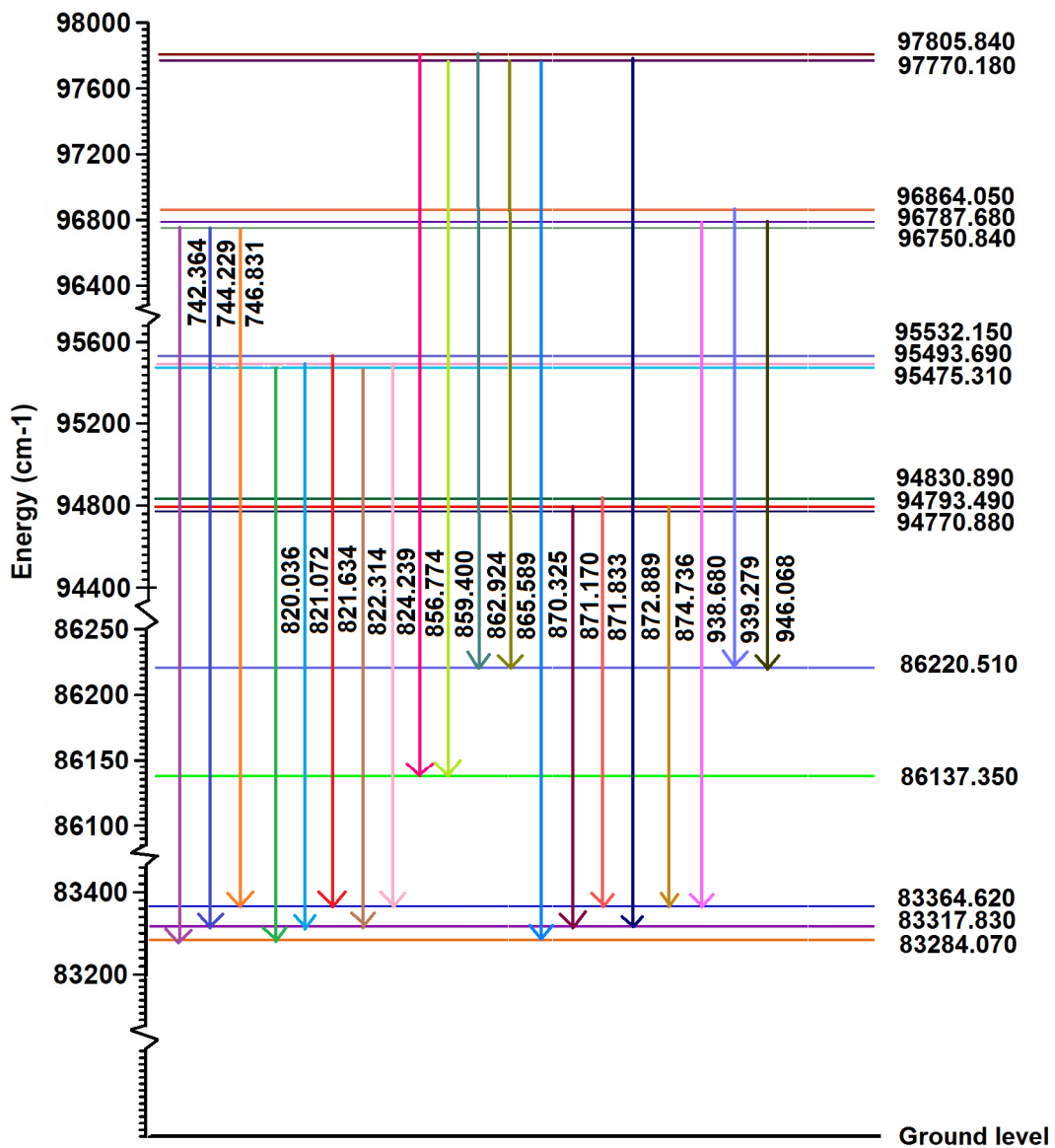


Fig. 4.7 Schematic of the atomic transitions in Nitrogen producing the considered atomic line radiation

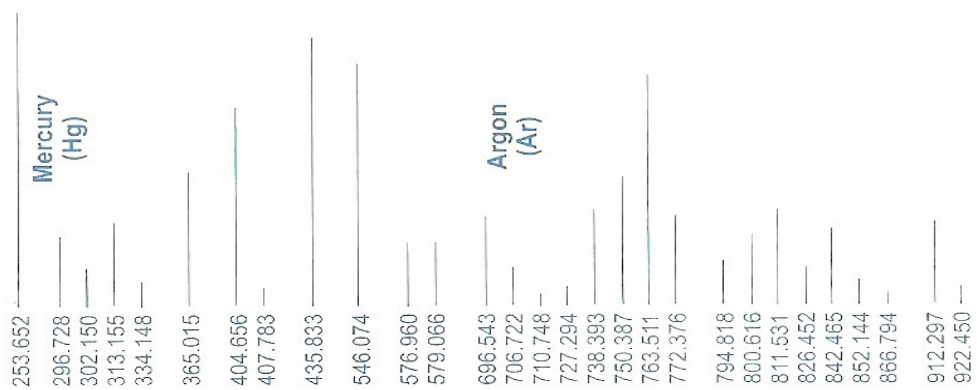
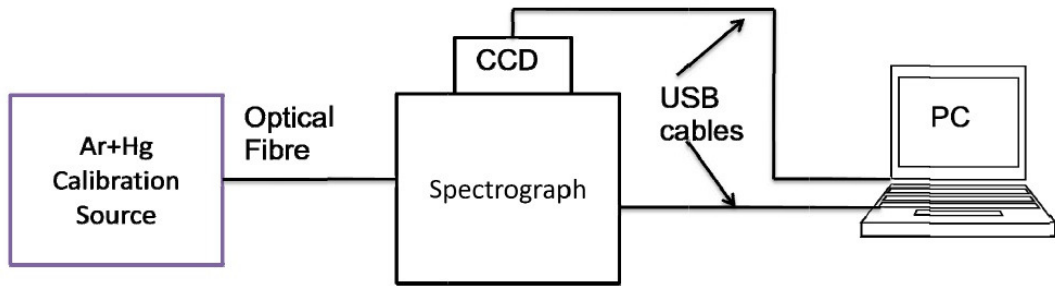


Fig. 4.8 Wavelength of radiation emitted by calibration lamp



**Fig. 4.9 Schematic for the spectrograph calibration.**

#### **4.7. Results and Discussion:**

To understand the axial distribution of temperature inside the plasma jet, spectra recorded for Argon and Nitrogen plasma are used as described above. The variation of the nozzle exit temperature as a function of arc current and gas flow rate for argon is presented in Fig.4.10. While the overall trend is increase in temperature with increase in current, the notable feature is the observed oscillatory behaviour of exit temperature as a function of arc current. This important fact, confirmed by repeated experiments in this study is not reported earlier.

The oscillatory behaviour originated from the competition between two counteracting forces:  $J \times B$  compressive body force & thermal expansive force due to Joule heating, undergoing inside the plasma torch. With increase in current, both  $J \times B$  compressive force as well as the thermal expansive force (Joule heating) increases. With increase in current, if effectively compressive force supersedes the thermal expansive force, the plasma volume starts shrinking. Since power is increased and plasma volume is now less, higher temperature is observed at the exit. However, as plasma volume shrinks,  $J$  increases due lower cross-sectional area, and ohmic heating increases as square of  $J$ . Thicker cold boundary layer surrounding the jet also helps in increasing plasma temperature by reducing conductive loss to the wall. A time comes

when thermal expansion supersedes the JxB compression and plasma volume starts expanding again. The boundary layer adjacent to torch inner wall becomes thinner and conductive heat loss to the wall becomes more. Larger volume of the plasma and greater heat loss to the wall result in lowering of temperature at the nozzle exit. However, with further increase in current, the situation may reverse again and the cycle keeps on repeating with increase in current. This is what is observed in this study [Fig.4.10].

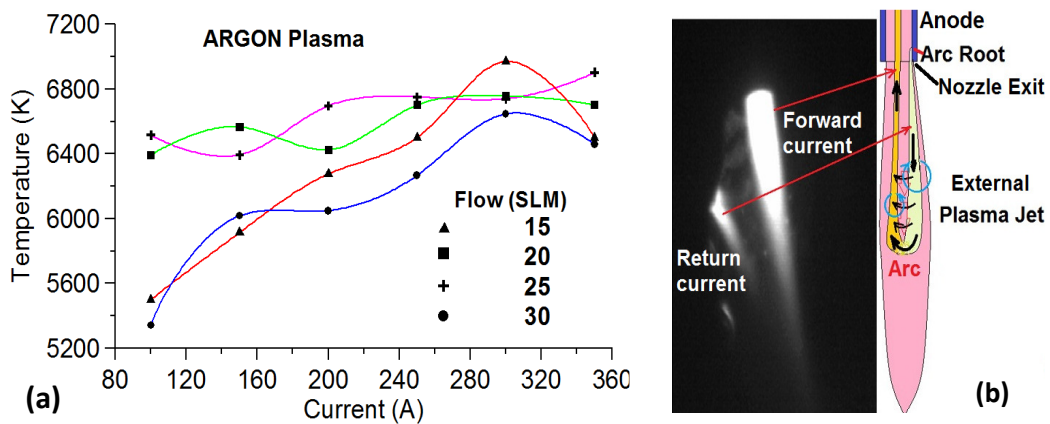


**Fig. 4.10 (a) Variation of nozzle exit temperature of argon plasma (b) Fast photographic image of the arc, showing extended current path beyond the nozzle exit**

The axial variation of temperature under different gas flow rate and arc current in argon plasma is presented in Fig.4.11-Fig.4.13. Current is varied from 100A to 350A. The steady part of the jet length was within 20mm - 30mm, depending on operating condition. Temperature measurement beyond this zone was not reliable as the jet becomes too unsteady for recording of spectrum. In this study gas flow rate is varied from 15 slpm to 25 slpm. While the overall behaviour is decrease in plasma temperature with increase in axial distance, sometimes plasma temperature is found to exhibit some higher order nonlinearity in the vicinity of the nozzle exit. This is an important observation and has enough potential to influence the thermal history of

particles in processing applications like plasma spraying, spheroidization, nanoparticles synthesis etc. Such behaviour, wherever observed have been confirmed through repeated measurements. To find the reason for such behaviour, a fast photography study is carried out and it has been observed that that depending on operating condition, arc current extends up to some distance beyond the nozzle exit [Fig.4.10(b)].The nonlinear interaction between the forward and return current in the flow affected area, external to nozzle exit, may result in the observed behaviour. It may also be noticed that the temperature drop in the tail zone is well behaved and exhibit no complex behaviour. The current free nature of the tail zone of the plasma jet may explain this behaviour. For the used plasma torch, the typical temperature of the argon plasma jet at the nozzle exit is around 6000k to 7000K. Obtained profiles of axial temperature variation under different currents are presented in Fig.4.11 to Fig.4.13 for gas flow rates 15 slpm, 20 slpm and 25 slpm respectively.

For a given plasma torch, the nitrogen plasma jet appears to be distinctly different from corresponding argon plasma jet in jet length, stability as well as temperature distribution when operated under similar current and gas flow rate. In this section we attempt a spectroscopic study of the nitrogen plasma jet to understand the variation of nitrogen plasma temperature at the nozzle exit as a function of arc current. Since the results from numerical simulation offer values of the nozzle exit temperature, we will make a comparison of these measured data with simulation results in chapter-7. The axial variation of plasma temperature after the nozzle exit is presented in this section. Compared to argon plasma the notable feature is observation of a long region of plasma column having significantly low gradient in temperature. The region probably originate from the fact that under same operating condition, a

nitrogen plasma jet produced by the torch is nearly ten times longer than corresponding argon plasma jet [see Fig.2.3].

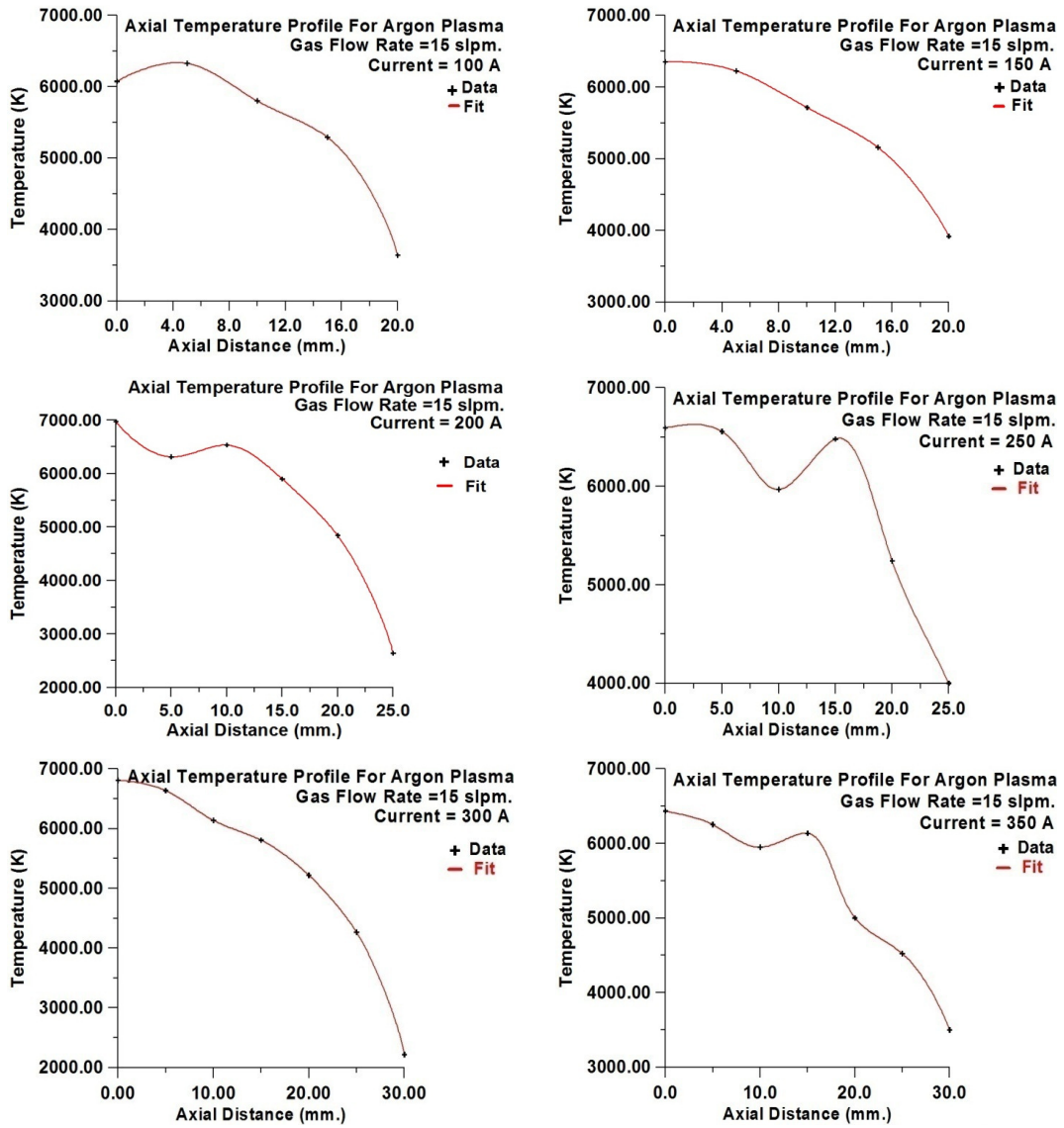
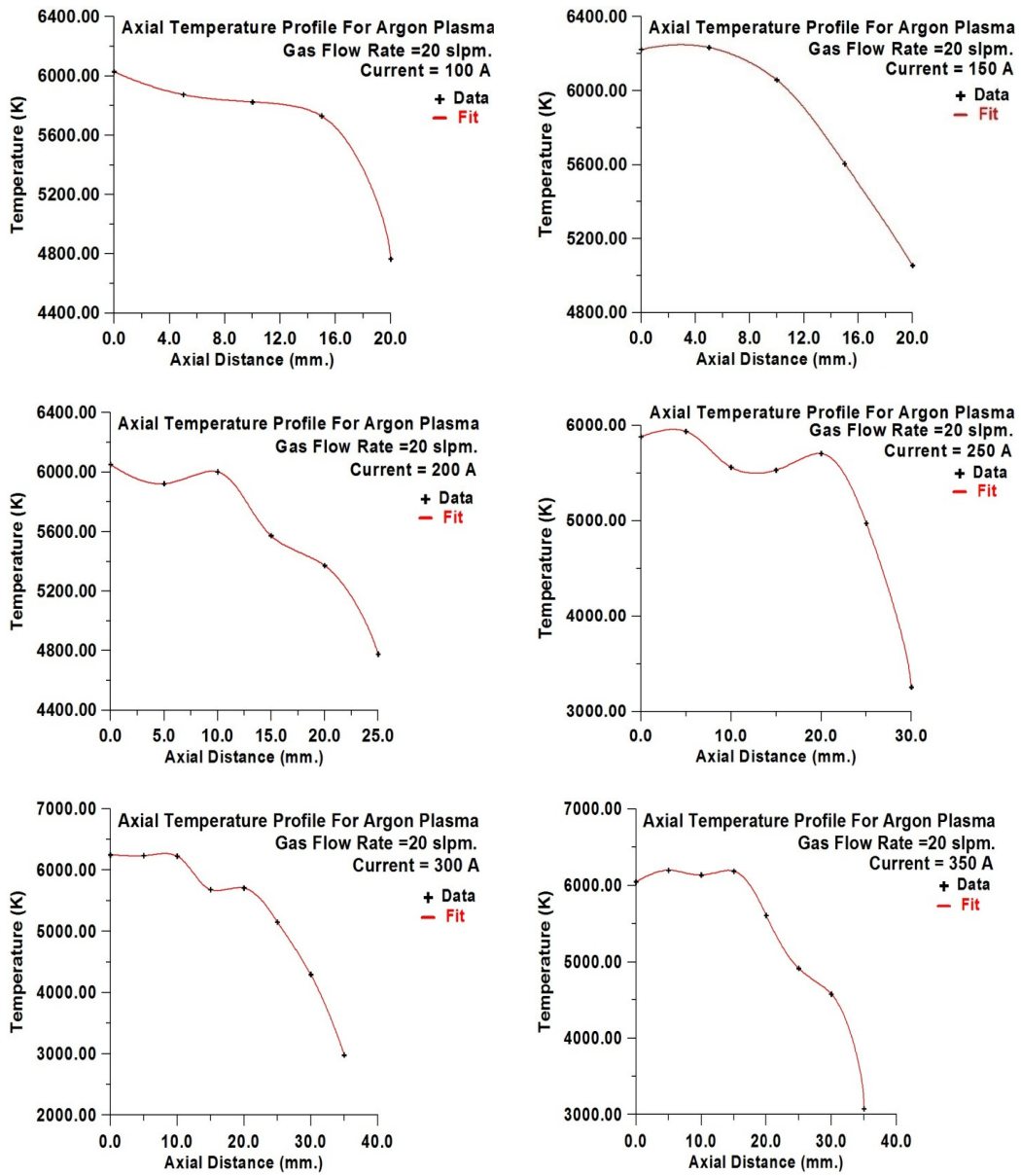
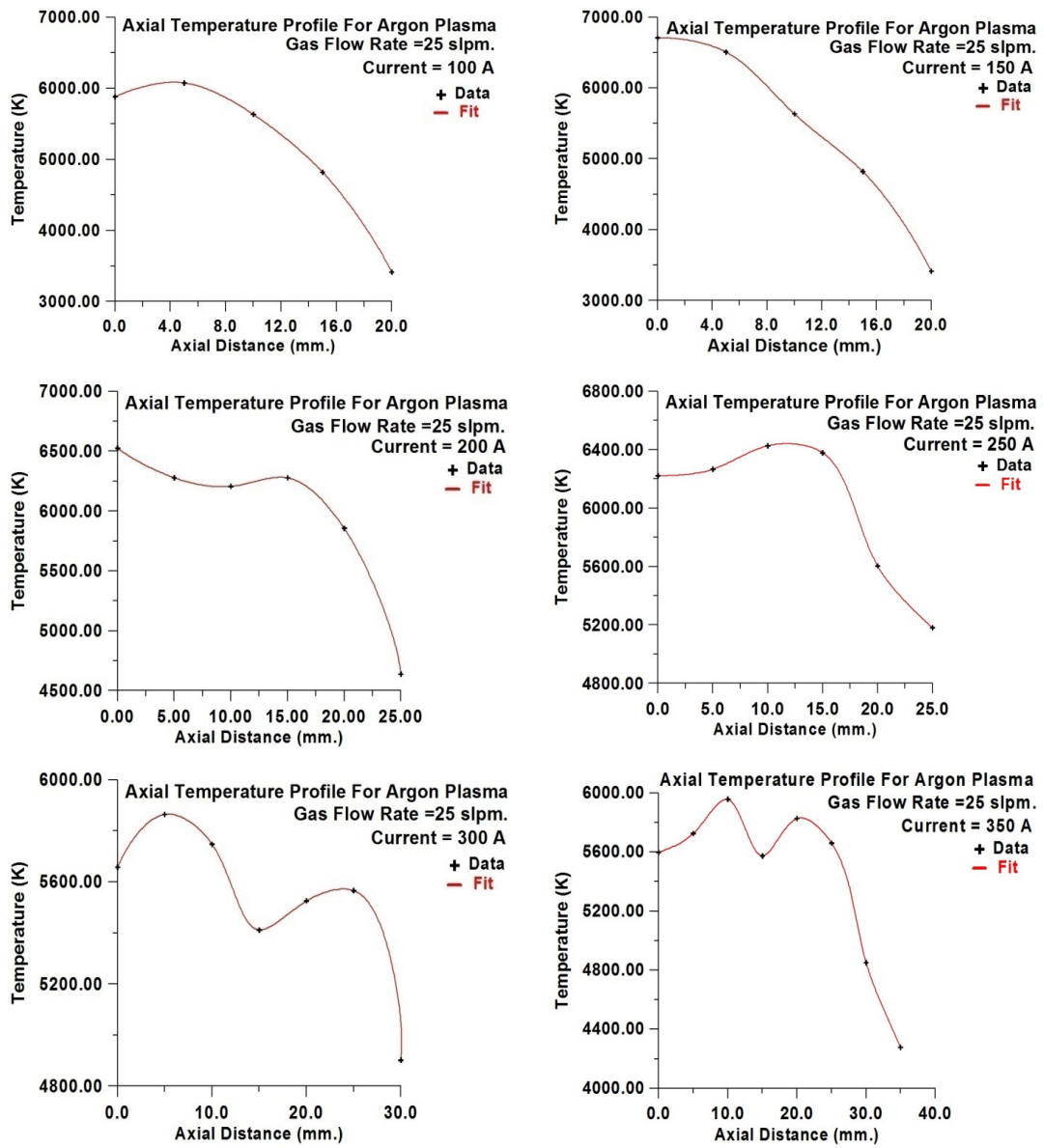


Fig. 4.11 Axial Temperature Profile of Argon plasma at 15 Slpm Gas Flow Rate.



**Fig. 4.12 Axial Temperature Profile of Argon plasma at 20 Slpm Gas Flow Rate**



**Fig. 4.13 Axial Temperature Profile of Argon plasma at 25 Slpm Gas Flow Rate**

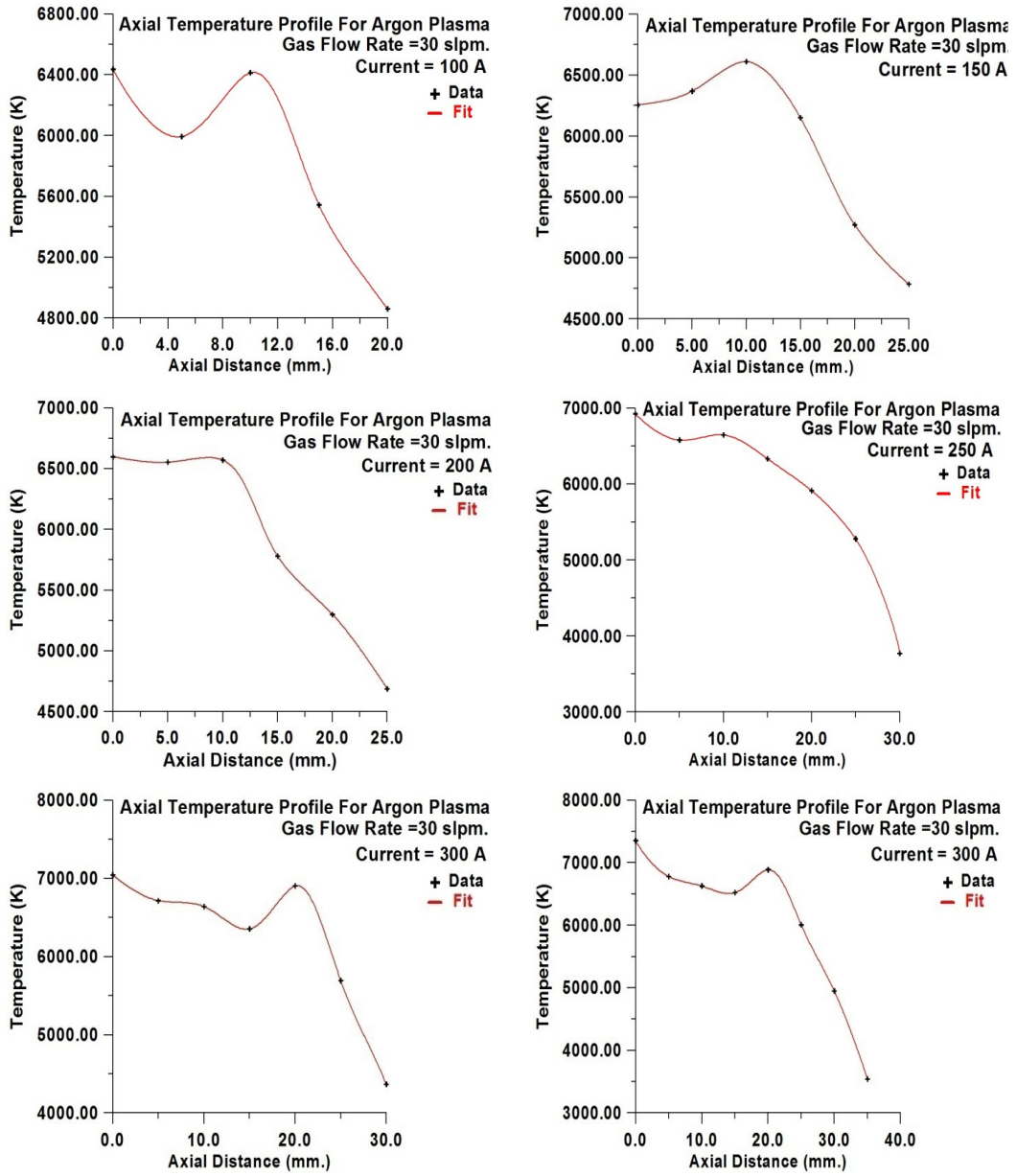


**Fig. 4.14 Axial Temperature Profile of Argon plasma at 30 Slpm Gas Flow Rate**

Axial variation of temperature in the nitrogen plasma jet, as obtained in the study is presented in Fig.4.15. For similar currents, observed higher temperature in nitrogen plasma compared to argon may be explained from the fact that nitrogen being a molecular gas, supports much higher voltage in the arc compared to argon. As a result, power content of a nitrogen plasma jet is much higher compared to argon under similar current and torch configuration. The oscillatory behaviour of axial temperature with axial distance, observed in argon, is present in nitrogen plasma jet too. It is observed from Fig.4.15, that operation at lower current is more prone to such oscillations in nitrogen plasma. As current increases, stronger interaction between the forward and return current inhibits such oscillation in the immediate vicinity of the nozzle exit and allows temperature to drop with distance following usual exponential law. However, as observed, the oscillations begin to appear at longer distances. Ohmic heating being the primary source of heat and the external current carrying plasma jet being a free jet, a high temperature zone in the jet must be followed by a low temperature zone as the free plasma jet expands getting heated and current density reduces as volume expands. The behaviour is nicely depicted in fig.4.15.

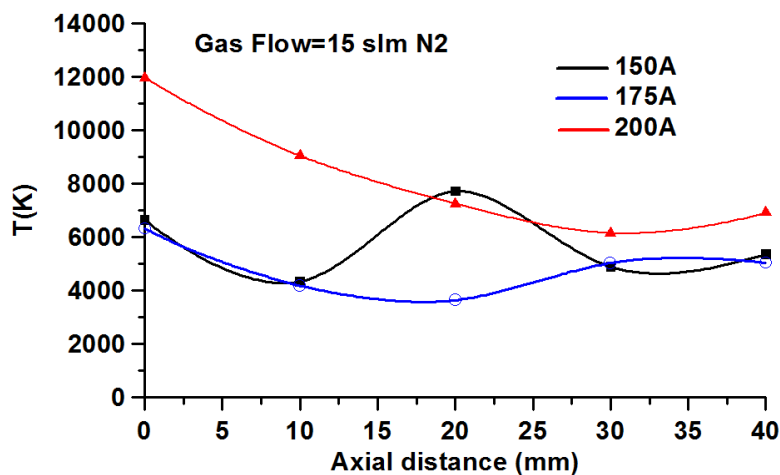


**Fig. 4.15** Variation of axial temperature in nitrogen plasma jet at 15 slpm of gas flow rate

Fig.4.16 presents variation of temperature of the nitrogen plasma at the nozzle exit as a function of arc current. For the chosen currents, numerical simulations are also carried out in chapter-7. It is found that the observed behaviour is in close agreement with the simulation results. The higher temperature at 180A is consistently observed in repeated measurements. It is observed in the numerical simulation in chapter-7 that a sharp transition in the flow configuration is associated near this current.

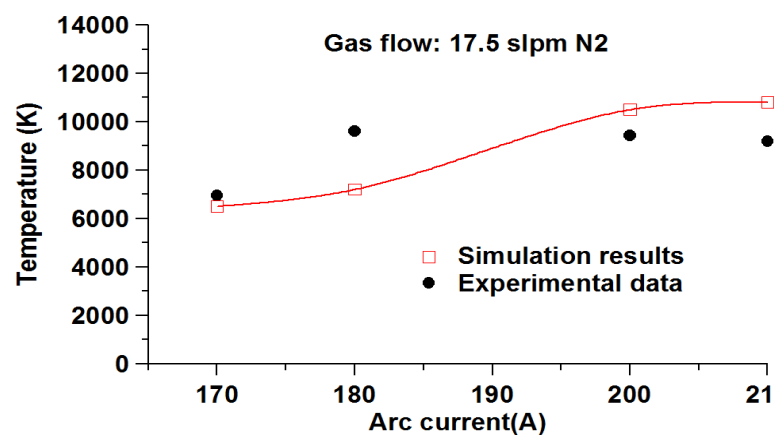


**Fig.4.16 Variation of central axis temperature of nitrogen plasma at the nozzle exit as a function of arc current and comparison with simulation results [chapter-7].**

#### 4.8. Conclusions:

This chapter presents determination of temperature of argon and nitrogen plasma jets under different operating conditions using Boltzman plot technique. Line spectra originating from pure atomic transitions are used to determine the temperature of plasma in both the cases. While temperature at the torch exit is studied as a function of arc current, axial variation of plasma temperature are also studied for argon and nitrogen plasma. A number of interesting facts are revealed from the study. For the same current and gas flow rates in a plasma torch, it is found that nitrogen plasma jet

possesses higher average temperature compared to argon. Higher supported power through higher arc voltage may be responsible for this. Axial variation in temperature after the nozzle exit are found to include oscillations originated through mutual interaction among jet current, self magnetic field and aerodynamic flow field. Such oscillations are observed in argon as well as nitrogen and confirmed through repeated measurements. For a given torch configuration, nitrogen is found to offer much longer (nearly ten times) plasma jet compared to argon under same current and gas flow rate. It has been clearly observed in nitrogen that as arc current increases the oscillating region moves away from the nozzle exit and an exponential drop in temperature prevails in the immediate vicinity of the nozzle. The finding is important as it can immensely influence the thermal history of the particles introduced inside a plasma jet for important processing works like plasma spraying, nanostructure synthesis, spheroidization etc. Obtained results are expected to contribute significantly in process optimization.

# **CHAPTER-5: Study of Instability in Nitrogen and Argon Plasma Jets**

## **Outline of the Chapter**

**5.1 Introduction**

**5.2 Experimental Setup**

**5.3 Diagnostic Tools**

**5.4 Results and Discussion**

**5.5 Conclusion**

# **Chapter: 5**

## **Study of Instabilities in Nitrogen and Argon Plasma Jets**

### **5.1. Introduction:**

In spite of widespread applications of arc plasma devices, its development and efficient utilization is obstructed by number of problems mainly associated with instabilities in arcs [31]. These problems affect the device life time as well as the quality of the processing works done. For example, in ideal plasma spray process, it is needed that the particles should melt properly before they impact on the substrate. However, the fluctuation in plasma temperature may affect the heating of the injected particles. The variation in plasma velocity may result in variation in the particle residence time and also variation in the particle trajectory. This may lead to poor performance as most of the particles may not be heated properly or may not reach the target. Process quality may degrade due to presence of unmelts.

1. While the study is important, possible no study on instabilities in nitrogen plasma has been reported earlier. However, a number of important studies on instabilities in argon [76, 82, 83] and argon-hydrogen plasma [36] have been reported.

This chapter investigates the behaviour of arc instabilities in atmospheric pressure argon and nitrogen plasma torches through study of time evolution of arc voltages in phase and frequency space. While a detail analysis of instabilities in arcs is quite involved and may itself be a subject of a thesis, scope of the present study is limited to the understanding of the voltage instabilities in argon

arc at typical operating conditions namely flow rates ranging from 15-30 slm at arc current around 350A. Since typical long nitrogen plasma jet, subject of the study, occurs around low flow rate of 15 slm, instabilities in nitrogen arc are studied around this flow rate at different power levels with current ranging from 125A to 300A.

A DC arc plasma torch in its simplest form contains two electrodes and the plasma generating gas passing between them, heated through ohmic heating by an established arc between the electrodes [Fig.5.1]. The point where the arc connects the anode is called the anode arc root.

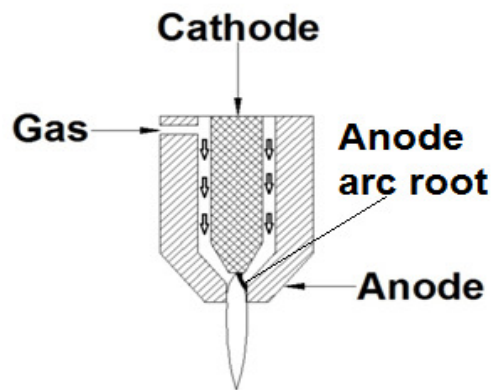


**Fig. 5.1 plasma generation in DC plasma torch**

The arc length changes either because of the movement of the anode arc root or due to change in the arc length due to fluid dynamic effects. The mutual interaction among thermal, electromagnetic and fluid dynamic effects introduces dynamic variation in the arc length and results in the observed unsteady behaviour in arc voltage. In recent studies such variations are found to exhibit chaotic nature, in which specific strange patterns appear in phase space and associated spectrum in the frequency space exhibits continuous nature. For dominant periodic behaviour specific peaks are observed in the frequency spectra. In practice, the fluid dynamic drag force tries to push the arc downstream of the anode nozzle and the electromagnetic force tries to

keep the arc length minimum in order to maintain minimum energy (Steenbeck minimum energy principle) configuration [73]. The competition between the balancing forces acting in the opposite directions under the influence of continuously varying thermodynamic and transport properties results in the observed variation in arc voltages.

Another reason for the plasma jet fluctuation may be the fluctuation in the power supply current. Ripples in the rectified ac current which oscillates with input three phase ac power supply frequency (150 Hz) may introduce a regular repetitive oscillation in the arc voltage. However, in this study, a constant current IGBT based DC power supply has been used which has negligible ripple compared to SCR based power supply. The observed voltage instability is therefore primarily linked to the change in arc length caused by thermal, electrical and fluid dynamic forces.

As the arc voltage varies, the power inside the plasma varies and consequently velocity, pressure and temperature of the plasma jet also fluctuate. The study of frequency spectra brings out the dominant frequencies present in the process when certain operating condition is set in. It is interesting to probe if the underlying process involves any such dominant frequencies. On the other hand, the study of behaviour in phase space allows us to get a first hand understanding about the possible nature of behaviour: periodic, chaotic or random. However, it must be mentioned that confirming nature of any arbitrary time series needs rigorous investigation like estimation of Lyapunov exponent and fractal dimension, not include in the present scope of this study [76, 82, 83]

## 5.2. Experimental setup:

The experimental setup for recording the voltage fluctuation is shown in figure 5.2. It consists of a plasma torch, constant current IGBT based DC power supply, a voltage divider circuit and an oscilloscope.

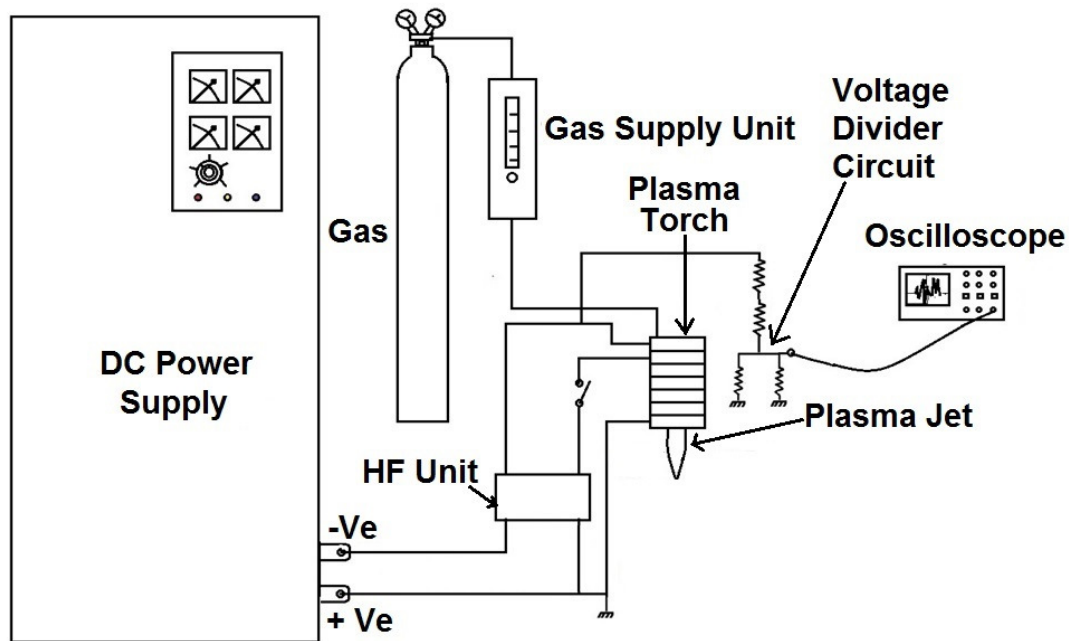


**Fig. 5.2 Experimental arrangement for acquiring voltage fluctuation data**

The details of the components used in the experiment are already described in chapter 2. The plasma torch operates with power up to 50 kW. The typical values for the arc current varies from 100 A to 500 A and that of the arc voltage varies from 50 to 150 V. Considering the fact that the oscilloscope can record a maximum of 30 V, only a certain fraction of the total arc voltage is given to the terminals of the oscilloscope using a voltage divider circuit. The setup used for the instability study is presented in Fig.5.2 and the details of the voltage divider circuit are given in Fig. 5.3.

Since the resistances in the circuit are known, the actual arc voltage can be obtained from the recorded voltage in the oscilloscope just by using a constant multiplicative factor.

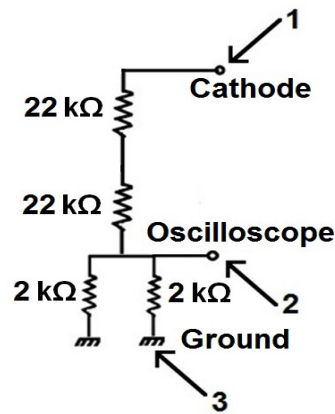


**Fig.5.3 Circuit diagram of the voltage divider circuit**

### 5.3. Diagnostic Tools:

The voltage fluctuation data obtained as a function of time are analysed with the help of real time behaviour, phase space behaviour and frequency space characteristics. The behaviour of a dynamical system can be classified as: steady, periodic, quasi-periodic, chaotic and random. The way in which they differ in time series, frequency and phase space behaviour is tabulated in Table – 5.1. [33]

**Table 5.1 Different types of dynamics and their representation**

Sr. No.	Type of dynamics	Time series behaviour	Phase portrait for the dynamic system	FFT behaviour
1	Steady	Value of the variable remain constant with time	Point	Only frequency at zero frequency is seen
2	periodic	Value of the variable shows simple periodic repetition	Simple orbit	Sharp peak at particular frequency is seen
3	Quasi-periodic	The variable shows complex periodic repetition	Complex orbit	Sharp peaks at number of frequencies is seen
4	chaotic	No repetition of the value of the variable	Specific strange looking pattern called ATTRACTOR	Continuous spectra with peaks at some frequencies
5	Random	No repetition of the value of the variable	Phase space is uniformly filled	Continuous spectra and no peaks at all

### Construction of Phase portrait:

Phase portrait is graphical presentation of the evolution of system behaviour in phase space. Packard et.al. [84] proposed a method for the construction of multidimensional phase space portrait from the measurement of a single variable. The present study uses the 'time delay method' by Packard et.al. for construction of the phase space. A time delay of  $25\Delta t$  is used for the construction of the phase plot in the present study,  $\Delta t$  being the sampling interval.

### Fast Fourier Transform: (FFT)

For frequency space analysis, the most widely used Radix-2 Cooley-Tukey algorithm for fast Fourier transform [FFT] is used. FFT is nothing but fast discrete Fourier transforms (DFT) achieving a great reduction in calculation time. In FFT, one express a discrete Fourier transform (DFT) of composite size  $N = N_1 N_2$  in terms of smaller DFTs recursively. Radix-2 method requires the number of data points as  $N=2^r$ . If there is a little short of data to complete  $N=2^r$ , necessary data points are augmented by padding zero. Such small augmentation does not alter the frequency feature of the signal but allows the algorithm applicable for the data set.

The discrete Fourier transform (DFT) of series  $x_n$  is defined as:

$$X_k = \sum_{n=0}^{N-1} x_n e^{-\frac{2\pi i}{N}nk} \quad (5.1)$$

where,  $k$  is an integer ranging from 0 to  $N-1$ .

In Radix-2 Cooley-Tukey algorithm, DFTs are computed for the even-indexed inputs ( $x_{2m} = x_0, x_2, \dots, x_{N-2}$ ) and of the odd indexed inputs ( $x_{2m+1} = x_1, x_3, \dots, x_{N-1}$ ), and

then combined to produce the DFT of the whole sequence. To realize FFT, the idea is performed recursively to reduce the overall runtime.

## **5.4. Results and discussion:**

### **5.4.1 Voltage instability in argon plasma:**

For a given current, observed instabilities in argon arc under different gas flow rates are presented in figure 5.4. The same as a function of arc current for a given flow rate is presented in figure 5.5. It is observed that for an arc current of 350 and a gas flow rate of 15 slpm, the arc voltage exhibits a highly periodic behaviour. FFT exhibits a sharp peak around 1 kHz and phase space reveals well defined periodic orbits of the dynamics. As flow rate increases, the periodic feature continues, but the dominant frequency of the dynamics near 1 kHz gradually shifts towards higher value. Finally at 30 slpm of gas flow, the dynamics switches from periodic to chaotic/random type. The dominant frequency near 1 kHz vanishes and instead, continuous looking spectra, characteristic feature of chaotic/random behaviour emerge. Similar trend of behaviour is observed at other currents too but with different gas flow rates for the transition.

The effect of increase in arc current on the behaviour of arc voltage in argon plasma is presented in figure 5.5. For a fixed gas flow rate of 30 slpm, it is observed that a variation in current from 100A to 350 A does not introduce much change in the dynamic behaviour of the arc voltage. Some degree of periodicity, exhibited by several dominant peaks in the FFT at lower arc current, gradually vanishes as current increases. Associated phase space diagrams are complex and may correspond to either random or chaotic behaviour.

#### **5.4.1 Voltage instability in nitrogen plasma:**

As already mentioned, relatively low gas flow rate around 15 slm is a necessary condition for operation of the torch with long plasma jet. Therefore, this study for instability in nitrogen arc does not include the effect of variation in flow. Normally, the variation in power of the jet is achieved by increasing the arc current. It is of interest to see how the instability features in nitrogen arc changes with increase in arc current.

Figure 5.6 illustrates the observed instability features of nitrogen plasma at a gas flow rate of 15 slpm with arc current varying from 125A to 300A. A clear double periodic behaviour is observed at arc current of 125A. One around 1.5 kHz and the other around 2.75 kHz [Fig.5.6(a)]. The behaviour is nicely reflected in the associated phase portrait also. The observation is of significance as it indicates that the associated physics is forcing the arc to perform two distinct types of repetitive movements. As current increases to 150A, the dominant dynamics near 1.5kHz persists but a bunch of new frequencies appear below 1.5 kHz. Notably, the dominant peak near 2.75 kHz vanishes. As current increase further to 175A, the frequency near 1.5 kHz also vanishes and a nearly continuous looking spectrum appears. As current increases further the frequency spectrum remains nearly unaltered. However at 200A the dominant frequency near 2.75 kHz reappears. As current increases to 225A this frequency vanishes again and never appears again at least up to a current of 300A. At higher current, the dynamics appears with a nearly continuous spectrum which indicates the dynamics may either be chaotic or random. Although the strange looking phase portrait indicates that the dynamics may be chaotic, further study is required to confirm.

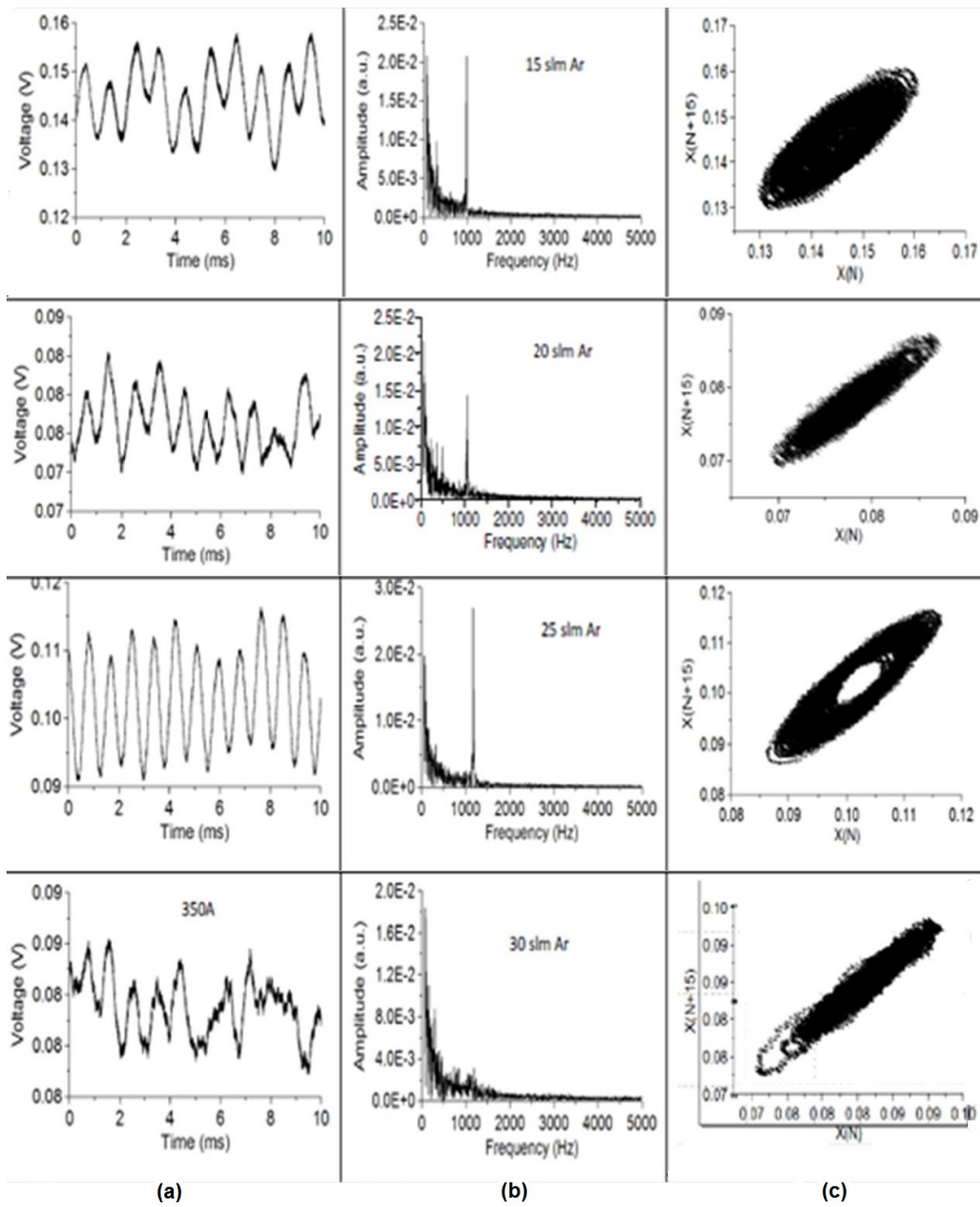


**Fig. 5.4** Features of voltage instability in Argon as a function of gas flow rate at a fixed arc current.

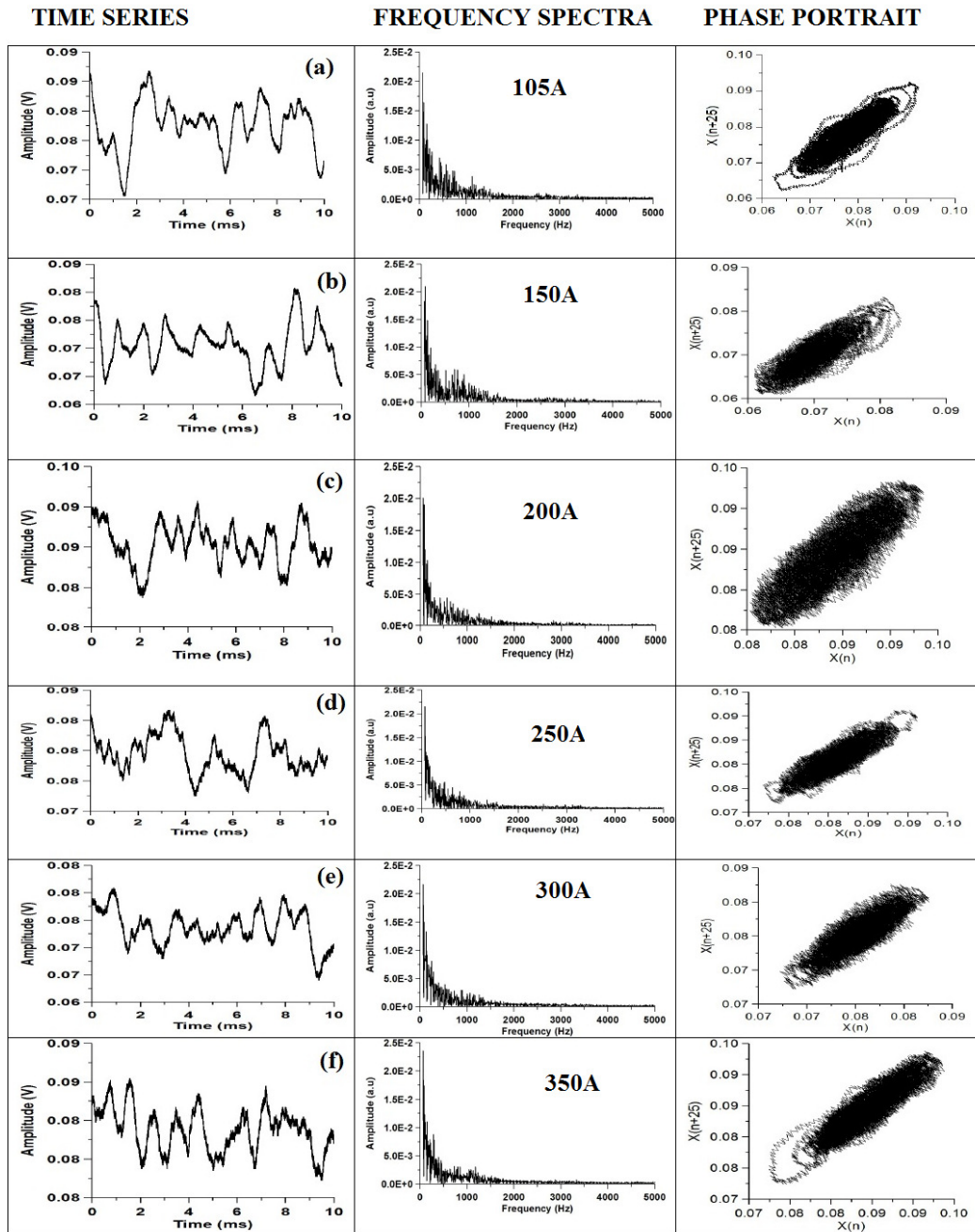


**Fig. 5.5** Features of voltage instability in Argon as a function of current at a fixed gas flow rate of 30slpm.

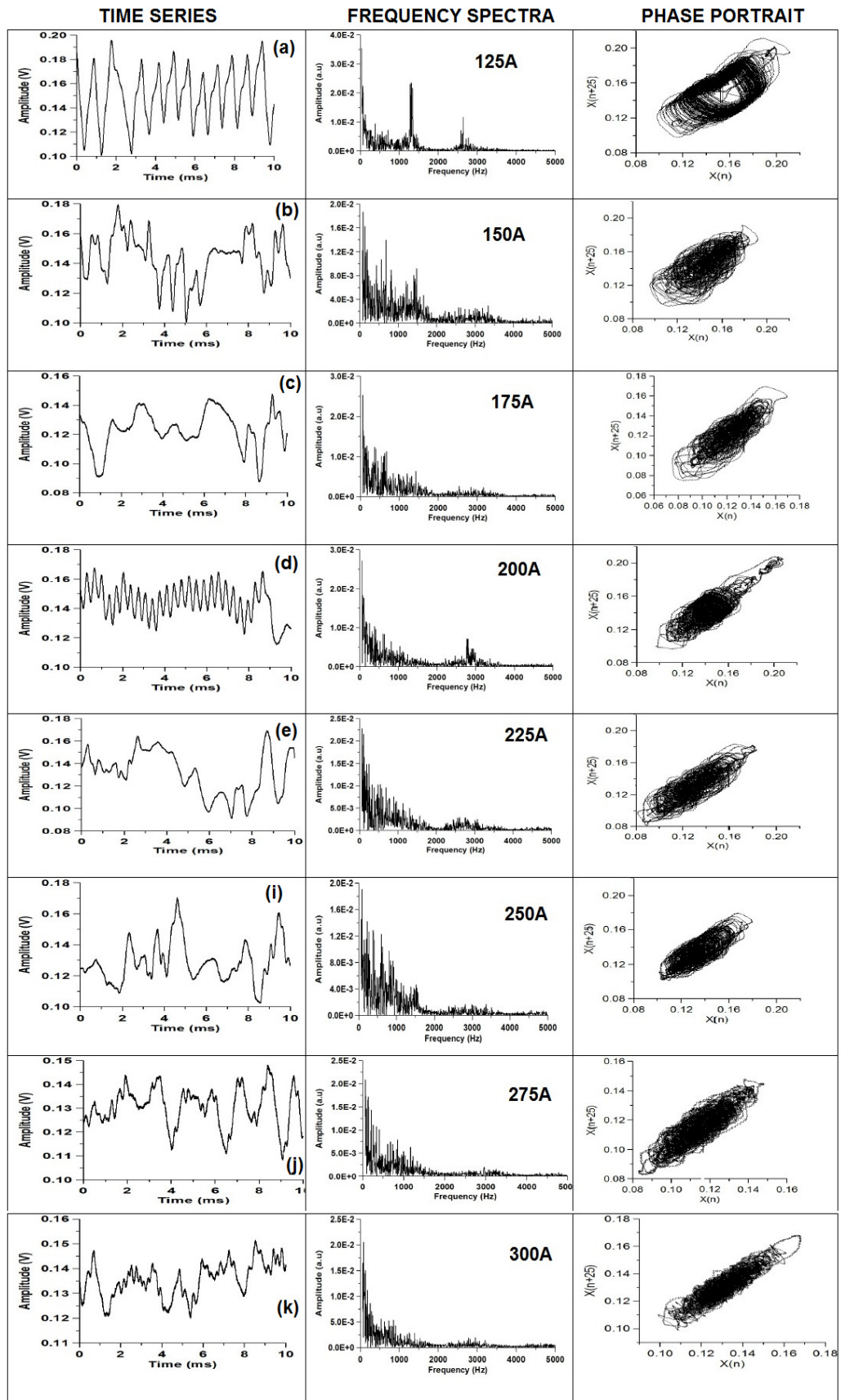


**Fig. 5.6** Features of voltage instability in Nitrogen plasma at the gas flow rate of 15 slpm and different arc currents.

### **5.5.Conclusion:**

Studies on inherent instabilities in argon and nitrogen arcs under typical operating conditions are investigated in this chapter through phase space and frequency space behaviour. It has been observed in both cases that at higher currents and higher flow rates the dynamics is either random or chaotic. At lower currents and lower flow rates the dynamics exhibit a number of interesting periodic behaviours. Observed, highly periodic behaviour in argon at low flow rate (up to 25 slpm) and doubly periodic behaviour in nitrogen at lower current (at 125A and 200A) are some of them. The studies are important as they allow us to know the possible nature of instabilities when a certain operating regime is chosen. The results may serve as important inputs for time dependent physics model of such arc behaviour to be developed in future. It may also help in optimising operating regime depending on process need.

# **CHAPTER-6: Thermodynamic and Transport Properties of Nitrogen Plasma under Thermal Equilibrium and Non-equilibrium Conditions**

## **Outline of the Chapter**

**6.1 Introduction**

**6.2 Determination of Thermodynamic Properties**

**6.3 Determination of Transport Properties**

**6.4 Results and Discussion**

**6.5 Conclusions**

# **Chapter: 6**

## **Thermodynamic and Transport Properties of Nitrogen Plasma under Thermal Equilibrium and Non-equilibrium Conditions**

### **6.1. Introduction:**

The chapter presents the calculation of thermodynamic and transport properties of nitrogen plasmas that serve as a basic indispensable input for numerical modeling, a fast emerging powerful field for design optimization and predicting parametric behaviour. The property data may also find important applications in analysis and interpretation of observed experimental behaviour under different operating conditions.

Deviations from thermal and chemical non-equilibrium are often encountered in so-called thermal plasma devices. Nitrogen plasma devices are somewhat special in this as they offer non-oxidizing atmosphere, higher arc voltage, and operation with usual tungsten based electrodes for numerous processing applications. So far most of the available data on properties are based on equilibrium considerations. Among the very few works on non-equilibrium properties, the major problem lies with the use of different definitions of screening length in the shielded coulomb potential for charged-charged interaction. Whether only the electrons or both electrons and ions participate in the shielding are the major issues. In one such work [52], the wide variations in the computed properties under these two different definitions of screening length are presented. In another work the non-equilibrium properties are presented considering

only the effect of electrons in the shielding. As ions are integrated part of the plasma and have obvious effect in the shielding, computed properties may be inaccurate if their effects are not accounted. A scope of ambiguity is thus introduced that which of the existing data is more appropriate for a specific application. In an attempt to remove the ambiguity, a different definition of screening length is proposed in a recent work [54]. Effects of both electrons and ions are included and properties are predicted in close agreement with the experimental data. This section of the thesis follows this approach and presents the thermodynamic and transport property data under equilibrium as well as thermal and chemical non-equilibrium.

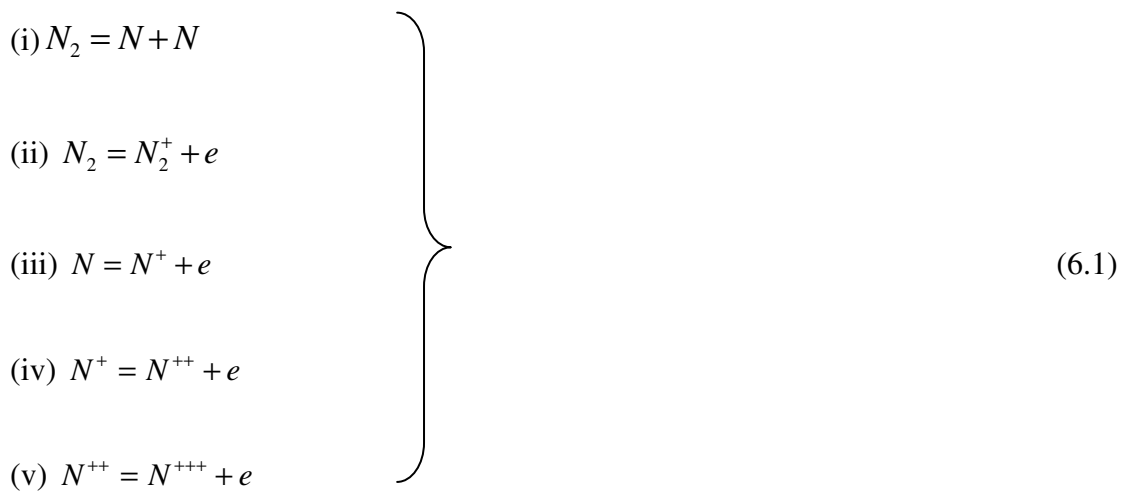
Assuming a seven species model of nitrogen plasma, thermodynamic and transport properties are calculated under thermal equilibrium and non-equilibrium conditions. Species densities, mass densities, specific heat, enthalpy, diffusion coefficients, viscosity, thermal conductivity, collision frequency and electrical conductivity are studied as a function of temperature, pressure and different degrees of temperature non-equilibrium. Effect of both electrons and ions are considered in the shielding for charged-charged interactions under shield coulomb potential and obtained results are found to be in excellent agreement with experimentally obtained results, especially at higher temperatures. Accounting up to third ionized states, results are presented with temperatures ranging from 300 to 50,000 K, the ratio of electron temperature ( $T_e$ ) to the heavy particle temperature ( $T_h$ ) ranging from 1 to 20 and the pressure ranging from 0.1 to 7 atmospheres. Under atmospheric pressure, results obtained for thermodynamic equilibrium ( $T_e=T_h$ ) are compared with number of published results under similar conditions.

Under chemical non-equilibrium, number densities inside the plasma are influenced by diffusive particle fluxes originating from species and temperature gradients. The ultimate effect can be accounted for by including a modified rate constant in the associated rate equations in place of chemical-equilibrium rate constants and defining a chemical non-equilibrium parameter 'c' as the ratio of the modified rate constant to the equilibrium rate constant [55]. Effects of chemical non-equilibrium on the computed properties are presented with 'c' ranging from 0.5 to 2.

Procedures followed in the determination of thermodynamic properties are briefly outlined in section 6.2. The same for transport properties are outlined in section 6.3. Major results obtained and their comparisons with data available from previously published reports are presented in Section 6.4. Conclusions are presented in section 6.5.

## 6.2. Determination of thermodynamic properties

Considering a seven species model of the nitrogen plasma, it is assumed that the species ( $N_2$ ,  $N_2^+$ ,  $N^+$ ,  $N^{++}$ ,  $N^{+++}$ ,  $N$ ,  $e$ ) originate through five independent reactions:



Accounted highest ionized state is  $N^{+++}$  and the highest temperature considered is 50000 K. N and e are considered as independent species and  $N_2$ ,  $N_2^+$ ,  $N^+$ ,  $N^{++}$ ,  $N^{+++}$  are considered as dependent species.

Computation of partition function is the first step in calculating the thermodynamic and transport properties. The total partition function for a given species of particles is the product of internal partition function and translational partition function. The internal partition function is again expressed as the product of electronic partition function, rotational partition function and vibrational partition function. The process of computing the total partition function is given in figure 6.1. The explicit formulae which are used for computing the internal and translational partition function of various species are presented in the Table 6.1 and Table 6.2 respectively.

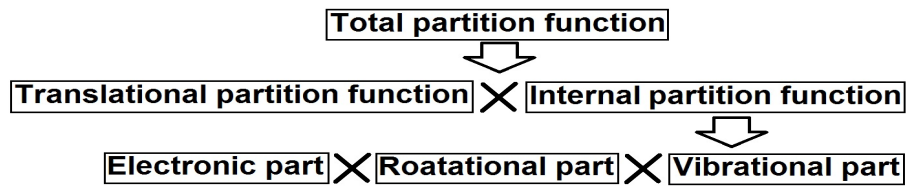


**Fig. 6.1 Algorithm for computing partition function**

**Table 6.1. Explicit form of internal partition function**

Species	Notation	Expression for internal partition function	Description of associated parameters
M (Molecule)	$Q_{rot}^M$	$Q_{rot}^M = \frac{T_h}{\Theta_{rot}}$	$\Theta_{rot}^M$ is the characteristic rotational temperature = 2.875 K for nitrogen
M (Molecule)	$Q_{vib}^M$	$Q_{vib}^M = \frac{\exp\left(-\frac{\Theta_{vib}}{2T_h}\right)}{1 - \exp\left(-\frac{\Theta_{vib}}{2T_h}\right)}$	$\Theta_{vib}^M$ is the characteristics vibrational temperature = 3394 K for nitrogen
MI (Molecular ion)	$Q_{rot}^{MI}$	$Q_{rot}^{MI} = \frac{T_h}{\Theta_{rot}}$	$\Theta_{rot}^{MI}$ is the characteristic rotational temperature = 2.780 K for nitrogen

MI (Molecular ion)	$Q_{vib}^{MI}$	$Q_{vib}^M = \frac{\exp\left(-\frac{\Theta_{vib}}{2T_h}\right)}{1 - \exp\left(-\frac{\Theta_{vib}}{2T_h}\right)}$	$\Theta_{vib}^{MI}$ is the characteristics vibrational temperature = 3175.9 K for $N_2^+$
A (Atom)	$Q_{el}^A$	$Q_{el}^A = \sum_j g_{Aj} \exp\left(-\frac{E_{Aj}}{k_B T_e}\right)$	
I (Ion)	$Q_{el}^I$	$Q_{el}^I = \sum_j g_{Ij} \exp\left(-\frac{E_{Ij}}{k_B T_e}\right)$	
D (Double ion)	$Q_{el}^D$	$Q_{el}^D = \sum_j g_{Dj} \exp\left(-\frac{E_{Dj}}{k_B T_e}\right)$	
T (Triple ion)	$Q_{el}^T$	$Q_{el}^T = \sum_j g_{Tj} \exp\left(-\frac{E_{Tj}}{k_B T_e}\right)$	
e(electron)	$Q_e^{int}$	2	

**Table 6. 2 Explicit form of the translational partition function**

Species	Translational partition function (V = volume of the system)
M (Molecule)	$Q_{tr}^M = V \cdot \left(\frac{2\pi m_M k_B T_h}{h^2}\right)^{3/2}$
MI (Molecular Ion)	$Q_{tr}^M = V \cdot \left(\frac{2\pi m_{MI} k_B T_h}{h^2}\right)^{3/2}$
A (Atom)	$Q_{tr}^M = V \cdot \left(\frac{2\pi m_A k_B T_h}{h^2}\right)^{3/2}$
I (Ion)	$Q_{tr}^M = V \cdot \left(\frac{2\pi m_I k_B T_h}{h^2}\right)^{3/2}$
D (Double ion)	$Q_{tr}^M = V \cdot \left(\frac{2\pi m_D k_B T_h}{h^2}\right)^{3/2}$
T (Triple ion)	$Q_{tr}^M = V \cdot \left(\frac{2\pi m_T k_B T_h}{h^2}\right)^{3/2}$
e(Electron)	$Q_{tr}^M = V \cdot \left(\frac{2\pi m_e k_B T_h}{h^2}\right)^{3/2}$

The computed total partition function of various species is then used for computing the thermodynamic and transport properties. The process of computing the thermodynamic and transport coefficients is presented graphically in figure 6.2.

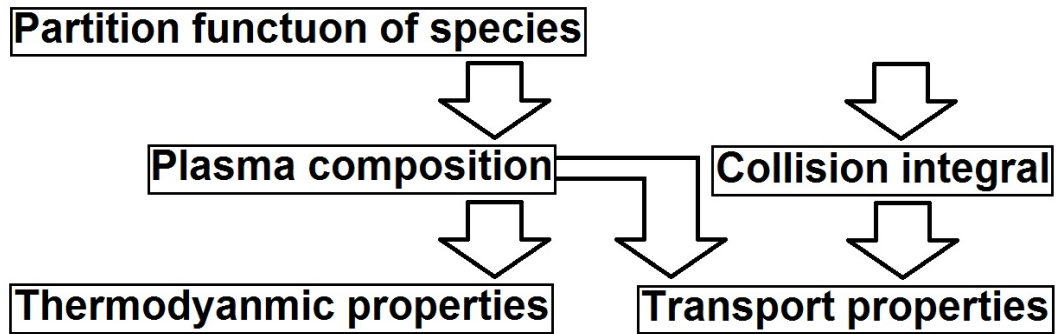


**Fig. 6.2 Algorithm for computing the thermodynamic and transport properties**

The plasma composition is calculated from the non-equilibrium Saha equation, the equation of charge neutrality and Dalton's law of partial pressure. The rate constants, reaction energies and the associated 2T- Saha equations used for computing the plasma composition are presented in the Table 6. 3.

**Table 6.3 Reactions, rate constants, associated Saha equations and reaction energies for nitrogen plasma system**

Sr. No (i)	Reaction	Non-equilibrium Saha equation	Rate constant (R <sub>i</sub> )	Reaction energy (Σ <sub>i</sub> in cm-1)
1	$N_2 = N + N$	$\frac{n_6^2}{n_1} = R_1$	$R_1 = \frac{\left\{ \left( \frac{2\pi n_6 k_B T_h}{h^2} \right)^{3/2} \right\}^2}{\left( \frac{2\pi m_1 k_B T_h}{h^2} \right)^{3/2}} \cdot \frac{\{Q_6(T_h)\}^2}{Q_1(T_h)} \exp\left[-\frac{\sum_1}{k_B T_h}\right]$	77,554
2	$N_2 = N_2^+ + e^-$	$\frac{n_2 \cdot n_7}{n_1} = R_2$	$R_2 = 2 \cdot \frac{Q_2(T_h)}{Q_1(T_h)} \cdot \left( \frac{2\pi m_7 k_B T_h}{h^2} \right)^{3/2} \cdot \exp\left[-\frac{\sum_2}{k_B T_h}\right]$	125,665
3	$N = N^+ + e^-$	$\frac{n_3 \cdot n_7}{n_6} = R_3$	$R_3 = 2 \cdot \frac{Q_2(T_h)}{Q_1(T_h)} \cdot \left( \frac{2\pi m_7 k_B T_h}{h^2} \right)^{3/2} \cdot \exp\left[-\frac{\sum_3}{k_B T_h}\right]$	117,345
4	$N^+ = N^{++} + e^-$	$\frac{n_4 \cdot n_7}{n_3} = R_4$	$R_4 = 2 \cdot \frac{Q_2(T_h)}{Q_1(T_h)} \cdot \left( \frac{2\pi m_7 k_B T_h}{h^2} \right)^{3/2} \cdot \exp\left[-\frac{\sum_4}{k_B T_h}\right]$	238,846
5	$N^{++} = N^{+++} + e^-$	$\frac{n_5 \cdot n_7}{n_4} = R_5$	$R_5 = 2 \cdot \frac{Q_2(T_h)}{Q_1(T_h)} \cdot \left( \frac{2\pi m_7 k_B T_h}{h^2} \right)^{3/2} \cdot \exp\left[-\frac{\sum_5}{k_B T_h}\right]$	382,625

The physical constants and notations used for computation are provided in Table 6.4.

**Table 6.4 Entities used in the computation of thermodynamic and transport properties**

Species index	1	2	3	4	5	6	7
Species	N <sub>2</sub>	N <sub>2</sub> <sup>+</sup>	N <sup>+</sup>	N <sup>++</sup>	N <sup>+++</sup>	N	e
Mass	M <sub>1</sub>	M <sub>2</sub>	M <sub>3</sub>	M <sub>4</sub>	M <sub>5</sub>	M <sub>6</sub>	M <sub>7</sub>
Number density	N <sub>1</sub>	N <sub>2</sub>	N <sub>3</sub>	N <sub>4</sub>	N <sub>5</sub>	N <sub>6</sub>	N <sub>7</sub>
No. of levels considered	Analytical	Analytical	178	330	287	366	2
Mass (amu)	28.016	28.016	14.008	14.008	14.008	14.008	5.49E-4

The rotational and vibrational constants which are needed for computing the associated quantities are collected from [85] and listed in Table 6.5.

**Table 6.5 Rotational vibrational constants of N<sub>2</sub> plasma system, D<sub>0</sub> is the dissociation energy of the molecules.**

Species index	Molecule	Vibrational constants		Rotational constants					Characteristics temperatures	
		$\omega_e$ (cm <sup>-1</sup> )	$\omega_e x_e$ (cm <sup>-1</sup> )	D <sub>0</sub> (eV)	B <sub>e</sub> (cm <sup>-1</sup> )	$\alpha_e$ (cm <sup>-1</sup> )	r <sub>e</sub> (Å <sup>0</sup> )	$\mu_0$ (amu)	$\Theta_{rot}$ (K)	$\Theta_{vib}$ (K)
1	N <sub>2</sub>	2358.57	14.324	9.759	1.9982	0.0173	1.0977	7.001	2.875	3394.0
2	N <sub>2</sub> <sup>+</sup>	2207.00	16.10	8.713	1.9318	0.0188	1.1164	7.001	2.780	3175.9

The relation for the conservation of total charge (criteria of charge neutrality) and total pressure (Dalton's law of partial pressures) are written below.

$$n_7 = n_2 + n_3 + 2n_4 + 3n_5 \quad (6.2)$$

$$p = p_1 + p_2 + p_3 + p_4 + p_5 + p_6 + p_7 \quad (6.3)$$

Now get the composition of the plasma we need to solve for n<sub>i</sub>, where i runs from 1 to 7.

For that we need seven independent equations involving n<sub>i</sub>. Five equations are obtained from five reactions as in Table 6.3 and two more equations are obtained as in (6.2) and (6.3). For a given temperature and pressure these seven equations are solved to obtain densities of seven species.

Once plasma composition is obtained, average density of the plasma can be computed using the following formula.

$$\rho = \sum_{i=1}^7 m_i n_i \quad (6.4)$$

The specific energy for various species are computed as Table 6. 6.

**Table 6.6 Formulae for specific energy of various species of particles**

Species	Formula	Explicit form
E	$\left(\frac{1}{\rho}\right) n_e k_B T_e^2 \left[ \frac{\partial \ln Q_{tr}^e}{\partial T_e} \right]_V$ $+ \left(\frac{1}{\rho}\right) n_e k_B T_e^2 \left[ \frac{\partial \ln Q_{int}^e}{\partial T_e} \right]_V$	$E_e = \frac{1}{\rho} \left( \frac{3}{2} n_e k_B T_e \right) + 0$
M	$\left(\frac{1}{\rho}\right) n_M k_B T_h^2 \left[ \frac{\partial \ln Q_{tr}^M}{\partial T_h} \right]_V$ $+ \left(\frac{1}{\rho}\right) n_M k_B T_h^2 \left[ \frac{\partial \ln Q_{int}^M}{\partial T_h} \right]_V$	$E_M = \frac{1}{\rho} \left[ \left( \frac{5}{2} n_M k_B T_h \right) + n_M k_B \Theta_{vib} \left( \frac{1}{2} + \frac{1}{\exp\left(\Theta_{vib}/T_h\right) - 1} \right) \right]_M$
MI	$\left(\frac{1}{\rho}\right) n_{MI} k_B T_h^2 \left[ \frac{\partial \ln Q_{tr}^{MI}}{\partial T_h} \right]_V$ $+ \left(\frac{1}{\rho}\right) n_{MI} k_B T_e^2 \left[ \frac{\partial \ln Q_{int}^{MI}}{\partial T_e} \right]_V$ $+ n_{MI} E_{formationMI}$	$E_{MI} = \frac{1}{\rho} \left[ \left( \frac{5}{2} n_{MI} k_B T_h \right) + n_{MI} E_0 + n_{MI} k_B \Theta_{vib} \left( \frac{1}{2} + \frac{1}{\exp\left(\Theta_{vib}/T_h\right) - 1} \right) \right]_{MI}$
A	$\left(\frac{1}{\rho}\right) n_A k_B T_h^2 \left[ \frac{\partial \ln Q_{tr}^A}{\partial T_h} \right]_V$ $+ \left(\frac{1}{\rho}\right) n_A k_B T_e^2 \left[ \frac{\partial \ln Q_{int}^A}{\partial T_e} \right]_V$ $+ n_A E_{formationA}$	$E_A = \frac{1}{\rho} \left[ \left( \frac{5}{2} n_A k_B T_h \right) + n_A E_d / 2 + n_A k_B T_e^2 \left( \frac{\partial \ln Q_{int}^A}{\partial T_e} \right)_A \right]$
I	$\left(\frac{1}{\rho}\right) n_I k_B T_h^2 \left[ \frac{\partial \ln Q_{tr}^I}{\partial T_h} \right]_V$ $+ \left(\frac{1}{\rho}\right) n_I k_B T_e^2 \left[ \frac{\partial \ln Q_{int}^I}{\partial T_e} \right]_V$ $+ n_I E_{formationI}$	$E_I = \frac{1}{\rho} \left[ \left( \frac{3}{2} n_I k_B T_h \right) + n_I \left( E_I + \frac{E_d}{2} \right) + n_I k_B T_e^2 \left( \frac{\partial \ln Q_{int}^I}{\partial T_e} \right)_V \right]$

D	$\left(\frac{1}{\rho}\right)n_D k_B T_h^2 \left[ \frac{\partial \ln Q_{tr}^D}{\partial T_h} \right]_V$ $+ \left(\frac{1}{\rho}\right) \left[ n_D k_B T_e^2 \left[ \frac{\partial \ln Q_{int}^D}{\partial T_e} \right]_V \right. \\ \left. + n_D E_{formationD} \right]$	$E_D = \frac{1}{\rho} \left[ \left( \frac{3}{2} n_D k_B T_h \right) + n_D \left( E_2 + E_1 + \frac{E_d}{2} \right) \right. \\ \left. + n_D k_B T_e^2 \left( \frac{\partial \ln Q_{int}^D}{\partial T_e} \right)_V \right]$
T	$\left(\frac{1}{\rho}\right)n_T k_B T_e^2 \left[ \frac{\partial \ln Q_{tr}^T}{\partial T_e} \right]_V$ $+ \left(\frac{1}{\rho}\right) \left[ n_T k_B T_e^2 \left[ \frac{\partial \ln Q_{int}^T}{\partial T_e} \right]_V \right. \\ \left. + n_T E_{formationT} \right]$	$E_D = \frac{1}{\rho} \left[ \left( \frac{3}{2} n_T k_B T_h \right) + n_T \left( E_3 + E_2 + E_1 + \frac{E_d}{2} \right) \right. \\ \left. + n_T k_B T_e^2 \left( \frac{\partial \ln Q_{int}^T}{\partial T_e} \right)_V \right]$

In the above expressions  $E_{formationX}$  stands for the energy required for the formation of the species of the particle X, where X may be molecular ion, atom, ion, double ion or triple ion,  $E_d$  is the dissociation energy per molecule,  $E_1$ ,  $E_2$  and  $E_3$  are the first, second and third ionization energies respectively.

Once the specific energy is known, specific enthalpy  $h_i$  of species i having density  $n_i$  and specific energy  $E_i$  is computed as:

$$h_i = E_i + (1/\rho)n_i k_B T_i \quad (6.5)$$

Explicit formulae used for computing the specific enthalpy per particle for various species is presented in the Table 6.7.

Specific heats are computed from respective specific energies and specific enthalpies employing standard thermodynamic relationships.

In this study results are presented with  $\theta$  ( $= T_e / T_h$ ) up to 20. It may be remarked that for higher  $\theta$ , initiation of electronic avalanches may significantly modify the composition, which is not accounted in this model. Highly energetic

electrons corresponding to high  $T_h$  and high  $\theta$  are primarily responsible for this. To avoid such situations results are presented with highest electron temperature not exceeding 50000K for any  $\theta$ .

**Table 6.7 Specific enthalpy of various species of particles**

Species	Formula	Explicit form
E	$h_e = E_e + kT_e$	$h_e = \frac{5}{2} n_e k_B T_e$
M	$h_M = E_M + kT_h$	$h_M = \left[ \left( \frac{7}{2} k_B T_e \right) + k_B \Theta_{vib} \left( \frac{1}{2} + \frac{1}{\exp(\Theta_{vib}/T_h) - 1} \right) \right]$
MI	$h_{MI} = E_{MI} + kT_h + E_0$	$h_{MI} = \left[ \left( \frac{7}{2} k_B T_e \right) + k_B \Theta_{vib} \left( \frac{1}{2} + \frac{1}{\exp(\Theta_{vib}/T_h) - 1} \right) + E_0 \right]$
A	$h_A = E_A + kT_h + \frac{E_d}{2}$	$h_A = \left[ \left( \frac{5}{2} k_B T_h \right) + \frac{E_d}{2} + k_B T_e^2 \left( \frac{\partial \ln Q_{int}^A}{\partial T_e} \right)_V \right]$
I	$h_I = E_I + kT_h + \frac{E_d}{2} + E_1$	$h_I = \left[ \left( \frac{5}{2} k_B T_h \right) + \frac{E_d}{2} + E_1 + k_B T_e^2 \left( \frac{\partial \ln Q_{int}^I}{\partial T_e} \right)_V \right]$
D	$h_D = E_D + kT_h + \frac{E_d}{2} + E_1 + E_2$	$h_D = \left[ \left( \frac{5}{2} k_B T_h \right) + \frac{E_d}{2} + E_1 + E_2 + k_B T_e^2 \left( \frac{\partial \ln Q_{int}^D}{\partial T_e} \right)_V \right]$
T	$h_T = E_T + kT_h + \frac{E_d}{2} + E_1 + E_2 + E_3$	$h_T = \left[ \left( \frac{5}{2} k_B T_h \right) + \frac{E_d}{2} + E_1 + E_2 + E_3 + k_B T_e^2 \left( \frac{\partial \ln Q_{int}^T}{\partial T_e} \right)_V \right]$

### 6.3. Determination of transport properties

Once the species concentration is determined as above, the various transport coefficients are determined following the first order perturbation technique of Chapman and Enskog [86,87]. In this method, the transport coefficients come in form of ratios of infinite determinants. The elements of the determinants usually appear in forms of complicated combination of bracket integrals. Chapman and Cowling [87] have shown that these integrals can be expressed as linear combinations of a set of integrals,  $\Omega_{ij}^{(l,s)}$ , defined as below:

$$\Omega_{ij}^{(l,s)} = \sqrt{\frac{2\pi k_B T^*}{m_{ij}^*}} \int_0^\infty \int_0^\infty \exp(-\gamma_{ij}^2) \gamma_{ij}^{2s+3} (1 - \cos^l \chi) b db .d\gamma_{ij} \quad (6.6)$$

where,  $k_B$  is the Boltzmann constant,  $m_{ij}^*$  and  $T_{ij}^*$  are effective mass and effective temperature of the colliding particles ( $i^{\text{th}}$  and  $j^{\text{th}}$ ).  $\chi$  is the deflection angle,  $b$  is the impact parameter and  $\gamma_{ij}$  is related to the relative velocity  $g_{ij}$  between  $i^{\text{th}}$  and  $j^{\text{th}}$  particle as following:

$$\gamma_{ij} = g_{ij} / \sqrt{2 k_B T^* / m_{ij}^*} \quad (6.7)$$

The angle of deflection,  $\chi$ , explicitly associates the interaction potential  $\Phi(r)$  as following:

$$\chi = \pi - 2b \int_0^\infty \frac{dr}{r^2 \sqrt{1 - \frac{2\Phi(r)}{m_{ij}^* g_{ij}^2} - \frac{b^2}{r^2}}} \quad (6.8)$$

In this study viscosity and binary diffusion coefficients are determined using 1st order approximation, diffusion coefficients and thermal conductivity of heavy particles are determined using 2nd order approximation, thermal diffusion coefficients of electrons,

thermal conductivity of electrons and electrical conductivity are determined using 3rd order approximation.

Values of the collision cross-sections  $Q_{ij}^{(l,s)}$  are obtained from collision integral values using the relationship:

$$Q_{ij}^{(l,s)} = \frac{\Omega_{ij}^{(l,s)}}{(s+1)! [2l+1 - (-1)^l]} \sqrt{\frac{k_B T_{ij}^*}{2\pi m_{ij}^*}} \quad (6.9)$$

In this study, twenty-eight independent interactions of five major types: neutral-neutral, ion-neutral (resonant), ion-neutral (non-resonant), charged-charged and electron-neutral are involved. These interactions are presented in the form of a chart as following.

**Table 6.8 The interaction chart for Nitrogen plasma**

Species index	(j)	1	2	3	4	5	6	7	
(i)	Species	N <sub>2</sub>	N <sub>2</sub> <sup>+</sup>	N <sup>+</sup>	N <sup>++</sup>	N <sup>+++</sup>	N	e	
1	N <sub>2</sub>	1-1	1-2	1-3	1-4	1-5	1-6	1-7	Neutral-Neutral
2	N <sub>2</sub> <sup>+</sup>	2-1	2-2	2-3	2-4	2-5	2-6	2-7	Ion-Neutral (resonant)
3	N <sup>+</sup>	3-1	3-2	3-3	3-4	3-5	3-6	3-7	Ion-Neutral (non-resonant)
4	N <sup>++</sup>	4-1	4-2	4-3	4-4	4-5	4-6	4-7	Charged-Charged
5	N <sup>+++</sup>	5-1	5-2	5-3	5-4	5-5	5-6	5-7	Electron-Neutral
6	N	6-1	6-2	6-3	6-4	6-5	6-6	6-7	
7	e	7-1	7-2	7-3	7-4	7-5	7-6	7-7	

Most of the collision integrals, used in this study are taken from the compilation by Capitelli et.al.[88]. Necessary cross-sections for neutral-neutral interaction between N<sub>2</sub>-N<sub>2</sub>, N<sub>2</sub>-N and N-N are computed using exponential repulsive type of potentials for T > 2000K. For T < 1000K Lennard-Jones type potential is used. Potential parameters are taken from experimental beam studies by Leonas et.al.[89]. The data for the range

between  $1000\text{K} < T < 2000\text{K}$  is obtained by smoothly linking the two datasets. For Molecule-molecule, molecule-atom and atom-atom interactions, not involving electrons, associated collision integrals are evaluated considering exponential repulsive potential and calculated from six coefficients  $a_1$  to  $a_6$  as following [88]:

$$\Omega^{(i,j)} = \frac{a_1 + a_2 \cdot (T_{ij}^*)^{a_3}}{a_4 + a_5 \cdot (T_{ij}^*)^{a_6}} \quad (6.10)$$

$T_{ij}^*$  is the reduced temperature as defined in the following:

$$T_{ij}^* = \frac{m_i T_j + m_j T_i}{m_i + m_j} \quad (6.11)$$

For electron-molecule and electron-atom interactions, the integrals are computed by direct numerical integration of relevant momentum transfer cross-sections available in literature. Collision integrals so computed may be obtained from nine coefficient values ( $a_1$  to  $a_9$ ) as following [88]

$$\Omega^{(i,j)} = \frac{a_3 \cdot [\ln T_{ij}^*]^{a_6} \cdot \exp \left[ \frac{\ln T_{ij}^* - a_1}{a_2} \right]}{\exp \left[ \frac{\ln T_{ij}^* - a_1}{a_2} \right] + \exp \left[ - \left( \frac{\ln T_{ij}^* - a_1}{a_2} \right) \right]} + a_7 \cdot \exp \left[ - \left( \frac{\ln T_{ij}^* - a_8}{a_9} \right)^2 \right] + a_4 \cdot [1 + (\ln T_{ij}^*)^{a_5}] \quad (6.12)$$

The coefficient values [ $a_1$  to  $a_6$ ] in equation (6.10) and [ $a_1$  to  $a_9$ ] in equation (6.13) are available in Ref.[88]. The Ion-neutral non-resonant interactions are computed using polarizability model. The collision integral assumes the following form:

$$\begin{aligned}
\Omega^{(1,1)}(T) &= \frac{425.4Z\alpha^{1/2}}{T^{1/2}} \\
\Omega^{(1,2)}(T) &= 0.833\Omega^{(1,1)}(T) \\
\Omega^{(1,3)}(T) &= 0.729\Omega^{(1,1)}(T) \\
\Omega^{(1,1)}(T) &= 0.871\Omega^{(1,1)}(T)
\end{aligned} \tag{6.13}$$

Z is the electronic charge of the ion (1 for singly ionized) and  $\alpha$  is the polarizability. Polarizability of N<sub>2</sub> and N are taken from literature as 1.76 and 1.13 respectively [85]

For interaction between N and N<sup>+</sup>, two distinct processes are involved: (a) diffusion type dominated by charge exchange process and (b) viscosity type - dominated by valence forces. For viscosity type interaction, collision integrals are computed using twelve potential curves [48]. For diffusion type interactions, the collision integrals are calculated from the dependency of charge transfer cross-section ( $S_{ex}$ ) on relative velocity ( $v$ )[88]

$$\begin{aligned}
S_{ex} &= \frac{(\gamma - \delta \ln v)^2}{2} \\
Q^l &= 2S_{ex}
\end{aligned} \tag{6.14}$$

$$\Omega^{(1,1)}(T) = \frac{1}{(kT)^3} \int_0^{\infty} d\varepsilon Q^{(1)} \varepsilon^2 \exp\left(-\frac{\varepsilon}{kT}\right)$$

Experimentally determined values of the parameters  $\gamma$  and  $\delta$  are taken from tabulation in Ref.[88]. A shielded coulomb potential is used for interactions between charged particles:

$$\Phi(r) = \left(\frac{e^2}{r}\right) \exp\left[-\frac{r}{\lambda_d}\right] \tag{6.15}$$

Where,  $\lambda_D$  is the Debye length,  $e$  is the electronic charge and  $r$  is the distance.  $\lambda_D$  is computed as:

$$\lambda_D = \sqrt{\frac{\epsilon_0 k_B T_e}{e^2 \sum_k Z_k^2 n_k}} \quad (6.16)$$

The summation is taken over all the charged species. The Coulomb parameter  $\Lambda$  is computed as:

$$\Lambda = \frac{2\lambda_D}{b_o} \quad (6.17)$$

Where  $b_0$  is the impact parameter between  $i^{\text{th}}$  and  $j^{\text{th}}$  species and calculated as following:

$$b_0 = \frac{Z_i Z_j}{8\pi\epsilon_0 k_B T_e} \quad (6.18)$$

Relevant collision integrals are then calculated using the closed form expressions [54]:

$$\Omega_{ij}^{(1,s)} = \sqrt{\frac{2\pi k_B T_{ij}^*}{m_{ij}^*}} \beta^2 b_0^2 \Gamma(s) \left[ \ln(\Lambda) - \frac{1}{2} - 2\bar{\gamma} + \Psi(s) \right] \quad (6.19)$$

$$\Omega_{ij}^{(2,s)} = 2 \sqrt{\frac{2\pi k_B T_{ij}^*}{m_{ij}^*}} \beta^2 b_0^2 \Gamma(s) \left[ \ln(\Lambda) - 1 - 2\bar{\gamma} + \Psi(s) \right] \quad (6.20)$$

where,

$$\bar{\gamma} = 0.5772; \Psi(s) \Big|_{s \neq 1} = \sum_{n=1}^{s-1} \frac{1}{n}; \Psi(1) = 0; \beta = 1.03 \quad (6.21)$$

Once the collision integrals are calculated, the diffusion coefficients are computed employing the equations (6.22) to (6.28). It may be remarked that the

collision integrals used in this study for charged-charged interactions are verified to offer excellent agreement with experimental data [54]

The diffusion due to pressure and species concentration gradients is controlled by general ambipolar diffusion coefficient ( $D_{ij}^a$ ) (GADC) and that due to temperature gradient is controlled by thermal ambipolar diffusion coefficient ( $D_i^{Ta}$ ) (TADC):

$$D_{ij}^a = \left( D_{ij} + \frac{\alpha_i}{\beta} \sum_{k=1}^s Z_k D_{kj} \right) \quad (6.22)$$

$$D_i^{Ta} = \left( D_i^T + \frac{m_i \alpha_i}{\beta} \sum_{k=1}^s \frac{Z_k D_k^T}{m_k} \right) \quad (6.23)$$

While a summary of the scheme used in the calculation of these coefficients is presented in figure 6.3, details of the calculation procedures are given below.

Following Ramshaw [90], the binary diffusion coefficient (BDC) between two particles  $i$  and  $j$  is calculated as:

$$D_{ij}^b = \frac{3 f_{ij} k_B^2 T_i T_j}{16 p m_{ij}^* Q_{ij}^{(1,1)} (T_{ij}^*)} \quad (6.24)$$

Here,  $T_i$  and  $T_j$  are temperatures of  $i^{\text{th}}$  and  $j^{\text{th}}$  particles respectively.  $T_{ij}^*$  and  $m_{ij}^*$  are effective temperature and effective mass respectively.

$p$  is pressure,  $Q_{ij}^{(1,1)}$  is the weighted average of gas kinetic cross-section over a Maxwellian distribution [91].  $k_B$  is the Boltzmann constant. Factor  $f_{ij}=1$  if  $i, j \neq e$ , and  $f_{ie}=f_{ei}=f(Z_i)$ ;  $f(1)=1.97$ ,  $f(2)=2.33$  and  $f(3)=2.53$  [90].

Once the temperatures are known, this diffusion coefficient can be computed directly using the above relation using already available  $Q_{ij}^{(1,1)}$  values from literature. For a seven species ( $N_2, N_2^+, N^+, N^{++}, N^{+++}, N, e$ ) nitrogen plasma there exist a total of forty nine BDCs.

First approximation to the general diffusion coefficient can be written as [86]:

$$D_{ij} = \frac{F^{ji} - F^{ii}}{m_j |F|} \quad (6.25)$$

where,  $F^{ij}$  is cofactor of  $F_{ij}$ , defined in terms of BDC ( $D_{ij}^b$ ) as [86]:

$$F_{ij} = \frac{1}{\rho} \left[ \frac{n_i}{D_{ij}^b} + \sum_{l \neq i} \frac{n_l m_j}{m_i D_{il}^b} \right] (1 - \delta_{ij}) \quad (6.26)$$

Thermal diffusion coefficients (TDC) of electrons are computed using third order approximation as [93]:

$$D_e^T = \frac{15 n_e^2 \sqrt{2 \pi m_e k_B T_e}}{4} \frac{\begin{vmatrix} q^{01} & q^{02} \\ q^{21} & q^{22} \end{vmatrix}}{\begin{vmatrix} q^{00} & q^{01} & q^{02} \\ q^{10} & q^{11} & q^{12} \\ q^{20} & q^{21} & q^{22} \end{vmatrix}} \quad (6.27)$$

TDC of heavy particles are computed using second order approximation the following relationships [93].

$$D_i^T = \frac{15 n_i \sqrt{2 \pi m_i k_B T_h}}{4} \begin{vmatrix} q_{jk}^{00} & q_{jk}^{01} & 0 \\ q_{jk}^{10} & q_{jk}^{11} & n_j \\ \delta_{ik} & 0 & 0 \end{vmatrix} \left( \begin{vmatrix} q_{jk}^{00} & q_{jk}^{01} \\ q_{jk}^{10} & q_{jk}^{11} \end{vmatrix} \right)^{-1} \quad (6.28)$$

The  $q_{ij}^{mp}$  elements in  $D_i^T$  and the elements in the determinants for  $D_e^T$  are computed in terms of average collision cross-sections as prescribed by Devoto [91]. Once these coefficients are known, the TADCs are calculated according to (6.23).

## Diffusion Coefficient Formalism for 2-T Plasma

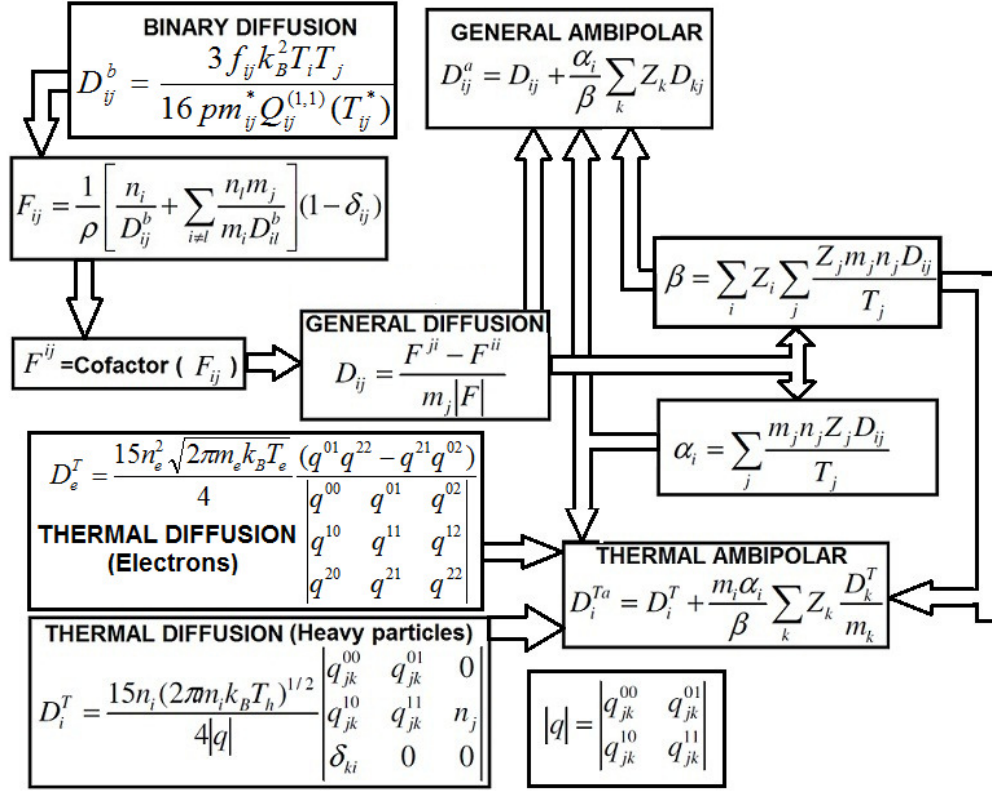


Fig . 6.3 Summary of the schemes used for computation of different diffusion coefficients under the framework of two-temperature non-equilibrium plasma.

### Thermal conductivity of electrons

The translational thermal conductivity of electrons in the third approximation is computed as [91]:

$$k_{tr,e} = \frac{75 n_e^2 k_B}{8} \left( \frac{2 \pi k_B T_e}{m_e} \right)^{1/2} \frac{1}{q^{11} - \frac{(q^{12})^2}{q^{22}}} \quad (6.29)$$

Expressions given by Devoto [91] for various  $q^{ij}$  elements in terms of collision cross-sections have been used in the computation.

### Thermal conductivity of heavy particles

Following Devoto [93], the translational thermal conductivity of heavy particles is computed as:

$$k_{tr,h} = -\frac{75k_B}{8} \frac{\sqrt{2\pi k_B T_h}}{|q|} \begin{vmatrix} q_{ij}^{00} & q_{ij}^{01} & 0 \\ q_{ij}^{10} & q_{ij}^{11} & n_i \\ 0 & n_j / \sqrt{m_j} & 0 \end{vmatrix} \quad (6.30)$$

The expressions for various  $q_{ij}^{(l,s)}$  elements in terms of collision cross-sections are available in Ref [93].

### Electrical conductivity

The electrical conductivity is computed in the third approximation in similar manner as prescribed by Devoto [91] as:

$$\sigma = \left( \frac{e^2 n m_e n_e}{\rho k_B T_e} \right) \left( \frac{3 n_e \rho}{2 n m_e} \right) \sqrt{\frac{2\pi k_B T_e}{m_e}} \begin{vmatrix} q^{11} & q^{12} \\ q^{21} & q^{22} \\ q^{00} & q^{01} & q^{02} \\ q^{10} & q^{11} & q^{12} \\ q^{20} & q^{21} & q^{22} \end{vmatrix} \quad (6.31)$$

where, 'e' is the electronic charge. The expressions for various  $q^{mn}$  elements in terms of collision cross-sections are available in Ref [91].

### Viscosity

Viscosity is computed using first approximation in the Sonine polynomial expansion as:

$$\mu = - \frac{5 \sqrt{2 \pi k_B T_h}}{2} \left| \begin{array}{c} \hat{q}_{ij}^{00} \\ n_j \end{array} \right| \begin{array}{c} n_j \sqrt{m_j} \\ 0 \end{array} \left| \left( \hat{q}_{ij}^{00} \right) \right|^{-1} \quad (6.32)$$

Associated elements of interest are computed in terms of cross-sections as given in Ref. [91]

### Reactive thermal conductivity of electrons and heavy particles

A formulation originally developed by Bose [94] has been used for computation of reactive thermal conductivities. A total of 5 reactions are involved in generation of the 7 species present. Species-r ( $r = 1$  to 5) is generated in the  $r^{\text{th}}$  reaction involving the species-6 (N) and species-7 (e). If  $\Delta h_r$  is the net change in enthalpy in the  $r^{\text{th}}$  reaction [Table-6.9], and  $\psi_r$  is the number flux vector of the  $r^{\text{th}}$  species, then the total reaction heat flux vector appears to be [86]:

$$q_R = - \sum_{r=1}^5 \Delta h_r \psi_r \quad (6.33)$$

where  $\psi_r$  is the particle flux vector. For a fixed total pressure, this can be written in terms of partial pressures ( $p_j$ ) and general ambipolar diffusion coefficients ( $D_{rj}^a$ ) as [86]:

$$\psi_r = \frac{n}{\rho k_B T_r} \sum_{j=1}^7 \frac{T_r}{T_j} m_j D_{rj}^a \nabla p_j \quad (6.34)$$

To estimate the contribution of reactive part alone, effect of temperature gradient and other external forces (except internal electric field) are neglected. Substituting (2.35) into (2.34), the total heat flux can be rewritten as:

$$q_R = - \left[ \sum_{r=1}^5 \Delta h_r \frac{n}{\rho k_B T_h} \sum_{j=1}^7 \frac{T_h}{T_j} m_j D_{rj}^a \frac{\partial p_j}{\partial T_e} \right] \nabla T_e - \left[ \sum_{r=1}^5 \Delta h_r \frac{n}{\rho k_B T_h} \sum_{j=1}^7 \frac{T_h}{T_j} m_j D_{rj}^a \frac{\partial p_j}{\partial T_h} \right] \nabla T_h \quad (6.35)$$

This has the form:  $q_R = k_{re} \cdot \nabla T_e + k_{rh} \cdot \nabla T_h$

The coefficient associated with  $\nabla T_e$  is defined as the reactive thermal conductivity of electrons and calculated as:

$$k_{re} = \sum_{r=1}^5 \Delta h_r \frac{n}{\rho k_B T_h} \sum_{j=1}^7 \frac{T_h}{T_j} m_j D_{rj}^a \frac{\partial p_j}{\partial T_e} \quad (6.36)$$

Similarly, the coefficient associated with  $\nabla T_h$  is defined as the reactive thermal conductivity of heavy particles and calculated as:

$$k_{rh} = \sum_{r=1}^5 \Delta h_r \frac{n}{\rho k_B T_h} \sum_{j=1}^7 \frac{T_h}{T_j} m_j D_{rj}^a \frac{\partial p_j}{\partial T_h} \quad (6.37)$$

The above definitions of reactive thermal conductivities enable easy separation of reactive contributions to plug into separate energy equations of electrons and heavy particles in the two-temperature CFD simulation.

To evaluate  $\partial p_j / \partial T_e$  and  $\partial p_j / \partial T_h$  terms appearing in the above equations, five reaction equations involved in generation of the plasma together with the equations for charge conservations, total pressure are considered. Taking logarithm of both side of these equations and then taking derivative with respect to  $T_e$ , 7 simultaneous algebraic equations are obtained in terms of  $\partial p_j / \partial T_e$  ( $j=1$  to  $7$ ). These equations are then solved to obtain the values of  $\partial p_j / \partial T_e$  terms. Similarly, derivative

of logarithm of these equations with respect to  $T_h$  provides the value of  $\partial p_j / \partial T_h$  terms.

**Table-6.9 The net change in enthalpy in different reactions**

Reaction No.	Change in Enthalpy	Expression
1	$\Delta h_1$	$\frac{3}{2}k_B T_h + 2k_B T_e^2 \frac{\partial \ln Q_{int}^A}{\partial T_e} - k_B \Theta_{vib} \left[ \frac{1}{2} + \exp\left(-\frac{\Theta_{vib}}{T_h}\right) \right] + E_d$
2	$\Delta h_2$	$-\frac{5}{2}k_B T_e + \frac{3}{2}k_B T_h + 2k_B T_e^2 \frac{\partial \ln Q_{int}^A}{\partial T_e} - k_B \Theta_{vib} \left[ \frac{1}{2} + \exp\left(-\frac{\Theta_{vib}}{T_h}\right) \right] - E_0 + E_d$
3	$\Delta h_3$	$-\frac{5}{2}k_B T_e + k_B T_e^2 \frac{\partial \ln Q_{int}^A}{\partial T_e} - k_B T_e^2 \frac{\partial \ln Q_{int}^I}{\partial T_e} - E_1$
4	$\Delta h_4$	$-5k_B T_e + k_B T_e^2 \frac{\partial \ln Q_{int}^A}{\partial T_e} - k_B T_e^2 \frac{\partial \ln Q_{int}^D}{\partial T_e} - (E_1 + E_2)$
5	$\Delta h_5$	$-\frac{15}{2}k_B T_e + k_B T_e^2 \frac{\partial \ln Q_{int}^A}{\partial T_e} - k_B T_e^2 \frac{\partial \ln Q_{int}^T}{\partial T_e} - (E_1 + E_2 + E_3)$

It may be noted that each of the two reactive conductivities defined above involve all species present. However, they are named after electrons and heavy particles because in the fluid dynamic equations, the first one appears in the electron energy equation and is associated with  $\nabla T_e$ , while the second one appears in the heavy particle energy equation and is associated with  $\nabla T_h$ . The reactive thermal conductivities are finally computed after evaluating the derivatives as described above.

### Chemical and thermal non-equilibrium:

Formalism similar to Ref.[55] has been used for study of thermodynamic and transport properties under chemical non-equilibrium. The conservation of the number density ( $n_k$ ) of species 'k' inside a plasma control volume reads as [95]:

$$\frac{\partial n_k}{\partial t} + \nabla \cdot (n_k \vec{u}) + \nabla \cdot \vec{g}_k = \dot{n}_k \quad (6.38)$$

$n_k \vec{u}$  is the convective flux and  $\vec{g}_k$  is the diffusive flux of species 'k'.

The diffusive flux can be written as [86]:

$$\vec{g}_k = \frac{n^2}{\rho} \sum_{j=1}^{\nu} m_j D_{kj}^a \left[ \nabla x_j + \left( x_j - \frac{\rho_j}{\rho} \right) \nabla \ln p \right] - \frac{n}{\rho} \sum_{j=1}^{\nu} \left( \frac{n_j Z_j e D_{kj}}{kT} \right) E^X - \frac{D_k^{aT}}{m_k} \nabla \ln T_k \quad (6.39)$$

$E^X$  is the external electric field,  $x_j$  is ratio of  $n_j$  to  $n$  and  $n$  is the total density. Equation (6.38) can be interpreted as a modified Saha equation including the effect of chemical non-equilibrium. To emphasize this fact we take the example of single ions for which the right side of equation (11(2.38)) appears as [95]:

$$\dot{n}_I = \alpha_I n_a \left[ S_2 - \frac{n_e n_I}{n_a} \right] \quad (6.40)$$

$S_2$  is the equilibrium rate constant of reaction-2 and  $\alpha_I$  is the recombination coefficients of ions. Equation (6.40) can now be written in the form:

$$\frac{n_e n_I}{n_a} = R_2 = S_2 - \Delta S_2 \quad (6.41)$$

This is similar to usual Saha equation but now takes into account chemical non-equilibrium through  $\Delta S_2$ .  $R_2$  is the ultimate rate constant for respective reaction (atom to ion formation in this case).

$$\Delta S_2 = \frac{1}{\alpha_i n_a} [\nabla \cdot (n_i \vec{u}) + \nabla \cdot \vec{g}_i] \quad (6.42)$$

In similar ways different rate constants  $R_i$ , equilibrium rates  $S_i$  and corresponding non-equilibrium contributions  $\Delta S_i$  can be obtained for  $i^{\text{th}}$  associated reaction.

Like temperature non-equilibrium parameter  $\theta$ , a chemical non-equilibrium parameter  $c_i$  can now be introduced to identify the exact effect of existing chemical non-equilibrium for the  $i^{\text{th}}$  associated reaction and corresponding influence on the estimated properties:

$$c_i = \frac{S_i - \Delta S_i}{S_i} \quad (6.43)$$

Under different pressures and thermal non-equilibria, results are presented with different regimes of chemical non-equilibrium parameters ' $c_i$ ' as well.

#### **6.4. Results and discussion**

Thermodynamic and transport properties, computed following the above formalism are presented in the following. The values of thermal non-equilibrium parameter  $\theta$  are chosen in a manner that clarity of presentation and ranges of interest are maintained. Highest value of  $\theta$  is limited to 20. Results are presented for pressure values: 0.1, 1.0, 4.0 and 7.0 atmospheres. Selected highest and lowest pressure values are close to respectively upstream and downstream pressures inside of typical arc plasma torches.

It is expected that  $0.5 < c_i < 2.0$  covers most of the practical cases of interest and results of chemical non-equilibriums are presented accordingly. The presence of dissociative reactions at lower temperatures makes some of the properties distinctly different from those of monatomic gasses. Thermodynamic properties are presented first. Transport properties are presented next. An extensive comparison of the obtained thermodynamic and transport properties with experimental and other theoretical results is presented after that. Results with chemical non-equilibrium are presented at the last. Numbers associated with the curves in the figures correspond to respective thermal non-equilibrium parameter ( $\theta$ ). Results presented up to Figure 6.27 assume  $c_i=1$  for all reactions. Figure 6.28 to Figure 6.31 include results with  $c_i \neq 1$  as well.

Variation of composition of atmospheric pressure nitrogen plasma as a function of electron temperature and thermal non-equilibrium is presented in Figure 6.4. The same for total number density as a function of pressure is presented in Figure 6.5. It may be pointed out that total number density is independent of  $\theta$ , although number density of individual species depends on it. Total number density together with associated mole fraction value may be used to obtain the actual density of individual species at a given temperature, pressure and thermal non-equilibrium. For higher thermal non-equilibrium, as the molecule gets dissociated to form atoms, availability of high electron temperature immediately ionizes them. Observed negligible atom density at higher  $\theta$  is a consequence of that.

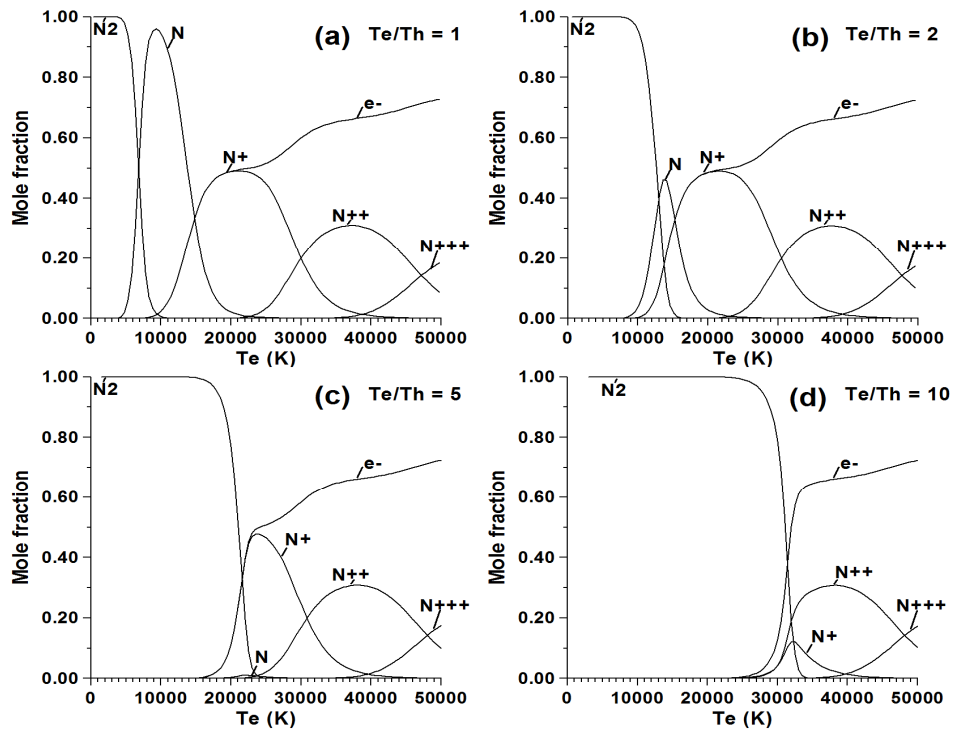


Fig. 6.4 Mole fraction of different species in nitrogen plasmas under different degrees of non-equilibrium at atmospheric pressure: (a)  $T_e/T_h=1$ , (b)  $T_e/T_h=2$ , (c)  $T_e/T_h=5$ , (d)  $T_e/T_h=10$ .

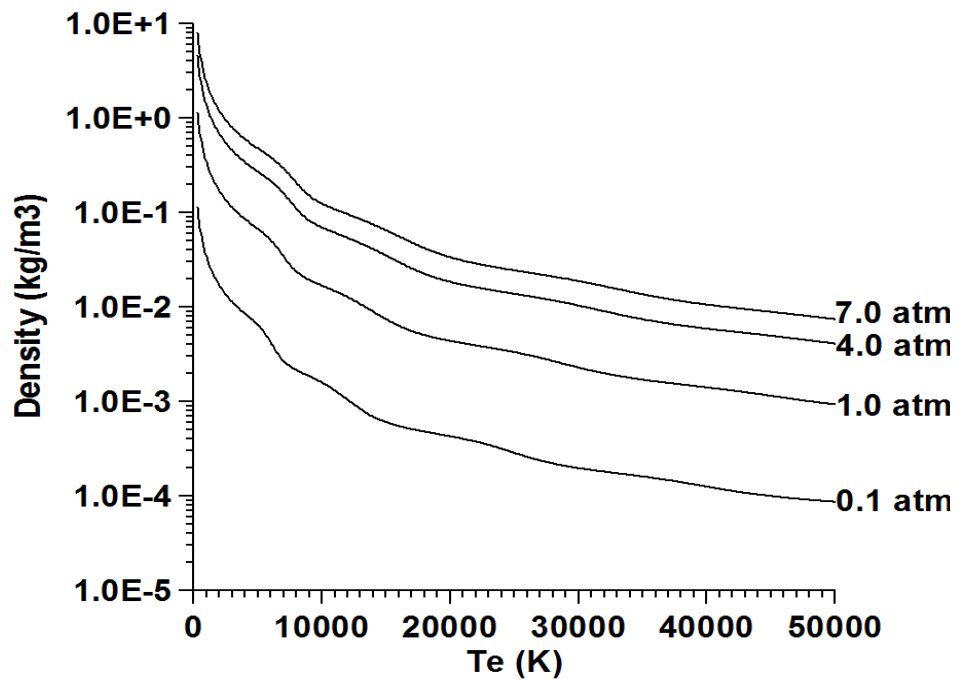
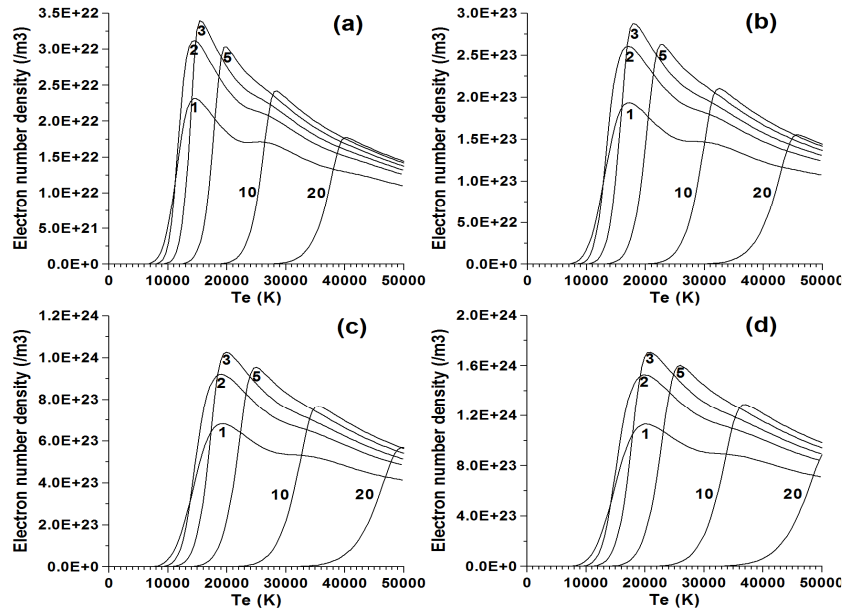


Fig. 6.5 Variation of density as a function of electron temperature with pressure as parameter

Figure 6.6 presents the variation of electron number density with  $p$ ,  $T_e$  and  $\theta$ . Although, there is a strong dependence on pressure, the trend of variation of electron density with  $\theta$  remains nearly similar for all pressures in the pressure range considered. For a given pressure, the peak in the electron density first increases with increase in  $\theta$  and then inherits a decreasing trend with increasing  $\theta$  for higher  $\theta$  values. For a given electron temperature as  $\theta$  increases, the temperature of the heavy species decreases and so does the partial pressure exerted by them. As total pressure is assumed constant, this induces an enhancement in the partial pressure of the electrons through increase in their number density. This is what is observed in Figure 6.6 for lower  $\theta$  values. However, if  $\theta$  is high enough, the realized  $T_h$  for a given  $T_e$  may not be sufficient to cause dissociation of  $N_2$  molecule. In such situations, the peaks in the electron density shift towards higher  $T_e$  values as  $\theta$  increases. However, if  $T_e$  increases, electron density must decrease, as total pressure is constant. Observed reducing peak heights of electron density at higher  $\theta$  values are consequences of this.

Variation of total enthalpy as a function of  $p$ ,  $T_e$  and  $\theta$  are presented in Figure 6.7. Unless some reactions (like dissociation, first ionization, second ionization etc.) are involved, the enthalpy increases almost linearly with  $T_e$ . Observed shifting of the enthalpy-temperature curves with increase in  $\theta$  may be explained in similar manner as above. For a given  $T_e$  and  $\theta$ , as pressure increases, average energy per particles decreases resulting in relatively lower heat content per unit mass of the plasma at higher pressure. Observed decrease in enthalpy with increase in pressure for a given  $T_e$  and  $\theta$  may be explained from this.



**Fig. 6.6 Electron number density variation: (a) 0.1 atmosphere, (b) 1 atmosphere, (c) 4 atmospheres, (d) 7 atmospheres. Number associated with each curve indicates  $T_e/T_h$  ratio.**

Specific heat at constant pressure ( $c_p$ ) for electrons and heavy particles as a function of  $p$ ,  $T_e$  and  $\theta$  are derived from derivatives of the respective enthalpy variation with respect to  $T_e$  and  $T_h$  and presented in Fig. 6.8 and Fig. 6.9 respectively. Steeper variations in enthalpy with respect to temperature for higher  $\theta$  result in the higher peaks of the specific heat values.

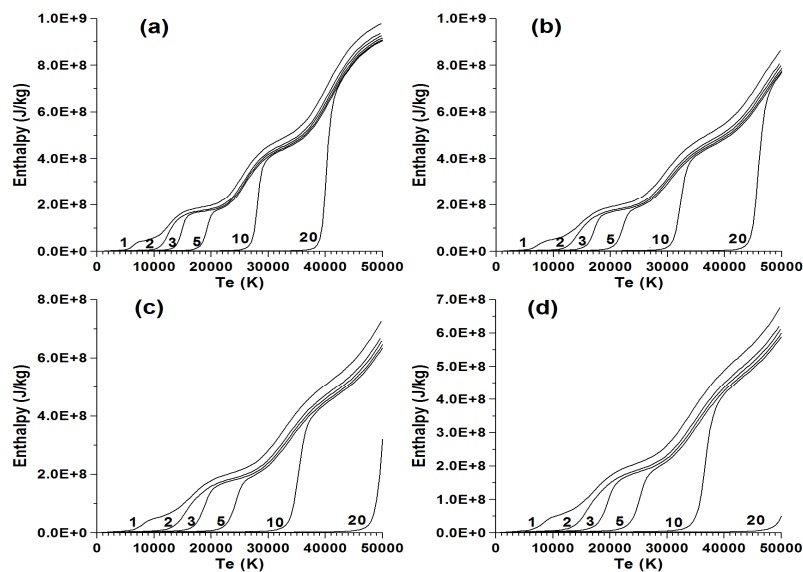


**Fig. 6.7 Total enthalpy variation: (a) 0.1 atmosphere, (b) 1 atmosphere, (c) 4 atmospheres, (d) 7 atmospheres. Number associated with each curve indicates  $T_e/T_h$  ratio.**

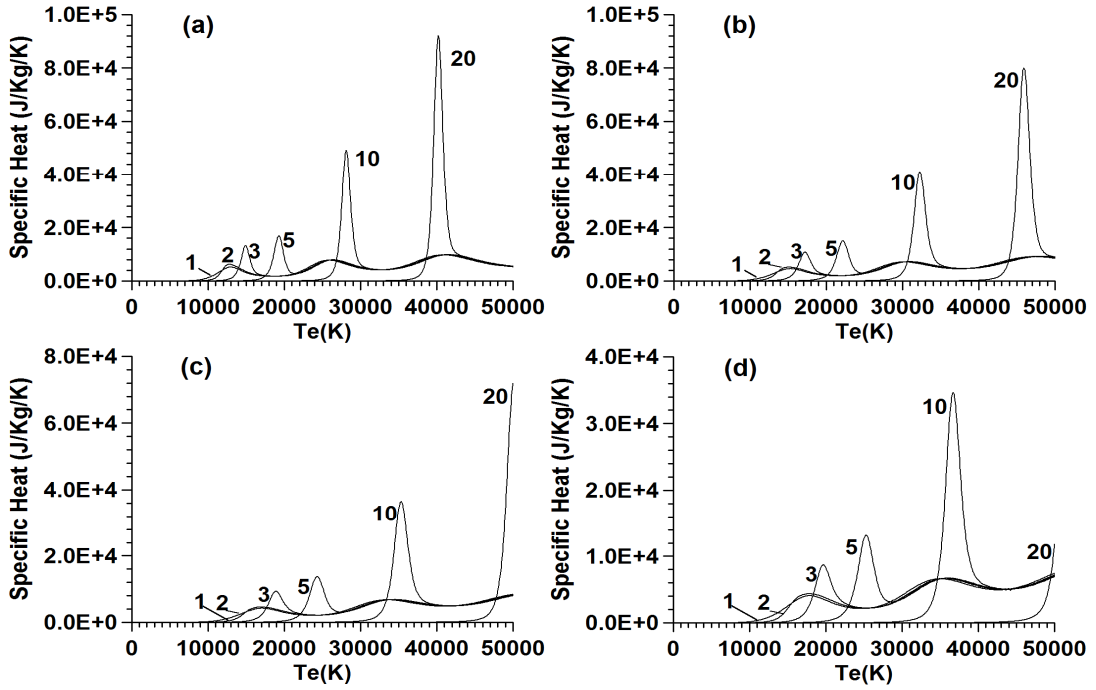


**Fig. 6.8** Variation of specific heat ( $c_p$ ) of electrons as a function of temperature: (a) 0.1 atmosphere, (b) 1 atmospheres, (c) 4 atmospheres, (d) 7 atmospheres. Number associated with each curve indicates  $T_e/T_h$  ratio.

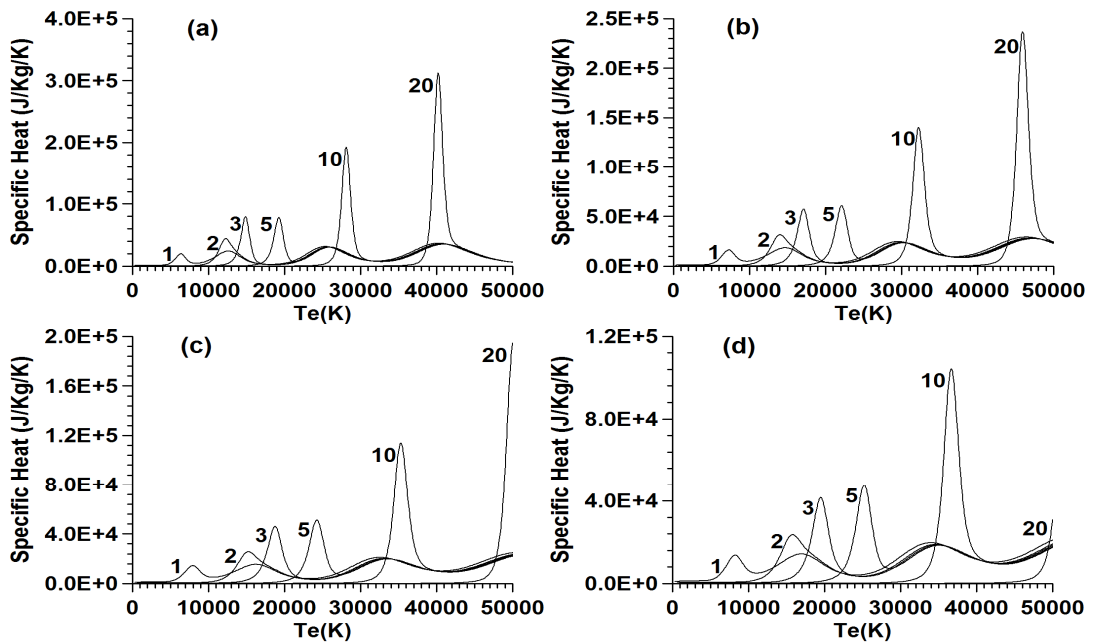


**Figure 6.9** Variation of specific heat of heavy particles as a function of temperature: (a) 0.1 atmosphere (b) 1 atmosphere, (c) 4 atmospheres, (d) 7 atmospheres. Number associated with each curve indicates  $T_e/T_h$  ratio.

## Results (DFC)

A systematic study of relevant diffusion coefficients, discussed in the previous sections, is presented here. A system containing large number of species associates too many diffusion coefficients and often it becomes impractical to present all of their behaviour as a function of temperature and pressure in a concise elegant form [50]. The task becomes further difficult as one attaches degree of thermal non-equilibrium as additional influencing parameter for systems under non-equilibrium. Nevertheless, the study of behaviour of each of these diffusion coefficients is very much important to understand the way they influence a particular reaction in a specific zone of processing plasma at a particular pressure, temperature and non-equilibrium. The diffusion coefficient data for binary diffusion coefficients (BDC), general diffusion coefficient (GDC), and general ambipolar diffusion coefficients (GADC) are presented for atmospheric pressure only. The results will help us to understand the nature of diffusion processes in wide range of processing plasmas that operate around atmospheric pressure. While ambipolar diffusion coefficients are the most relevant ones for the systems under plasma state, both BDC and GDC are presented in this study for clear identification of the effect of the ambipolar contribution in the associated diffusion processes. Considering lesser volume of data, behaviour of TDC and TADC as a function of electron temperature is presented for three different pressures: 0.1 atm, 1 atm and 2 atm. To maintain reasonable clarity of the graphical presentation, the thermal non-equilibrium parameter is varied only from 1 to 5 in all the graphs.

## Binary Diffusion Coefficients

Binary diffusion coefficient for atmospheric pressure nitrogen plasma as a function of electron temperature is presented in Figure 6.10 under different degrees of thermal non-equilibrium. For the considered system, a total of 49 diffusion coefficients arise. However, as  $D_{ij}^b = D_{ji}^b$ , only 28 BDC, as presented in figure 6.10 are of interest. In general, the coefficients exhibit an exponential rise with increase in electron temperature and for a given electron temperature and pressure, the coefficient values decrease with increase in thermal non-equilibrium. The self-diffusion coefficient of electrons exhibits very weak dependence on thermal non-equilibrium and the BDC involving heavy species are at least an order of magnitude lower than the same involving heavy species and electrons. For the considered system, the highest self-diffusion coefficient is observed for electrons. Among heavy species, the atoms exhibit higher self-diffusion compared to the molecules. For interactions involving ionic species, relevant self-diffusion coefficient decreases as the charge state increases.

Binary diffusion coefficients are independent of the species composition. Nearly parabolic dependence of the BDCs on the electron temperature arises from the fact that the coefficient values depend on the product of temperature of the associated species. For a given electron temperature, an increase in the thermal non-equilibrium corresponds to a decrease in the heavy species temperature. Observed decrease in the BDC values involving heavy species with increase in thermal non-equilibrium results from this. For the same reason, the BDCs for self diffusion of electrons exhibit almost no dependence on the thermal non-equilibrium.

## General Diffusion Coefficients (GDC)

The temperature dependence of GDC at atmospheric pressure under different thermal non-equilibriums is presented in figure 6.11. To restrict the volume of data, only some illustrative examples of the GDCs are presented here. However, considering the fact that GADC data can be directly used for 2-T CFD simulation, the complete set of data for GADC derived from these GDCs are presented in Fig. 6.12. Features observed for GDCs are automatically inherited by GADCs. By definition, the GDC involving identical species are zero. In general,  $D_{ij} \neq D_{ji}$ . For  $i \neq j$ , the coefficients exhibit nearly zero values at lower temperatures, positive values at higher temperatures and decrease with increase in thermal non-equilibrium. Appreciably higher general diffusion coefficient values are observed when diffusion involves electron as one of the participants. For diffusion of nitrogen molecules into species other than electrons, the coefficients exhibit nearly similar behaviour. However, for diffusion into electrons, the coefficient values are several orders of magnitude higher [Fig. 6.11(a)].

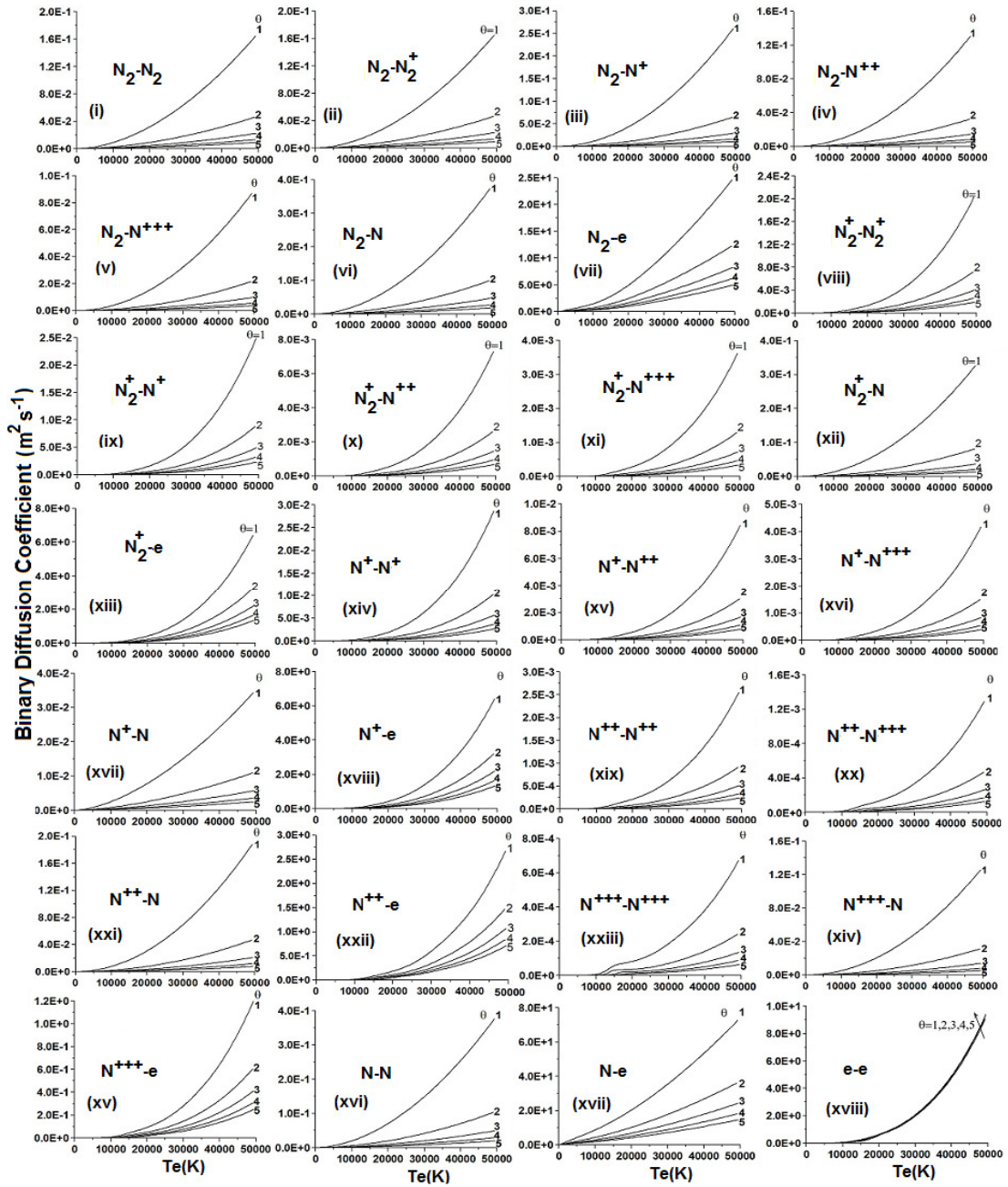


**Fig. 6.10** Variation of binary diffusion coefficients (BDC) of the considered species in nitrogen plasma as a function of electron temperature at P=1 atm.

The GDCs of molecular ions exhibit the largest peak near 10000K and a relatively weaker peak around 26000K in the considered temperature range [Fig. 6.11(b)]. Except for electrons and molecules, the behaviour does not change much with change in the other diffusing species. The coefficient values are significantly higher for diffusion into electrons. Although, positions of the peaks do not have strong dependence on the thermal non-equilibrium, the coefficient values have. They exhibit a strong nonlinear decrease with increase in degree of non-equilibrium.

The GDCs for singly ionized nitrogen exhibit appreciable dependence on the degree of thermal non-equilibrium as well as the diffusing species. The trend of behaviour itself is markedly different as the participating species differ. For diffusion into molecules, after certain temperature, the coefficient values increase with increase in temperature, reach a peak near 26000 K and then decrease [Fig. 6.11 (c)]. The position of this peak on temperature axis is nearly independent of the degree of thermal non-equilibrium. However, the peak height decreases fast with increase in thermal non-equilibrium. Position of a tiny peak noticed at lower temperature, has strong dependence on the degree of thermal non-equilibrium. For diffusion into molecular ion, the coefficients exhibit two distinct peaks at two different temperatures. Interestingly, while the first peak appreciably shifts towards higher temperature zone with increase in non-equilibrium, the second peak is fairly insensitive to it. Heights of the peaks decrease with increase in non-equilibrium. For diffusion into nitrogen atoms, the GDC again exhibits two peaks. Position of the peak occurring at lower temperature is sensitive to thermal non-equilibrium. But the peak at higher temperature is fairly insensitive to it. Observation of large peak at higher temperature for  $\theta=1$  is a significant observation for GDC involving  $N^+$  and  $N$  [Fig.

6.11(d)]. For diffusion into double ions, triple ions and electrons, the coefficients first increase with increase in temperature, reach a peak at certain temperature and then decreases [Fig. 6.11(e)]. With further increase in temperature, the coefficient values again increase with increase in temperature. Height of the associated peaks significantly reduces with increase in thermal non-equilibrium. For diffusion involving electrons, values of the coefficients are several orders of magnitude higher compared to others.

The GDC for diffusion of double ions into atoms is presented in Fig. 6.11(f). Nearly similar features are observed for diffusion into molecules and atoms. A relatively small peak at lower temperature, a large peak at higher temperature at every non-equilibrium and decreasing peak values with increasing thermal non-equilibrium are some of the major features observed. Diffusion of double ions into molecular ion and single ion also exhibit similar features. When plotted as a function of temperature, the coefficients exhibit two peaks for every non-equilibrium: one at lower temperature and the other at higher temperature. The first peak shifts towards higher temperature and diminishes in height as the degree of non-equilibrium increases. However, the second peak remains mostly unchanged in position but decreases in height for the same. The coefficients for diffusion of double ions into triple ions and electrons also exhibit similar features. After exhibiting two peaks at relatively lower temperatures, the coefficients again start increasing with further increase in temperature. The first peak remains higher than the second peak for every non-equilibrium and shifts its position towards higher temperature as well as diminishes in height as non-equilibrium increases.

For the molecules and atoms as diffusing species, the coefficients for diffusion of triple ions exhibit extremely small values below 35000K followed by a sudden increase. For diffusion of triple ions into molecular ion, single ion and double ion, the coefficients exhibit nearly similar trends of behaviour. A peak at lower temperature, followed by a plateau and a sharp rising section are the typical features exhibited by these coefficients [Fig 6.11(g)]. For diffusion into electrons, the coefficient values are significantly higher. After the peak at lower temperature, an elongated plateau region is observed.

Almost identical trends are observed for the diffusion of nitrogen atom into rest of the species [Fig. 6.11(h)]. Non-equilibrium dependent relatively smaller peak at lower temperature, followed by a plateau and a sharp rising region are the typical features of these coefficients. Like other cases, the coefficients involving electrons are several orders of magnitude higher.

For diffusion of electrons into rest of the species, the GDCs exhibit nearly similar behaviour [Fig. 6.11(i)]. Initially, the coefficients increase with increase in temperature, reach a peak at certain temperature and then decrease. After reaching a minimum the coefficients again start increasing with increase in temperature. Other than  $\theta=1$ , the peak heights are comparable. While for a given non-equilibrium, the coefficients for different diffusing species are of the same order of magnitude, the coefficients involving molecules and molecular ions exhibit slightly lower values compared to the rest.

Unlike binary diffusion coefficients, the GDCs depend on species composition. The GDCs have the tendency to inherit the feature of increasing coefficient values with increase in temperature similar to the binary diffusion

coefficients, wherefrom they are derived. However, due to dependencies on the species, GDC involving any two specific species exhibit peaks at regions where associated species densities exhibit a peak. For example, the associated peak near 8000K for GDCs involving  $N_2^+$  occurs as  $N_2^+$  density peaks at this temperature [Fig. 6.11 (b)]. Similarly, the peak near 12000K for GDC involving N and  $N_2$  [Fig. 4 (h) (6.11(h))] and the peak near 42000K for GDC involving  $N^{++}$  and N [Fig. 6.11(f)] occur as respectively nitrogen atom and double ion densities reach a peak at those temperatures. However, the ultimate behaviour and the position of the observed peaks in the GDC at a given pressure are decided by the dominating species densities together with the modulation imposed by the overall mass density that reduces with increase in temperature and the relevant values of the binary diffusion coefficients which increases for the same. Relatively smaller peak observed around 26000K in many of the GDCs mainly owes to the contribution from the high population of singly ionized nitrogen ions at this temperature. Lower rest mass and higher mobility of the electrons compared to rest of the species result in the significantly higher GDCs for cases involving electrons.

### **General Ambipolar Diffusion Coefficients (GADC)**

A total of 49 GADC, presented in Fig. 6.12 (a)-(r), Fig. 6.13 (a)-(r) and, Fig. 6.14 (a)-(m), are derived from respective GDC through the formalism described in section-II. While the GDCs are zero for diffusion between identical species, the GADCs are not so because of the presence of the nonzero second term in equation (6.22) [Fig. 6.12 (a,i,q), Fig. 6.13 (g,o), Fig. 6.14 (e,m)]. Although, ambipolar effects

originate due to presence of charge particles, by definition, non-zero ambipolar diffusion coefficients are possible for neutral particles as well. In such cases, the ambipolar diffusion coefficients are same as the GDC owing to zero contribution from ambipolar effects. When compared with respective GDC, the ambipolar contribution can be directly estimated from the data presented in respective cases. As these coefficients are based on the GDC, the trends of behaviour observed here are automatically inherited in respective cases. Pronounced ambipolar effects are observed for cases involving diffusion of electrons into other species [Fig. 6.14 (g)-(m)]. The effect reduces the coefficient values by at least an order of magnitude.

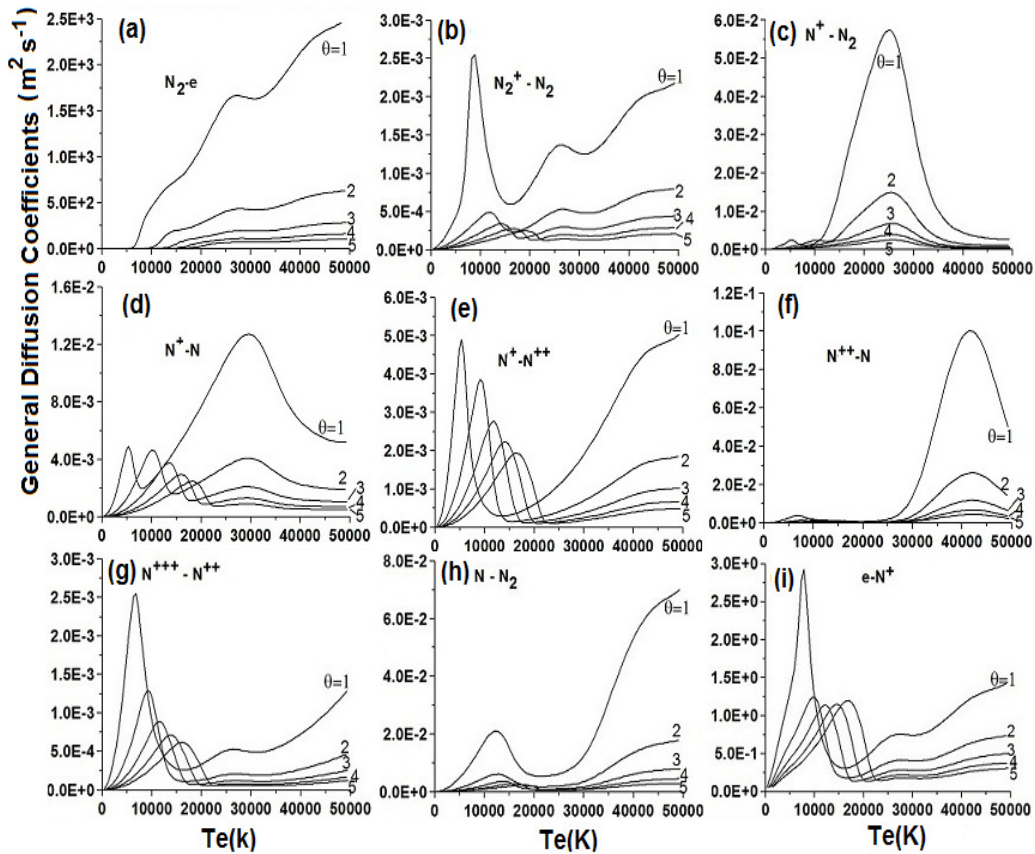


**Fig. 6.11 Behaviour of selected general diffusion coefficients (GDC) as a function of electron temperature and thermal non-equilibrium at P=1 atm.**

## Thermal Diffusion Coefficients (TDC)

Markedly different features, observed for TDC, are presented in Fig. 6.15. While the BDC are always either zero or positive, the TDC are found to be positive, zero as well as negative. Unlike BDC, the trend is different for different species. The coefficients for molecular nitrogen always exhibit positive values that increase with increase in pressure and decrease with increase in thermal non-equilibrium [Fig. 6.15 (a), (h), (o)]. The coefficient values initially increase, reach a peak at certain temperature and then decrease with further increase in temperature. Associated peaks shift towards higher temperature with increase in thermal non-equilibrium.

Compared to molecules, the coefficient values for molecular ions are extremely small (mostly zero or negative) [Fig. 6.15 (b), (i), (p)]. For singly charged ions, the TDC are again found to be either zero or positive. However, unlike molecules, two peaks are observed at two different temperatures which shift towards higher temperatures with increase in pressure and decrease in values with increase in thermal non-equilibrium [Fig. 6.15 (c), (j), (q)]. For double ions, the thermal diffusion coefficient values exhibit zero, negative as well as positive values. The coefficient values are close to zero at lower temperature, exhibit negative coefficient values after that and then become positive as temperature increases further [Fig. 6.15 (d),(k),(r)]. Notably, for a given pressure, the transition from negative to positive occurs at a particular electron temperature, irrespective of the degree of thermal non-equilibrium. Observed negative diffusion coefficients are of special importance as they can lead to self-constriction in plasma. Similar to other species, the peaks in the TDC shift towards higher electron temperature as pressure increases. However, for a given pressure, the electron temperature at which the peaks in the TDC occur, are not very

sensitive to degree of thermal non-equilibrium. For triple ions the thermal diffusion coefficient is either zero or negative in the range of temperatures investigated [Fig. 6.15 (e), (l), (s)]. At lower temperature, the value is close to zero. As temperature increases, the coefficients become more and more negative and reach a peak at certain temperature. For a given pressure, higher the thermal non-equilibrium lesser is the negative peak height. However, the electron temperatures at which the negative peaks occur are again almost independent of the existing thermal non-equilibrium. The TDC of nitrogen atoms exhibit either zero or negative values [Fig. 6.15 (f), (m), (t)]. For  $\theta=1$ , it exhibits two peaks. However, for  $\theta \geq 2$  only one peak is observed. For a given pressure, as  $\theta$  increases the coefficient values decrease. For  $\theta > 3$ , the coefficient values are very close to zero. Variation in pressure does not have significant impact on the coefficient values and peak positions. The TDC of the electrons are found to be close to zero at lower temperatures and positive at higher temperatures [Fig. 6.15 (g), (n), (u)]. With increase in electron temperature, the coefficient values increase. The rate of increase is higher at higher pressures. While at lower temperatures, the coefficient values decrease significantly with increase in thermal non-equilibrium, at higher temperatures they are very weakly sensitive on it.

Similar to general diffusion coefficients, TDCs also depend on species composition. For any particular species, the TDC is zero when its population is zero. For non-zero population, the associated TDC is determined by the population together with the collisional interactions with the other species and the nature of the interactions. The later is contained in the determinants involving associated collision integrals in the expression for TDC in eq. (2.28). The negative thermal diffusion coefficients, observed in N,  $N_2^+$  and  $N^{++}$ , are intrinsic to the collisional characteristics

of the respective species in the evolved species environment. The ratio of the determinants in the expression for TDC goes negative resulting in the negative diffusion coefficients observed in these cases. The observation of two peaks in the TDCs for N (for  $T_e/T_h = 1$ ) results from the fact that with increase in temperature,  $N_2$  dissociates to form N and the TDC (negative) for N start increasing. However, after some temperature, further increase in the population of N reduces the negative TDC value causing a minimum near 10,000K, where the population of N atom reaches a maximum. With further increase in the temperature, the population of N atoms reduces through ionization forming  $N^+$  and the negative TDC starts increasing again forming the second peak. In the same manner, as associated TDC reaches a minimum near 22000K where  $N^+$  density reaches a maximum, the two peaks occur in the TDC of  $N^+$ . The resonant charge transfer plays important role in reducing the diffusion involving neutral and charged species. With variation in the thermal non-equilibrium, behaviour of the peaks changes due to shifting of the position of the minima on the  $T_e$  axis. Higher mobility of the electrons results in the observed higher TDCs values for cases involving electrons.

### **Thermal Ambipolar Diffusion Coefficients (TADC)**

TADC for nitrogen plasma under different pressure, temperature and thermal non-equilibrium are presented in Fig. 6.16 (a)-(u). The coefficients are obtained by adding ambipolar contribution to respective TDC as described by equation (6.23). Unlike GADCs, the TADCs are appreciably changed by ambipolar effects. For nitrogen molecules, the coefficients are close to zero but positive at low temperature,

increases with increase in temperature, reaches a peak at certain temperature and then decreases with further increase in temperature. Unlike TDC, the TADC for molecules become negative as temperature increases further [Fig. 6.16 (a)]. Similar negative TADC at higher temperature are observed for other species as well [Fig. 6.16 (b)-(g)]. The observation is important in the sense that enhanced negative TDC caused by ambipolar effect may result in self-constriction, an important phenomenon, affecting ranges of thermal and fluid dynamic behaviour in plasma. For molecular ions, the coefficients are close to zero at lower temperature but become more and more negative as temperature increases [Fig. 6.16 (b)]. The nitrogen ions exhibit only positive coefficients for  $\theta = 1$ . However, for higher non-equilibrium, positive to negative transition takes place at certain temperature and the coefficients remain negative for further higher temperatures. For double ions, the coefficients switch from positive to negative to positive values, depending the temperature of the plasma. The coefficients are close to zero but positive at lower temperatures, become negative after that, then again become positive after certain temperature and may again become negative or remain as positive depending on the degree of non-equilibrium. For triple ions the TADC are always positive for  $\theta = 1$ . However, for higher non-equilibrium, the coefficients are initially positive but close to zero, then goes negative at higher temperatures. The nitrogen atoms exhibit negative TADC with two peaks for  $\theta = 1$ . For higher non-equilibrium, only one peak is observed. The TADC for electrons are substantially different from respective TDC due to ambipolar effects. Apart from variation in the coefficient values, nearly similar behaviour is observed at other pressures studied.

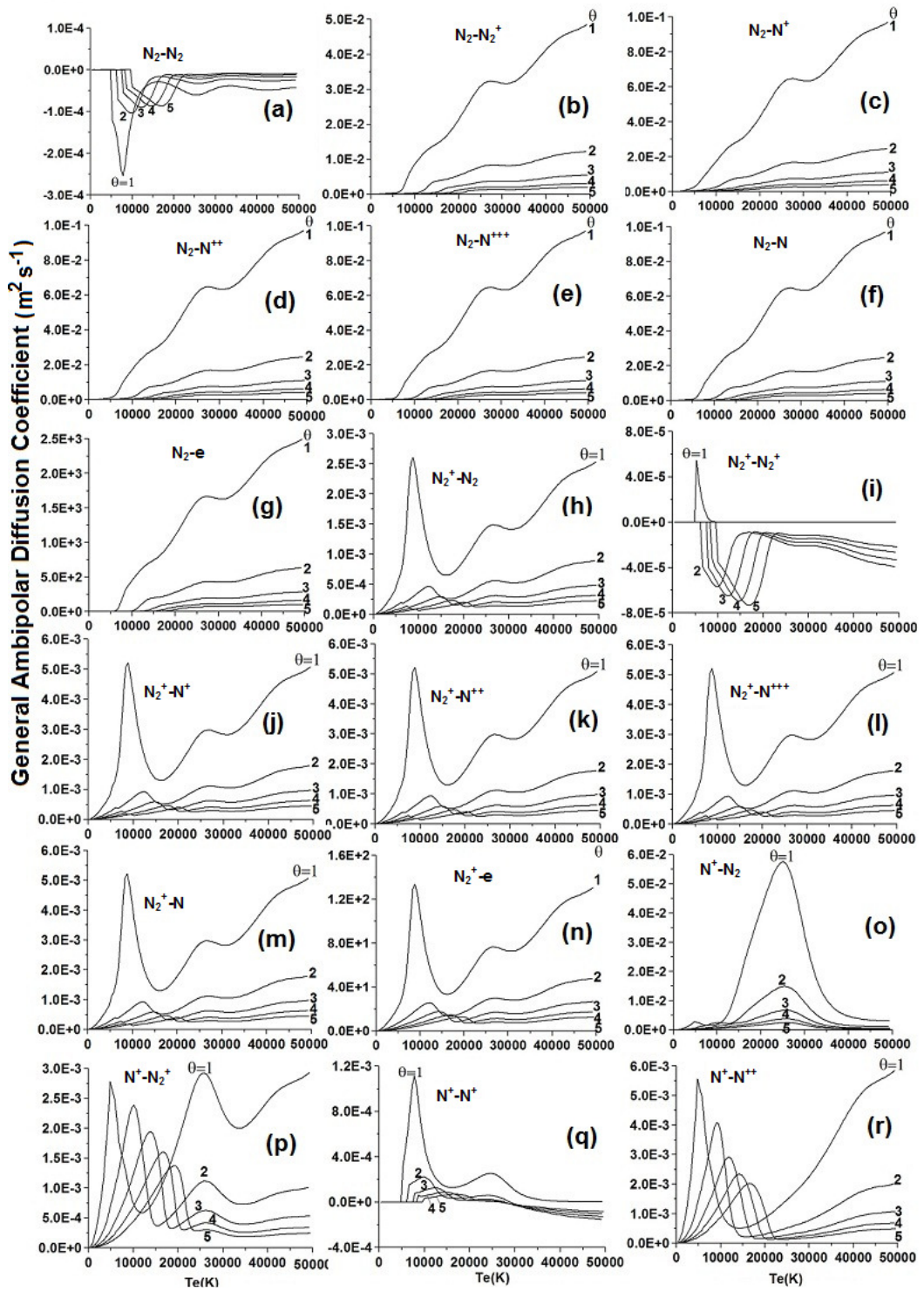


**Fig. 6.12** Behaviour of general ambipolar diffusion coefficients (GADC) as a function of electron temperature and thermal non-equilibrium at P=1 atm.

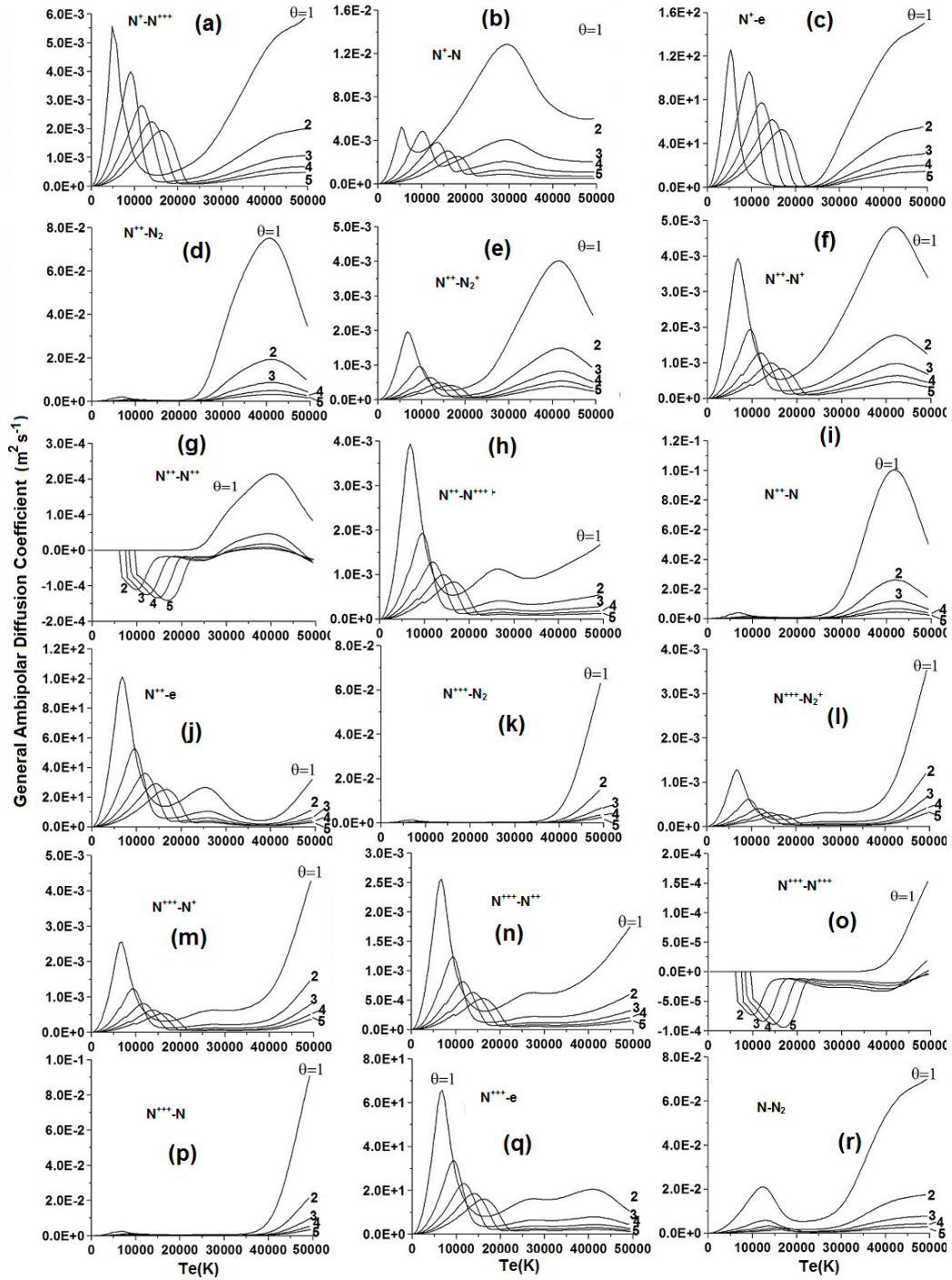


**Fig. 6.13 Behaviour of general ambipolar diffusion coefficients (GADC) as a function of electron temperature and thermal non-equilibrium at P=1 atm.(continued)**

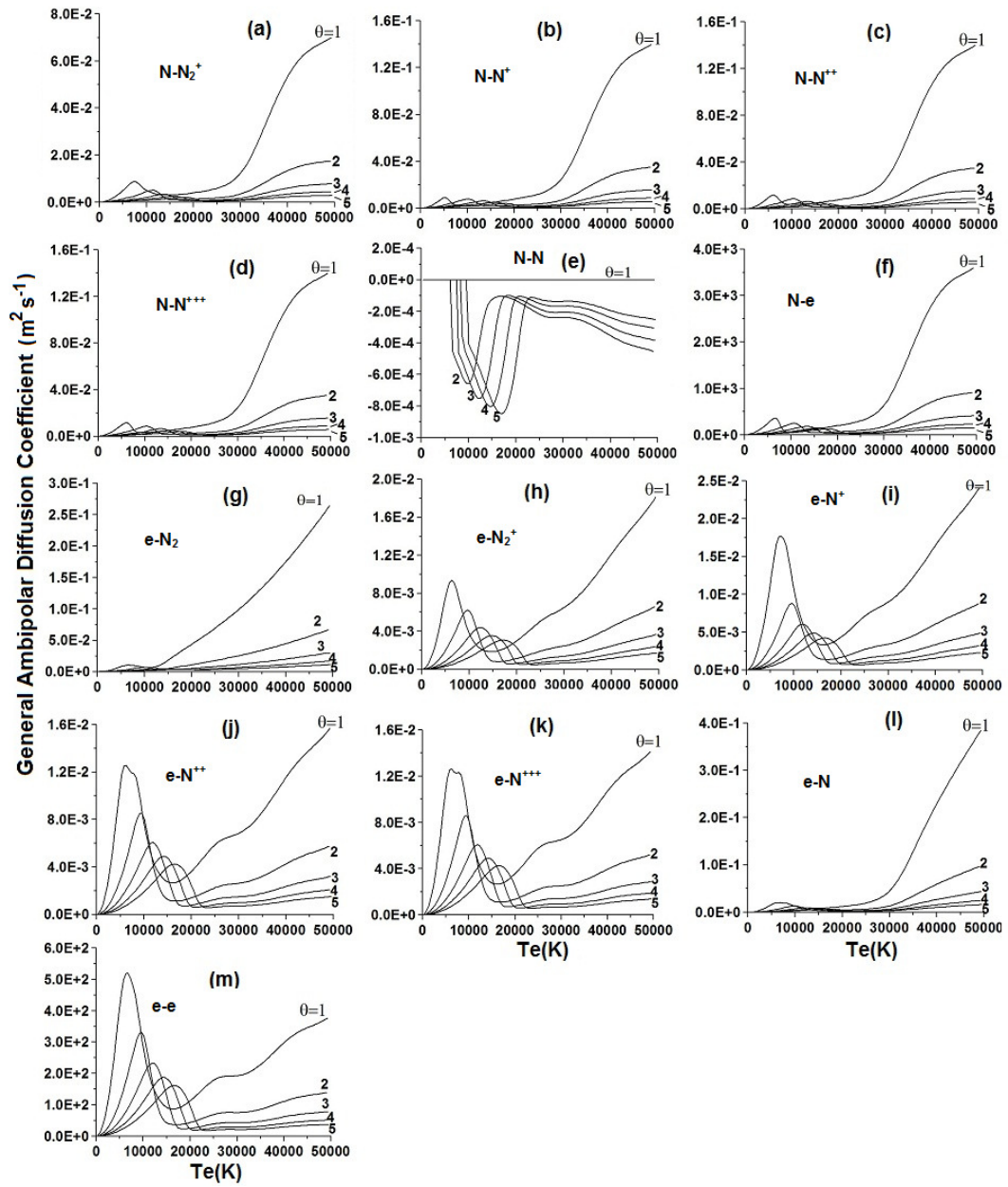


**Fig. 6.14** Behaviour of general ambipolar diffusion coefficients (GADC) as a function of electron temperature and thermal non-equilibrium at P=1 atm.

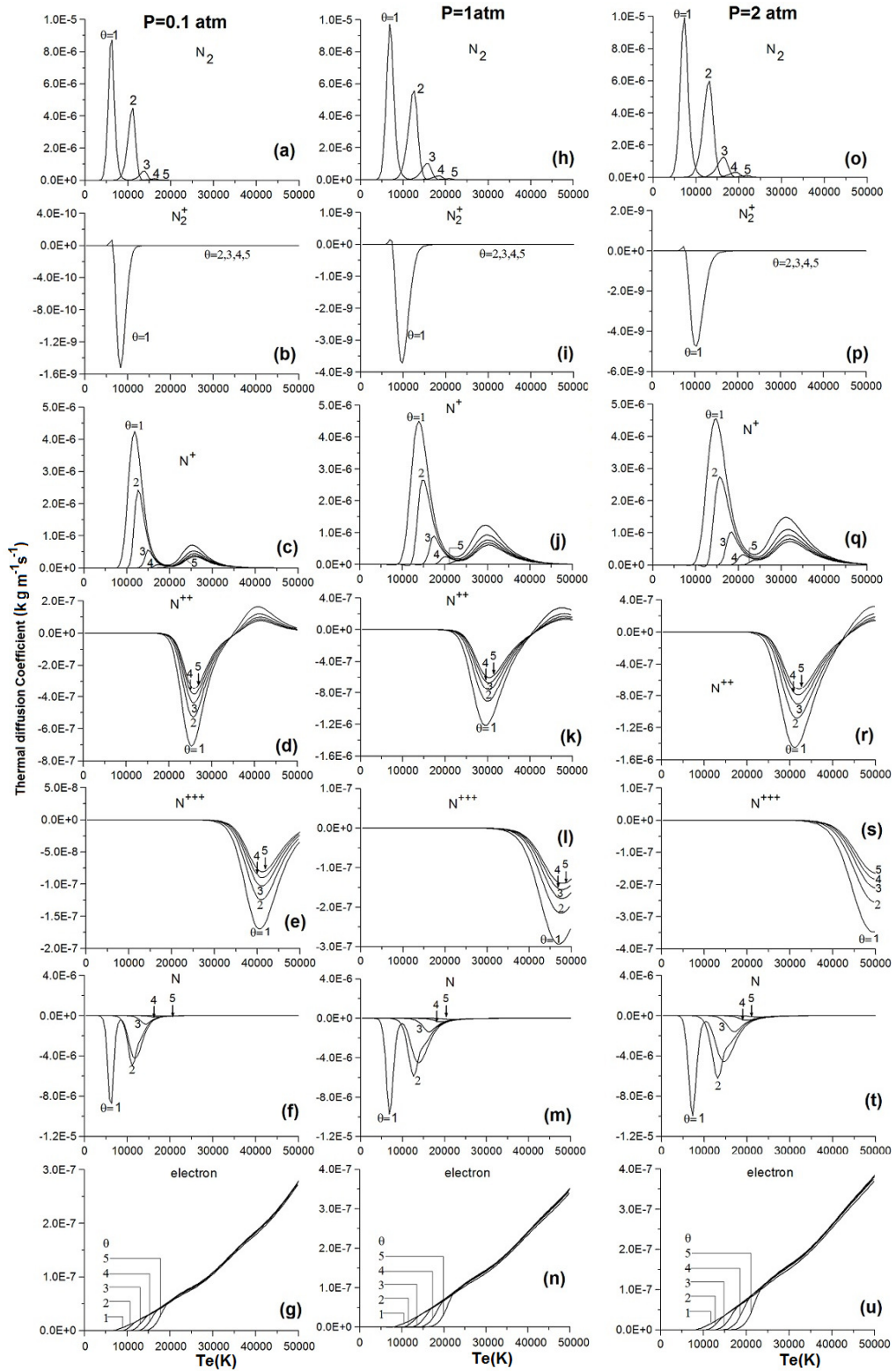


**Fig. 6.15** Variation of thermal diffusion coefficients (TDC) of different species in nitrogen plasma as a function of electron temperature at three different pressures: 0.1 Atm, 1 atm and 2 atm.

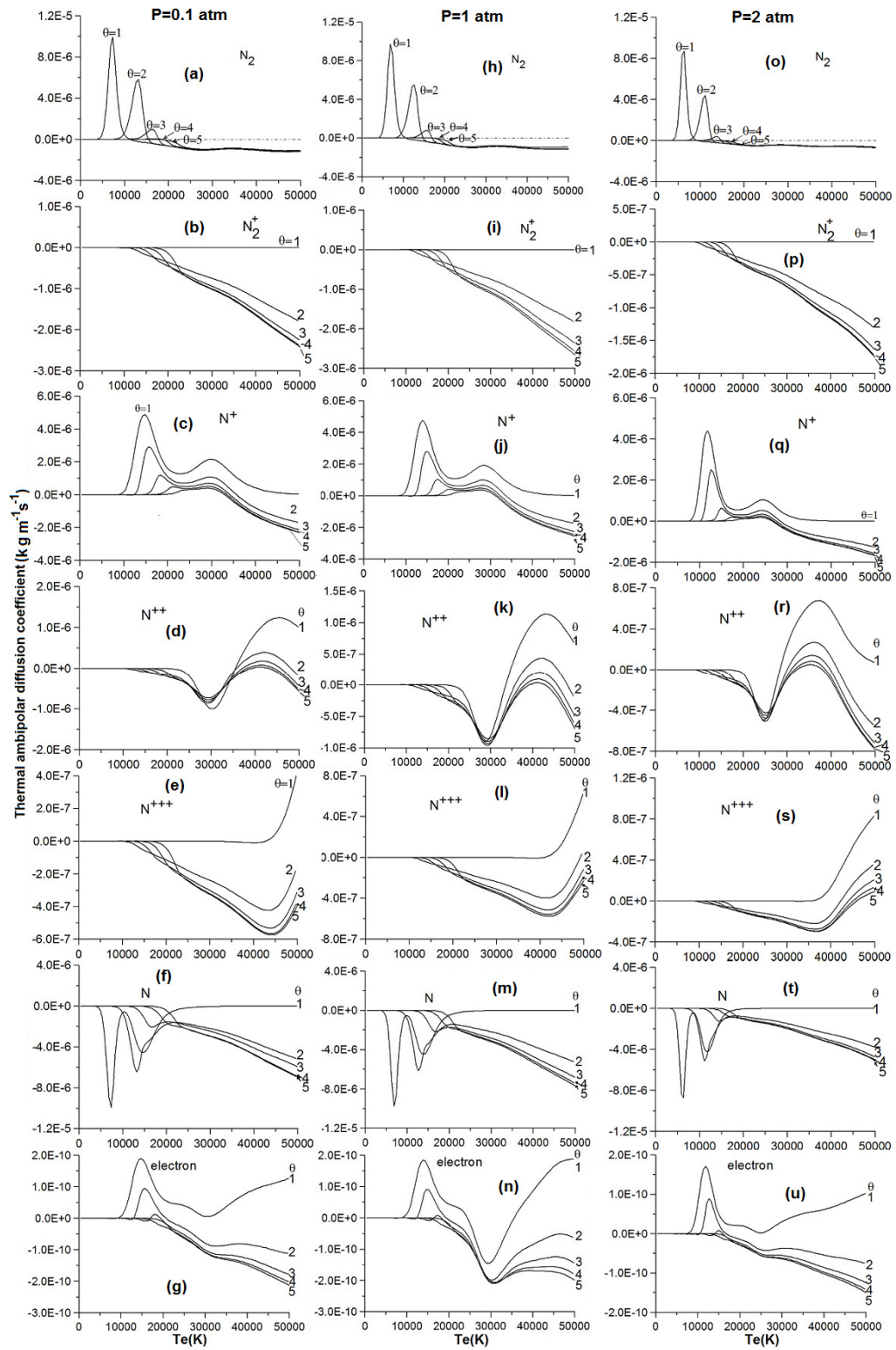


**Fig. 6.16** Variation of thermal ambipolar diffusion coefficients (TADC) of the species in nitrogen plasma as a function of electron temperature at three different pressures:0.1 Atm, 1 atm and 2 atm.

## Comparison of Diffusion Coefficient Data with Literature

A comparison of the results from the present study with those reported in literature is presented in this section. Since most of the data published in literature on diffusion coefficient are for LTE plasma, scope of comparison with non-equilibrium data is limited. However, in a recent study on thermo-physical properties of nitrogen plasmas under thermal equilibrium and non-equilibrium conditions, Wang et. al. [53][52] presented temperature dependence of electron TDC of nitrogen plasmas under different degrees of thermal non- equilibrium. Apart from comparison with this data, the rest of the comparisons are under LTE conditions.

A comparison of our results with the non-equilibrium data by Wang et al. is presented in Figure 6.17 (a). Good agreement is observed over wide range of temperature and thermal non-equilibrium. Use of different sets of collision integrals may account for the deviations observed whatsoever.

In an attempt to determine the transport properties of ionized species in LTE plasma, BDC of N-N, N-N<sup>+</sup> and e-N<sup>+</sup> have been reported by Selle and Riedel [96]. The BDC for N-N interactions are also reported by Cubley and Mason [97], Yun and Mason [98], Levin et al. [99] and Capitelli and Devoto [48]. As observed in Figure 2(b) (6.17), diffusion coefficients estimated in the present work for N-N interactions bear excellent agreement with the results of Capitelli et.al., Selle et.al. Levin et al. However, like others, a wide deviation is observed with the data by Cubley et al. and Yun et al. The deviations occur primarily due to different Born Mayer parameters used in their calculation [96].

Gupta et. al. [100] calculated the BDC of e-N<sup>+</sup> interactions. Collision integrals, calculated for a fully ionized gas by Yos [101] were used first and then corrected considering partial pressure of electrons. Respective diffusion coefficients are presented by curve 'a' and curve 'b' respectively in Fig. 6.17 (c). These coefficients vary over several orders of magnitude as temperature increases. While, an overall good agreement is observed, results obtained from the present work exhibit an excellent agreement with the results of Selle and Riedel at lower temperature and Gupta et al. at higher temperature. The observed differences arise primarily due to differences in the used collision integrals  $\Omega_{ij}^{(1,1)}$ .

The resonant charge transfer plays important role in reducing the diffusion involving neutral and charged species. Results from the present computation for N-N<sup>+</sup> interactions is compared in Fig. 6.17 (d) with the works of Selle and Riedel [96], Levin et al. [99], Capitelli and Devoto [49][48] and Yos [101]. Our results are in excellent agreement with most of the reported results but like others differ from the results of Yos [101].

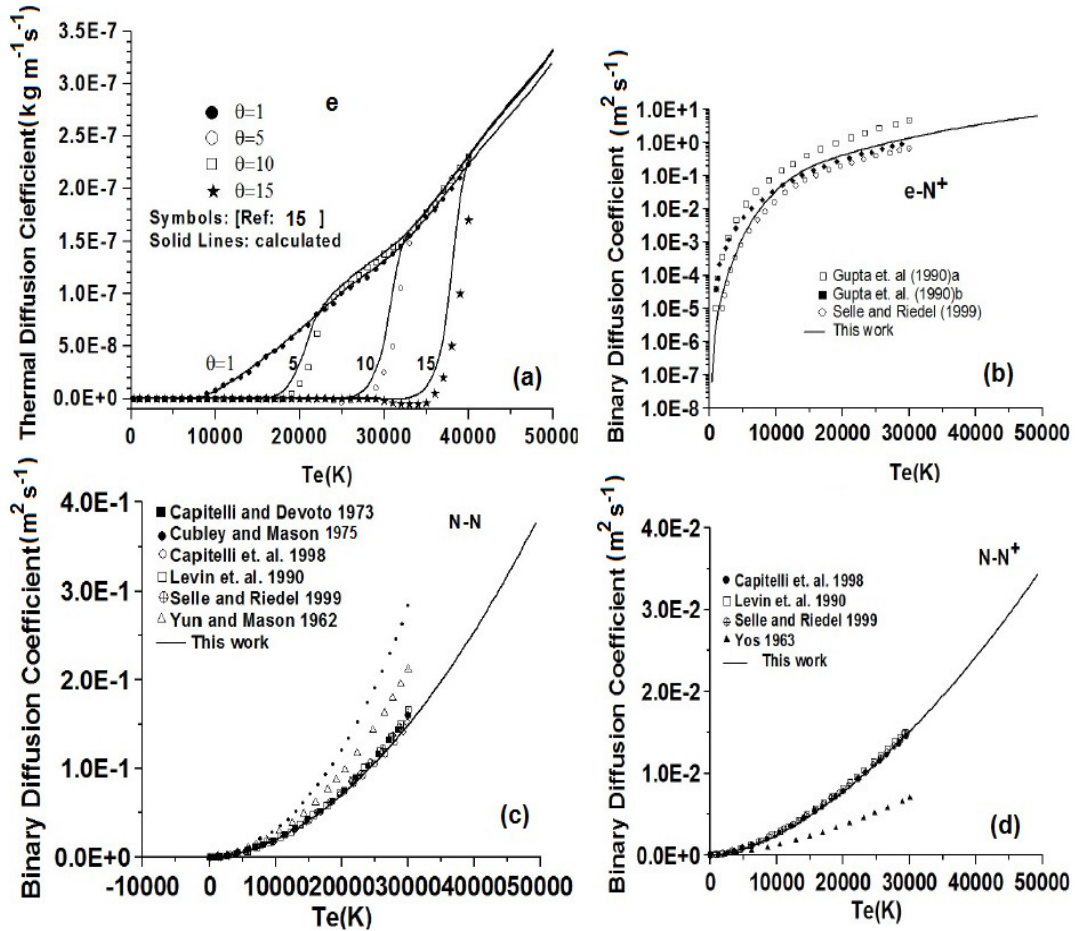


**Fig. 6.17 Comparison of diffusion coefficient data (a) Thermal diffusion coefficient of electron (b) Binary diffusion coefficient involving electron and first ion of nitrogen (c) Binary diffusion coefficient involving nitrogen atoms and (d) Binary diffusion coefficient involving nitrogen atom and first ion of nitrogen. In each graph, solid lines present results of this work and symbols present data reported in literature. Obtained results are in excellent agreement with most of the recently calculated results.**

Variation of total thermal conductivity of nitrogen and its electronic, heavy species and reactive components with electron temperature are presented in Figure 6.18. While the electronic component increases quadratically with electron temperature, the reactive component remains active only when some reactions like dissociation, first ionization, second ionization etc. are active. The heavy species contribution on the total thermal conductivity is low and significant only in the relatively lower temperature zone. The translational thermal conductivities of

electrons and heavy particles for various  $\theta$  and pressure values are presented in Figure 6.19 and Figure 6.20 respectively. For a given  $\theta$ , once the dissociation temperature has been reached, the thermal conductivity of electrons swiftly approaches the curve followed by lower  $\theta$  values. For different  $\theta$  values, the variations of reactive thermal conductivity as a function of electron temperature are presented in Figure 6.21 and Figure 6.22, respectively for electrons and heavy particles. While for electrons, the peaks are observed at first and second ionization, for heavy particles the peaks appear at the molecular dissociation temperature. The reactive thermal conductivity depends on the variation of the number density of particles with temperature. Sharper variations in the number density with  $T_h$  at higher  $\theta$  for heavy particles result in the gradually increasing size of the peaks with  $\theta$  for the heavy particle thermal conductivity. Availability of higher number density of particles at higher pressure increases the magnitude of the thermal conductivity for both electrons and heavy particles. Variation of total thermal conductivity as a function of electron temperature and  $\theta$  are presented in Figure 6.23.

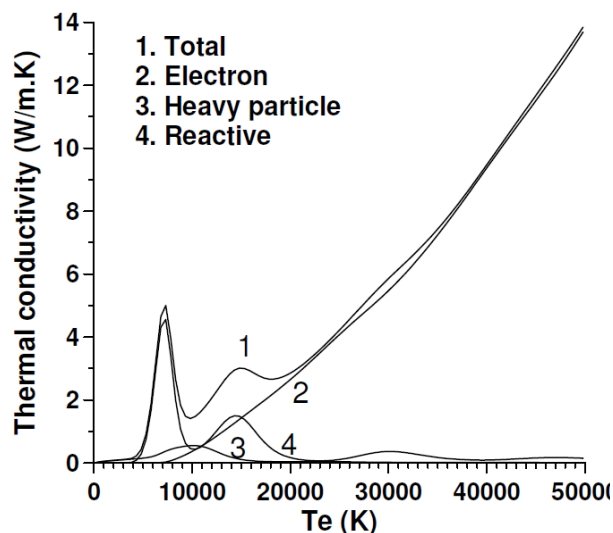


**Fig. 6.18 Components of the thermal conductivity of nitrogen under thermal and chemical equilibrium at atmospheric pressure.**

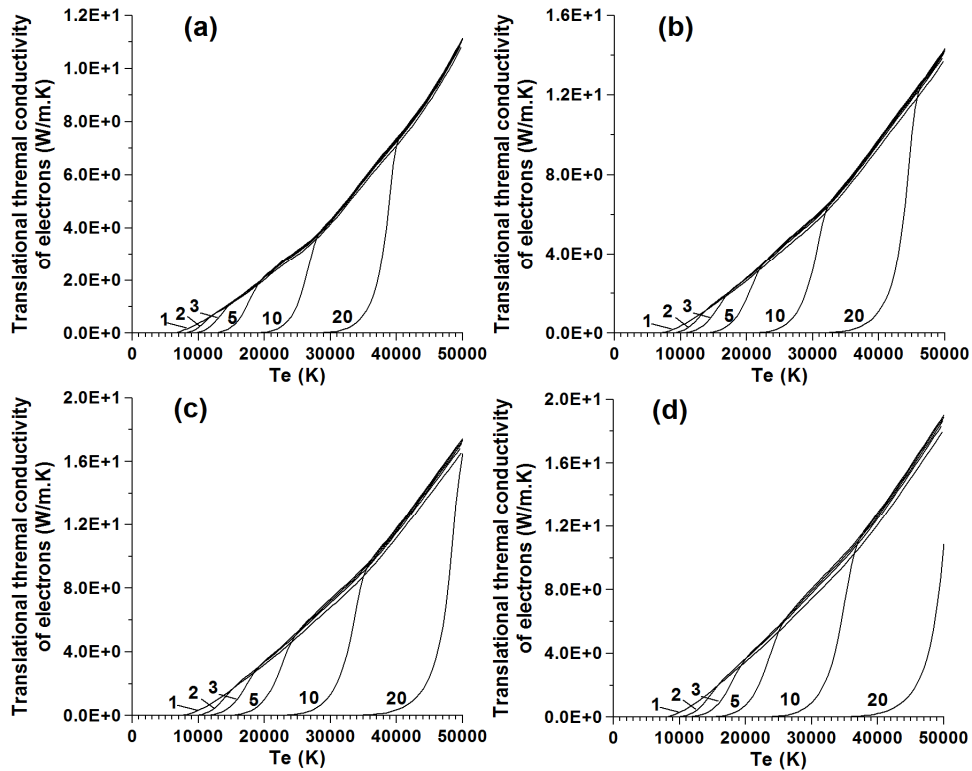


**Fig. 6.19** Translational thermal conductivity of electrons: (a) 0.1 atmosphere, (b) 1 atmosphere, (c) 4 atmospheres, (d) 7 atmospheres. Number associated with each curve indicates  $T_e/T_h$  ratio.

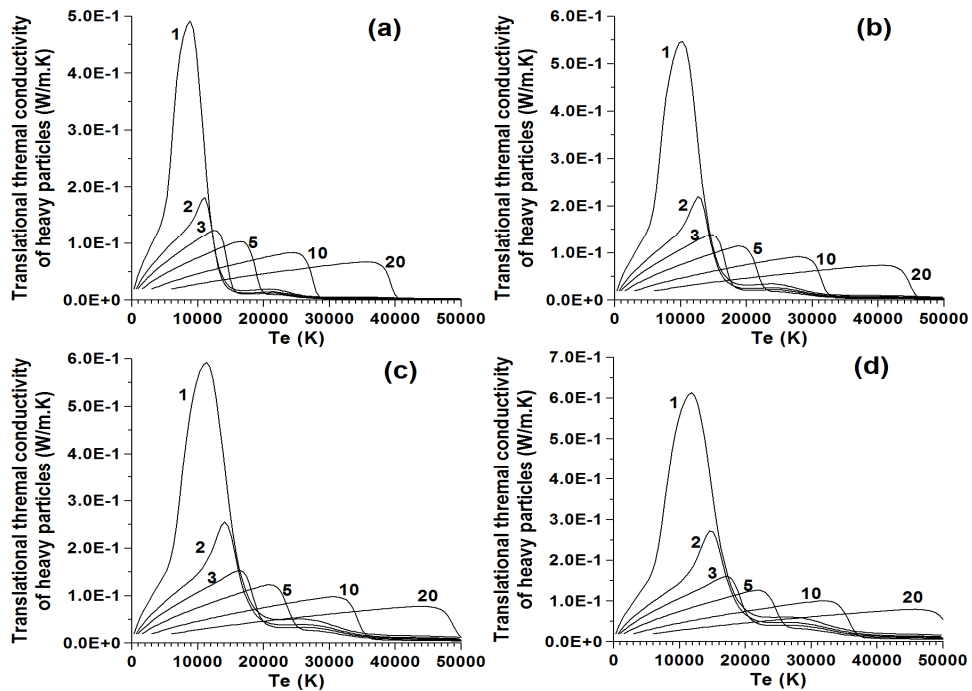


**Figure 6.20** Translational thermal conductivity of heavy particles (a) 0.1 atmosphere, (b) 1 atmosphere, (c) 4 atmospheres, (d) 7 atmospheres. Number associated with each curve indicates  $T_e/T_h$  ratio.

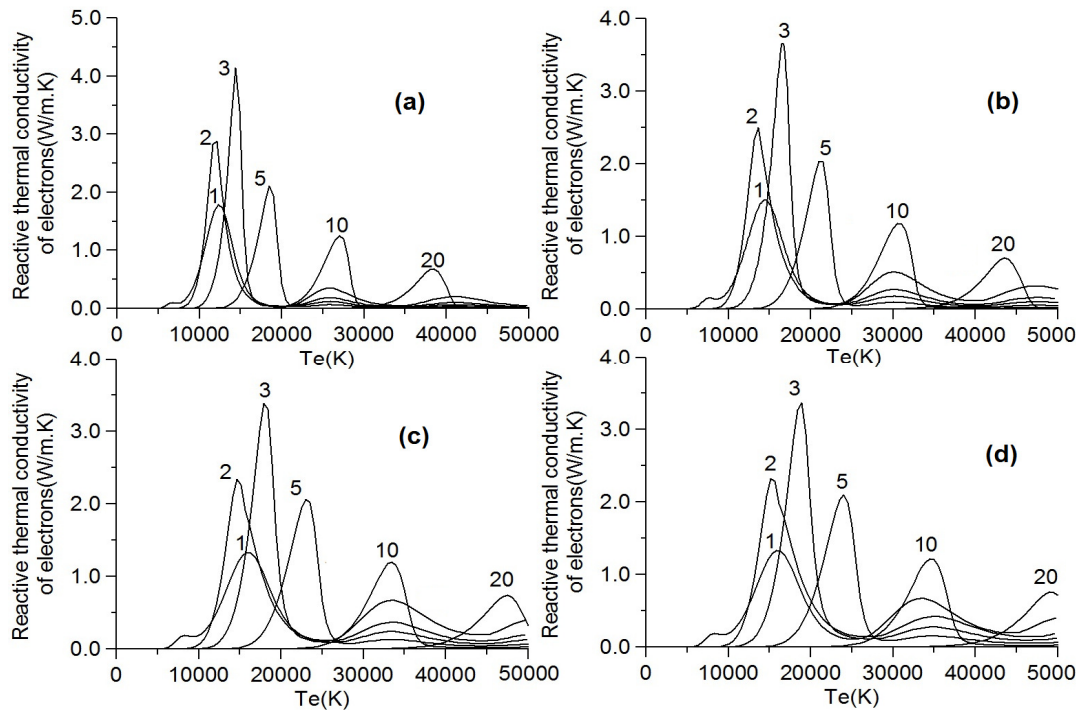


**Figure 6.21** Reactive thermal conductivity of electrons: (a) 0.1 atmosphere, (b) 1 atmosphere, (c) 4 atmospheres, (d) 7 atmospheres. Number associated with each curve indicates  $T_c/T_h$  ratio.

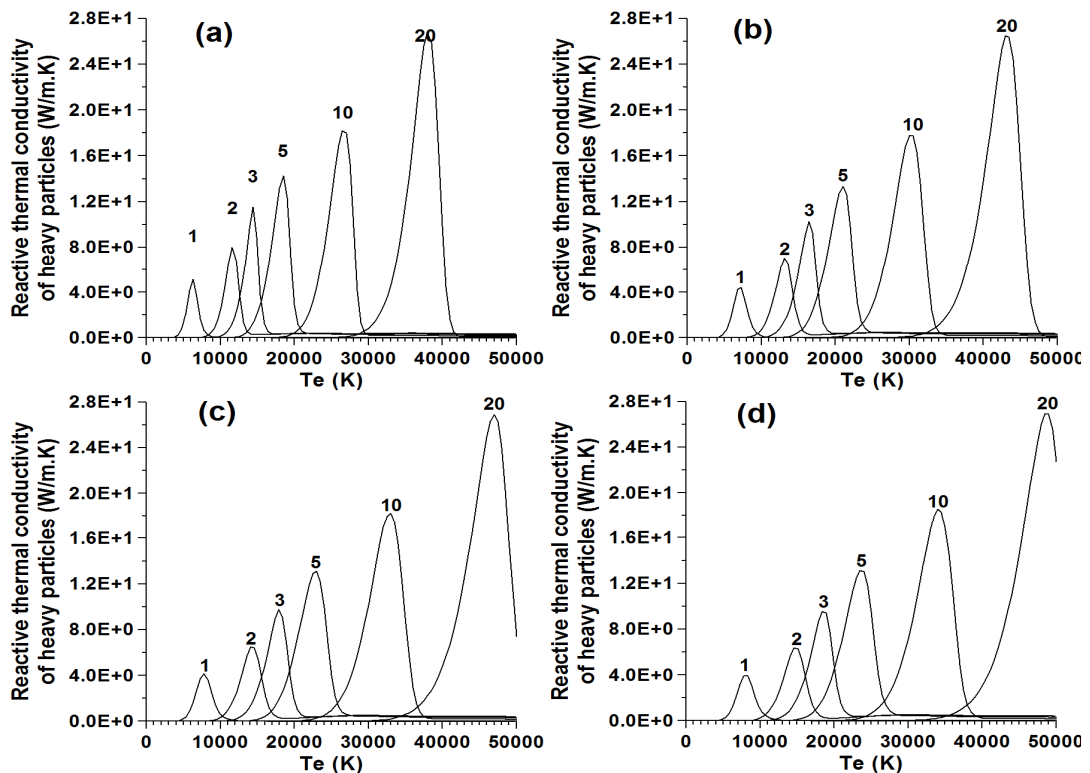


**Figure 6.22** Reactive thermal conductivity of heavy particles: (a) 0.1 atmosphere, (b) 1 atmosphere, (c) 4 atmospheres, (d) 7 atmospheres. Number associated with each curve indicates  $T_c/T_h$  ratio.

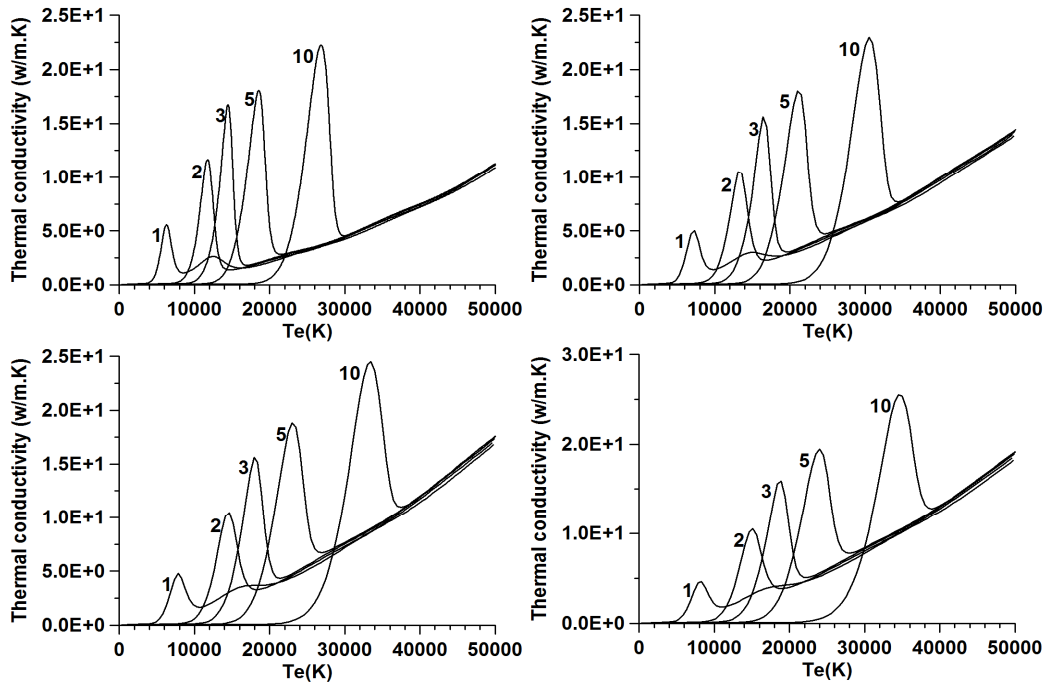


**Figure 6.23** Variation of total thermal conductivity as a function of  $T_e$ ,  $\theta$  and pressure: (a) 0.1 atmosphere, (b) 1 atmosphere, (c) 4 atmospheres, (d) 7 atmospheres. Number associated with each curve indicates  $T_e/T_h$  ratio.

Variation of the electrical conductivity with electron temperature is presented in Figure 6.24. As it is a property of electrons alone, it exhibits higher values at higher pressures due to availability of higher electron densities. With higher  $\theta$  values, the electrical conductivity starts rising fast after the dissociation temperature has been reached and then quickly reaches near the values observed for lower values of  $\theta$  at that  $T_e$ .

Variation of viscosity with pressure, temperature and  $\theta$  are presented in Figure 6.25. With increasing  $\theta$ , the viscosity values decrease and the peaks in the viscosity shift towards higher  $T_e$  values. The viscosity increases with increasing pressure.

Volumetric collision frequencies between electrons and heavy particles are presented in Figure 6.26. Decrease in collision frequency with electron temperature is

primarily caused by a decrease in number density of electrons with temperature. The shift of the peaks can be explained again by the behaviour of the dissociation temperature for a given  $\theta$ .

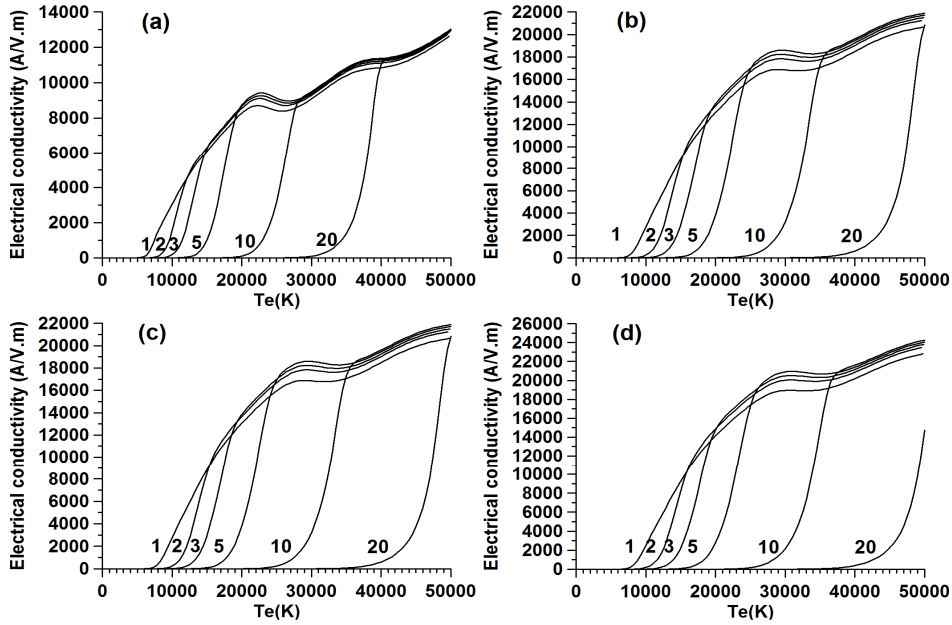


**Figure 6.24** Variation of electrical conductivity as a function of  $T_e$ ,  $\theta$  and pressure: (a) 0.1 atmosphere, (b) 1 atmosphere, (c) 4 atmospheres, (d) 7 atmospheres. Number associated with each curve indicates  $T_e/T_h$  ratio.

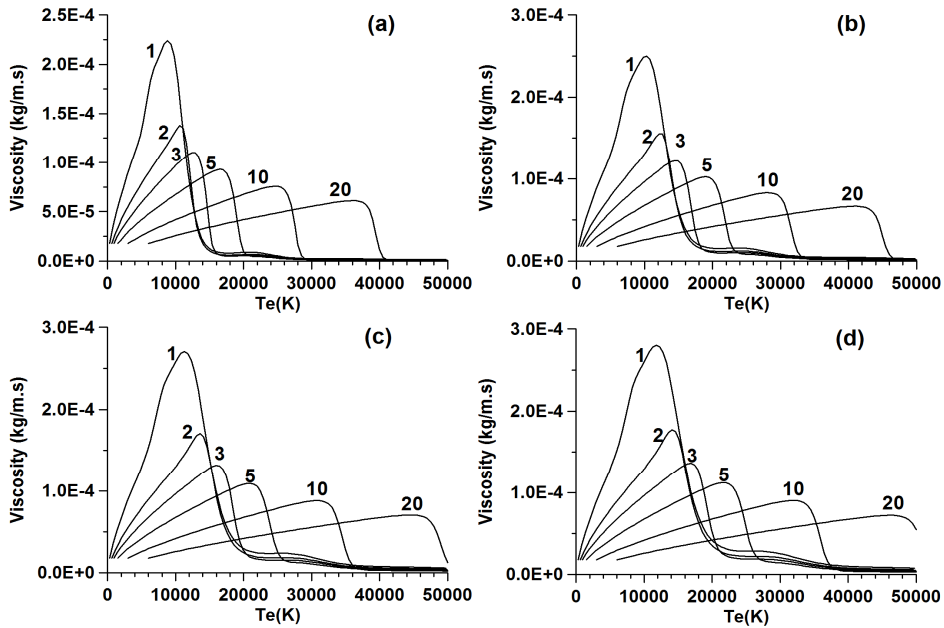


**Figure 6.25** Variation of viscosity as a function of  $T_e$ ,  $\theta$  and pressure (a) 0.1 atmosphere, (b) 1 atmosphere, (c) 4 atmospheres, (d) 7 atmospheres. Number associated with each curve indicates  $T_e/T_h$  ratio.

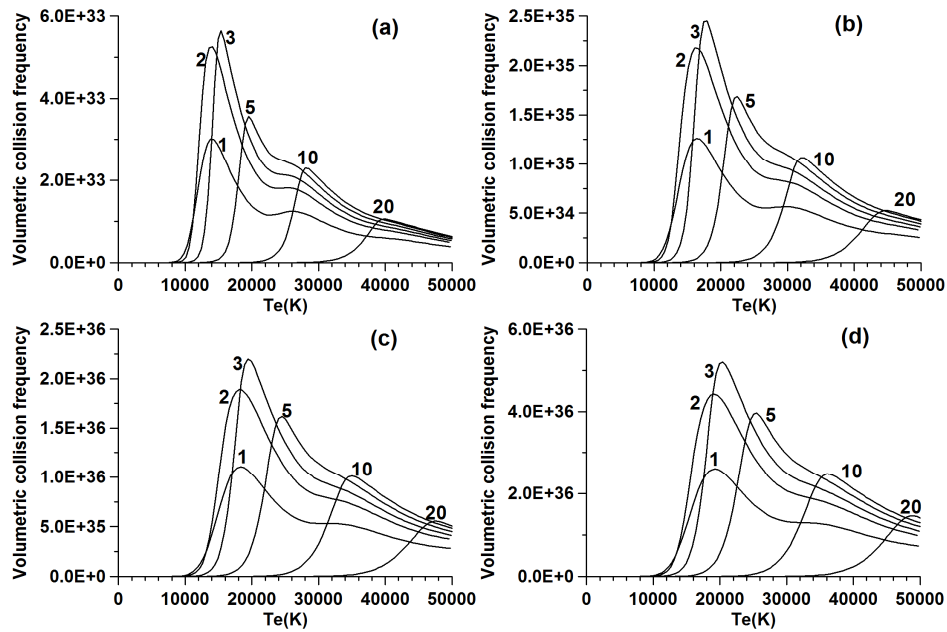


**Figure 6.26 Volumetric collision frequency as a function of  $T_e$ ,  $\theta$  and pressure: (a) 0.1 atmosphere, (b) 1 atmosphere, (c) 4 atmospheres, (d) 7 atmospheres. Number associated with each curve indicates  $T_e/T_h$  ratio.**

An extensive comparison of the obtained properties with the major works reported in literature are presented in Figure 6.27. Comparisons are primarily made with two types of data: experimental (Tsitelauri [46], Plantikow[102], Herman and Schade [47], Neuberger [103], Asinovsky [104]), Guevara [45] and theoretical (Capitelli et.al. [48], Boulos et.al. [105], Murphy et.al.[50], [53], Yun et.al. [44], Colombo et.al. [51] Wang et.al. [52]). Other than the works by Colombo et.al. [51] and Wang et.al.[52], rest of the studies are reported for systems under thermal and chemical equilibrium. Non-equilibrium results by Wang et. al. are interesting in the sense that two widely varying results obtained from two different considerations are presented together. One set of results corresponds to the cases where only the electrons are considered in the shielding (curves are indexed by '(1)' in the figures) and the other set corresponds to the cases where both the electron and the ions are considered (curves are indexed by '(2)' in the figures). Together with equilibrium

results, comparisons are also made with results under thermal non-equilibrium conditions, wherever possible. While an overall excellent agreement is observed in all the cases, better match with the experimental results are arrived at the present study compared to previous studies. For example, while most of the earlier theoretically calculated electrical conductivity values exhibit a tendency to deviate from the experimentally observed values at higher temperatures, the values obtained from the present study give a much closer match.

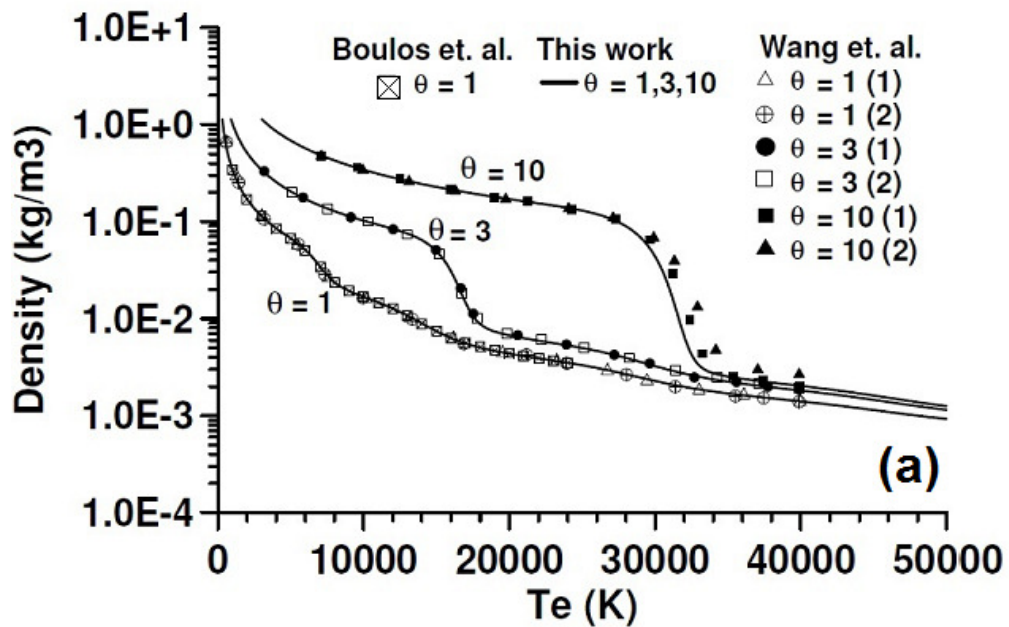


**Figure 6.27(a) Comparison of calculated mass density with previously reported results**

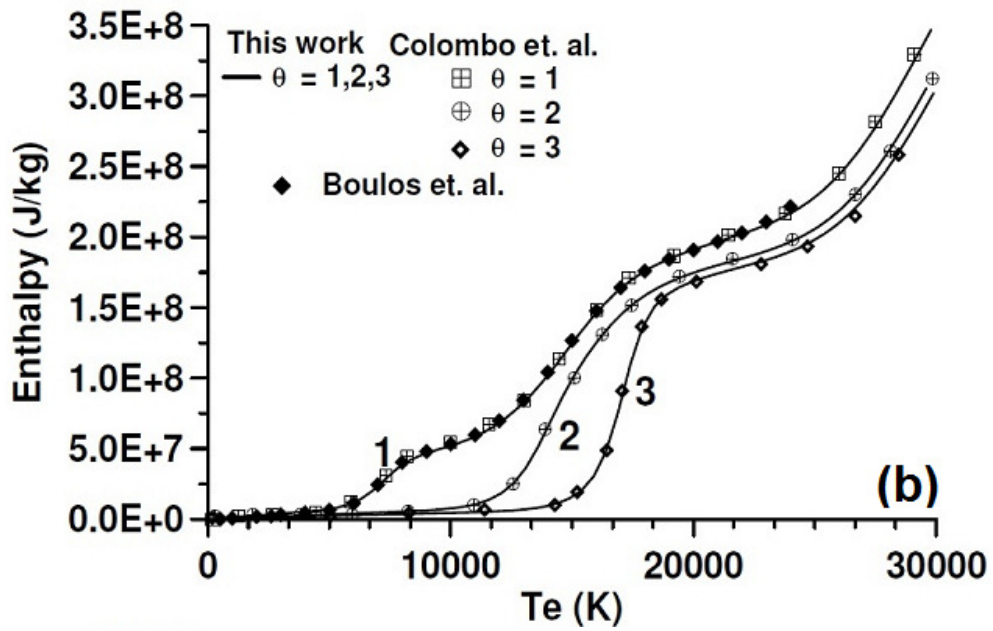


Figure 6.27 (b) Comparison of calculated enthalpy with previously reported results

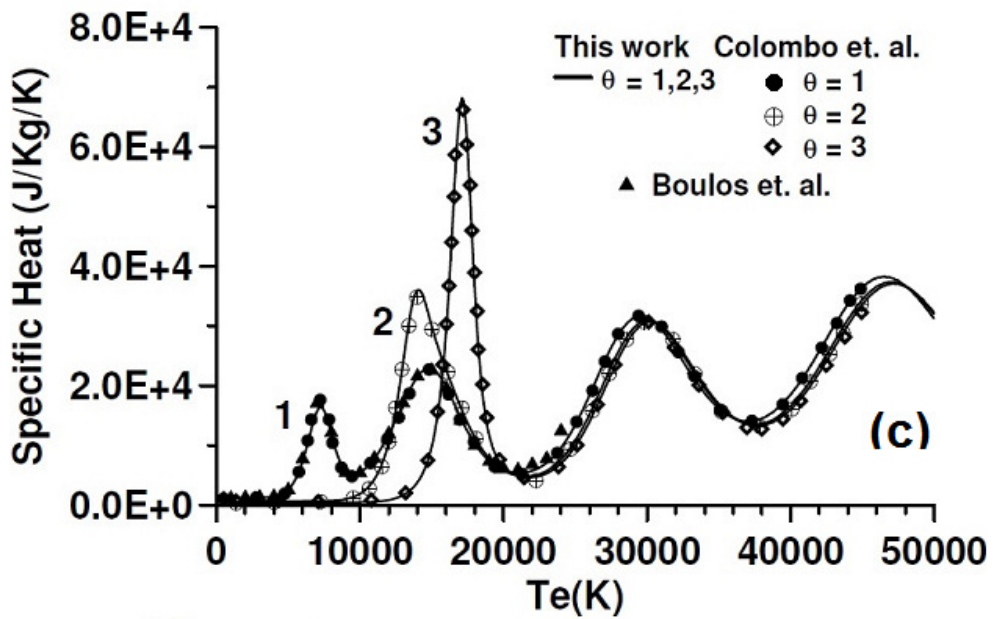


Figure 6.27 (c) Comparison of calculated specific heat with previously reported results

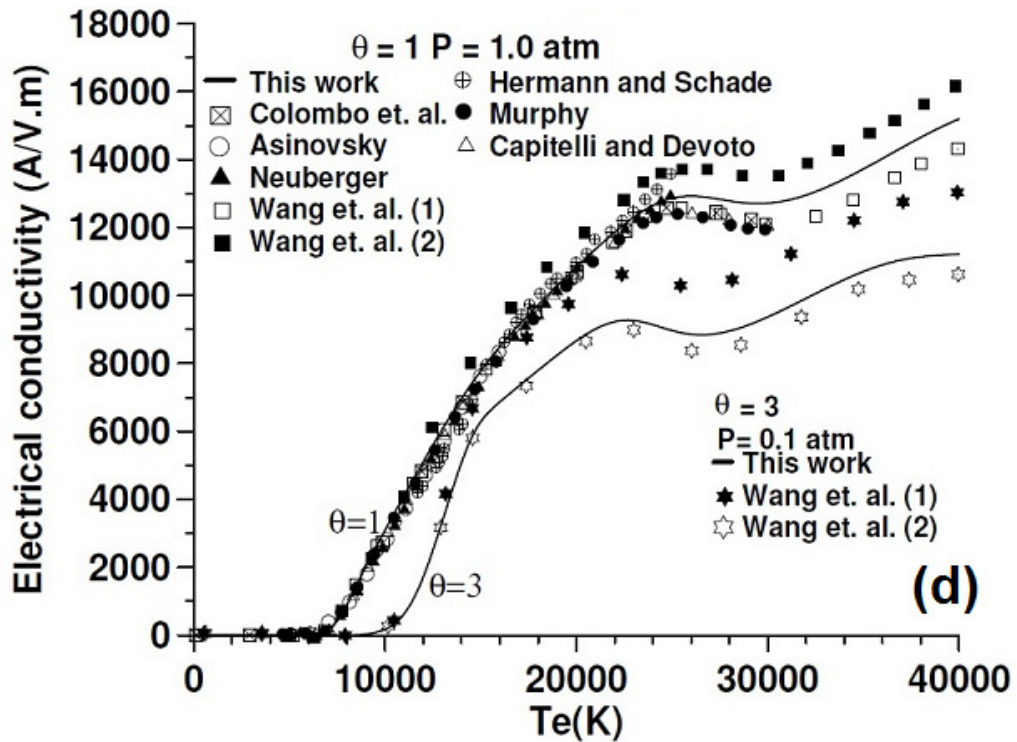


Figure 6.27 (d) Comparison of calculated electrical conductivity with previously reported results

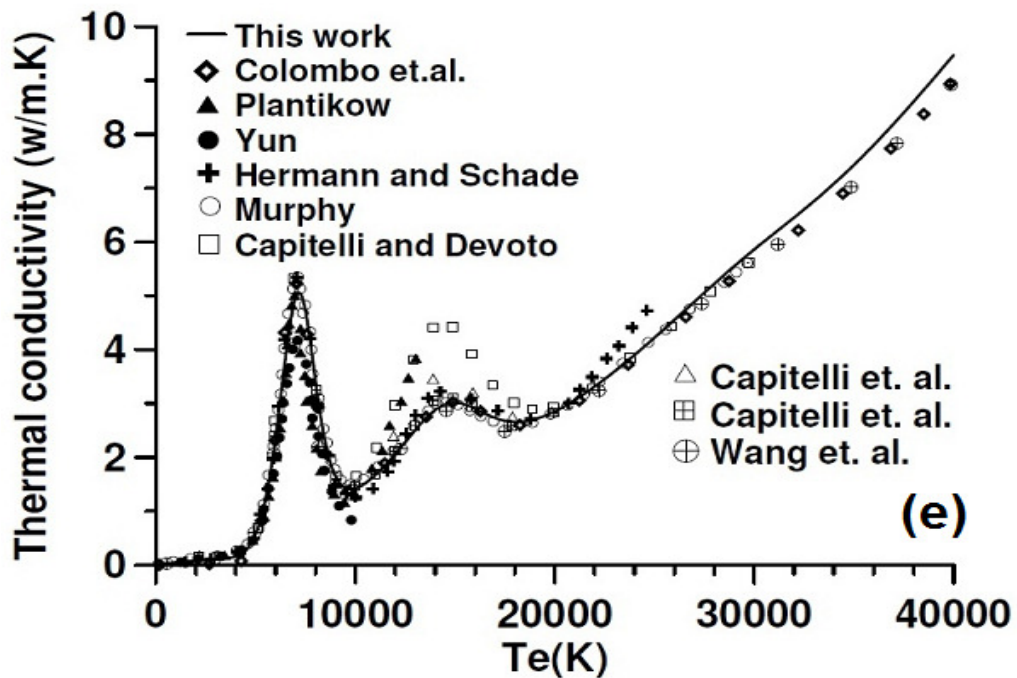
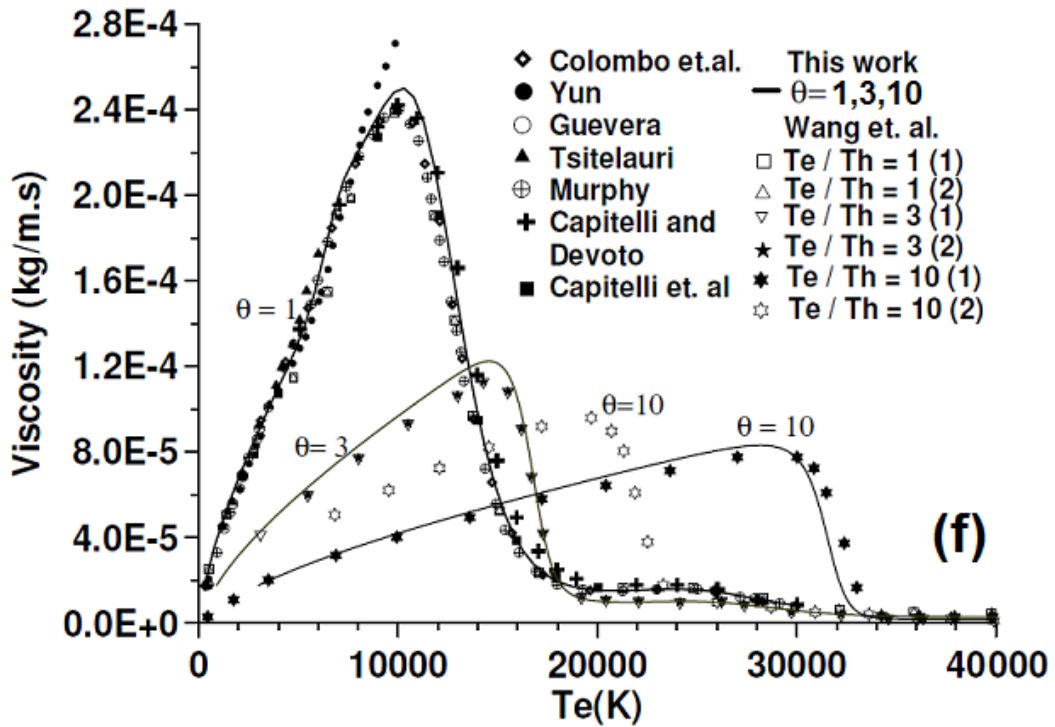


Figure 6.27 (e) Comparison of calculated thermal conductivity with previously reported results



**Figure 6.27 (f) Comparison of calculated viscosity with previously reported results**

Comparison of the calculated physical density values of nitrogen with those reported by Boulos et.al. [105] are presented in Fig. 6.27 (a). It is observed that for equilibrium, associated temperature dependences of the density values offer excellent agreement for equilibrium. For non-equilibrium, the agreement is similar when compared with the results of type (1) [considered shielding by electrons alone] of Wang et.al. [52]. However, our results for non-equilibrium are significantly different from the results of type (2) [considered shielding by both electrons and ions] by Wang et. al..

A comparison of the calculated temperature dependence of the enthalpy with those reported by Colombo et.al.[51] and Boulos et.al. [105] is presented in Fig. 6.27 (b). It is observed that our results match exactly with these reported data both for equilibrium as well as non-equilibrium.

Fig. 6.27(c) compares temperature dependence of specific heat of nitrogen with the results of Colombo et.al. [51] and Boulos et.al. [105]. Almost an exact match is observed at all temperatures.

Calculated values of electrical conductivity data are compared in Fig. 6.27 (d) with the works by Herman and Schade [47], Neuberger [103], Asinovsky [104], Capitelli et.al. [48], Murphy et.al. [50], [53], Colombo et.al. [51] and Wang et.al. [52]). At relatively lower temperatures, agreement with all the data are very good for both equilibrium as well as non-equilibrium. However, as temperature increases our results follow the trend of experimentally observed behaviour [54] and deviates from the calculated electrical conductivity values reported earlier.

Calculated temperature dependence of thermal conductivity is compared in Fig. 6.27 (e) with the results of Plantikow [102], Herman and Schade [47], Capitelli et.al. [48], Murphy et.al. [50], [53], Yun et.al.[44], Colombo et.al. [51], Wang et.al.[52]. Excellent agreement is observed with most of the reported results. The significant deviation observed with the calculated values of Capitelli et.al. between 10,000 and 20,000 K is primarily due to use of highly underestimated charge-exchange cross-sections for the N+-N interaction.

Temperature dependence of the viscosity of nitrogen is compared in Fig. 6.27 (f) with the results of Tsitelauri [46], Guevara [45], Capitelli et.al.[48], Murphy et.al.[50],[53], Yun et.al. [44], Colombo et.al.[51] and Wang et.al.[52]). In general, a very good agreement is observed both for equilibrium as well as non-equilibrium. Use of similar potential in calculation of associated collision integrals may be the reason for such close agreement. The discrepancy observed with the calculated values of Yun et.al.[44] beyond 10000 K is due to the fact that they did not consider the influence of

ionization. When compared with the non-equilibrium data of Wang et.al. [52], it is observed that our results match closely with the results of Wang et.al. when they consider the screening by electrons alone [data marked by '(1)'].

The effect of chemical non-equilibrium on various properties is presented in figure 6.28 to figure 6.31. The total thermal conductivity, the electrical conductivity and the viscosity in addition to the enthalpy have been chosen for this study. For simplicity of presentation, the chemical non-equilibrium parameters in these figures are assumed to be equal for all reactions:  $c_1 = c_2 = c_3 = c$ .  $c=1$  corresponds to chemical equilibrium. Figure 6.28 and Figure 6.29 present results at pressures of 1 and 7 atmospheres respectively for  $\theta = 1$ . It is observed that at lower temperatures, deviations due to chemical non-equilibrium are relatively small. However, at higher temperatures, these deviations are appreciable. Similar scenario is observed in the properties presented in Figure 6.30 and Figure 6.31 for  $\theta = 3$  and similar pressures. The effect of variations in  $c_i$  is more pronounced at higher temperatures.

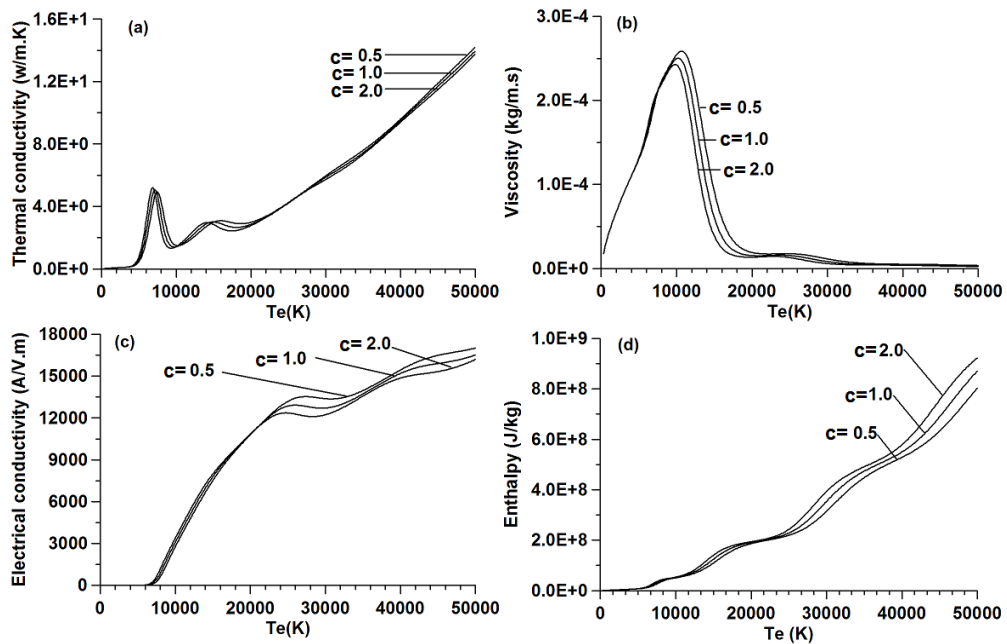


**Figure 6.28** Effect of chemical non-equilibrium on transport and thermodynamic properties at  $p=1\text{Atm}$  and  $T_e/T_h = 1$ : (a) Total thermal conductivity, (b) Viscosity, (c) Electrical conductivity, (d) Enthalpy.

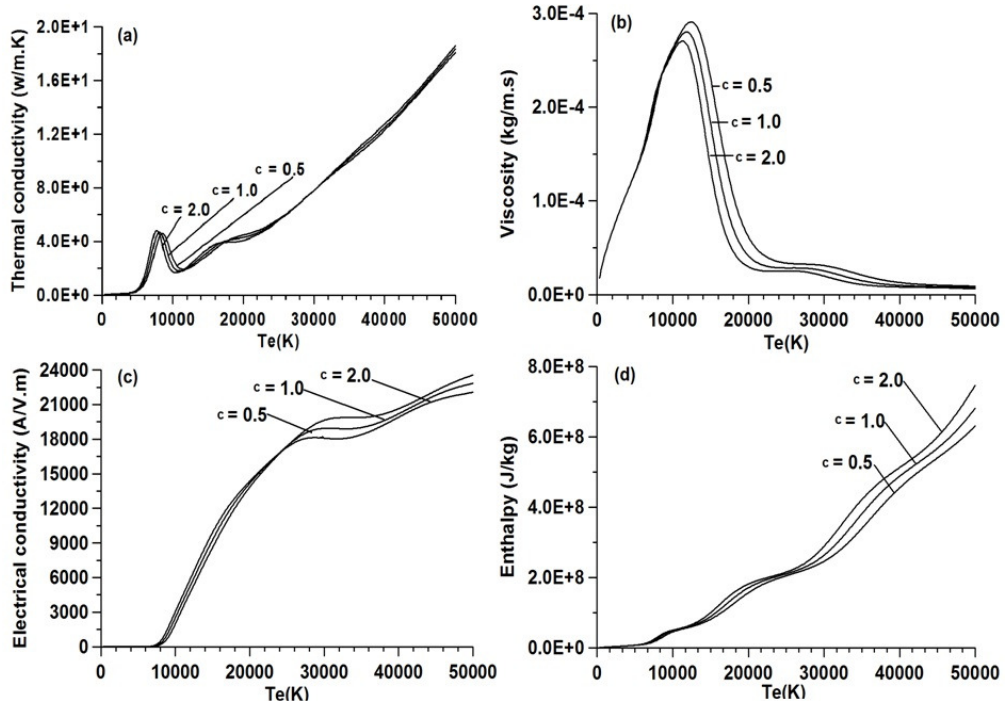


**Figure 6.29** Effect of chemical non-equilibrium on transport and thermodynamic properties at  $p=7\text{Atm}$  and  $T_e/T_h = 1$ : (a) Total thermal conductivity, (b) Viscosity, (c) Electrical conductivity, (d) Enthalpy

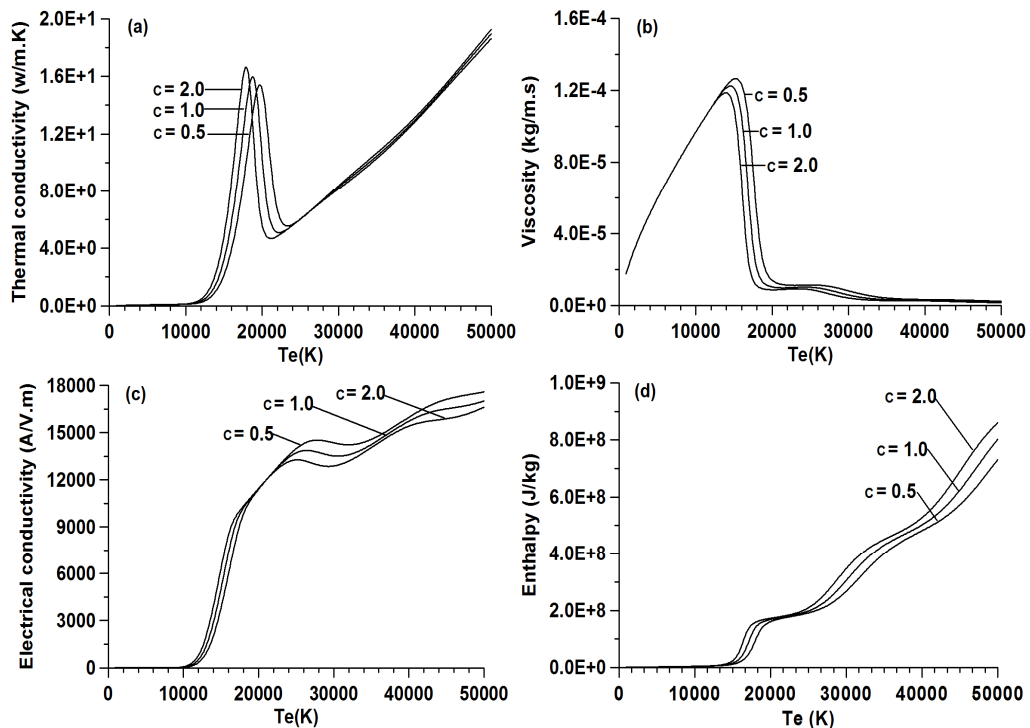


**Figure 6.30** Effect of chemical non-equilibrium on transport and thermodynamic properties at  $p=1\text{Atm}$  and  $T_e/T_h = 3$ : (a) Total thermal conductivity, (b) Viscosity, (c) Electrical conductivity, (d) Enthalpy.

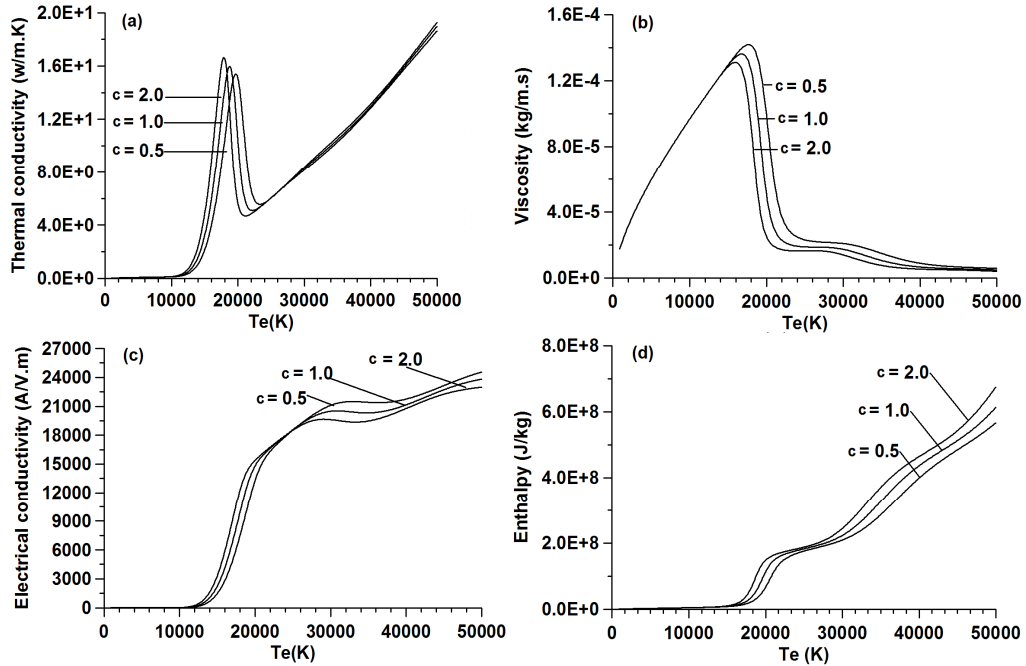


**Figure 6.31** Effect of chemical non-equilibrium on transport and thermodynamic properties at  $p=7$  Atm and  $T_e/T_h = 3$ : (a) Total thermal conductivity, (b) Viscosity, (c) Electrical conductivity, (d) Enthalpy.

## 6.5. Conclusions

Thermodynamic and transport properties of nitrogen plasma, a primary prerequisite for numerical modeling, is calculated in this chapter. Along with equilibrium properties, thermodynamic and transport properties under thermal and chemical non-equilibrium are also presented. Although, only the equilibrium properties are used in the CFD simulation study presented in the next chapter, the obtained non-equilibrium properties form a solid base to expand the future scope of non-equilibrium CFD modeling in nitrogen plasma.

Computed values of non-equilibrium thermodynamic and transport properties for pure nitrogen are presented as a function of temperature, pressure, temperature non-equilibrium parameter  $\theta$  and chemical non-equilibrium parameter  $c$ . Respective

ranges covered for them are 300K to 50000K, 0.1 atmosphere to 7 atmospheres, 1 to 20 and 0.5 to 2. We believe the covered ranges are sufficient for non-equilibrium simulations of wide range of nitrogen plasma devices. Presented results for  $\theta=1$  and  $c=1$  reduces to the properties under equilibrium situation for which a number of results from various authors are available. Equilibrium CFD simulation of the nitrogen plasma torch presented in the next chapter uses the equilibrium properties calculated in this chapter. Extensive comparisons of the obtained results with previously published results are presented under equilibrium and non-equilibrium conditions and an overall excellent agreement is observed.

# **CHAPTER-7: Numerical modelling of atmospheric nitrogen plasma torch under thermal equilibrium and non-equilibrium condition**

## **Outline of the Chapter**

**7.1 Introduction**

**7.2 Governing Equation**

**7.3 Method of Solution**

**7.4 The Boundary Conditions**

**7.5 Results and Discussion**

**7.6 Conclusions**

## **Chapter: 7**

# **Numerical Modelling of Atmospheric Nitrogen Plasma Torch under Thermal Equilibrium and Non-Equilibrium Condition**

### **7.1. Introduction**

This chapter presents the CFD simulation of the addressed nitrogen plasma torch. Such simulations are very much necessary to understand the device physics for design optimization, reliability enhancement as well as catering specific application needs. Direct non-invasive experimental investigation fails to probe the distribution of thermal, fluid dynamic and electromagnetic field distribution inside the device due to mechanical obstruction by the torch wall itself. Invasive experimental studies using probes also fail as no probe material can withstand the kind of high temperature, exists inside the torch. Therefore, such simulation studies are extremely important as this may be the only way to understand the thermal, fluid dynamic and electromagnetic field distribution inside the device.

A large number of simulation studies exist on simulation of arc plasma jets [56-69]. However, most of them deal with argon plasma [56-63]. Among very few studies on nitrogen arc, some report on transferred arc nitrogen plasma devices [64-67] and some deals non-transferred arc plasma torches operating with mixture of argon and nitrogen [68,69]. Practically no simulation study is carried out on segmented electrode pure nitrogen plasma torches, operating at moderate power level and delivering long plasma jet.

In the present simulation study it has been assumed that the plasma is an electrically conducting continuum fluid following usual Navier-Stokes equation with source terms appropriately modified by the effects of electromagnetic interactions. It is further assumed that the plasma is steady, axi-symmetric and optically thin. Effect of gravity on the plasma is ignored.

The CFD simulation uses the frame work of two temperature modeling. Under this the plasma is assumed to be composed of two sub-gases: one is consisting of electrons and other is composed of all other heavy particles such as atoms, ions and molecules. Under the framework of 2T-model, the electrons are assumed to be in equilibrium among them at temperature  $T_e$  and the rest of the heavy species are in equilibrium among themselves at temperature  $T_h$  (different from  $T_e$  in general). The model is general and equilibrium simulation ( $T_e=T_h$ ) comes as a part of it.

Section 7.2 describes the general form of governing equations and control volume approach. Section 7.3 presents the discretized form of governing equation. The SIMPLE algorithm and pressure-velocity coupling is presented in section 7.4. Section 7.5 present the final form of governing equations used in the modelling. The mathematical model for the problem is presented in section 7.6. The method of solution is presented in section 7.7, the computational domain is described in section 7.8. Boundary conditions used in the simulation is given in section 7.9. The thermodynamic transport properties used in the calculation is presented in section 7.10 and section 7.11 presents the results and discussion. Conclusions are presented in section 7.12.

## 7.2. Governing equations:

CFD simulation is the study of transport phenomena occurring in fluid through theoretical modelling. The governing equations of fluid flow represent mathematical statement of the conservation laws of the physics:

1. The mass of the fluid is conserved (conservation of mass)
2. The rate of change of momentum equals the sum of forces on a fluid particle (Newton's second law or conservation of momentum)
3. The rate of change of energy is equal to the sum of the rate of heat addition to the particle and the rate of work done on the fluid particle. (First law of thermodynamics or conservation of energy)

CFD simulation is nothing but numerical solution of the associated conservation equations for mass, momentum and energy. The fluid is divided into number of infinitesimal volume element which contains large number of fluid particles. The laws of physics are applied to each and every volume element and the solution of the conservation equation is obtained. An infinitesimal volume element is bounded by finite number of surfaces, within which source or sink or both of a quantity can coexist. The behaviour of the fluid is expressed in terms of the macroscopic properties, such as velocity, pressure, density, temperature and their time derivatives. These may be thought of as averages over suitably large numbers of molecules. A fluid particle or a point in a fluid is than the smallest possible element of fluid whose macroscopic properties are not influenced by individual molecules. The control volume is fixed in space and the fluid is moving through the fluid element.

The governing equations and the procedure of solution are described in the following sections.

The general form of governing equations assumes the following form,

$$\frac{\partial}{\partial t}(\rho\phi) + \text{div}(\rho \vec{v}\phi) = \text{div}(\Gamma \text{grad } \phi) + S \quad (7.1)$$

Where,  $\phi$  is the variable,  $\rho$  is the mass density,  $\vec{v}$  is the velocity,  $\Gamma_\phi$  is the coefficient of diffusion and  $S$  is the source term. The first term in the left hand side of the relation is unsteady term, and the second term is convective term. In the right hand side, first term is the diffusive term and second term is the source term. Thus qualitatively, it may be written as,

$$\text{Unsteady term} + \text{Convective term} = \text{Diffusive term} + \text{Source term}$$

The equation tells that, in any particular control volume, at any particular instant of time, the net production of the variable  $\phi$  is exactly balanced by the convection and diffusion of the same variable i. e. the net inward flux of the variable  $\phi$  is exactly balanced by the net outward flux. In order to obtain results for velocity distribution, temperature distribution, current density distribution, potential distribution etc., the basic conservation equations including conservation of mass, momentum, energy and charge are solved. Since the computational domain is cylindrical in nature, all the governing equations are written in cylindrical co-ordinate system and solved accordingly.

### 7.2.1 Continuity Equation:

The continuity equation is based on the law of conservation of mass. So for the mass balance inside the fluid element we need,

$$\begin{array}{l} \text{Rate of increase of mass} \\ \text{in the fluid element} \end{array} = \begin{array}{l} \text{Rate of mass flowing} \\ \text{into the fluid element} \end{array}$$

The general form of continuity equation can be written as,

$$\frac{\partial \rho}{\partial t} + \nabla \cdot (\rho \vec{v}) = 0 \quad (7.2)$$

Hence the continuity equation in cylindrical co-ordinate system can be written as,

$$\frac{\partial \rho}{\partial t} + \frac{1}{r} \frac{\partial}{\partial r} (r \rho v_r) + \frac{1}{r} \frac{\partial}{\partial \theta} (\rho v_\theta) + \frac{\partial}{\partial z} (\rho v_z) = 0 \quad (7.3)$$

Since we are dealing with steady state equations, the first term will be zero and the continuity equation or the mass conservation equation becomes,

$$\nabla \cdot (\rho \vec{v}) = 0 \quad (7.4)$$

Or

$$\frac{1}{r} \frac{\partial}{\partial r} (r \rho v_r) + \frac{1}{r} \frac{\partial}{\partial \theta} (\rho v_\theta) + \frac{\partial}{\partial z} (\rho v_z) = 0 \quad (7.5)$$

### 7.2.2 Momentum conservation equations:

This is based on the Newton's second law of motion i.e. the net force on a volume element is the product of its mass and its acceleration. In CFD, the forces acting on a fluid element are broadly classified as body forces and surface forces.

**Body forces:**

Body forces are those force which apply directly on the volumetric mass of the fluid element, such as gravitational force and electromagnetic force.

In a conducting fluid like plasma, there are two type of body forces:

- (1) Gravitational force per unit volume:  $\rho \vec{g}$
- (2) Electromagnetic body force per unit volume:  $\vec{j} \times \vec{B}$

Hence the net body force per unit volume can be written as:

$$\vec{F}_B = (F_B)_x \hat{i} + (F_B)_y \hat{j} + (F_B)_z \hat{k} = \rho \vec{g} + \vec{j} \times \vec{B} \quad (7.6)$$

**Surface forces:**

Surface forces are those forces which act on the surface of the fluid element e.g. normal stress and tangential stress. As shown in figure 7.1, there are six tangential stress term and three normal stress terms which contribute to the surface forces in the three directions.

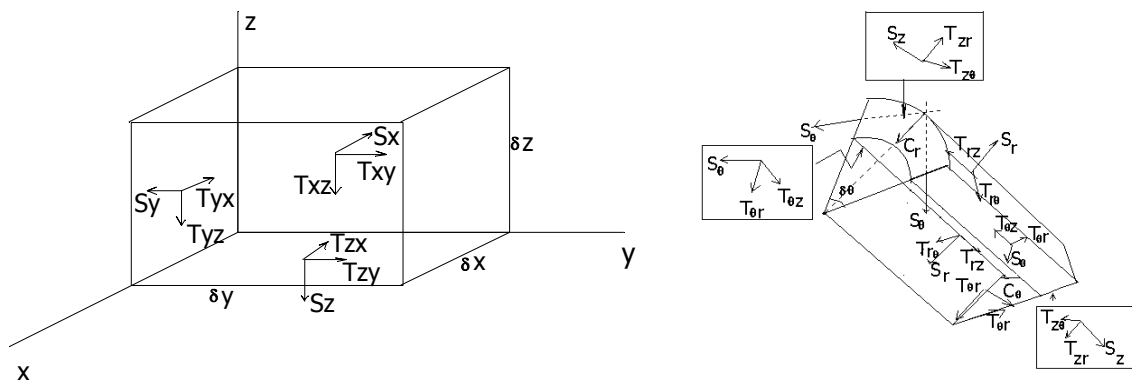


**Fig. 7.1 Stress components in a fluid element in Cartesian co-ordinate and cylindrical coordinate system.**

The expression for the three components of the momentum conservation equation in cylindrical coordinate system is written in the following sections.

**Radial component of momentum conservation equation:**

The radial component of momentum equation can be written as:

$$\bar{\nabla}(\rho \vec{v}_r) + \frac{\partial(\rho v_r)}{\partial t} = -\frac{\partial p}{\partial r} + \bar{\nabla} \cdot (\mu \bar{\nabla} v_r) + \Sigma_r \quad (7.7)$$

Where,  $\Sigma_r$  is written as,

$$\Sigma_r = \frac{1}{r} \frac{\partial}{\partial r} \left( r \mu \frac{\partial v_r}{\partial r} \right) + \frac{1}{r \partial \theta} \left[ \mu \left( \frac{\partial v_\theta}{\partial r} - \frac{v_\theta}{r} \right) \right] + \frac{\partial}{\partial z} \left( \mu \frac{\partial v_z}{\partial r} \right) - \frac{2\mu}{r} \left( \frac{1}{r} \frac{\partial v_\theta}{\partial \theta} + \frac{v_r}{r} \right) + \rho \left( \frac{v_\theta^2}{r} \right) + (F_B)_r \quad (7.8)$$

$(F_B)_r$  is the body force given as,  $(F_B)_r = (j_\theta B_z - j_z B_\theta)$

For a steady state solution, the unsteady term can be eliminated. Hence the radial component of momentum conservation equation is written as,

$$\bar{\nabla}(\rho \vec{v}_r) = -\frac{\partial p}{\partial r} + \bar{\nabla} \cdot (\mu \bar{\nabla} v_r) + \Sigma_r \quad (7.9)$$

**Axial component of momentum conservation equation:**

In similar manner, the axial component of momentum conservation equation can be written as,

$$\frac{\partial(\rho v_z)}{\partial t} + \bar{\nabla}(\rho \vec{v}_z) = -\frac{\partial p}{\partial z} + \bar{\nabla} \cdot (\mu \bar{\nabla} v_z) + \Sigma_z \quad (7.10)$$

Where,  $\Sigma_z$  is given as,

$$\Sigma_z = \frac{1}{r} \frac{\partial}{\partial r} \left( r \mu \frac{\partial v_r}{\partial z} \right) + \frac{1}{r} \frac{\partial}{\partial \theta} \left( \mu \frac{\partial v_\theta}{\partial z} \right) + \frac{\partial}{\partial z} \left( \mu \frac{\partial v_z}{\partial z} \right) + (F_B)_z \quad (7.11)$$

And  $(F_B)_z$  is the z-component of the body force and it can be written as,

$$(F_B)_z = (j_r B_\theta - j_\theta B_r)$$

Since we are dealing with steady state solution the unsteady term can be removed and the axial component of the momentum conservation equation can be written as,

$$\vec{\nabla} \cdot (\rho \vec{v} v_z) = -\frac{\partial p}{\partial z} + \vec{\nabla} \cdot (\mu \vec{\nabla} v_z) + \Sigma_z \quad (7.12)$$

#### **Azimuthal component of momentum conservation equation:**

The azimuthal component of the momentum conservation equation can be written as,

$$\frac{\partial (\rho v_\theta)}{\partial t} + \vec{\nabla} \cdot (\rho \vec{v} v_\theta) = -\frac{\partial p}{\partial \theta} + \vec{\nabla} \cdot (\mu \vec{\nabla} v_\theta) + \Sigma_\theta \quad (7.13)$$

where,

$$\begin{aligned} \Sigma_\theta = & \frac{1}{r} \frac{\partial}{\partial r} \left( r \cdot \frac{\mu}{r} \cdot \frac{\partial v_r}{\partial \theta} \right) - \mu \frac{\partial}{\partial r} \left( \frac{v_\theta}{r} \right) + \frac{\mu}{r} \left( \frac{\partial v_\theta}{\partial r} + \frac{1}{r} \frac{\partial v_r}{\partial \theta} - 2 \frac{v_\theta}{r} \right) \\ & + \frac{1}{r} \frac{\partial}{\partial \theta} \left[ \left( \frac{\mu}{r} \frac{\partial v_\theta}{\partial \theta} + 2 \mu \frac{v_r}{r} \right) \right] + \frac{\partial}{\partial z} \left[ \left( \frac{\mu}{r} \frac{\partial v_z}{\partial \theta} \right) \right] - \rho \frac{v_r v_\theta}{r} + (F_B)_\theta \end{aligned} \quad (7.14)$$

and the azimuthal component of body force  $(F_B)_\theta$  is given as,  $(F_B)_\theta = (j_z B_r - j_r B_z)$

For steady state solution, the time dependent term is removed and the azimuthal component of momentum conservation equation is written as,

$$\vec{\nabla} \cdot (\rho \vec{v} v_\theta) = -\frac{\partial p}{\partial \theta} + \vec{\nabla} \cdot (\mu \vec{\nabla} v_\theta) + \Sigma_\theta \quad (7.15)$$

### 7.2.3 The energy conservation equation in LTE plasma:

In case of plasma in thermodynamic equilibrium, energy balance inside a fluid element is governed by the following mechanisms:

- a. Work done by the viscous stress inside the fluid. ( $W_\mu$ )
- b. Rate of heat transfer through conduction ( $H_X$ )
- c. Rate of volumetric heat generation due mechanisms such as joule heating and change of energy due to charge particles owing to temperature gradient ( $U_P$ )
- d. Rate of volumetric heat loss such as radiation loss ( $U_R$ )
- e. Change in internal energy ( $U_C$ )
- f. Rate of volumetric heat loss or gain due to collisional exchange ( $U_X$ )

Hence for an infinitesimal volume element of the plasma with volume  $dV$  enclosed by surface area of  $dA$  the energy equation can be represented by first law of thermodynamics and it can be written as:

$$U_N = H_x + W_x + U_P + U_R + U_C + U_X \quad (7.16)$$

Where,  $U_N$  is the volumetric rate of change of the internal energy. The term  $U_P$  can be expressed as the sum of volumetric generation of heat due to Ohmic heating and volumetric change of energy by the charge particles due to temperature gradient. Hence it can be written as,  $U_P = U_O + U_J$ . Contribution of various mechanisms to the energy equation is explained below.

- a. Volumetric rate of change of Internal energy:

If  $E$  is the internal energy per unit mass than  $U_N$  can be written as,

$$U_N = \rho \cdot \frac{d(E)}{dt} \quad (7.17)$$

b. Rate of external heat transfer to the fluid through conduction ( $H_X$ )

According to the Fourier's law, if  $k$  is the thermal conductivity of the fluid, than, the rate at which heat is flowing out of the volume element through the surface area is proportional to the rate of decrease of heat in the volume element. The rate at which heat is flowing out of the volume element through the surface area  $dA$  is given as,

$\iint_{\text{surface}} k(\vec{\nabla}T) \cdot d\vec{A}$  and the rate at which, heat in the volume element reduces is given as

$\iiint \rho \cdot \frac{dQ}{dt} \cdot dV$  . Converting the volume integral into surface integral we obtain,

$$H_x = \rho \frac{dQ}{dt} = \nabla \cdot (k \nabla T) \quad (7.18)$$

where,  $T$  is the temperature and  $k$  is the thermal conductivity of the fluid. In case of plasma in local thermal equilibrium,  $T$  represents both the electron temperature and heavy particle temperature. The thermal conductivity is the total thermal conductivity and can be expressed as the sum of thermal conductivity of electrons and that of heavy particles. So it can be written as,  $k = k_e + k_h$ , where,  $k_e$  is the thermal conductivity of the electrons and  $k_h$  is the thermal conductivity of heavy particles.

c. Change of energy due to charge particle content: ( $U_P$ )

There are two ways through which energy is associated with charged particle in the plasma and they are generation of energy through the Ohmic heating ( $U_O$ ) and energy transport through heat conduction by the charge particles because of the

temperature gradient ( $U_J$ ). Because of the finite resistivity of the plasma, Ohmic heating plays an important role in generating heat. Ions being heavier than electrons, the contribution of ion current to the total current is very small. The volumetric rate of heat generation in the plasma by Ohmic heating is given as,

$$U_0 = \vec{j} \cdot \vec{E} \quad (7.19)$$

$\vec{j}$  is the total current density and in cylindrical co-ordinate system it can be written as  $\vec{j} = j_r \hat{r} + j_\theta \hat{\theta} + j_z \hat{z}$ . Since  $\vec{j} = \sigma \vec{E}$  (Generalized Ohm's law), the volumetric rate of heat generation by Ohmic heating can be written as,

$$U_0 = \sigma(E_r^2 + E_\theta^2 + E_z^2) \quad (7.20)$$

The other mode through which energy is associated with the charged particle is transport of heat by them through heat conduction by virtue of its temperature gradient and it can be written as,

$$U_J = \frac{5}{2} \frac{k_B}{e} (\vec{j} \cdot \vec{\nabla} T) \quad (7.21)$$

#### d. Radiation loss ( $U_R$ )

It is very difficult to derive an exact theoretical expression for the volumetric heat loss through radiation because of the associated processes such as emission, absorption and very high temperature gradient. In this study we have used the experimental data by Krey and Morris [106] to include the effect of radiation loss. Appropriate extrapolations have been used where data was not available. The

estimated radiation loss as a function of temperature of nitrogen plasma as obtained by Krey and Morris is presented in Fig.7.2.

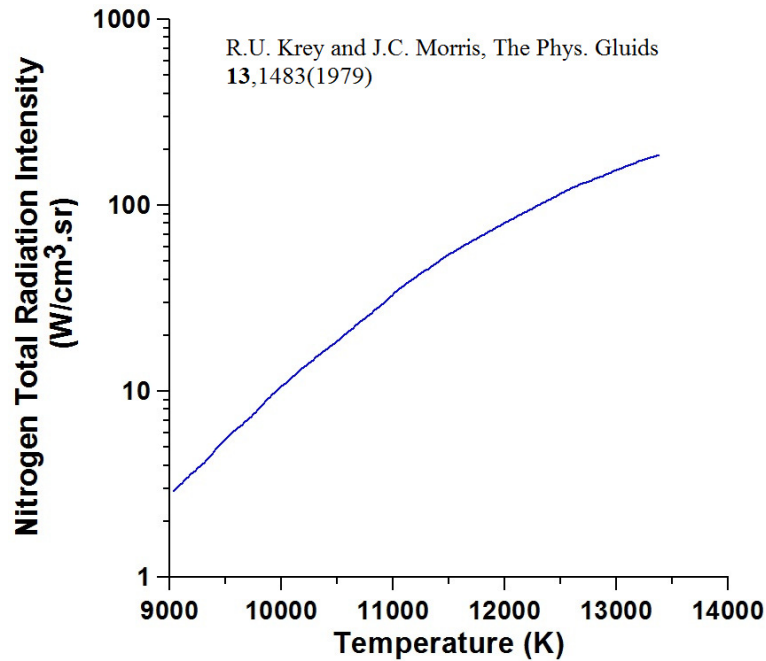


**Fig. 7.2 Variation of radiation loss with temperature in nitrogen plasma**

e. Rate of change of energy due to chemical reaction: ( $U_C$ )

This quantity depends on particular nature of the reactive gases, and can be assumed to be zero for most of the inert gases in high enthalpy arc plasma devices.

f. Rate of volumetric heat loss or gain due to collisional exchange ( $U_X$ )

Plasma contains various species of particles including electron, atom, and ions. In plasma at higher pressure, collisions among the particles play important role in energy transport. For collision among electron and a given species of particles  $S$ , the average energy loss by an electron per unit time depends on collision cross-section  $\Sigma_s$ , relative speed between electron and heavy particles  $v_{eS}$  and average energy loss of an electron

per collision with heavy particle. Hence the rate of volumetric energy loss of electron is given as

$$\begin{aligned}
 U_X &= n_e \sum_s n_s v_{es} \Sigma_s (\Delta E_x)_s \\
 &= \sum_s \frac{2m_e}{m_s} \frac{3}{2} k_B \Sigma_s n_s n_e \overline{v_{es}} (T_e - T_h)
 \end{aligned} \tag{7.22}$$

Where,  $k_B$  is the Boltzmann constant,  $m_e$ ,  $n_e$  and  $T_e$  represents the mass, number density and temperature of electrons respectively.  $m_s$ ,  $n_s$  are the mass and number density of particle of species  $s$  respectively.  $T_h$  is the heavy particle temperature. The average energy loss of an electron per collision is than given by the following expression.

$$(\Delta E_x)_s = \frac{2m_e}{m_s} \cdot \frac{3}{2} k_B (T_e - T_h) \tag{7.23}$$

Hence the rate of volumetric heat loss by electrons per unit time is given as the following.

$$U_X = \sum_s \frac{2m_e}{m_s} \frac{3}{2} k_B \Sigma_s n_s n_e \left( \frac{8k_B T_e}{m_e \pi} \right) (T_e - T_h) \tag{7.24}$$

From the above expression it is quite evident that, when the plasma is in thermodynamic equilibrium there is no such energy transfer occurs.

So the final form of the energy equation can be obtained by adding the different contribution to the energy equation. Hence as written earlier, the complete energy equation can be written as,

$$U_N = H_x + W_x + U_P + U_R + U_C + U_X$$

Substituting the different contribution in the above equation we obtain,

$$\rho \frac{d(E)}{dt} = \bar{\nabla} \cdot (k \bar{\nabla} T) - \rho (\bar{\nabla} \cdot \bar{v}) + \Phi + U_P - U_R + U_C + U_X \quad (7.25)$$

According to the equation of continuity we have,

$$\frac{d\rho}{dt} + \rho (\bar{\nabla} \cdot \bar{v}) = 0$$

Substituting in equation (7.25), we obtain

$$\frac{d}{dt} \left[ E + \frac{P}{\rho} \right] = \frac{1}{\rho} \bar{\nabla} \cdot (k \bar{\nabla} T) + \frac{1}{\rho} \frac{dp}{dt} + \frac{1}{\rho} [\Phi + U_P - U_R + U_C + U_X] \quad (7.26)$$

Since, enthalpy of the gas per unit mass is given as  $h = E + P/\rho$ , we can write,

$$\rho \frac{dh}{dt} - \frac{dp}{dt} = \bar{\nabla} \cdot (k \bar{\nabla} T) + \Phi + U_P - U_R + U_C + U_X \quad (7.27)$$

In plasma, enthalpy  $h$  includes the kinetic energy of electrons, that of heavy particles, and ionization energy of different particles also. For LTE plasma, the exchange term do not appear. When convective losses are included for an nonreactive LTE plasma, the above equation appears under steady state as:

$$\bar{\nabla} \cdot (\rho \bar{v} h) = \bar{\nabla} \cdot (k \bar{\nabla} T) + \frac{5}{2} \frac{k_B}{e} (\bar{j} \cdot \bar{\nabla} T) + \sigma (E_r^2 + E_\theta^2 + E_z^2) - U_R$$

#### 7.2.4. Final form of governing equations:

This study presents a steady state, two dimensional, axis symmetric model for simulation of nitrogen plasma. Hence the unsteady term is not present in the equation.

Being axis symmetric, the model is two dimensional. The equation (7.1) for general form of the conservation equations in steady state reduces to:

$$\vec{\nabla} \cdot (\rho_f \vec{v} \phi) = \vec{\nabla} \cdot (\Gamma_\phi \vec{v} \phi) + S_\phi \quad (7.28)$$

where,  $\phi$  is the quantity conserved,  $\rho_f$  is the mass density of fluid  $f$  for momentum equation and mass density times specific heat for temperature equations,  $\Gamma_\phi$  is the corresponding diffusion coefficient and  $S_\phi$  is the associated source term.  $\vec{v}$  is the velocity vector having axial, radial and azimuthal components,  $v_z$ ,  $v_r$ , and  $v_\theta$  respectively. The final form of the governing equations used for the simulation is given table-7.1. In the table,  $\phi$  is the electric potential,  $p$  is the pressure.  $j_r$  and  $j_z$  are the radial and axial components of current density.  $\nu$ ,  $\sigma$  and  $c_{ph}$  are, respectively, viscosity, electrical conductivity and specific heat of heavy particles. Viscous dissipation is neglected in electron energy equation. Since the flow is assumed to be laminar, so no turbulent equation has been included in this study.  $k_e$  and  $k_h$  are, respectively, effective thermal conductivity of electrons and heavy particles. The self induced magnetic field ( $B_\theta$ ) at radial location  $r$  is computed by integrating  $j_z$ :

$$B_\theta(r) = \frac{\mu_0}{r} \int_0^r j_z y dy \quad (7.29)$$

Where,  $\mu_0$  is permeability of vacuum.

**Table 7.1 Terms of the general governing equation (7.28)**

Conservation of	$\phi$	$\Gamma_\phi$	$S_\phi$
Mass	1	0	0
Axial momentum	$v_z$	$v_{eff}$	$-\frac{\partial p}{\partial z} + \frac{1}{r} \frac{\partial}{\partial r} \left[ r v_{eff} \left( \frac{\partial v_{eff}}{\partial z} \right) \right] + \frac{\partial}{\partial z} \left( v_{eff} \frac{\partial v_z}{\partial z} \right) - \frac{2}{3} v_{eff} \frac{\partial}{\partial z} (\vec{\nabla} \cdot \vec{v}) + j_r B_\theta$
Radial momentum	$v_r$	$v_{eff}$	$-\frac{\partial p}{\partial r} + \frac{1}{r} \frac{\partial}{\partial r} \left[ r \mu \left( \frac{\partial v_r}{\partial r} \right) \right] + \frac{\partial}{\partial z} \left( v_{eff} \frac{\partial v_z}{\partial z} \right) - 2 v_{eff} \frac{v_r}{r^2} - \frac{2}{3} v_{eff} \frac{\partial}{\partial z} (\vec{\nabla} \cdot \vec{v}) + \rho \frac{v_\theta^2}{r} - j_r B_\theta$
Azimuthal momentum	$v_\theta$	$v_{eff}$	$-\rho \frac{v_r v_\theta}{r} - v_{eff} \frac{v_\theta}{r^2}$
Potential	$\phi$	$\sigma$	0
Heavy particle temperature	$T_h$	$k_h + C_{ph} k_{th}$	$2 v_{eff} \left[ \left( \frac{\partial v_r}{\partial r} \right)^2 + \left( \frac{\partial v_z}{\partial z} \right)^2 + \left( \frac{v_r^2}{r^2} \right) \right] + v_{eff} \left[ \left( \frac{\partial v_r}{\partial z} + \frac{\partial v_z}{\partial r} \right)^2 + \left( \frac{\partial v_\theta}{\partial r} - \frac{v_\theta}{r} \right)^2 + \left( \frac{\partial v_\theta}{\partial z} \right)^2 \right] - \frac{2}{3} v_{eff} (\vec{\nabla} \cdot \vec{v})^2 - p (\vec{\nabla} \cdot \vec{v}) + E_{ch}$
Electron temperature	$T_e$	$k_e$	$\frac{j_r^2 + j_z^2}{\sigma} + \frac{5}{2} \frac{k_B}{e} \left( j_z \frac{\partial T_e}{\partial z} + j_r \frac{\partial T_e}{\partial r} \right) - 4\pi U_r - E_{ch}$

$E_{ch}$  in Table -7.9 is the rate of energy transfer from electrons to heavy particles and can be presented as given in the equation 7.30.

$$E_{ch} = \sum_h \frac{3}{2} k_B (T_e - T_h) n_e \left( \frac{2m_e}{m_h} \right) \bar{v}_{eh} \quad (7.30)$$

$n_e$  and  $n_h$  are, respectively, number density of electrons and heavy particles.  $m_e$  and  $m_h$  are their respective masses.  $\bar{v}_{eh}$  is the average volumetric collision frequency between electrons and heavy particles and it is calculated as given in equation (7.31).

$$\bar{v}_{eh} = \bar{c}_e n_h Q_{eh} \quad (7.31)$$

Where,  $Q_{eh}$  is the collision cross-section between electrons and heavy particles, and  $\bar{c}_e$  is the average thermal speed of electrons.

### 7.3. Method of Solution:

For solution of the governing equations, two codes are used in unison. The first one is a fluid dynamic solver and the second one is a property routine. The property routine works as explained in the chapter for thermodynamic and transport properties. In the fluid dynamic solver, the solution of the governing equations are performed starting with an initial guess for potential, electron temperature, heavy particle temperature, pressure and velocity inside the computational domain. A SIMPLE like algorithm of Patankar[107] is used to solve the equations under a finite volume discretization technique. The computer code FAST-2D [108], an extension of the program originally developed by Majumdar [109], has been appropriately modified to adopt flexible grid and include additional equations for electron temperature, heavy species temperature, joule heating, radiation loss, electromagnetic body force and collisional exchange term. Updated values of the solved quantities in the CFD solver is passed to the kinetic equations to obtain the updated distribution of number densities in each iteration. The updated number density distributions and associated temperature profiles are then used by the property routine to recalculate the properties for use in

the next iteration. Iteration continues until the solution of the quantities reach a steady state. The finite volume grid used in the study is presented in Fig.7.3. Obtained steady state results are checked for grid invariance.

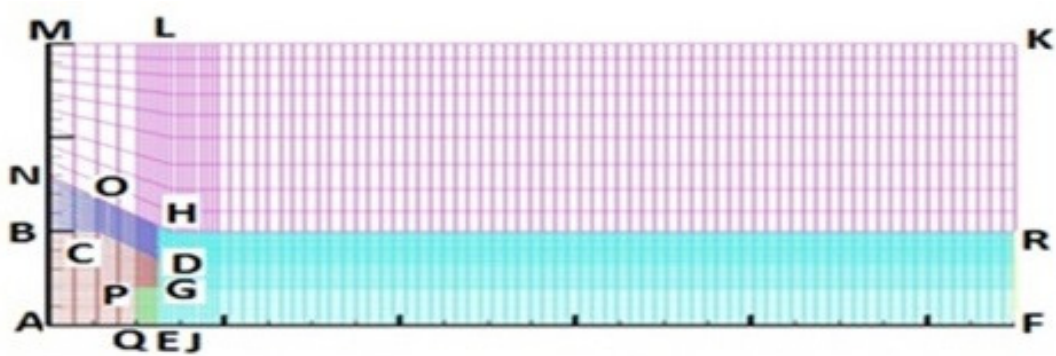


**Fig. 7.3 Computational domain used in the study**

#### **7.4. The Boundary Conditions**

The computational domain used for the study is shown in figure 7.3. It includes the cathode, anode. ABCDEA is the cathode and it is made up of tungsten. It has a conical tip with cone angle of  $24^{\circ}$ . AB is the base of the cathode and DE is the tip of the cathode. The dimensions of AB and DE are 5.0 and 3.5 mm respectively. Cubic profile is used for the current density. The diameter of current emitting region is 1/3 of the original diameter of the cathode. The torch used for the study is a non-transferred arc DC segmented plasma torch consisting of seven segments including cathode. The anode and the segments between cathode and anode form the nozzle. RF is the torch nozzle exit and its diameter 10 mm. MNHRKM forms the anode, and it is made up of copper. The wall temperature for the anode is 600 K. The current connection is considered to be diffused. BN is the gas inlet. The plasma gas injection point is located at some upstream location. The pressure at the upstream point is 2 atm. The orifice diameter is 2 mm. The gas injection process is swirl injection and the gas enters the torch through an orifice which makes an angle of  $20^{\circ}$  with the axis. The

axial, radial and azimuthal velocity computed from gas flow rate and orifice diameter are 20.6, 0.0, 6.77 m/s respectively. The details of the employed boundary conditions are given in Table 7.2. The potential along the line DE is updated in every iteration to  $\Phi = \Phi_j$ , a profile which is self consistent with the assumed current density profile over the cathode surface. Since the nozzle is conducting, for the solution of the nozzle has been included in the computational domain and a boundary condition is applied in on MLK and RK boundaries. Since the torch is operating in non-transferred arc mode, the boundary condition  $\partial\phi/\partial z = 0$  is appropriate which means a constant potential at these boundaries.

**Table: - 7.2 Boundary conditions used in the simulation**

Boundary	p	$V_z$	$V_r$	$V_\theta$	$T_e(K)$	$T_h(K)$	$\phi(v)$
BN	4.74 atm	u	0	$-\text{utan}(20)$	300	300	$\frac{\partial\phi}{\partial z} = 0$
RF	-	$\frac{\partial v_z}{\partial z} = 0$	0	$\frac{\partial v_\theta}{\partial z} = 0$	$\frac{\partial T_e}{\partial z} = 0$	$\frac{\partial T_h}{\partial z} = 0$	$\phi = 0$
EF	-	$\frac{\partial v_z}{\partial r} = 0$	0	$\frac{\partial v_\theta}{\partial r} = 0$	$\frac{\partial T_e}{\partial r} = 0$	$\frac{\partial T_h}{\partial r} = 0$	$\frac{\partial\phi}{\partial r} = 0$
NOHR	-	0	0	0	$\frac{\partial T_e}{\partial r} = 0$	600	-
BCDG	-	0	0	0	1000	1000	-
GE	-	0	0	0	3000	3000	$\phi = \phi_j$
MLK	-	-	-	-	-	-	$\frac{\partial\phi}{\partial n} = 0$
RK	-	-	-	-	-	-	$\frac{\partial\phi}{\partial z} = 0$

## 7.5. Results and discussion:

### Temperature distribution:

The distribution of plasma temperature within the plasma torch for four values of electrical current including 170A, 180A, 200A, 210A is presented in figure 7.4. It can be seen that, the zone of high temperature zone gradually extends from cathode to anode as current increases. The axial temperature between the cathode and anode for electrical currents below 200 A is found to drop because the arc is more constricted near the cathode. This causes thermal expansion of the heated gas in the vicinity of the cathode which in turn reduces the temperature in the downstream location. Axial temperature near the anode further increases as the arc is constricted again in this region in the downstream. Observed two lobes in the temperature distribution is a result of this. Significant change in the temperature distribution pattern is observed as one goes from 170A to 180A.

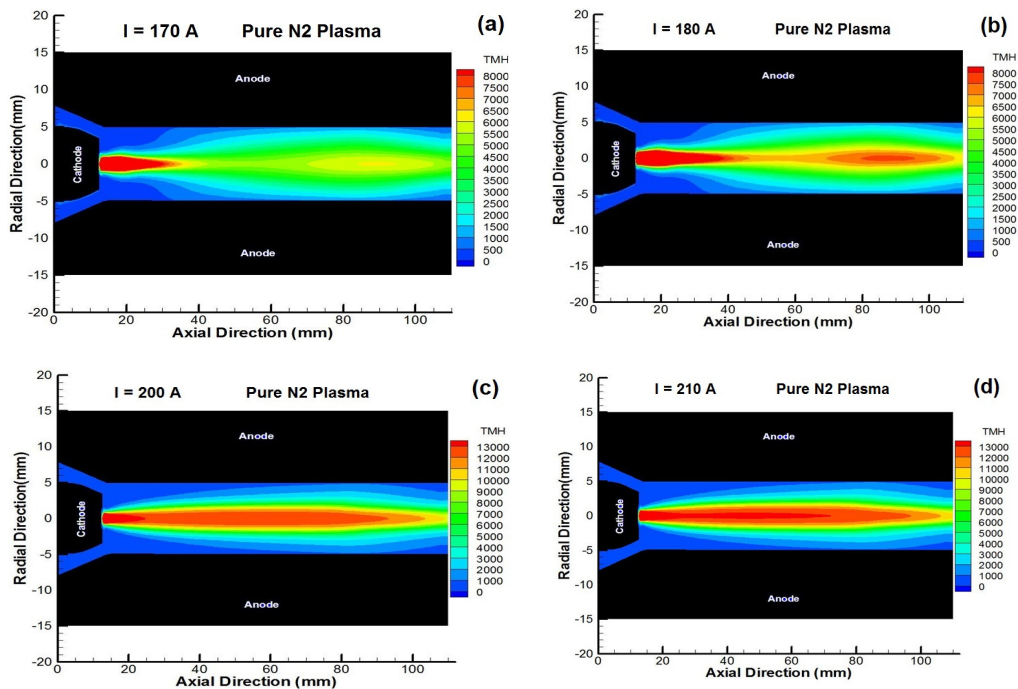


**Fig. 7.4 Nitrogen plasma temperature distribution inside the plasma torch for different currents, (a) 170A, (b) 180A, (c) 200A and (d) 210A. Flow 17.5 slpm N<sub>2</sub>**

However, the axial temperature distribution pattern does not change much as the current goes 200 A and above. The plot of axial temperature profiles and the radial temperature profiles at the nozzle exit are given in figure 7.5 (a) and (b) respectively. Significant jump in the temperature distribution as current switches from 180A to 200A are observed in Figure 7.5. Spectroscopic measurements of plasma temperature at the nozzle exit under the said operating conditions also exhibit similar features as presented in the next section.

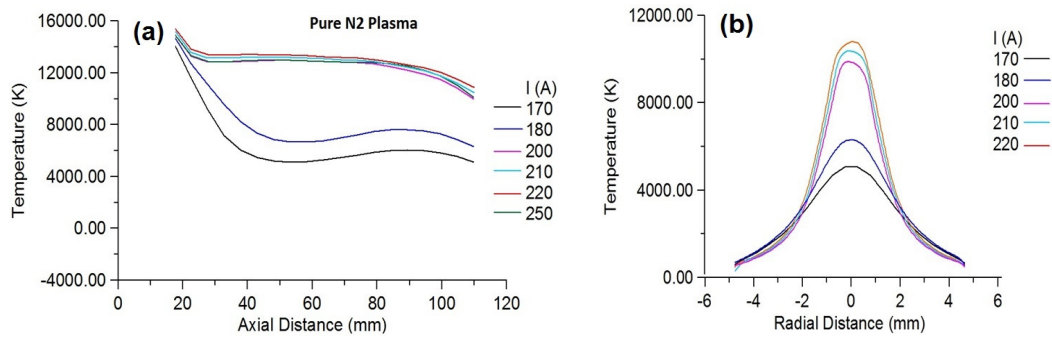


**Fig. 7.5 Axial and radial plasma temperature profile of nitrogen plasma. (a) axial temperature profile, (b) radial temperature profile.**

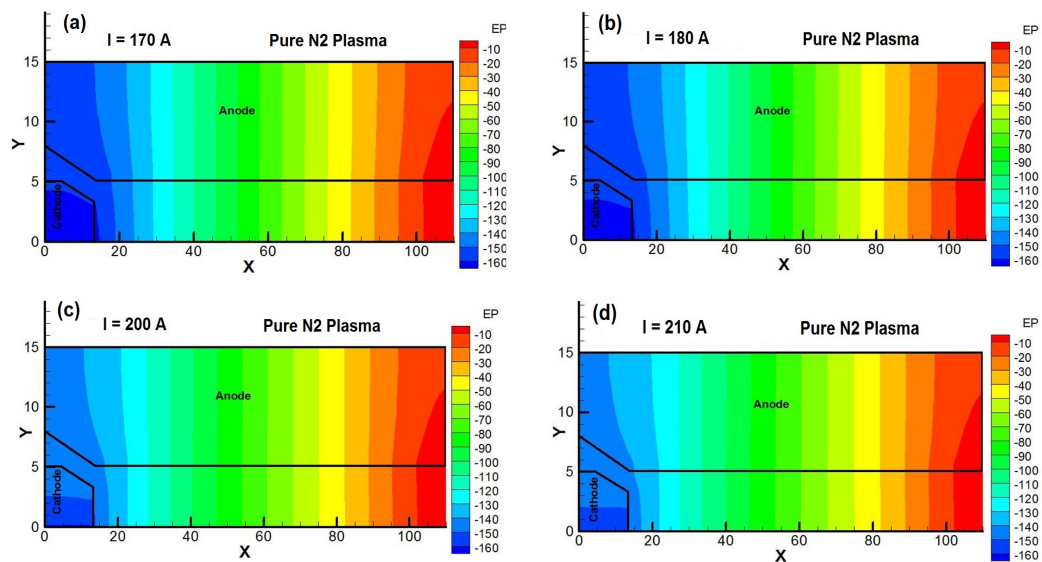


**Fig. 7.6 Potential distribution inside the torch at different currents, (a) 170A, (b) 180A, (c) 200A and (d) 210A.**

### Potential distribution:

The distribution of potential inside the plasma torch for the four current values is presented in figure 7.6. A potential drop exceeding 150V is observed. While nearly similar nature of potential distribution is observed at the considered arc currents, the equipotential zone near the cathode shrinks as current increases. Obtained variation in the potential along the torch axis is shown in figure 7.7. Except near the cathode, almost a linear variation in the potential is observed for all currents. Significant variation in the potential distribution as current changes from 180A to 200A may be noted. Since voltage drop across the arc is an easily measurable quantity, obtained results are verified experimentally in the next section.

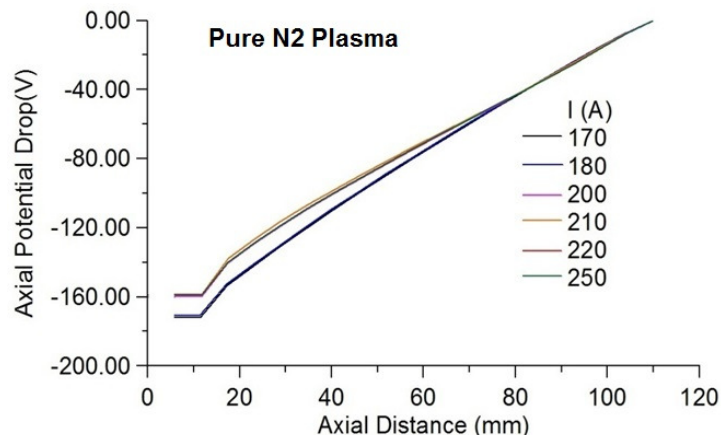


**Fig. 7.7 Variation of axial potential for different current values in the plasma column**

### Velocity distribution:

The distribution of velocity inside the plasma torch is shown in figure 7.8. As the plasma channel is long enough, nearly a fully developed flow is observed. Maximum velocity observed at the exit is around 380 m/s. Overall radial distribution of axial velocity is nearly parabolic. Step like features originate from the sharp

transitions between current carrying and non-current carrying zones in the plasma jet. The current carrying region includes ohmic source terms while non-current regions do not have any.

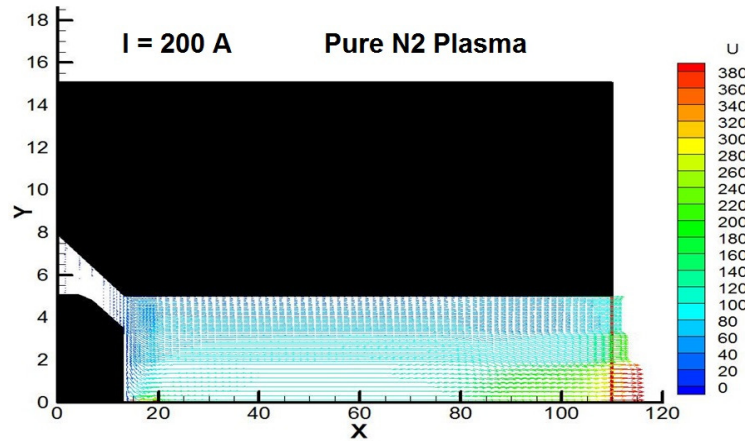


**Fig.7.8 Velocity distribution inside the plasma torch**

#### **Validation of the simulation result:**

The total arc voltage drop and plasma temperature at the nozzle exit are measured through experiments and compared with the above simulation results under similar operating conditions. Results are presented in Figure 7.9. An excellent agreement between the measured and the simulated voltage drop is observed. It can be seen that, as the current varies from 170A to 180A, the arc voltage maintains almost a constant value both theoretically and experimentally. Similar behaviour is observed as arc current changes from 200A to 220A. However, experimentally observed distinct change in the potential for transition from 180A to 200A is slightly smeared out in the simulation results.

Comparison of experimental and simulated plasma temperature at the nozzle exit is presented in Fig.7.10. Apart from the results at 180A, the observed agreements

are good. Since theoretically it is found that around 180A a transition zone exists, the experimental system may exhibit significant change in behaviour for slight change in experimental condition. Observed mismatch between experimental and theoretical results at 180A might have originated from this.

Nice agreement between the theoretical and the experimental results suggests that the proposed model of the nitrogen plasma torch is reasonably accurate.

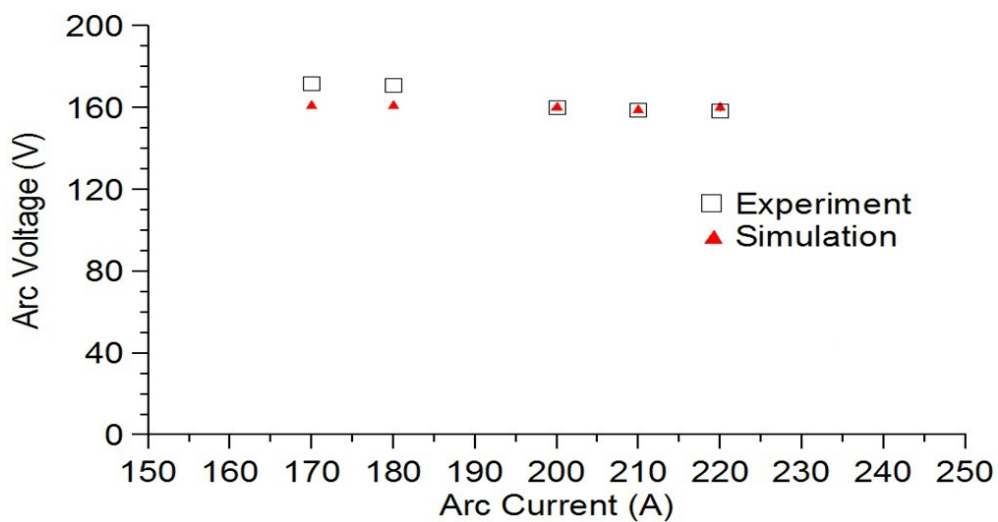


Fig.7. 9 Comparison of experimental and simulated arc voltages

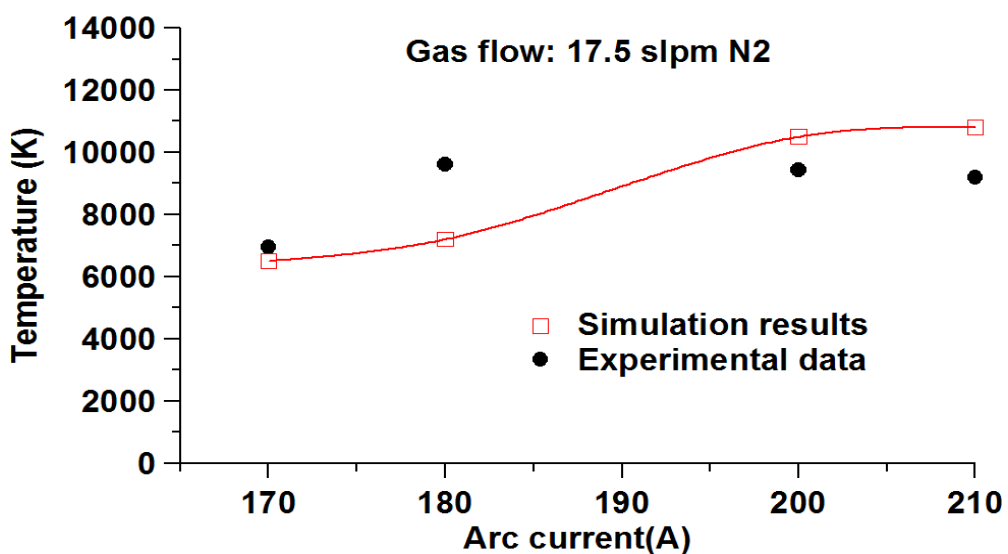


Fig.7. 10 Comparison of experimental and simulated plasma temperature

## 7.6. Conclusions

This chapter of the thesis presents a steady state two-dimensional laminar model of DC non-transferred arc nitrogen plasma torch. The torch is modelled in terms of usual Navier Stokes equations modified by appropriate source terms originating from the current carrying nature of the plasma fluid. Associated conservation equations for mass, momentum and energy are solved using SIMPLER like algorithm under finite volume formalism. A modified version of the code FAST-2D is used as solver. Results of the simulation study are presented in terms of temperature, velocity and potential distribution. It has been observed that under the chosen operating conditions there exists a distinct change in the temperature distribution inside the plasma torch for currents less than 200A and that above 200A. Similar feature is observed for the axial potential distribution also. The potential distribution inside the plasma torch remains almost similar for all values of current. However, the voltage drop in the plasma for current more than 200 A is more than that for values of current below 200A. Nearly parabolic velocity distributions with tiny step like features are observed at the torch exit. Reasons for observed behaviour are explained. Obtained temperatures at the nozzle exit and total arc voltage drops are compared with experimental data. Overall very good agreements between experimental and simulation results support correctness of the used model.

# **CHAPTER-8: Conclusions**

## **Outline of the Chapter**

### **8.1 Summary and Conclusions**

### **8.2 Scope for Future Work**

# Chapter: 8

## Conclusions

### 8.1 Summary and Conclusions

DC plasma torches serve as highly concentrated high enthalpy heat sources for numerous processing applications. Nano-synthesis, waste treatment, spraying, welding, cutting, material processing are few examples. Processes like plasma spraying and synthesis of nano-particles of very high melting point materials demand melting or complete evaporation of the injected particles. Such processes require higher power of the plasma jets together with long enough dwell time of the injected particles inside the plasma under high heat flux. A longer plasma jet with uniform heat flux profile may offer easier control over the melting or evaporation process through proper management of the particle residence time inside the plasma. Although, Nitrogen is long known for its higher arc voltage compared to Argon and its ability to work with common thoriated tungsten cathodes, very few works are reported on thermal and fluid dynamic features of nitrogen plasma jet under different operating conditions. The present study targets this problem and develops a specially designed tungsten cathode segmented electrode plasma torch with nozzle diameter 10 mm for generation of long uniform plasma jet of nitrogen plasma at low and moderate power levels (<50kW). The same torch is suitable for operation with Argon as well. The torch may cater to a range of applications including nano-synthesis and efficient spray coating of refractory ceramics. The thermal, electrical and fluid dynamic behaviour of generated nitrogen plasma jet is investigated through experiments, modelling and simulation under different operating conditions. For comparison purpose similar

studies are made on argon plasma with the same torch. The results are directly relevant to associated application areas.

For heat flux study of argon and nitrogen plasma jets, a double calorimeter device is designed and developed. The plasma jet is characterized by the achieved heat flux profile and temperature distribution. Emission spectroscopic studies are made to determine jet temperature. The instabilities in nitrogen and argon arcs under different operating conditions are analyzed through study of their behaviour in phase and frequency space. The thermodynamic and transport properties needed in the CFD simulation are calculated from ab-initio theoretical calculation. The calculated properties are used to perform CFD simulation of the nitrogen arc to obtain distribution of temperature, velocity, potential and current density inside the nitrogen plasma torch.

Variations in heat flux profile for argon and nitrogen plasma are investigated over a wide range of power level and axial distance. For Argon plasma, the power is varied from 6.6 kW to 52 kW and for Nitrogen plasma the same is varied from 31.98 to 51.03 kW. Obtained heat flux profiles under various operating conditions at different axial distances are characterized in terms of profile width  $R_g$  and peak heat flux  $\Phi_0$ . Obtained results are compared with the results reported in literature.

The axial variations of temperature in argon and nitrogen plasma jets under different operating conditions are determined using Boltzman plot technique. Atomic line spectra are used to determine the temperature of plasma in both the cases. Temperature at the torch exit as a function of arc current and axial variations of plasma temperature are investigated. It has been observed that nitrogen plasma jet possesses higher average temperature compared to argon for similar currents due to

higher supported power through higher arc voltage. One important finding is oscillating variation of axial temperature along the jet axis of the torch for both nitrogen and argon. The fact is explained through mutual interaction among jet current, self magnetic field and aerodynamic flow field. As arc current increases the oscillating region moves away from the nozzle exit and usual exponential drop in temperature prevails near the nozzle. As thermal history of particles depend on the temperature profile, the observed oscillation will play significant role in important processing works like plasma spraying, nanostructure synthesis, spheroidization etc. Another important finding is much longer (nearly ten times) plasma jet in nitrogen compared to argon under same current and gas flow rate for the chosen operating conditions. Obtained results are expected to contribute significantly in the process optimization in different applications.

Inherent instabilities in the developed torch for argon and nitrogen plasma are investigated through phase space and frequency space behaviour under different operating conditions. In both the cases, either random or chaotic dynamics are observed at higher currents and higher flow rates. However, the dynamics exhibit a number of interesting periodic behaviour at lower currents and lower flow rates. Highly periodic behaviour in argon at low flow rate (up to 25 slpm) and doubly periodic behaviour in nitrogen at lower current (at 125A and 200A) are some of the interesting features. From application point of view it is important to know the kind of instabilities exist in a torch under various operating regime. Obtained results may therefore serve as important inputs for parameter optimization in different process needs.

The thermodynamic and transport coefficients serve as indispensable input for numerical simulation. The thesis determines these properties for nitrogen plasma over a wide range of temperature, pressure, thermal and chemical non-equilibrium using Chapman-Enskog approach. Use of a newly proposed definition of charge-charge collision integral and inclusion of thermal and chemical con-equilibrium are novelty of the study. Variation of species densities, mass densities, specific heat, enthalpy, viscosity, thermal conductivity, collision frequency and electrical conductivity are computed as a function of temperature, pressure and different degree of temperature non-equilibrium. Temperature included in the study range from 300 K to 45,000 K, the ratio of electron temperature ( $T_e$ ) to the heavy particle temperature ( $T_h$ ) ranges from 1 to 30 and the pressure ranges from 0.1 to 7 atmospheres. An extensive comparison of the results with the published experimental and theoretical results under similar conditions is provided. An excellent overall agreement is observed.

For a theoretical support of the observed thermal and fluid dynamic behaviour a steady state two-dimensional laminar LTE model of the addressed DC non-transferred arc nitrogen plasma torch is developed. Usual Navier-Stokes equations with appropriately modified source terms are solved using SIMPLER like algorithm under finite volume approach. Distribution of temperature, velocity and potential inside the torch are obtained and compared with experimental data. Both experimentally and theoretically, a distinct change in the temperature and potential distribution inside the plasma torch are observed for the transition from 180A to 200A. Except for this transition region, an overall good agreement is observed between the experimental and theoretical data.

## **8.2 Scope for future work**

- Study of heat flux under normal and oblique incidence for different types of nozzle designs, gases and gas mixtures.
- Study of axial and radial temperature profile for different nozzle designs, gases and gas mixtures.
- Study of time synchronized behaviour of voltage, optical and acoustic instabilities in arcs of different gasses and their nonlinear dynamical analysis.
- Direct probing of the arc instabilities through fast photography.
- Study of thermodynamic properties and transport coefficient for different gases and gas mixtures and modelling corresponding device behaviour.

## Bibliography

- [1] Venkatramani N, Thermal Plasmas in Material Processing, Bull. Mater., Sci., Vol. - 18, No. - 6, pp. – 741-754, 1995
- [2] Boulos M I, Thermal Plasma Processing, IEEE Transactions on Plasma Science, Vol.-19, No.-6, pp.-1078-1089, 1991
- [3] Yanpeng S, Yong N, Angshan W, Dengxiang J, Fengwen Y and Jianbing J, Carbon Dioxide Reforming of Methane to Syngas by Thermal Plasma, Plasma Science and Technology, Vol.-14, No.-3, pp.-252-256, 2012
- [4] Tahara H and Ando Y, Study of Titanium Nitride Deposition by Supersonic Plasma Spraying, Vacuum, Vol.- 83, pp.- 98–101, 2009
- [5] Nayak B B, Arc Plasma Nitriding of Graphite Surface Towards Production of a Hard Carbon Nitride Case, Surface and Coatings Technology, Vol.-201, pp.-2639-2647, 2006
- [6] Yamazato M, Higa A, Oshiro T, Toyama H, Maehama T and Toguchi M, Preparation of Carbon Nitride Films by DC Arc Plasma Jet CVD, Diamond and Related Materials, Vol.-15, pp.- 917-920, 2006
- [7] Balasubramanian C, Godbole V P, Rohatgi V K, Das A K and Bhoraskar S V, Synthesis of Nanowires and Nanoparticles of Cubic Aluminium Nitride, Nanotechnology, Vol.-15, pp.-370-373, 2004

- [8] Kishigami T, Heberlein J V R, and Pfender E, Experimental Investigation of Heat Transfer Between Plasma Jets and Substrate, Int. Symp. on plasma chemistry - 10 (Bochum), 1.3-11 pp.-1, 1991
- [9] Monerie-Moulin F, Gitzhofer F, Fauchais P and Boulos M I, Study of Heat Flux Transmitted by a DC Ar-H<sub>2</sub> Spraying Plasma Jet to a Cold Substrate, Thermal Plasma Applications in Minerals Metallurgical Processing (Warrendale, PA: Minerals, Metals and Material Society), ed. N El-Kaddah pp.-125, 1992
- [10] Ghorui S, Das A K and Venkatramani N, Study of Stagnation Enthalpy Profiles in a Plasma Plume: Comparison between Computation and Experiments, Plasma Sources Sci. Technol. Vol.-9, pp.-108-115, 2000
- [11] Asmann M, Wank A, Kim H, Heberlein J and Pfender E, Characterization of the Converging Jet Region in a Triple Torch Plasma Reactor, Plasma Chemistry and Plasma Processing, Vol.-21, pp.-37-63, 2001
- [12] Meng X, Pan W, Zhang W and Wu C, Heat Flux Characterization of DC Laminar-plasma Jets Impinging on a Flat Plate at Atmospheric Pressure, Plasma Sci. and Technol., Vol.-3, pp.-953-958, 2001
- [13] Tu X, Yu L, Yan J, Cen K and Cheron B, Heat Flux Characteristics in an Atmospheric Double Arc Argon Plasma Jet, Appl. Phys. Letters Vol.-93, pp.-151501-1-3, 2008
- [14] Cheron B G, Robin L and Vervisch P, Parietal Heat Flux Measurement in a Nitrogen Plasma Jet, Meas. Sci. Technol., vol.-3, pp.-58-61, 1992
- [15] Adcock B D and Plumtree W E G, On Excitation Temperature Measurements in a Plasma-Jet and Transition Probabilities for Argon Lines, J. Quant. Spectrosc. Radiat. Transfer., Vol.-4, pp.-29-39, 1964

- [16] Snyder S C, Reynolds L D, Lassahn G D, Fincke J R and Shaw C B Jr.,  
Determination of Gas-Temperature and Velocity Profiles in an Argon Thermal-  
Plasma Jet By Laser-Light Scattering, Physical Review E, vol.-47, No.-3, pp.-1996-  
2005, 1993
- [17] Fincke, J R, Snyder S C, and Swank W D, Comparison of Enthalpy Probe and  
Laser Light Scattering Measurement of The Thermal Plasma Temperatures and  
Velocities, Rev. Sci. Instrum., vol.-64, pp.-711-718, 1993
- [18] Joshi N K, Sahasrabudhe S N, Sreekumar K P and Venkatramani N, Variation of  
Axial Temperature in Thermal Plasma Jets, Meas. Sci. Technol. Vol.-8, pp.-1146-  
1150, 1997
- [19] Gregori G, Schein J, Schwendinger P, Kortshagen U, Heberlein J and Pfender E,  
Thomson Scattering Measurements in Atmospheric Plasma Jets, Physical Review E  
Vol.-59, No.-2, pp.-2286-2291, 1999
- [20] Feng X, Enthalpy Probe Technique for Thermal Plasma Diagnostics, Plasma  
Science & Technology, Vol.-5, No.-4, pp.-1909-1914, 2003.
- [21] Tu X, Cheron B G, Yan J H and Cen K F, Electrical and Spectroscopic  
Diagnostic of an Atmospheric Double Arc Argon Plasma Jet, Plasma Sources Sci.  
Technol. Vol.-16, pp.-803-812, 2007
- [22] Wang P J, Tzeng C C, and Liu Y, Thermal Temperature Measurements of Plasma  
Torch by Alexandrite Effect Spectropyrometer, Advances in Optical Technologies,  
vol.-2010, pp.-656421-1-7, 2010

- [23] Hlina J and Sonsky J, Time-Resolved Tomographic Measurements of Temperatures in a Thermal Plasma Jet, *J. Phys. D: Appl. Phys.* Vol.-43, pp.-055202-1-9, 2010
- [24] Emilie L B and Charles de I, Experimental Characterization of an Argon Laminar Plasma Jet At Atmospheric Pressure, *J. Phys. D: Appl. Phys.* Vol.-44, pp.-415201-1-9, 2011
- [25] Yan J H, Tu X, Ma Z Y, Cen K F, B G. Cheron, Rotational and Vibrational Temperatures of Atmospheric Double Arc Argon-Nitrogen Plasma, *Chin. Phys. Lett.*, Vol.-24, No.-5, pp.-1317-1320, 2007
- [26] Belevtsev A A, Chinnov V F and Isakaev E K, Emission Spectroscopy of Highly Ionized High-Temperature Plasma Jets, *Plasma Sources Sci. Technol.*, Vol.-15, pp.-450-457, 2006
- [27] Tu X, Cheron B G, Yan J H, Yu L, and Cen K F, Characterization of an Atmospheric Double Arc Argon-Nitrogen Plasma Source, *Physics of Plasmas*, Vol.-15, pp.-053504-1-10, 2008
- [28] Vardelle A, Baronnet J M, Vardelle M, and Fauchais P, Measurements of the Plasma and Condensed Particles Parameters in a DC Plasma Jet, *IEEE Transactions on Plasma Science*, Vol.-Ps-8, No. 4, pp.-417-424, 1980
- [29] Jahn R E, Temperature Distribution and Thermal Efficiency of Low Power Arc-Heated Plasma Jets, *Brit. J. Appl. Phys.*, Vol.-14, pp.-585-588, 1963
- [30] Prevosto L, Kelly H, and Mancinelli B R, Langmuir Probe Diagnostics of an Atmospheric Pressure, Vortex-Stabilized Nitrogen Plasma Jet, *Journal of Applied Physics* Vol.-112, pp.-063302-1-7, 2012

- [31] Pfender E, Thermal Plasma Technology: Where Do We Stand and Where Are We Going?, Plasma Chemistry and Plasma Processing, Vol.-19, No.-1, pp.-1-31, 1999
- [32] Fauchais P, Understanding Plasma Spraying, J. Phys. D: Appl. Phys. Vol.-37, pp.-R86-R108, 2004
- [33] Ghorui S and Das A K, Application of Nonlinear Dynamic Techniques to High Pressure Plasma Jets, Journal of Physics: Conference Series, Vol.-208, pp.-012057-1-15, 2010
- [34] Coudert J F, Planche M P, and Fauchais P, Characterization of D.C. Plasma Torch Voltage Fluctuations, Plasma Chemistry and Plasma Processing, Vol.-16, No.-1, pp.-211S-227S, 1996
- [35] Coudert J F, Rat V and Rigot D, Influence of Helmholtz Oscillations on Arc Voltage Fluctuations in a DC Plasma Spraying Torch, J. Phys. D: Appl. Phys., Vol.-40, pp.-7357-7366, 2007
- [36] Ghorui S, Vysohlid M, Heberlein J V R, and Pfender E, Probing Instabilities in Arc Plasma Devices Using Binary Gas Mixtures, Physical Review E, Vol.-76, pp.-016404-1-13, 2007
- [37] Krowka J, Rat V and Coudert J F, Investigation and Control of DC Arc Jet Instabilities to Obtain a Self-Sustained Pulsed Laminar Arc Jet, J. Phys. D: Appl. Phys., Vol.-46, pp.-505206-1-13, 2013
- [38] Ghorui S, Sahasrabudhe S N, Murthy P S S, Das A K, and Venkatramani N, Experimental Evidence of Chaotic Behavior in Atmospheric Pressure Arc Discharge, IEEE Transactions on Plasma Science, Vol.-28, No.-1, pp.-253-260, 2000
- [39] Ghorui S, Sahasrabudhe S N, Murthy P S S, Das A K, and Venkatramani N, Dynamic Characteristics of a Hollow Copper Electrode Plasma Torch Through

- Measurement and Analysis of Acoustic, Optical, and Voltage Fluctuations, IEEE Transactions on Plasma Science, Vol.-28, No.-6, pp.-2179-2186, 2000
- [40][41] Duan Z and Heberlein J, Arc Instabilities in a Plasma Spray Torch, Journal of Thermal Spray Technology, Vol.-11, No.-1, pp.-44-51, 2002
- [41] Zhao W, Tian K, Tang H, Liu D and Zhang G, Experimental Studies on the Unsteadiness of Atmospheric Pressure Plasma Jet, J. Phys. D: Appl. Phys., Vol.-35, pp.-2815-2822, 2002
- [42] Cheron B G, Bultel A, and Delair L, Experimental Study of a Double Arc Nitrogen Plasma: Static and Dynamic Behavior, IEEE Transactions on Plasma Science, Vol.-35, No.-2, pp.-498-508, 2007
- [43] Ghorui S, Heberlein J V R and Pfender E, Non-Equilibrium Modeling of an Oxygen-Plasma Cutting Torch, J. Phys. D: Appl. Phys. Vol.-40, pp.-1966-1976, 2007
- [44] Yun K S, Weissman S and Mason E A, High Temperature Transport Properties of Dissociating Nitrogen and Dissociating Oxygen, Phys. Fluids Vol.-5, pp.-672-678, 1962
- [45] Guevara F A, McInteer B B and Wageman W E, High Temperature Viscosity Ratios For Hydrogen, Helium, Argon, and Nitrogen, Phys. Fluids, Vol.-12, pp.-2493-2505, 1969
- [46] Tsitelauri N N, Candidate's Dissertation, ENIN Academy of the Sciences of the USSR, 1969
- [47] Hermann W and Schade E, Transport Properties of Nitrogen up to 26,000 °K, Z. Phys. Vol.-233, pp.- 333-350, 1970
- [48] Capitelli M and Devoto R S, Transport Coefficients of High Temperature Nitrogen, Phys. Fluids Vol.-16, pp.-1835-1841, 1973

- [49] Capitelli M, Gorse C and Fauchais P, Transport Coefficients of High Temperature N<sub>2</sub>-H<sub>2</sub> Mixtures, J. Phys. (Paris) Vol.-38, pp.-653-657, 1977
- [50] Murphy A B and Arundell C J, Transport Coefficients of Argon, Nitrogen, Oxygen, Argon-Nitrogen, and Argon-Oxygen Plasmas Plasma, Plasma Chemistry and Plasma Processing, Vol.-14, pp.-451-490, 1994
- [51] Colombo V, Ghedini E and Sanibondi P, Thermodynamic and Transport Properties in Non-Equilibrium Argon, Oxygen and Nitrogen Thermal Plasmas, Prog. Nucl. Energy, Vol.-50, pp.-921-933, 2008
- [52] Wang W, Rong M, Yan J D, Murphy A B and Spencer J W, Thermophysical Properties of Nitrogen Plasmas Under Thermal Equilibrium and Non-Equilibrium Conditions, Phys. Plasmas, Vol.-18, pp.-113502-1-18, 2011
- [53] Murphy A B, Transport Coefficients of Plasmas in Mixtures of Nitrogen and Hydrogen, Chemical Phys. Vol.-398, pp.-64-72, 2012
- [54] Ghorui S and Das A K, Collision Integrals for Charged-Charged Interaction in Two-Temperature Non-Equilibrium Plasma, Phys. Plasmas, Vol.-20, pp.-093504-1-8, 2013
- [55] Ghorui S, Heberlein J V R and Pfender E, Thermodynamic and Transport Properties of Two-Temperature Oxygen Plasmas, Plasma Chemistry and Plasma Processing, Vol.-27, pp.-267-291, 2007
- [56] Westhoff R and Szekely J, A Model of Fluid, Heat Flow, and Electromagnetic Phenomena in a Non-Transferred Arc Plasma Torch, J. Appl. Phys., Vol.-70, pp.-3455-3466, 1991

- [57] Bauchire J M, Gonzalez J J and Gleizes A, Modeling of a DC Plasma Torch in Laminar and Turbulent Flow, Plasma Chemistry and Plasma Processing, Vol.-17, No.-4, pp.-409-432, 1997
- [58] Hsu K C and Pfender E, Two-Temperature Modeling of the Free-Burning, High-Intensity Arc, J. Appl. Phys. Vol.-54, pp.-4359-4366, 1983
- [59] Kaddani A, Zahrai S, Delalondre C and Simonin O, Three-Dimensional Modelling of Unsteady High-Pressure Arcs in Argon, J. Phys. D: Appl. Phys., Vol.-28, pp.-2294-2305, 1995
- [60] Zhao G Y, Dassanayake M and Etemadi K, Numerical Simulation of a Free-Burning Argon Arc with Copper Evaporation from the Anode, Plasma Chemistry and Plasma Processing, Vol.-10, No.-1, pp.-87-98, 1990
- [61] Gleizes A, Bouaziz M, Gonzalez J J and Razafinimanana M, Influence of the Anode Material on an Argon Arc, IEEE Transactions on Plasma Science, Vol.-25, No.-5, pp.-891-896, 1997
- [62] Schmidt H P and Speckhofer G, Experimental and Theoretical Investigation of High-pressure Arcs-Part I: The Cylindrical Arc Column (Two-Dimensional Modeling), IEEE Transactions on Plasma Science, Vol.-24, No.-4, pp.-1229-1238, 1996
- [63] Speckhofer G and Schmidt H P, Experimental and Theoretical Investigation of High-pressure Arcs-Part 11: The Magnetically Deflected Arc (Three-Dimensional Modeling), IEEE Transactions on Plasma Science, Vol.-24, No.-4, pp.-1239-1248, 1996

- [64] Chen D M and Pfender E, Modeling of The Anode Contraction Region of High Intensity Arcs, IEEE Transactions on Plasma Science, Vol.-Ps-8, No.-3, pp.-252-259, 1980
- [65] Wilhelmi H, Wimmer W and Pfender E, Modeling of the Transport Phenomena in the Anode Region of High Current Arcs, Numerical Heat Transfer, Vol.-8, pp.-731-749, 1985
- [66] Chau S W, Hsu K L, Lin D L, Chen J S, and Tzeng C C, Modelling and Experimental Validation of A 1.2 MW DC Transferred Well-Type Plasma Torch, Computer Physics Communications Vol.-177, pp.-114-117, 2007
- [67] Peng Z, Yue-Dong M and Masaaki N, Volt - Ampere Characteristics of a Nitrogen DC Plasma Arc with Anode Melting, Chin. Phys. B, Vol.-22, No.-6, pp.-064701-1-9, 2013
- [68] Selvan B, Ramchandran K, Sreekumar K P and Ananthapadmanabhan P V, Modeling of Non-Transferred Argon-Nitrogen Plasma Arc and Plasma Jet, 23<sup>rd</sup> National Symposium on Plasma Science And Technology, Journal of Physics: Conference Series, Vol.-208, pp.- 012047, 2010
- [69] Ghorui S and Das A K, Exploring Chemical and Thermal Non-Equilibrium in Nitrogen Arcs, Journal of Physics: Conference Series Vol.-406, pp.-012012-1-8, 2012
- [70] Ion Arc Technology Pvt. Ltd., Coimbatore, India
- [71] Ocean Optics, USA, [www.oceanoptics.com](http://www.oceanoptics.com)
- [72] Hameg Instrumentrts, Germany, [www.hameg.com](http://www.hameg.com)
- [73] Collares M P and Pfender E, Effect of Current Connection to the Anode Nozzle on Plasma Torch Efficiency, IEEE Trans. Plasma. Sci. Vol.-25, pp.-864-871, 1997

- [74] Sanders N, Etemadi K, Hsu K C and Pfender E, Studies of the Anode Region of a High - Intensity Argon Arc, *J. Appl. Phys.* Vol.-53, pp.-4136-4145, 1982
- [75] Pfender E, Energy Transport in Thermal Plasmas, *Pure and Appl. Chem.*, Vol.-52, pp.-1773-1800, 1980
- [76] Ghorui S and Das A K, Origin of Fluctuations in Atmospheric Pressure Arc Plasma Devices, *Phys. Rev. E*, Vol.-69, pp.-026408-1-7, 2004
- [77] Ghorui S, Sahasrabudhe S N, Murthy P S S and Das A K, Current Transfer in DC Non-transferred Arc Plasma Torches, *J. Phys. D: Appl. Phys.* Vol.-43, pp.- 245201-1-18, 2010
- [78] Kovitya P and Lowke J J, Two-dimensional Analysis of Free Burning Arcs in Argon, *J. Phys. D: Appl. Phys.*, Vol.-18, pp.-53-70, 1985
- [79] Murphy A B, Boulos M I, Colombo V, Fauchais P, Ghedini E, Gleizes A, Schram D C, *Advanced Thermal Plasma Modelling*, *High Temp. Material Process.* Vol.-12, pp.-255-336, 2008
- [80] Mermet J M, *Inductively Coupled Plasma Spectrometry and its Application*, Chapter-2, Ed. Steve J. Hill, Sheffield Academic press, England, pp.-43-44, 1999
- [81] *Introduction to Plasma Spectroscopy*, Springer series on atomic, optical and plasma physics, Springer Verlag Berlin Heidelberg, 2009
- [82] Ghorui S and Das A K, Theory of Dynamic Behaviour in Atmospheric Pressure Arc Plasma Devices: Part-I: Theory and System Behaviour, *IEEE Transactions on Plasma Science*, Vol.-32, pp.-296-307, 2004
- [83] Ghorui S, Sahasrabudhe S N, Murthy P S S and Das AK, Theory of Dynamic Behaviour in Atmospheric Pressure Arc Plasma Devices: Part-II: Validation of Theory

with Experimental Data, IEEE Transactions on Plasma Science, Vol.32, pp.-308-315, 2004

[84] Packard N H, Crutchfield J P, Farmer J D, and Shaw R S, Geometry from a Time Series, Physical Review Letters, Vol.-45, pp.-712-716, 1980

[85] Huber K P and Herzberg G, Molecular Spectra and Molecular Structure: IV. Constants of Diatomic Molecules, Van Nostrand Reinhold Co, New York, JANAF Thermochemical Tables, 1979

[86] Hirschfelder J O, Curtiss C F and Bird R B, Molecular Theory of Gases and Liquids, 2nd edn., Wiley, New York, 1964

[87] Chapman S and Cowling T G, The Mathematical Theory of Non-Uniform Gases, Cambridge University Press, Cambridge, 1952

[88] Capitelli M, Gorse C and Longo S, Collision Integrals of High-Temperature Air Species, J Thermo. Phys. Heat Transfer Vol.-14, pp.-259-268, 2000

[89] Leonas V B, Studies of Short-Range Intermolecular Forces, Soviet Physics Uspekhi, Vol.-15, pp.- 266-280, 1973

[90] Ramshaw J D, Simple Approximation for Thermal Diffusion in Ionized Gas Mixtures, J. Non-euilib. Thermodyn., Vol.-21, pp.-233-238, 1996

[91] Devoto R S, Transport Properties of Ionized Monatomic Gases, Phys. Fluids, Vol.-9, pp.-1230-1240, 1966

[92] Li H P and Chen X, Diffusion in Two-Temperature Partially Ionized Gases, Chin. Phys. Lett., Vol.-18, pp.-547-549, 2001

[93] Devoto R S, Simplified Expressions for the Transport Properties of Ionized Monatomic Gases, Phys. Fluids, Vol.-10, pp.-2105-2112, 1967

- [94] Bose T K, Kannappan D and Seeniraj R V, On Reactive Heat Conduction for Multiple Ionized Two-Temperature Argon Plasma, *Warme-und Stoffubertragung* Vol.-19, pp.-3-8, 1985
- [95] Mitchner M and Kruger C H, *Partially Ionized Gases*, Wiley, New York, 1973
- [96] Selle S and Riedel U, Transport Properties of Ionized Species, *Annals of the New York Academy of Science*, Vol.-891, pp.-72-80, 1999
- [97] Cubley S J and Mason E A, Atom-Molecule and Molecule-Molecule Potentials and Transport Collision Integrals for High-Temperature Air Species, *Phys. Fluids* Vol.-18, pp.-1109-1111, 1975
- [98] Yun K S and Mason E A, Collision Integrals for the Transport Properties of Dissociating Air at High Temperatures, *Phys. Fluids*, Vol.-5, pp.-380-386, 1962
- [99] Levin E, Patridge H and Stallcop J R, Collision Integrals and High Temperature Transport Properties for N-N, O-O, and N-O, *J. Thermophys.* Vol.-4, pp.-469-477, 1990
- [100] Gupta R N, Yos JM, Thomson RA, Lee KM NASA Reference publication 1232. NASA Langley Research Center, Hampton, VA 54, 1990
- [101] Yos J M Technical Memorandum RAD-TM-63-7. AVCO Corporation, Wilmington, MA, 1963
- [102] Plantikow U, Transport Coefficients of the N<sub>2</sub>-Plasma up to 13,000 °K, *Z. Phys.*, Vol.-237, pp.-388-402, 1970
- [103] Neuberger A W, Composition, Electrical Conductivity, and Total Radiation of Nitrogen Plasma, *AIAA J.* Vol.-13, pp.-3-4, 1975

- [104] Asinovsky E I, Kirillin A V, Pakhomov E P and Shabashov V I, Experimental Investigation of Transport Properties of Low-Temperature Plasma by Means of Electric Arc, Proc. IEEE, Vol.-59, pp.-592-601, 1971
- [105] Boulos M I, Fauchais P and Pfender E, Thermal Plasmas Fundamentals and Applications, Vol.-1, Plenum Press, New York, 1994
- [106] Krey R U, Morris J C, Experimental Total and Total Line radiations of Nitrogen, Oxygen, and Argon Plasmas, Thet Phys. Fluids, pp. 1483-1486, 1970
- [107] Patankar S V, Numerical Heat Transfer and Fluid Flow, McGraw-Hill, New York, 1980
- [108] Zhu J, FAST-2D: A Computer Program for Numerical Simulation of Two-Dimensional Incompressible Flows with Complex Boundaries, Report No. 690, Institute of Hydromechanics, University of Karlsruhe, Germany, 1991
- [109] Majumdar S, Development of a Finite-Volume Procedure for Prediction of Fluid Flow Problems with Complex Irregular Boundaries, Report No. SFB 210/T/29, University of Karlsruhe, Germany, 1986